Identification of Biomolecules using Thermoplastic Nanofluidic Devices for Applications in Single-Molecule Sequencing

By

© 2022

Chathurika Rathnayaka

M.S.C., Sam Houston State University, 2018

M.S.C., Postgraduate Institute of Science, University of Peradeniya, Sri Lanka 2015

B.Sc., University of Peradeniya, Sri Lanka, 2012

Submitted to the graduate degree program in Department of Chemistry and the Graduate Faculty of the University of Kansas in partial fulfillment of the requirements for the degree of Doctor of Philosophy.

Chairperson: Prof. Steven A. Soper

Prof. Susan M. Lunte

Prof. Robert C. Dunn

Prof. Mikhail V. Barybin

Prof. Sara E. Wilson

Date Defended: 02 May 2022

The dissertation committee for Chathurika Rathnayaka certifies that this is the approved version of the following dissertation:

Identification of Biomolecules using Thermoplastic Nanofluidic Devices for Applications in Single-Molecule Sequencing

Chairperson: Prof. Steven A. Soper

Date Approved: 09 May 2022

Abstract

We are developing an innovative Single-Molecule Sequencing (SMS) strategy that consists of enzymatically cleaving intact RNAs using a processive enzyme to generate individual ribonucleotide monophosphates (rNMPs). This can be achieved using a processive enzyme, such as exoribonuclease 1 (XRN-1). We have recently shown that this enzyme can be tethered to a solid support and processively clip in the 5' → 3' direction an RNA strand into its constituent rNMPs when activated by the cofactor, Mg^{2+}. The released rNMPs are then electrokinetically transported through a nanochannel one-at-a-time with the electrophoretic travel time through a nanometer column used to identify each rNMP. Therefore, a thorough understanding of the electrophoretic properties of the rNMPs through nanochannels made from thermoplastics that determine their molecular-dependent mobility will allow high identification accuracy of the rNMPs.

In this study, the electrophoretic properties of the rNMPs were investigated in different nanochannel materials. Here, we thermally fusion bonded different plastic substrates containing nanochannels (100 nm × 100 nm, width × depth, and 100 μm in length) with a cover plate made from COC and the change in the electroosmotic flow was investigated by varying UV/O_3 dosing time, which changed the amount of surface charge, after device assembly. Nano-electrophoresis of the rNMPs labeled with an ATTO-532 dye reporter were tracked using an epifluorescence microscope. Micro-electrophoresis of ATTO-532 tagged rNMPs were investigated but could not achieve baseline resolution for the rCMP/rAMP couple. Nanoscale electrophoresis of the dye-labeled rNMPs were explored in both poly(methyl methacrylate) (PMMA) and COC nanochannel devices and higher resolution (>1.5) was achieved with the COC nanochannel device for all four rNMPs compared to PMMA. The results acquired for COC nanoscale electrophoresis indicated high identification accuracy (>99%) of the rNMPs. Furthermore, we were able to separate the

methylated rNMPs from their non-methylated counterparts, which will provide insight for identifying epitranscriptomal modifications using our SMS strategy.

Our final exonuclease time of flight (X-TOF) nano sensor will utilize label-free rNMPs by using resistive pulse sensing (RPS) that used in-plane nanopores. Therefore, we investigated a simple method for tailoring the size of in-plane nanopores for sensing label-free rNMPs. The nano sensor consists of 2 in-plane pores that flank a nanometer flight tube (length = 5 μm; width × depth = 50 × 50 nm) fabricated in thermoplastics via replication technology. We could reduce the width and depth of the in-plane nanopores from ~30 × 30 nm to ~17 × 10 nm during the thermal fusion bonding (TFB) process, which placed a cover plate over the imprinted substrate under a controlled pressure and temperature to form enclosed nanofluidic devices. Increased pressures during TFB caused the size of the in-plane pore to be reduced. The in-plane nanopores fabricated with different TFB pressures were utilized to detect single λ-DNA molecules via RPS, which showed a higher current amplitude in devices bonded at higher TFB pressures. Using this method, we also showed the ability to tune the pore size to detect single rNMP molecules. Translocation of rNMPs through in-plane pores were initially explored using O_2 plasma treated PMMA devices and 1× NEBuffer 3 at pH 7.9; low event frequency was observed due to a combination of ion exclusion and electroosmostic forces arising from surface carboxy groups. The surface carboxylic acid groups generated via O_2 plasma activation was modified with ethanolamine via EDC/NHS coupling chemistry. Ethanolamine modification of thermoplastics was characterized by sessile water contact angle measurements and attenuated total reflectance Fourier transform infrared spectroscopy (ATR-FTIR). The surface charge and electroosmotic flow (~10 fold) were found to be reduced upon ethanolamine modification of the PMMA surface. The event frequency of the dual in-plane nanopore sensor (60 events/s for 10 nM rAMPs) increased significantly upon ethanolamine

modification. The average ToF, current blockage amplitude, and dwell time for rAMPs was 4.14 ± 0.97 ms, 425.89 ±175.89 pA, and 0.31 ±0.26 ms, respectively.

Furthermore, we investigated geometrical effects on the sampling efficiency of rNMPs using the dual in-plane nanopore sensor. We showed increased capture efficiency with tapered geometries via both experimental and COMSOL simulations. We utilized the dual in-plane nanopore device with 5 μm and 10 μm long nano flight tubes and showed an increase in identification accuracy with increasing length of the nano-flight tube. Moreover, we generated scatter plots to identify rNMPs based on two variables and PCA plots showed correlation of each factor (peak amplitude, TOF, dwell time) in the identification of rNMPs. Furthermore, ablation of the PMMA substrate was demonstrated upon activation with UV/O_3 light, which was not seen with COP nanofluidic devices. In addition, dual in-plane nanopore devices were fabricated in COP using injection molding, which showed the ability to be used in label-free identification of rNMPs based upon unique molecular-dependent TOFs.

In addition, we studied the electrokinetic identification of peptides using thermoplastic nanochannels, which will be utilized in single molecule peptide fingerprinting. We performed nanoscale electrophoresis of peptides using different electrophoretic conditions, such as electric field strength, and material effects including modified surfaces. We used O_2 plasma activated PMMA/COC, UV/O_3 activated COC/COC, and ethanolamine modified PMMA/COC hybrid devices to perform nanoscale electrophoresis at different electroosmotic flow conditions. We also showed efficient identification of several peptides using free solution nanoscale electrophoresis via their molecular-dependent mobilities with efficiencies >99.99% in unmodified PMMA/COC and ethanolamine modified PMMA/COC nanofluidic devices.

Acknowledgments

This dissertation has become a reality with the kind support and help of many individuals. I would like to extend my sincere thanks to all of them. Foremost, I would like to express special gratitude to my advisor, Professor Steven Allan Soper, for his guidance, advice, and encouragement toward the completion of PhD career. Without his guidance and persistent help this dissertation would not have been possible. I would also like to express my gratitude towards my dissertation committee members, Prof. Susan M. Lunte, Prof. Robert Dunn, Prof. Misha Barybin and Prof. Sara Wilson for their suggestions toward completing this dissertation and for their valuable time.

In addition, I would like to thank all Soper research group members, past and present. A special thank you goes to Dr. Maggie Witek, Dr. Matt Hupert, Dr. Charuni Amarasekara, Dr. Uditha Athapattu, Dr. Thilanga Pahattuge, Dr. Kumuditha Weerakoon-Rathnayake, Dr. Anishkumar Manoharan, Dr. Zheng Zhao, Chad Vietz, Hanna Nguyen, Katie Childers, Khurshed Akabirov, Maximillian Chibuike and Ian Freed. I would also like to thank our collaborators, Dr. Sunggook Park, Dr. Junseo Choi, Dr. Adam Hall, and Mr. Aaron Nagel, for their support in carrying out the research projects.

Finally, I would like to thank my beloved and supportive husband, Sanjaya Gamaethige for his advice, guidance, and encouragement through the duration of this work. I would also like to express my gratitude, my parents, my brother and my daughter for their unconditional love, encouragement and support throughout my life.

Table of Contents

List of Figures

design of the dual in-plane nanopores used for COMSOL simulations. The pore and intervening 5 μm long nanochannel were assumed to be cylindrical. In order to understand if a change of in-plane nanopore diameter would cause an increase in conductance, the pore diameter was varied from 10-50 nm while the length was kept constant at 30 nm. **(B)** The electric potential data from COMSOL simulations shows that the majority of the potential drop appears across the two nanopores and the nanochannel implying that the overall conductance is contributed by the two nanopores and the nanochannel. **(C)** The current density was plotted from which the current and the subsequent conductance was calculated (I/V). **(D)** Conductance (nS) calculated from COMSOL for varying pore widths in 1 M KCl. There was a linear increase in conductance with increasing pore width. **(E)** Variation of measured conductance through the dual in plane nanopore PMMA and COP devices at different bonding conditions using an electrolyte of 1 M KCl ($n \geq 3$). There was a decrease in conductance with increase in bonding pressure, but with no statistical differences at pressures above 130 psi ($p > 0.05$). The conductance results agree with the pore size determined using AFM and SEM and were also correlated to the COMSOL results. The y-axis scales of graphs for (**D**) and (**E**) are adjusted according to their corresponding x-axis and hence the range might be different. 118

Figure 3.5 λ-DNA translocation through the dual in-plane PMMA nanopores and the ramifications of the size of the nanopore on peak amplitude. (A) Schematic of the λ-DNA translocation through the in plane dual nanopore device that gives rise to a negative peak as the DNA enters the first pore. Since the contour length of the DNA is longer than both the pores, there is a second subsequent peak when the DNA co-resides in both the pores. The DNA then leaves the pores very quickly which makes the current return to the baseline. (B) Detected current transient trace typically observed in a time interval of 400 s as a result of λ-DNA translocation and magnified

List of Tables

Abbreviations and Acronyms

LOC	Lab-on-a-chip
POCT	Point-of-care-testing
nEP	Nanoscale electrophoresis
nEC	Nanoscale electrochromatography
AFM	Atomic force microscopy
SEM	Scanning electron microscopy
NIL	Nano imprint lithography
EDL	Electric double layer
PDMS	Polydimethylsiloxane
PMMA	Poly(methyl methacrylate
EOF	Electroosmotic flow
MD	Molecular dynamics
EBL	Electron beam lithography
FIB	Focused ion beam milling
COC	Cyclic olefin copolymer
PC	Poly carbonate
PET	Polyethylene terephthalate
T_g	Glass transition temperature
IM	Injection molding
ICM	Injection compression molding
LIF	Laser induced fluorescence
TLS	Thermal lens spectrometry

RPS	Resistive pulse sensing
DIC-TLM	Differential interference contrast thermal lens microscopy
EK	Electrokinetic
FL	Fluorescein
ssDNA	Single stranded DNA
dsDNA	Double stranded DNA
dNMPs	Deoxynucleotide monophosphates
PEGDA	Polyethylene glycol diacrylate
TOF	Time-of-flight
NGS	Next generation sequencing
c-DNA	Complementary DNA
RNA-seq	RNA sequencing
RT	Reverse transcriptases
SMS	Single-molecule sequencing
PNPase	Polynucleotide phosphorylase
rNDPs	Ribonucleotide diphosphates
P_i	Inorganic phosphate
αHL	α-Hemolysin
XRN1	Exoribonuclease 1
rNMPs	Ribonucleotide monophosphates
DMF	Dimethylformamide
HPLC	High performance liquid chromatography
LRMS	Low-resolution mass spectra

IPA	Isopropyl alcohol
ACP	Air cushion press method
rRNA	Ribosomal RNA
tRNA	Transfer RNA
mRNA	Messenger RNA
m6A	N6-methyladenosine
m1A	N1-methyladenosine
5-mC	5-methylcytidine
5-hmC	5-hydroxymethylcytidine
TFB	Thermal fusion bonding
P-SPEL	Pressed self-perfection by liquefaction
PI	Polyimide
SNR	Signal-to-noise ratio
ssRNA	Single-stranded RNA
HF	Hydrofluoric acid
KOH	Potassium hydroxide
TPGDA	Tri(propylene) glycol
TMPTA	Trimethylolpropane
ATR-FTIR	Attenuated total reflectance Fourier transform infrared spectroscopy
COP	Cyclic olefin polymer
FEB	Focused electron beam
PCA	Principal component analysis

Chapter 1: Nanofluidic Devices for Separation of Biomolecules

This chapter is based on the following manuscript,

"Nanofluidic Devices for Biomolecular Separations"

Reprinted with permission from – {**Rathnayaka, C.***; Amarasekara, C. A.*; Soper, S. A. Nanofluidic Devices for Separation of Biomolecules. Submitted for publication in *Journal of Chromatography A.*

* These authors contributed equally to this work.

1.1 Introduction

There are numerous applications of analytical separations that have enabled a number of biotechnology areas, such as determining the results of molecular biological reactions that generate products requiring identification (*i.e.*, biomolecules). A few examples include PCRs for DNA fingerprinting, DNA sequencing when using Sanger approaches, multi-dimensional separations for proteomics, and mutation detection and scanning assays for *in vitro* diagnostics. Conventional electrophoresis and chromatography can provide both qualitative (what is in the sample) and quantitative (how much of each component is in the sample) information to either provide clinical information of discovery of new biomarkers to associate with certain clinical indications across many disease states. Chromatographic methods have been the mainstay of biological and biomedical separations for a long time, this technique typically requires large input sample volumes, slow development times, and provides limited separation efficiency due to technique-dependent dispersion effects. Recently, electrophoresis has been found to address these issues by requiring smaller sample volumes and typically generates higher efficiencies due to plug flow and no kinetic issues arising from mass transfer between immiscible phases as well as no Eddy dispersion because of the need for no packed columns. However, in some cases sieving matrices are required to affect the electrophoretic separation, for example in the case of nucleic acids.

Miniaturization of analytical separations, for example microchip electrophoresis, has many benefits including further reducing the sample/reagent volume requirements, the ability to perform parallel analyses to enable high throughput processing, reduced separation times, and the potential for integrating the separation steps with lab-on-a-chip (LOC) devices that can perform sample preparation to enable point-of-care testing, POCT.[1, 2] In the past decades,

there have been impressive developments in the field of microfluidic devices for many bioanalytical separations and several concepts have been commercialized.[3, 4]

As an example of the benefits of capillary and microchip electrophoresis, capillary gel electrophoresis in the context of Sanger sequencing offered some attractive advantages compared to slab-gel electrophoresis, such as the ability to use higher electric field strengths reducing development time, simplicity of operation by negating the need for gel pouring, reduced sample consumption, and higher electrophoretic resolution.[5-7] Later, microchip electrophoresis was used for Sanger sequencing and its main advantage was the need for a reduced separation column length (50 cm → 10 cm) allowing for reduced development time increasing throughput, and also allowing for integration of sample pre-processing to the separation platform.[8-10] However, it should be noted that the transition from capillary to microchip electrophoresis did not offer new separation modalities due to similarities in the cross-section of the separation columns (~75 × 75 μm). However, in microchip electrophoresis, shorter columns were typically used providing shorter development times and thus, higher throughput.

Although microchip electrophoresis has been useful in several bioanalytical applications, nanofluidics is quite different due to unique nanoscale phenomena occurring on this length scale that is not associated with microchip separations due to scaling effects. Here we define nanofluidics as devices that use either one (nanoslits) or two (nanochannels) dimensions that are <~100 nm. We will also discuss extended nanofluidics and that is defined as the use of columns with at least 1 dimension >150 nm, but <1 μm.[11]

Unique separations can be observed using nanofluidics due to phenomena that occurs only

on the nanometer scale including high surface area-to-volume ratios, potential EDL overlap creating parabolic flow for electrically driven systems, transverse electromigration, concentration polarization, surface charge dominating flow, and surface roughness effects.[12] All of the aforementioned nanoscale phenomena can have profound impacts on a separation and therefore, unique separations can be undertaken using nanofluidics such as those that occur for nanoscale electrophoresis (nEP) [13] and nanoscale electrochromatography (nEC).[12, 14] A unique feature of nanofluidics is that the relevant length scale is comparable with the range of surface and interfacial forces in fluids, such as van der Waals forces and electrostatic and steric interactions. When a fluidic channel approach nanoscale dimensions, changes in the dominating forces together with the transport dynamics, deviate from typical micro- and macroscale descriptions.[15, 16] In addition, due to increased surface area-to-volume ratio in nanochannels, surface charge governed transport becomes apparent.[13] Wall adsorption and desorption of molecules is another important aspect associated with nanofluidics. Adsorption/desorption events can be reversible or irreversible depending on the magnitude of the interaction energy and are utilized by many nEC separations using nanofluidic channels, which can be done in open channels due to the smaller diffusional distances.[14, 17]

The development of new technologies for both the creation of nanostructures and their inspection, such as electron beam lithography and focused ion beam milling for fabrication, and atomic force microscopy (AFM) and scanning electron microscopy (SEM) for inspection, has created the opportunity for using nanoscale columns for routine use in analytical separations. In addition, techniques such as nanoimprint lithography (NIL) and nano-injection molding provide the ability to replicate nanometer structures into a variety of materials in a high production mode to reduce device cost to increase accessibility of nanoscale columns.

With the advent of these fabrication techniques to allow increasing the availability of nanoscale columns, new insights into nanofluidics in a variety of fields including bioengineering, medicine, and chemistry have been realized.[18] Furthermore, significant developments in molecular dynamic simulations have become useful in understanding ion transport, separation behaviour, and surface effects within nanometer domains.[19, 20]

1.2 Unique phenomena affecting separations in nanofluidic devices

Nanofluidics is the study of fluid behaviour inside or around objects of which at least one dimension (depth, width, or length) is <~100 nm. Length scales extended in the range of 100 – 1000 nm is also relevant and is known as extended nanofluidics.[21] Nanoslits are defined as conduits with one dimension <100 nm, while nanochannels are conduits with two dimensions <100 nm.[11, 22] Unique physical phenomena that are not observed in the micro- and macroscale domains can dominate in nanoscale domains providing new separation modalities. Nanoscale-dependent phenomena include concentration polarization, ion current rectification, and altered liquid properties (see Figure 1.1).[21] In this section, we will discuss unique nanoscale phenomena that can influence nCE and nEC separations.

1.2.1 Electric double layer (EDL) and zeta potential (ζ)

Almost every surface is electrically charged when in contact with an electrolyte. This charge is gained through either dissociation or association of ions covalently bound to the surface or through non-covalent adsorption of ions. Ions in solution with opposite charges compared to the surface charge (counter-ions) are attracted to the surface while ions with similar charges (co-ions) compared to the surface charge are repelled from the surface. These

electrostatic interactions combined with Brownian diffusion create two layers of ions next to the surface: (i) A fixed layer of ions called the Stern layer; and (ii) a mobile layer of ions called the diffuse layer. These layers together form the electrical double layer, EDL. Ions in the Stern layer are tightly bound to the surface and hence, this layer does not completely shield the surface charge. As such, more ions from solution are attracted to the surface to shield the surface charge, but yet are not tightly bound. Instead, these ions move freely due to Brownian motion creating a layer of mobile ions known as diffuse layer.[23, 24]

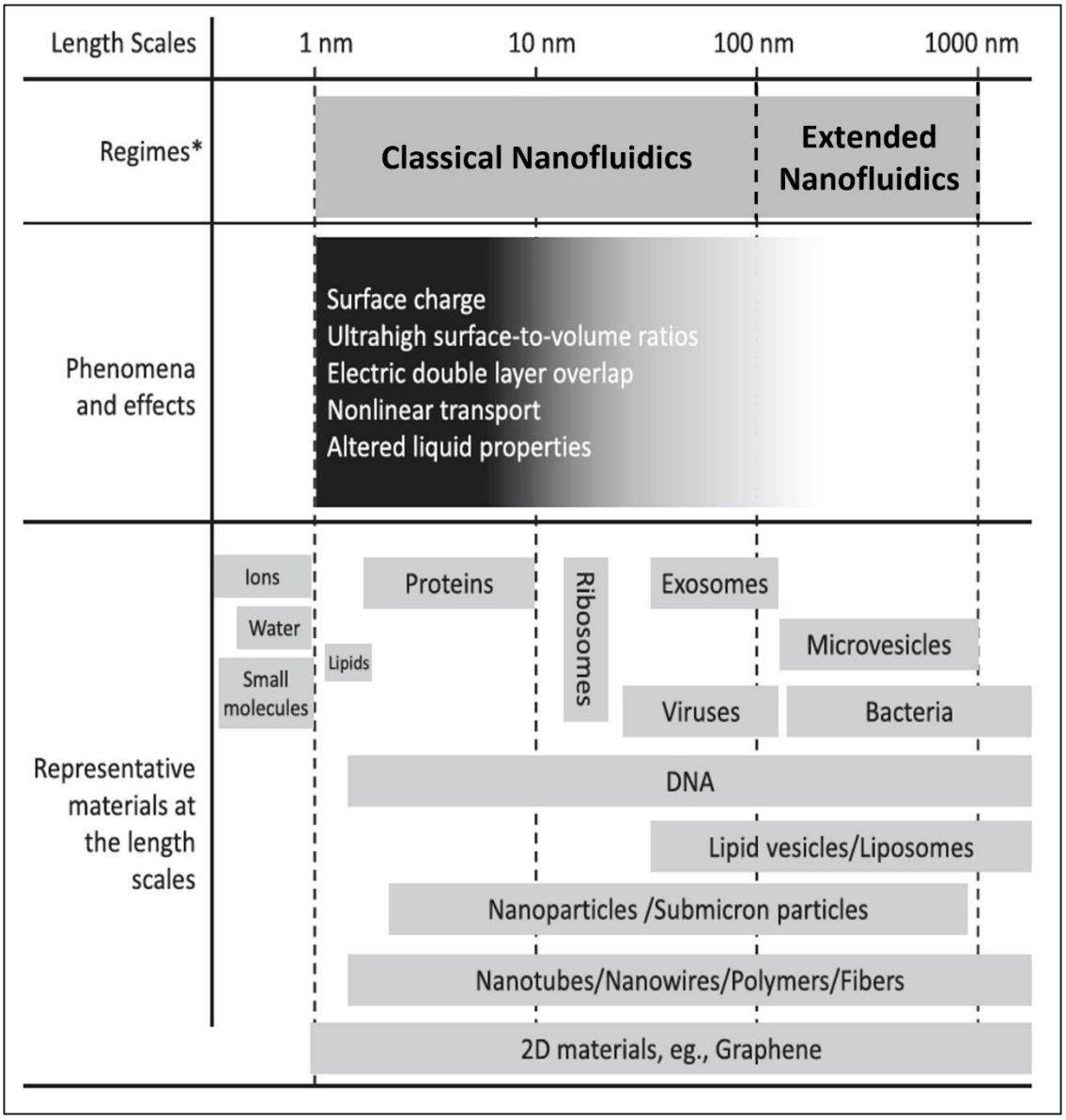

Figure 1.1 Representation of materials and nanometric object at the same length scales as nanofluidics, where unique transport phenomena and effects occur. Reproduced with slight modifications and permission from ref. 21.

The thickness of the EDL, which is known as the Debye length (λ_D), can be described by equation (1);

$$\lambda_D = \left(\frac{\varepsilon k_B T}{e^2 \sum_{i=1}^{n} Z_i n_{\infty,i}}\right)^{1/2} \quad (1)$$

where ε is the electric permittivity of the liquid, k_B is the Boltzmann constant, T is the absolute

temperature, e is the charge of an electron, z_i is the charge of the i^{th} ion and n_i is the number density of the i^{th} ions (summed over all ions comprising the carrier electrolyte).[24] The interface between the Stern and diffuse layer is known as the shear plane. As can be seen from equation (1), $\lambda_D \propto ([I])^{1/2}$, where $[I]$ is the ionic strength of the electrolyte solution. The electric potential at the shear plane is described as the zeta potential (ζ), which measures the electric charge developed on a solid surface in contact with an aqueous solution, which also depends on λ_D. From equation (1), λ_D depends on the ion concentration, ion valency and size, pH, and temperature of the solution. As a result, each solid-liquid interface will have a unique ζ. A mathematical expression for ζ is given by equation (2);[25, 26]

$$\zeta = \frac{2kT}{e} \ln\left[\frac{2e\sigma_s \lambda_D}{\epsilon_0 \epsilon_r k_B T} + \sqrt{1 + \frac{(2e\sigma_s \lambda_D / \epsilon_0 \epsilon_r kT)^2}{4}} \right] \quad (2)$$

where σ_s is the surface charge and k is the Boltzmann constant. Sze *et al*. reported that ζ for surfaces in KCl and $LaCl_3$ solutions varied between -88 to -66 mV and -110 to -68 mV for glass and PDMS surfaces, respectively, independent of the channel size and driving voltage.[27] Uba *et al.* reported ζ for PMMA nanochannels that were O_2 plasma activated and reacted with ethanolamine, which were -59 and 38 mV, respectively.[26]

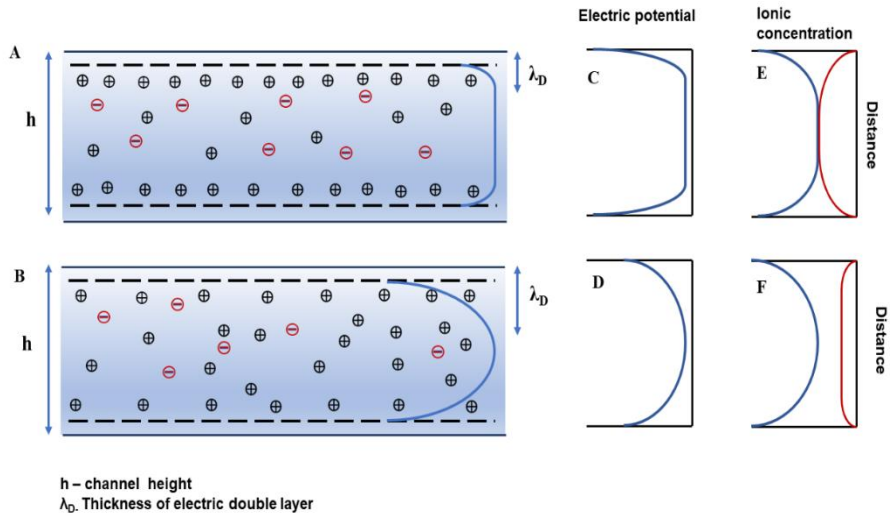

Figure 1.2 Schematic diagram of overlapped and non-overlapped EDL in a nanochannel. **(A)** When the Debye length is much smaller than critical channel dimensions, the solution towards the center of channel becomes neutral. **(B)** When there is an overlapping EDL, the solution becomes charged. **(C)** Electric potential decays rapidly closer to the channel wall and in the center, it becomes neutral in non-overlapped EDL conditions. **(D)** In an overlapping EDL, the electric potential at the center of channel does not become neutral and is influenced by surface charge. **(E)** The concentration of anions (red) and cations (blue) in a non-overlapping EDL scenario is equal to the bulk concentration. **(F)** In an overlapping EDL scenario, the concentration of cations (counter-ions) become much higher than that of anion (co-ions). Reproduced with permission from ref. 28.

The ratio of the channel height (h) and λ_d can be used to describe the state of electroneutrality of the bulk solution within a nanochannel or nanoslit. When $h/\lambda_D >> 1$, the solution towards the center of the channel becomes electrically neutral and has an equal number of co-ions and counter-ions. The flow profile becomes classically plug-like flow (Figure 1.2).[28] However, for $h/\lambda_D \approx 1$, there can be EDL overlap leading to the loss of electroneutrality with excess counter-ions. In this case, the flow profile becomes more parabolic in shape, and is known as Poiseuille-like flow.[29]

When there is plug flow, two ions with the same electrophoretic mobility but with different charges will move at the same speed. However, when the EDL is thick compared to channel dimensions giving rise to parabolic flow, there will be a distribution of ions along the channel transverse axis due to repulsion effects by walls with more highly charged ions traveling through the nanochannel or nanoslit closer to the channel centroid. This combined with the parabolic flow

will make ions move at different velocities depending on their charge, because the center-line has higher velocity than near the channel wall and thus, the higher charged counter-ions will be repelled from the wall and move towards the middle of the channel and possess higher velocity. However, less charged counter-ions will move closer to the channel wall and have a lower velocity. This phenomenon is called transverse electromigration (Figure 1.3).[24, 30, 31]

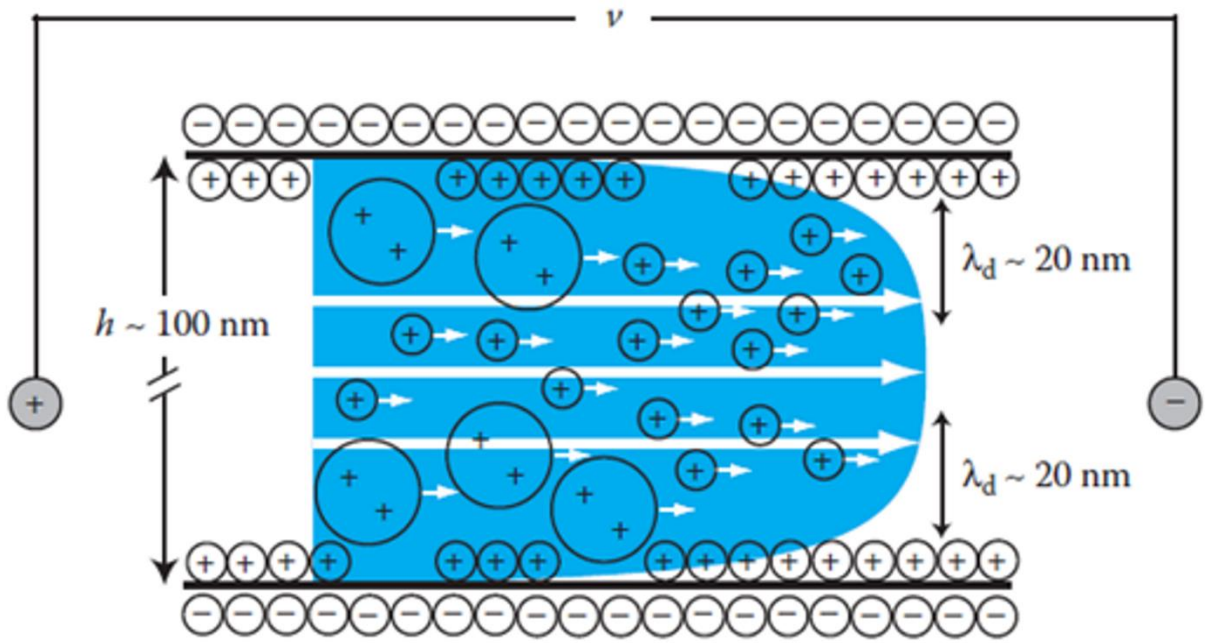

Figure 1.3 Diagram representing transverse electromigration effects observed with overlapped EDL. In this case, faster moving +1 ions will separate from slower moving +2 ions. Reproduced with permission from ref. 24.

1.2.2 Electroosmotic flow (EOF)

Studies on EOF have been reported as early as the 18th century, where Reuss first discovered that flow in capillaries could be induced by clay particles in water under an external electric field.[32] Wiedmann reported theories of electrokinetics supporting the findings by Reuss.[33] Since then, several theories have evolved describing the EOF. For example, Helmholtz and Smoluchowickz derived the electrical double layer theory.[34, 35] When the channel wall is negatively charged,

negatively charged ions (co-ions) in solution are attracted towards the anode while positively charged ions (counter-ions) are attracted towards the cathode. The movement of the excess counter-ions results in a viscous drag of the surrounding liquid creating a bulk flow in the presence of an external electric field, which creates the EOF.[24]

When the EDL is thin or when the EOF occurs in a large channel, the EOF has a flat flow profile compared to hydrodynamic flow, which is parabolic.[36] The advantage of a flat EOF profile is that molecules in the channel will experience the same velocity regardless of their radial position. This results in high-efficiency electrokinetic separations due to reductions in Taylor dispersion.[37-39]

The EOF velocity (v_{eof}) can be described by equation (3), where ε is the dielectric constant of the buffer, E is the applied electric field, and η is the viscosity of the buffer. EOF can also be expressed by equation (4), which shows its dependency on buffer characteristics, such as the dielectric constant, viscosity, and ζ.[36]

$$v_{eof} = \varepsilon\zeta E/4\pi\eta \qquad (3)$$

$$\mu_{eof.} = \varepsilon\zeta / 4\pi\eta \qquad (4)$$

Several studies have reported the EOF of nanochannels optically by monitoring the travel rate of zwitterionic dyes like Rhodamine B [31, 40] or the current monitoring method.[26, 41-43] Jacobson *et al.*[40] measured the EOF of 98 nm nanochannels by using the travel rate of Rhodamine B and compared to the EOF in microchannels. They observed a 35% decrease in the EOF of nanochannels compared to microchannels. They stated that EDL overlap in the nanochannels was

responsible for the decreased EOF compared to microchannels.

Uba *et al.*[26] measured the EOF for O_2 plasma activated and ethanolamine modified PMMA nanochannels using the current monitoring method. The values obtained for O_2 plasma activated and ethanolamine modified PMMA nanochannels were 1.02 ±0.02 $\times 10^{-4}$ cm^2/Vs and -0.75 ±0.02 $\times 10^{-4}$ cm^2/Vs, respectively. They stated that these values were lower than the EOF obtained for PMMA microfluidic channels (O_2 modified microchannels, EOF = 4.43 ±0.58 $\times 10^{-4}$ $cm^2/$ Vs and -1.34 ±0.21 $\times 10^{-4}$ cm^2/Vs, respectively) and suggested that the lower ζ in nanofluidic channels could be the reason for the lower EOF values in nanochannels.

Peng *et al.*[43] investigated the EOF of PDMS nanoslits having depths ranging from 20 to 250 nm and compared to 5 μm (depth and width) microchannels. Specifically, they studied the effects of channel dimensions, concentration of background electrolyte, and the electric field strength on the EOF using the current monitoring method. According to their observations, when the EDL was thin (0.01 M KCl, EDL 3-5 nm), the EOF did not vary with channel dimensions. In contrast, at low electrolyte concentrations (0.001 M KCl, EDL ~10 nm), they observed decreases in the EOF for nanoslits of depths <100 nm where EDL overlap occurred. They observed that for very small nanoslits (< 89 nm), decreasing electrolyte concentration led to decreases in the EOF due to EDL overlap.

1.2.3 Surface roughness effects

Surface roughness is ubiquitous in many nanofluidic and even microfluidic devices, which can occur either during fabrication or due to adsorption of molecules to the surface or surface modification. Surface modification not only can modify the surface chemically, but also induce sub-nanometer and nanometer roughness changing the surface morphology.[44] Strong fluid-wall

interactions are observed in nanochannels and nanoslits and the effect of surface roughness on fluid flow is significant compared to microchannels.[44-46]

Molecular dynamic (MD) studies discovered that surface roughness has a large influence on the EOF and surface wettability depending on the magnitude of the roughness height (h_r).[47] There is significant changes in EOF velocity and ion distribution when h_r and λ_D are similar; the effect becomes insignificant when λ_D is much larger than h_r.[45] According to Zhang *et al.*,[48] the fluid flow experiences greater resistance on rough surfaces causing molecules to stick onto the surface of nanochannels or nanoslits requiring more time to escape from concave regions. In addition, their simulations showed a decrease in ζ and EOF with increasing roughness, which was similar to other MD simulations.[49] Surface roughness can also induce dielectrophoretic trapping and fluid recirculation within a nanochannel leading to field-dependent mobilities. However, roughness effects are more prominent at low electric field strengths than high electric field strengths.[50-52].

1.2.4 Concentration polarization

When molecules are electrokinetically or hydrodynamically transported to/from nanochannels and the electroneutral bulk solution, which can occur in microchannels, molecules can concentrate on one side of a nanochannel and become dilute on the other, which is called "concentration polarization." Concentration polarization occurs at the interface of microchannels and nanochannels due to the increased flux of ions within the nanochannel arising from enhanced transport of selective ions within the EDL.[53-55] When the EDL spans the dimensions of the nanochannel, counter-ions are able to pass through the EDL while co-ions are excluded resulting in the accumulation of counter-ions and co-ions at the inlet and outlet of a nanochannel, respectively. Doubly charged ions will be strongly attracted to the double layer; hence at the same

ionic strength, the total ionic concentration of divalent counter-ions in the nanochannel becomes higher than singly charged ions. Therefore, at low ionic strengths (increased EDL thickness) and non-adsorbing conditions, there will be an increase in the electric current and fluid transport, while at high ionic strengths and adsorbing conditions the ζ-potential decreases leading to a decrease in the streaming current.[55] While concentration polarization has been applied as a technique for the pre-concentration of analytes, it has a negative effect on entry of charged molecules into nanochannels, such as DNA, RNA, and nucleotides through negatively charged nanochannel walls.[56]

As a final note, lower velocity profiles may be observed within nanochannels when compared to microchannels due to EDL overlap[55] giving rise to electroviscosity effects.[55, 57, 58] The decrease in channel dimensions can cause the ratio of the apparent to true viscosities to be as high as 1.3 depending on the material of the channel wall, spatial size, and shape of the nanochannel. This increase in viscosity leads to an apparent decrease in the EOF within nanochannels and can also reduce the diffusion coefficient of migrating analytes, which can reduce longitudinal dispersion in nanochannels compared to microchannels.

1.3 Fabrication of nanofluidic devices

Fabrication of nanostructure is a critical undertaking for realizing the use of nanofluidic devices for a variety of areas, because it can dramatically affect the accessibility of nanochannel devices based on cost considerations. In addition, the mode of fabrication can determine the performance of the nanofluidic device. For example, dry etching can create surface roughness that is typically not seen for wet etching when fabricating channels in inorganic substrates.

Nanofabrication methods have evolved significantly during the last decade. Several reviews have extensively discussed various techniques that can be utilized to fabricate nanochannel devices.[11, 59, 60] The choice of fabrication method is usually determined by the desired nanostructure dimensions and the substrate of choice such as inorganic, elastomeric, or thermoplastic.[11] Due to diffraction limit conditions, the use of conventional photolithography cannot reach the desired sub-100 nm dimension required for nanochannels and as such, the fabrication requires electron beam lithography (EBL) or focused ion beam milling (FIB). In the case of nanoslits, the microscale-dimension (width) can be fabricated using conventional photolithography while the depth, which is in the nanometer domain, is achieved using well-defined etching times.[11]

The choice of material is critical in selecting the fabrication method for the nanofluidic device as well. Current nanofabrication methods typically utilize inorganic materials such as silicon,[61] glass,[62] or quartz.[63] However, recent efforts have focused on using thermoplastics including poly(methylmethacrylate), PMMA,[64] cyclic olefin copolymer, COC,[65] polycarbonate, PC,[66] and polyethylene terephthalate, PET.[67] The elastomer, polydimethylsiloxane, PDMS, can also be used as a substrate for nanochannels,[68] but is not considered to be a thermoplastic. Even though silicon, glass, and quartz exhibit excellent optical properties, the ultimate cost of fabricating these nanofluidic devices are high compared to thermoplastic nanofluidic devices due to the lengthy fabrication process and the requirement of EBL or FIB direct milling for the fabrication of sub-100 nm structures.[69] Nanofluidic device fabrication using thermoplastics is cost effective because of the fact that thermoplastics can use replication-based fabrication techniques.[22, 26] Because the glass transition temperature (T_g) of thermoplastics is comparatively low, replication can be used to make the prerequisite structures using the appropriately patterned molding tool. However, the

low T_g of thermoplastics does create challenges in assembling devices due to structure deformation. Moreover, the hydrophobic surfaces associated with thermoplastics would inhibit their use in many nanoscale separations due to difficulties in filling with aqueous solvents, but thermoplastics can be converted into a more hydrophilic surface via oxygen plasma or UV/O_3 treatment.[22, 70]

In general, nanofabrication methods are divided into two major categories according to the process involved: "top-down" and "bottom-up" methods. In the top-down approach, the desired nanostructures are created using patterning tools and employ hot-embossing, imprinting, or injection molding, which leaves an open faced channel network.[71, 72] While most nanofluidic devices are made via top-down approaches, they require enclosure of the patterned channels using an assembly step in which a cover plate is bonded to the patterned substrate preferably without deforming the underlying nanostructures. In contrast, bottom-up approaches use molecular or atomic components to build up complex nanoscale structures by directed self-assembly.[73] In these methods, atoms and small molecules are used as the building blocks for the fabrication of nanostructures. Herein we will focus on summarizing top-down approaches that are widely used in nanofluidic device fabrication. These methods include conventional lithography, high energy beam processing methods, and replication-based methods.[74]

1.3.1 Conventional lithography methods

Conventional photolithography involves the use of light to generate a pattern in a photoresist spun over a Si wafer with a mask used to define the pattern (Figure 1.4A).[75] This is followed by reactive ion etching (dry) or wet etching to transfer the pattern into the Si substrate following resist

development. Because conventional lithography is used, the width of the structures is limited by diffraction and as such a typical width that can be achieved here is ~1 μm. The nanometer dimension is determined by the etching time; thus, only nanoslits can be made using this method. After structures are transferred into the substrate, assembling a cover plate to the device is required. Most of the early research using nanofluidic devices for biomolecule separations were fabricated in this way and used glass as the substrate.[60, 76-79] As noted, wet or dry etching can be used to transfer patterns into the underlying substrate, and each has its advantages and disadvantages. For example, dry etching requires sophisticated equipment, but can make vertical sidewalls whereas wet etching is much less equipment intensive but is difficult to make vertical side walls unless anisotropic etching is employed. Also, wet etching can create smoother surfaces compared to dry etching.

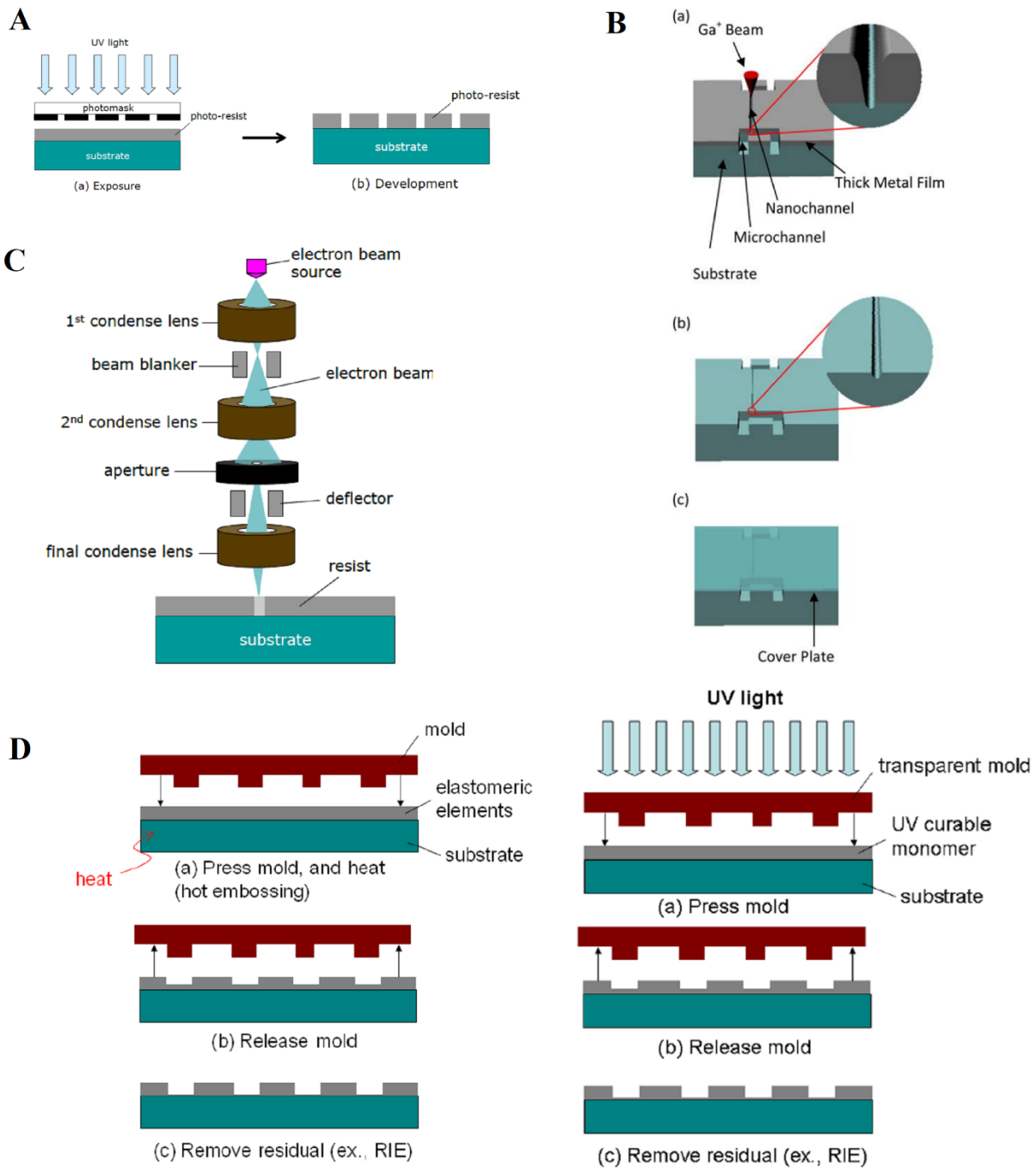

Figure 1.4 A schematic diagram representing an overview of nanofabrication methods. **(A)** Main steps involving in photolithography including [a] photoresist coated substrate is exposed to UV light; [b] removal of exposed photoresist by immersing in a resist developer. **(B)** Steps used in focused ion beam milling using Ga^+ ions. Reproduced with permission from ref 82. **(C)** An illustration of electron beam lithography where an electron beam is focused on a resist film to create a pattern by exposing dot by dot. **(D)** An illustration of nanoimprint lithography (left) and UV nanoimprint lithography (right). Reproduced with permission from ref. 75.

1.3.2 High energy beam processing lithography

High energy beam processing is another top-down approach where the nanofluidic structures are patterned through direct writing into the substrate by electron (EBL), proton, or focused ion beams (FIB). These high energy beam methods can produce nanostructures with 2D resolution allowing for the fabrication of nanochannels. EBL and FIB are predominantly used for nanostructure fabrication. In EBL, nanopatterns are initially defined in a thin layer of electron beam (e-beam) resist using a beam of focused electrons. The focused e-beam interacts with the resist and modifies the resist's property to make it soluble/insoluble and is followed with a development step. An example e-beam reactive resist is PMMA, which was developed in the 1960s.[80] Nanofeatures as small as 10 nm have been fabricated using EBL.[81] Following e-beam patterning and subsequent development, patterns are transferred into the underlying substrate by wet or reactive ion etching.

FIB has become an attractive method for the fabrication of nanofluidic devices and uses a focused beam of high energy ions, such as Gallium (Ga), to sputter atoms from the substrate. By optimizing the beam current and utilizing thick conductive sacrificial metal layers, this method has been able to fabricate sub-5 nm structures.[82] An overview of ion beam and electron beam processes are shown in Figure 1.4B and Figure 1.4C, respectively. Over the years, several research groups have utilized EBL or FIB to develop nanofluidic structures in inorganic substrates, such as glass and fused silica, for biomolecule separations.[42, 83, 84]

Although high energy beam methods can produce high quality nanofluidic channels even below 10 nm (width and depth), these methods rely on direct writing of each device and in some cases, the process is slow due to the need for direct writing. This results in high manufacturing cost and low production rates, which can hamper widespread use of nanoscale devices.

1.3.4 Nanoimprint lithography

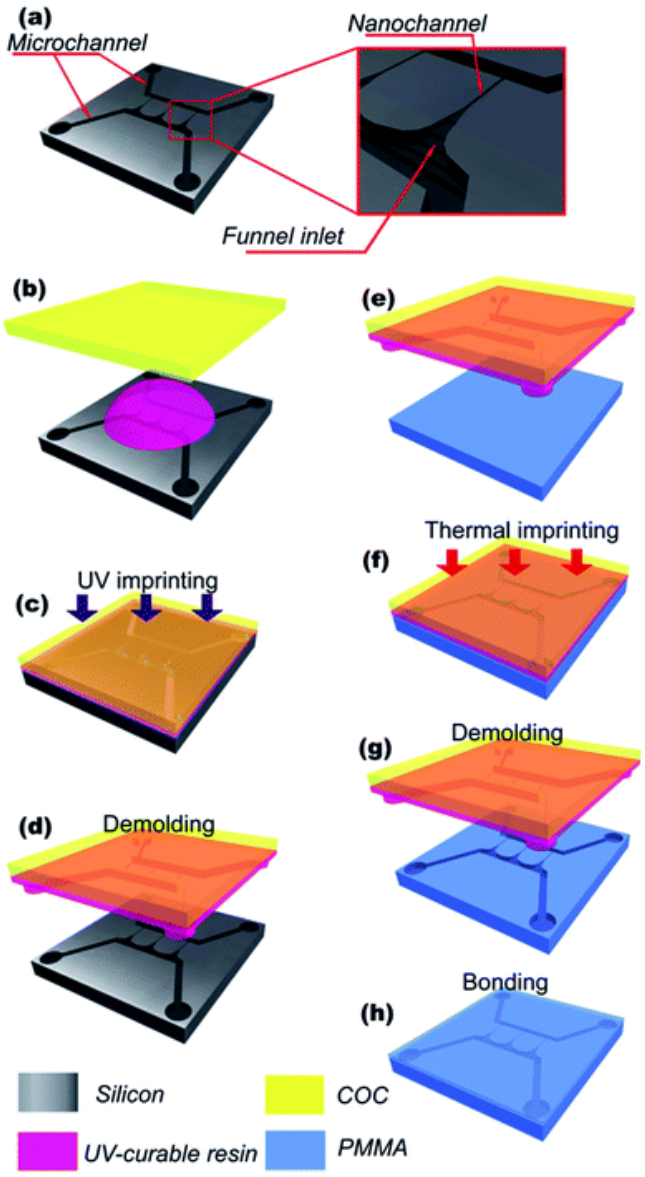

Figure 1.5 A schematic diagram representing an overview of nanofabrication method that utilizes NIL. This method uses a combination of UV-NIL and thermal NIL, which increases production rate and reduces device cost. (**a**) Silicon master, which consists of microchannels and funnel inlet for nanochannels; (**b**)-(**d**) fabrication steps to produce polymer stamp in a UV curable resin by UV imprinting from the silicon master; (**e**)-(**g**) fabrication steps to emboss nanofluidic structures in PMMA by imprinting from resin stamp; (**h**) bonding step with PMMA to build enclosed nanofluidic device. Reproduced with permission from ref. 88.

Nanoimprint lithography (NIL) is a high-resolution patterning method, which has been targeted for applications requiring medium-scale production of nanoscale devices.[85, 86] In NIL, a hard mold

with the desired nanostructures is used to imprint structures into a polymer substrate; both microstructures and nanostructures can be imprinted. The substrate is heated above its T_g to enable material flow around the mold's structures. Then, its temperature is lowered to solidify the replicated patterns and finally the mold is removed carefully. The mold with the nanostructures can be generated using any of the aforementioned techniques such as conventional photolithography, EBL, or FIB. Use of a hard mold for fabrication retains the nanostructures with minimal deformation following repeated cycles. Although NIL does eliminate the need for using lithography for producing each device, there are a few limitations. Heating/cooling cycles and high pressures applied during imprinting can cause stress and wear on the hard molds. Also, viscosity of the imprinted material can limit the minimum feature size and feature density. However, to overcome these later issues, the use of low viscosity UV-curable resins can be used, which enhances the fluidity of the imprinted material. This process is known as UV-nanoimprint lithography (Figure 1.4D).[75]

Our team has developed a new NIL-based fabrication method to make nanofluidic devices that is shown schematically in Figure 1.5.[22, 87, 88] In this method, a Si master is fabricated using a combination of photolithography to make microstructures and FIB milling to make the necessary nanoscale structures (*i.e.*, nanochannels). The Si master is then used to make a resin stamp via UV-NIL and the resin stamp is employed to make the final devices in the appropriate thermoplastic via thermal NIL. We have found that the Si master can make >100 resin stamps and the resin stamp can produce >20 devices.

1.3.5 Nano-injection molding

Mass production of fluidic chips requires injection molding (IM) to increase throughput, which has been demonstrated for microfluidic devices.[89-91] The attractive nature of IM is that while setup costs can be high, as the number of units required for a particular application increases, the production costs go down and can be lower than even microfluidic PDMS chips made via soft lithography.[91] The lower cycle times for IM, under 1 min depending on the complexity of the parts, lead to significantly higher production rates for IM.

Nanofluidic devices can take advantage of robust fabrication technologies to produce devices such as NIL, or injection compression molding (ICM), which is similar to IM, but uses a clamping force after polymer injection into the mold cavity to provide better replication fidelity for nanometer-scale structures.[92-94] However, the use of ICM to fabricate nanofluidic structures has been limited by: (i) Fabrication of high quality mold inserts. Basic requirements for mixed-scale molds include high shape repeatability to help manufacturing quality control, long molding tool lifetime to reduce the frequency of tool change over, low friction, minimal chemical interaction, and low cost and high speed molding tool fabrication. (ii) Molding of multi-scale features can cause inhomogeneous filling and stress at different locations of the molded structures. This can result in molding failure due to locally incomplete filling, undesirable deformation, and partial/total ripping of molded parts. (iii) Demolding failure due to severe warping and/or local substrate bending, making it difficult to generate a tight seal between the fluidic substrate and cover plate.

The Larsen group demonstrated IM of high aspect ratio, sub-100 nm pillar arrays in COC using electroplated Ni molds coated with fluorinated silane molecules.[95] Cutkosky electroplated Cu molds for gecko-like feet, with critical dimensions between 50-90 nm.[96] In addition, a few reports demonstrated enclosed nanofluidic devices with IM-produced substrates.[65]

1.4 Detection methods for biomolecule separations in nanofluidic devices

Decreasing the physical dimensions of devices to the nanoscale results in ultra-small amounts of analytes that must be detected and demands high sensitivity detection. When channel dimensions are decreased, the number of analytes present in the confined volume decreases accordingly and may approach the single molecule level. The probability (P_v) of molecules occupying a probe volume (P) can be calculated using the following equation;

$$P_v = CN_AP \qquad (5)$$

where C is the molecular concentration (mol L^{-1}), and N_A is Avogadro's number.[97] For example, when the nanochannel size is 50 × 50 nm (width and depth) and using a focused laser beam with a diameter of 1 µm, $P = 2.5 \times 10^{-18}$ L or 2.5 aL. For a concentration of analyte that is 1 nM, P_v = 1.5 molecules.

Therefore, single molecule sensitivity is often required in these experiments even for moderate concentrations. In addition, these dimensions are nearly equal or shorter than the wavelength of visible light and thus, many optical methods employing geometrical optics may have issues due to diffraction effects.[14, 98] Among the methods used for detection, laser-induced fluorescence (LIF), thermal lens spectrometry (TLS), and resistive pulse sensing are widely utilized in nanofluidics.[14] A summary and diagram of some of these detection methods are shown in Figure 1.6.

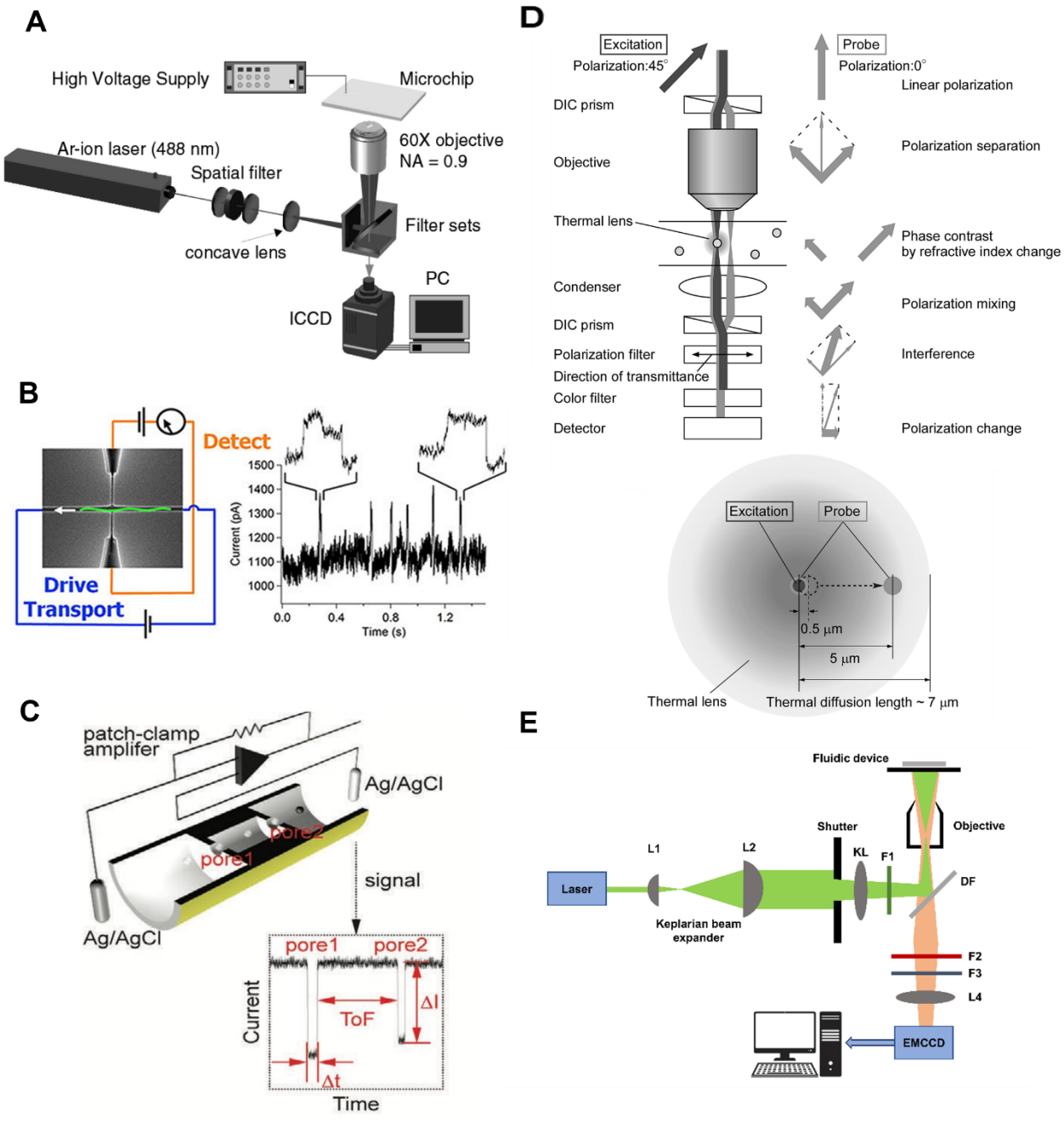

Figure 1.6 A schematic diagram representing the detection methods used in nanoscale separation studies. **(A)** Laser induced wide field fluorescence imaging system equipped with a CCD (charge coupled detector). Reproduced with permission from ref. 100. **(B)** Resistive pulse sensing of analytes migrating through a nanopore. Reproduced with permission from ref. 103. **(C)** Schematic of dual-nanopore time-of-flight (TOF) sensor, which consists of a pair of in-plane nanopores poised on either side of a nanochannel used as the nanochannel column for nanoscale electrophoresis. Reproduced with permission from ref. 105. **(D)** Components in differential interference contrast thermal lens microscope. Reproduced with permission from ref. 109. **(E)** The optical setup of fluorescence imaging system for nanoscale electrophoresis; Keplerian beam expander (L1, L2) laser line filter (F1), dichroic filter (DF) long pass filter (F2), band pass filter (F3) and CCD camera (L4). Reproduced with permission from ref.120.

Laser-induced fluorescence (LIF) is widely used because fluorophores can be excited and

detected selectively and with low limits-of-detection. In addition, when the detection volume is decreased, the sensitivity of fluorescence is enhanced due to reduced background generated by impurities and Rayleigh/Raman scattering.[99] For the majority of nanoscale separations, wide field epifluorescence systems are used (see Figure 1.6A and 1.6E).[26, 100, 101] However, for single-molecule experiments, LIF-confocal microscopy is used. This single molecule method is widely used for detecting DNA molecules stained with intercalating dyes in nanochannels.[102]

Resistive pulse sensing (RPS) is another method used in nanofluidics (Figure 1.6B and 1.6C).[103] When an analyte enters a three-dimensional nano-constriction known as a nanopore, the analyte will displace a fraction of carrier electrolyte ions and result in a measurable change in the pore resistance, which corresponds to a change in current. The change in current can be described using the following equation;

$$\Delta I = I_0 - V([\mu_{K+} + (1-S)\mu_{Cl-}]n_{KCl}e)\left(\frac{4h_{eff}}{\pi d_{eff}^2} + \frac{1}{d_{eff}}\right)^{-1} \qquad (6)$$

where I_0 is open pore current, V is the applied voltage, μ_{K+} is the mobility of K^+ ions, μ_{Cl-} is the mobility of Cl^- ions, $n_{KCl}$is the number density of KCl, e is the elementary charge, h_{eff} is effective length of the pore, d_{eff} is effective diameter of the pore, S is the fraction of excluded negative ions.[104] According to the above equation, the change in current through a nanopore is inversely proportional to the effective diameter of that pore. Our team recently reported work to tailor the size of thermoplastic in-plane nanopores during a thermal fusion bonding process, which served to place a cover plate over a nanofluidic network formed using a top-down fabrication process, and under controlled pressure and temperature, could reduce the pore size to improve the signal-to-noise ratio for RPS.[56]

There have been electrokinetic separations performed that utilize in-plane nanopore detection of analytes undergoing nanoscale separation. For example, detection of virus capsid or nucleotides used a pair of in-plane nanopore sensors flanking an electrophoresis nano-column (Figure 1.6C).[98, 105, 106] In these examples, the analytes were identified using their molecular-dependent electrophoretic mobility, which was determined by the travel time the analyte took to travel through the column.

Thermal lens spectrometry (TLS) is another detection method that has been used for microfluidic and nanofluidic applications to detect non-fluorescent analytes.[107] However, conventional TLS cannot be applied directly to nanoscale experiments as the principle is based on refraction of light. Shimzu *et al.*[108, 109] modified conventional TLS and developed a new TLS detector known as a differential interference contrast thermal lens microscope (DIC-TLM), which exploits a local change in refractive index of a solution and was used to detect analytes in naoslits (500 nm in depth and 5 μm in width) with a 250 aL detection volume (see Figure 1.6D). Non-labelled bovine serum albumin molecules were detected using TLS in extended nanochannels.[110]

1.5 Biomolecule separations in nanofluidic devices

Nanofluidic devices for biomolecular separations offers some distinct opportunities compared to microchip electrophoresis because of several unique phenomena that occur at the nanometer dimension, but not within the microscale domain. As such, separations that are intractable for microchip electrophoresis can be realized when using nanoscale columns in many cases. For instance, microchip electrophoresis of DNAs require the use of either three-dimensional sieving gels or entangled hydrophilic polymers to affect the separation due to the free draining behaviour of DNA.[111, 112] In contrast, gel free separations of DNAs can be achieved in nanofluidic devices.[13]

In addition to nEP, nEC or chromatography can be undertaken using open nanochannels due to reduced diffusional distances. Advantages of nanoscale chromatography in non-packed columns include high separation efficiency due to the absence of Eddy diffusion, fast separations because of the need for shorter length columns, and not requiring packing of the column with beads serving as the stationary phase.[113] In this section nEP and nEC separations of biomolecules will be discussed as well as extended nanoscale chromatographic methods.

1.5.1 nEP and nEC separations of biomolecules in nanofluidic devices

Recent review articles have presented an overview on the theories and experimental studies for electrokinetic (EK) based separations in nanochannels, including nEP and nEC.[13, 30, 55] As noted earlier, the EDL can be a predominant factor in determining the efficiency of the separation in nanochannels due to potential overlap (i.e., $h/\lambda_D \approx 1$). EDL overlap can distort the normal plug-like flow profile seen in microchip electrophoresis and also induce non-uniform electric fields in the normal direction with respect to the wall resulting in ionic concentration gradients arising from the equilibrium between electromigration and diffusion of ions. This transverse concentration gradient not only depends on the EDL thickness, but also on the surface charge density, valence number of the electrolyte ions, and temperature.[30, 31] Another factor affecting EK motion of molecules in nanochannels is channel dimensions. The spreading of suspended Brownian particles in a flowing bulk fluid along the flow direction is known as hydrodynamic dispersion.[114] Hydrodynamic dispersion in nanoslits is controlled by the width of the cross section rather than by the depth of the nanoslit. However, for charged molecules in nanochannels the equilibrium between electromigration and diffusion effects their dispersion as molecular diffusion can be constrained by the non-uniform electric field within the EDL.

Early efforts focused on nanoscale EK separations dealt with DNA separations because they have numerous applications in areas such as sequencing, mutation detection, forensics, biometric fingerprinting, and identification of pathogens. In addition to DNA separations, there have been a few studies on protein and amino acid nanoscale separations. In this section, several studies reporting on EK separations in nanofluidic devices are discussed.

One of the first nEP DNA separations involved using an entropic trap fabricated by shaping a microchannel with an alternating sequence of shallow (75 - 100 nm) and deep (300 nm) wells. The shallow regions were designed to have depths smaller than the radius of gyration of DNA. When DNA molecules were electrokinetically driven through a microchannel, they were trapped temporarily at the entrance of shallow wells.[115] Surprisingly, longer molecules had higher escape rates from the traps as they possessed a larger surface area that was in contact with the boundary of the micro/nanowell, thereby increasing their probability of entry.[77, 115] The separation efficiency in nanochannels using entropic trap arrays was found to be higher at high electric field strengths.[77] Fu *et al.*[76] further developed the entropic trapping method using a device geometry with symmetric wells (Figure 1.7A, B) that addressed the problem of separating small DNA molecules; Figure 1.7C shows SEMs of the device. In their study, they were able to separate five different lengths of DNA in ~10 min over a 5 mm long channel (see Figure 1.7D). They integrated the basic device geometry used in their previous study into a two-dimensional nanofluidic filter array, which allowed for different separation mechanisms other than entropic trapping, such as Ogston and electrostatic sieving.[116] Furthermore, this device was able to separate molecules in a continuous flow mode of operation over a broad range of sizes. The authors also showed the separation of SDS-protein mixtures; separation resolution was found to improve by decreasing electric field strengths due to chromatographic effects (Figure 1.7E).

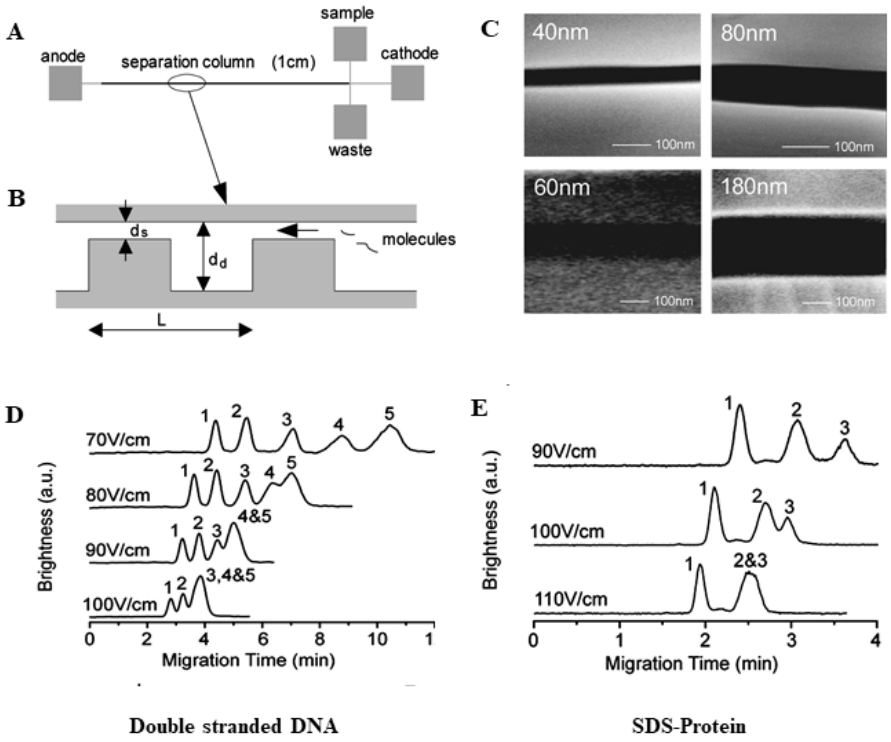

Figure 1.7 (A) Layout of the nanofilter array chip with four buffer access reservoirs (anode, cathode, sample, and waste), a 1 cm separation channel and a T-shaped injector. **(B)** A schematic diagram of the cross section of the separation channel in nanofilter array chip consists of thin (ds) and thick (dd) regions with equal lengths. **(C)** Scanning electron microscopy images of the thin regions in nanofilter array chip with different depths. **(D)** Electropherograms for the separation of double stranded DNA with different lengths: 1) 50bp; 2) 150 bp; 3) 300 bp; 4) 500bp; 5) 766 bp at different electric field strengths. **(E)** Electropherograms for the separation of SDS-protein complexes: 1) cholera toxin subunit B; 2) lectin phytomagglutinin-L; 3) low density human lipoproteins at different field strengths**.** Reproduced with permission from ref. 76.

Cross *et al.*[117] showed free solution separation of DNAs traveling through nanoslits with depths of 19 and 70 nm. The device used in these experiments consisted of two microfluidic channels coupled to nanoslits (Figure 1.8). Fluorescence measurements revealed length-dependent nEP separations of DNA (2000 - 10000 bp) that were electrokinetically driven though the nanoslits in the absence of any sieving matrix. When channel dimensions were on the same order as the size of the molecules migrating through the channel, steric interactions influenced the separation. They suggested that surface interactions with channel walls due to confinement lead to length-dependent mobility of DNAs in free solution.

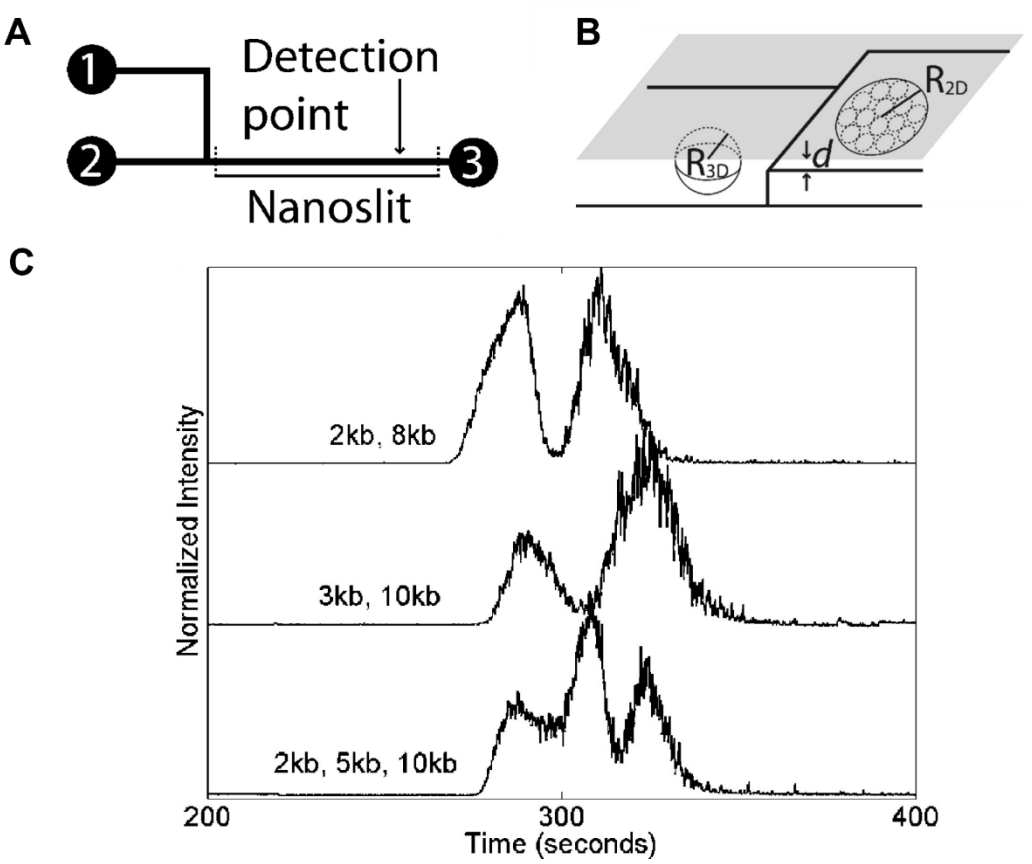

Figure 1.8 (A) A schematic diagram of the nanoslit device used for the separation and the length of the separation channel is 3-4 cm. **(B)** A schematic of the cross-sectional transition of DNA from its three-dimensional relaxed state to squished state when forced into nanochannel in two dimensions where the molecule becomes a pancake-like entity composed of sub-blobs of DNA with a diameter equal to channel height. **(C)** Electropherograms showing the separation of mixture of DNA molecules in 19 nm deep channel. Reproduced with permission from ref. 117.

Pennathur *et al.*[100] reported free solution nEP separations of DNA oligonucleotides in nanoslits (Figure 1.9). A mixture of fluorescently-labeled double stranded (ds) DNAs with sizes of 10, 25, 50 and 100 bps, fluorescein (FL), and fluorescein-12-UTP (FL-12-UTP) were separated in fused silica nanoslits having different depths (40 nm, 100 nm and 1560 nm). They also showed the separation of different lengths of DNA in free solution, which was not possible in microchannels. In their study, they investigated the effect of background electrolyte concentration on the separation by varying sodium borate concentrations ranging from 1 – 100 mM; the best separation resolution was obtained at 10 mM buffer concentration. The authors observed a length-dependent

migration order, which was influenced by the thickness of the EDL (λ_D), λ_D/h, and l/h parameters were varied to explore optimal conditions for the separation. At 10 mM (λ_D/h ≈ 3%), the migration order was FL, FL-12-UTP, and 10, 25, 50 and 100 bp DNA oligonucleotides ($\mu_{FL} < \mu_{UTP} < \mu_{10bp} < \mu_{25bp} < \mu_{50bp} < \mu_{100bp}$). The authors also observed the same migration order for a 5 mM carrier electrolyte concentration (λ_D/h ≈ 4%). Even though the migration order was the same, poorer separation resolution was observed for 20 mM and 100 mM buffers.

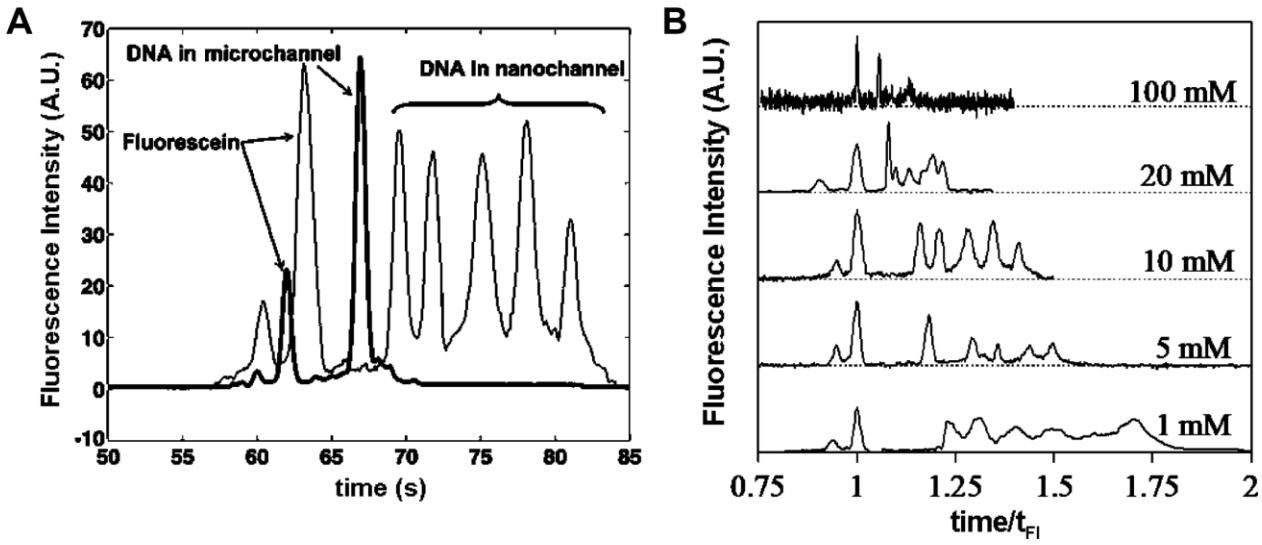

Figure 1.9 (A) Schematic of nanochannel electrophoresis of rod-like oligonucleotides. Important length scales are the depth of the channel (2h), the length of the dsDNA (l), and the Debye length (λ_D). **(B)** Measured electropherograms for electrokinetic separations of fluorescein, UTP, and a 10-100 bp oligonucleotide ladder in a 100 nm deep channel. Electropherograms are shown for separations in five different concentrations of sodium borate. t_{FI} is the residence time of fluorescein in each experiment. Reproduced with permission from ref. 100.

At low buffer concentrations, for example 1 mM (λ_D/h ≈ 0.10), the migration order changed compared to higher ionic strength buffers. At low ionic strengths, the effects of ion density and EDL coupling compete with each other to determine the net axial migration rate; transverse electromigration in the axial and transverse directions and steric-wall interactions played a role in determining migration and resolution.

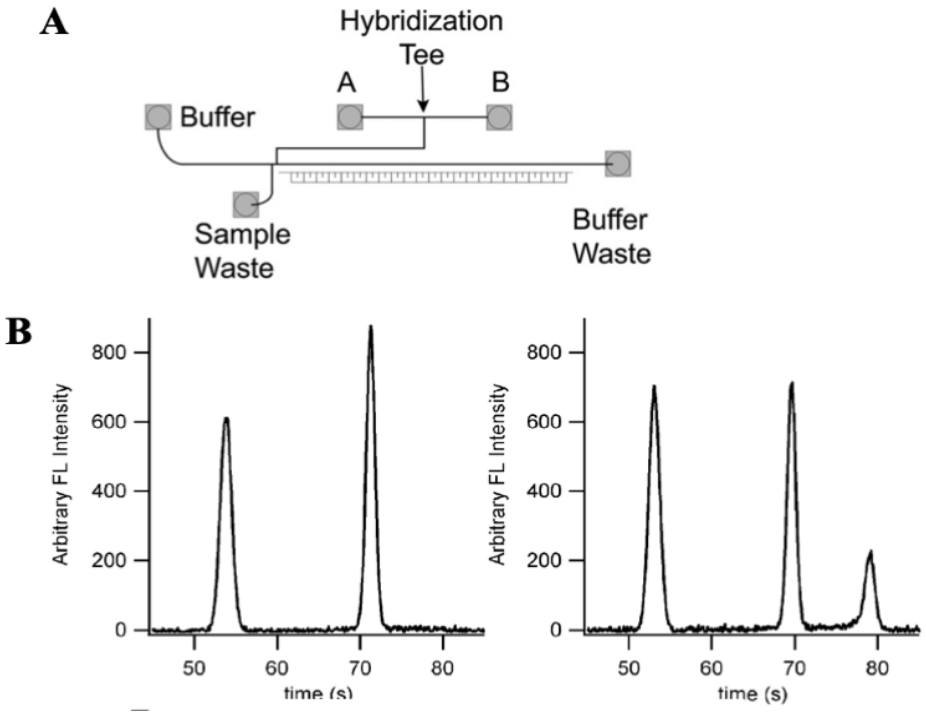

Figure 1.10 (A) The schematic illustrates the 5-port device layout, including sample wells (A and B), mixing tee, offset tee injector, and separation channel. **(B)** Electropherogram of the separation of single stranded DNA (left) and electropherogram of single stranded DNA plus the double stranded DNA (right) after hybridization step. Reproduced with permission from ref. 118.

In 2009, Huber *et al.*[118] was able to perform free solution separations of single stranded ssDNA and double stranded (ds) DNA (generated by hybridization of a probe to a ssDNA target) in 200 nm deep nanoslits. As depicted in Figure 1.10A, the device consisted of a 5-port variation of the common cross-injection chip. Instead of a single sample port, there were two sample ports (A and B) as supply channels that intersected at a mixing T. The oligonucleotide probe with sequence of 5′-TCTCCTTCTGCTCTCTTCTC-3′ was labelled with Alexa Flour 488 and a laser-induced fluorescence microscope equipped with an EMCCD camera was used for detection. Solutions were electrokinetically driven through the initial T for mixing to initiate hybridization, which continued as the sample passed through the channel into the injection region. Small sample plugs were driven to the separation column via EOF as it dominated over electrophoresis. As seen in Figure 1.10B,

there was a clear separation of ssDNA and dsDNA in free solution in these nanoslit devices. According to their results, the ssDNA migrated faster than ddDNA molecules. Moreover, they performed kinetic studies on the hybridization of DNA over time and observed the depletion of the ssDNA peak in the nEP while obtaining the hybridized dsDNA peak.

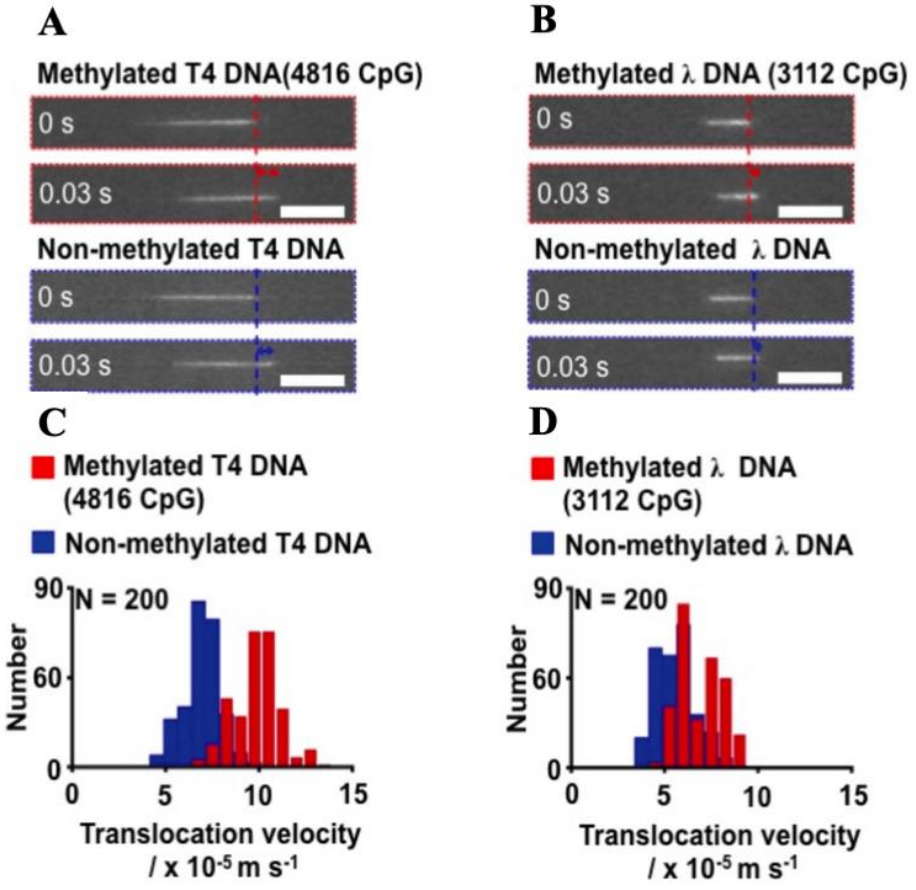

Figure 1.11 The velocity measurement of methylated and non-methylated DNA translocated inside the nanochannel. Arrows show the translocation distance of DNA in 0.03 s. **(A)** Fluorescence images of translocation of methylated and non-methylated T4 DNA inside the nanochannel. Scale bars are 10 μm. **(B)** Translocation of methylated and non-methylated λ DNA. Scale bars are 10 μm. Histogram of translocation velocities of methylated and nonmethylated **(C)** T4 DNA molecules and **(D)** λ DNA for n=200, respectively. Reproduced with permission from ref. 119.

Sun *et al.*[119] observed an electrophoretic velocity difference between methylated and non-methylated DNA in gel-free quartz glass extended nanochannels with dimensions of 300 × 300 nm (depth × width). They used λ-DNA and T4-DNA in their methylated and non-methylated forms

with all of the model DNAs stained with YOYO-1 dye, which is a bis-intercalating dye. As depicted in the fluorescent images shown in Figure 1.11A and B, there was a clear difference in the electrophoretic mobilities of methylated and non-methylated T4-DNA and λ-DNA. They observed methylated DNA migrated faster than non-methylated DNA. They suggested that the coefficient of friction of methylated DNA was lower than that of non-methylated DNA, allowing methylated DNA to transit the extended nanochannel faster than non-methylated DNA.

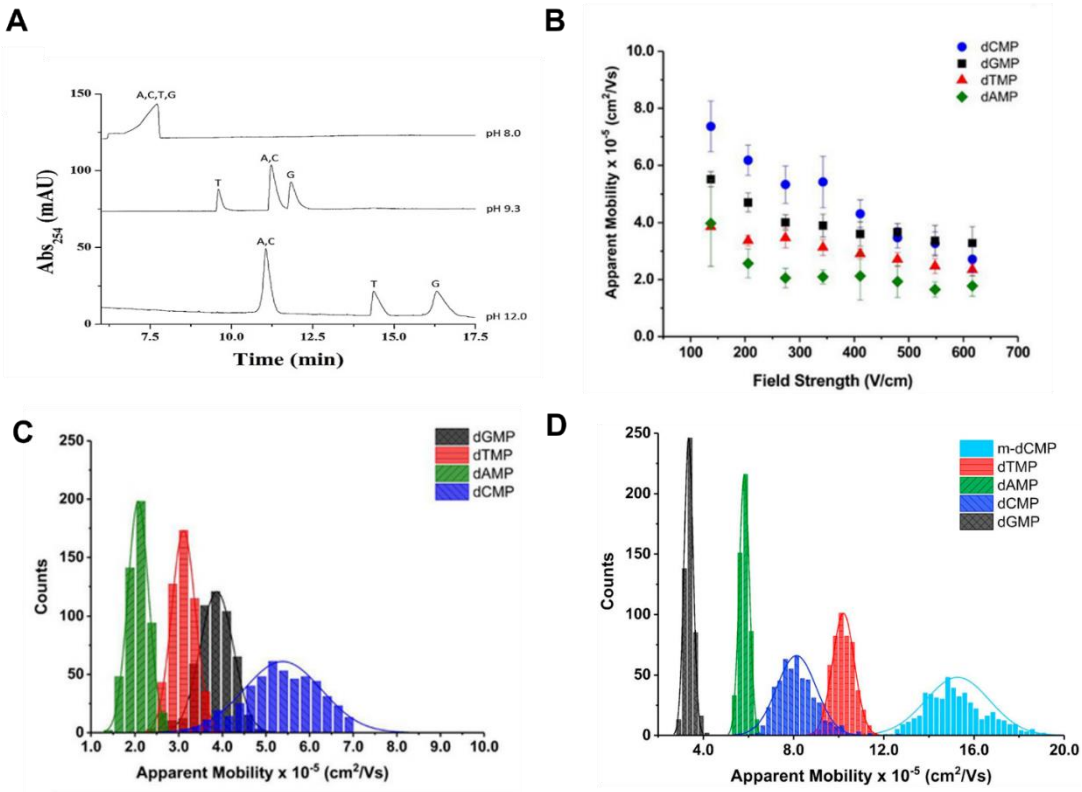

Figure 1.12 (A) Microscale electrophoresis of dNMPs at varying pH values (field strength=310 V/cm). **(B)** Apparent mobility versus the electric field strength, histograms of apparent mobilities at field strength of 342 V/cm at pH **(C)** 8.3 and **(D)** 10.3, for ATTO 532 labelled dNMPs injected into a nanochannel that was 110 x 110 nm (width and depth; L=100 µm) and used PMMA as the substrate with a COC cover plate. The electrokinetic used a buffer of 44.5 mM TB). Reproduced with permission from ref. 52.

Amarasekara *et al.* was able to identify ssDNAs via mobility matching in gel-free thermoplastic nanochannels with dimensions of 100 nm x 100 nm (depth and width) that were ~110 µm in length, which was not possible using microchip electrophoresis. They used ATTO 532

labelled ssDNAs that possessed three different lengths (Oligo 35, Oligo 50 and Oligo 70).[120] The results showed that the free solution identification of electrokinetically driven ssDNAs through nanochannels was dominated by chromatographic effects, nEC. They showed an increase in the migration time over a fixed nanochannel column length with increased length of the oligonucleotide, consistent with a higher propensity of the longer ssDNAs to interact with the channel wall. In this example, the nanochannels were made from a thermoplastic (*i.e*., PMMA).

O'Neil *et al*. investigated the electrokinetic transport properties of deoxynucleotide monophosphates (dNMPs) in nanochannels fabricated in PMMA via NIL including the effects of electric field strength, surface effects, and the carrier electrolyte's ionic concentration and pH (8.3 and 10).[52] Initially, this group performed microscale electrophoresis of the dNMPs using 89 mM TB buffer, which showed comigration of all dNMPs at pH 8.0. They also carried out nanoscale electrophoresis at pH 9.3 and 12.0; but they were not able to differentiate between dAMP and dCMP based on mobility matching (Figure 1.12A). In these experiments, the dNMPs were labelled with ATTO 532 fluorescent reporter to track their motion through nanochannels using a single-molecule fluorescence microscope operated in a wide-field epi-illumination format and equipped with an EMCCD camera. The study showed an electric field dependent apparent mobility of dNMPs in nanochannels (Figure 1.12 B). They assumed that changes in the apparent mobility of the dNMPs arose from intermittent motion and recirculation that was field-dependent.[121] However, using nanoscale electrophoresis they were able to identify all four dNMPs through their molecular-dependent apparent mobilities at an electric field strength of 342 V/cm. They observed >99% identification accuracy at pH 10 (Figure 1.12 C and D). Moreover, they were able to identify all dNMPs within a few seconds.

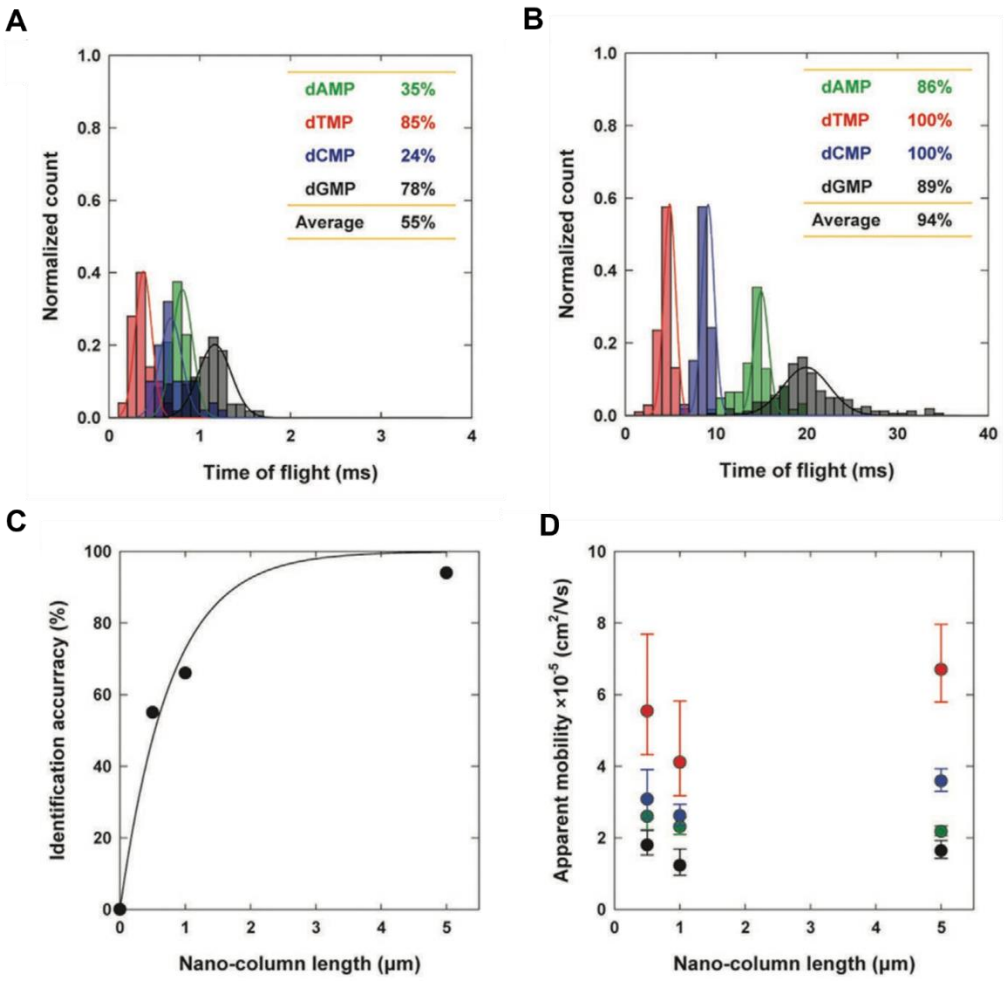

Figure 1.13 Histograms for the normalized counts of time-of-flight for dNMPs using nanosensors with **(A)** 0.5 μm **(B)** 5 μm long nanochannel column. **(C)** Identification accuracy vs nano-column length. **(D)** Apparent mobility vs length of the nanochannel column. Data were acquired with dNMPs at pH 10 in 1m KCl and 0.5X Tris borate EDTA buffer (TBE) under a driving voltage of 3 V. Reproduced with permission from ref. 105.

Amarasekara *et al*. reported the electrokinetic identification through mobility matching of ribonucleotide monophosphates (rNMPs) in thermoplastic microchannels and nanochannels,[122] which were made from PMMA or COC. They were not able to achieve baseline resolution of rAMP and rCMP (E = 1000 V/cm) using microchip electrophoresis. The identification of ATTO-532 labelled rNMPs were next investigated in hybrid (PMMA/COC) and non-hybrid (COC/COC)

nanochannel devices using a 1× NE buffer at pH 7.9. The average resolution of the rNMPs was >4 in PMMA/COC devices (range = 1.4 – 7.8) as well as COC/COC devices (range = 1.94 – 8.88). Also, the migration time for PMMA/COC devices was different compared to COC/COC devices; this was believed to be due to changes in the surface chemistries. Furthermore, the magnitude of the apparent mobilities of the rNMPs in COC/COC devices was smaller compared to that of PMMA/COC devices which was due to the differences in the EOF for each material. The observed identification accuracy using mobility matching of rNMPs for both COC and PMMA devices was >99%.

Choi *et al.*[105] showed the identification of label-free dNMPs via electrophoretic mobility matching using thermoplastic nanofluidic devices consisting of two in-plane nanopores with an intervening nanochannel column possessing a length of 0.5 μm, 1 μm, and 5 μm (see Figure 1.13C). The nanochannel column was fabricated in polyethylene glycol diacrylate (PEGDA) using NIL (Figure 1.5) and the dNMPs were electrokinetically driven through the gel-free column using different applied voltages. PEGDA is a hydrogel and the surface charge density is less compared to O_2 plasma or UV/O_3 activated thermoplastic nanofluidic devices; the dNMPs migrated according to their charge at pH 8.0, but at pH 10.0 the dNMPs migrated with the EOF. Migration of dNMPs through the first nanopore generated a blockade signal from one pore and then electrokinetically migrated through the nanochannel and entered the second in-plane pore generating another current blockade signal. The time difference between these two signals was taken as the time-of-flight (TOF) of each dNMP; each dNMP are identified through their molecular-dependent TOF, which is directly related to their apparent mobility. The nanoscale electrophoresis of these dNMPs was performed using different background electrolytes, pH, and the length of the nanochannel column; they observed better TOF identification accuracies at pH

10. Even though at higher pH they observed better identification accuracy, the migration times remained the same at pH 8.3 and 10. When the nanochannel length was increased from 500 nm to 5 μm, they observed improved identification accuracy, which was 55% and 94%, respectively. They mentioned that the nanoscale electrophoresis of dNMPs was a combination of nEC and nEP.

There have been only a few reports on protein separations using nanoscale electrophoresis. Fu *et al.* [76] was able to separate a mixture of three SDS protein complexes based on their molecular weights using a nanofilter array chip (Figure 1.7E). The gap size of the nanofilter array chip was 40 nm – 180 nm and the separation length was 5 mm. They found that small SDS-protein complexes migrated faster than larger ones. The resulting separation occurred at a column length of 570 μm and a time of 30 s. Schoch *et al.*[123] showed the separation of proteins by utilizing diffusion characteristics of charged molecules in a silicon-based nanofluidic device having 50 nm nanoslits. When the pH of the solution was changed, the charge of the protein can be either negative or positive (pH < pI – positive net charge; pH > pI – negative net charge), which is known as the Donnan effect. Using this approach, the authors were able to separate three lectin proteins having the same molecular weight, but different pI values by varying the pH from 6 to 11. Electrostatic interactions became significant with increasing surface charges in the nanochannel, thus providing a mechanism for separation based on different diffusion coefficients.

Kuo *et al.*[124] proposed a different separation device where vertically stacked microchannels were connected by nano-porous membranes. These membranes can be considered arrays of nanochannels where the transport properties depend on surface charge density and can be controlled by applying an external voltage. Under normal operation, separation in the main microchannel followed standard electrophoresis principles. The gating voltage was then timed to allow the transport of a specific analyte through the membrane and to the collection channel. By

applying this principle, the authors showed the separation of a mixture of amino acids.

1.5.2 Chromatographic separations of biomolecules in extended nanofluidic devices

For nanometer sized channels, because of the high surface-area-to-volume ratio, interfacial forces such as surface tension, becomes dominant. As a result, fluid transport becomes difficult via pressure driven flow and thus, it is easier to utilize EK transport. A graphical representation of the pressure drop as a function of channel height was demonstrated by Conlisk *et al.*[16] According to their study, when a nanoslit approached 10 nm in depth, 3 atm was required to drive an aqueous flow through the channel at 1 μL/min. However, for EK pumping, the required voltage drop across the nanochannel was 0.33 V to achieve the same volume flow rate. A specialized pump would be required to deliver this low flow rate and this creates practical challenges. However, several studies have reported on pressure driven nano-chromatographic separations and these will be highlighted below.

Many of the nano-chromatographic separations utilized open tubular channels with coated walls to avoid the limitations that exist with packed columns.[125] Utilizing open tubular channels has an advantage over packed columns by eliminating Eddie diffusion, which can reduce the separation efficiency.[126, 127] Tsukahara *et al.*[128] developed a pressure driven fluidic control system that could be utilized with nanofluidic systems. The fluidic control system was based on air pressure and was able to control flow in a 100 nm extended nanochannel for a chip with a pressure range of 0.003 - 0.4 MPa, flow rate of 0.16 - 21.2 pL/min, and residence time range of 24 - 32.4 ms.

First reports on extended nano-chromatographic separations were carried out using a bare fused silica capillary with a radius of 500 nm and 46 cm in length for the separation of

oligonucleotides ranging between 5 - 20 bps, long DNA molecules ranging from 0.5 - 10 kbps, and DNA of 75 bps - 20 kbps all of which were fluorescently labelled.[129] They utilized a three-valve system for pressure injection. The authors were able to obtain baseline separation for all of the DNAs in free solution and the mechanism for the separation was explained by a chromatographic model. In a fused silica extended nano-capillary with a negatively charged surface, cations were directed near the wall while anions were concentrated towards the center of the nano-capillary due to electrostatic interactions between the ions in solution and the charged surface. When pressure driven flow was introduced into the capillary, the solution at the center of the tube moved faster than the solution closer to channel wall due to the no-slip condition and fully developed laminar flow generated by the pressure driven flow. Therefore, more negatively charged (*i.e.*, larger) DNA fragments eluted earlier than smaller ones. Moreover, the authors studied the effects of buffer concentration, capillary radius, and elution pressure on the separation. When the channel radius was increased from 500 nm to 1000 nm, they observed poor separation resolution. Optimum separation resolution was obtained at 50 μM buffer concentration, however when buffer concentration was higher (>100 μM) separation resolution decreased.

Kitamori *el al.*[130] introduced a novel chromatographic separation named femto-liquid chromatography (flc) for the separation of negatively charged dye molecules including fluorescein (-2 charge) and sulforhodamine B (-1 charge) using pressure driven flow. They were able to separate these molecules within 30 s and fluorescein with a higher negative charge eluted later than sulforhodamine B. They claimed that the EDL thickness in the nanochannel had a significant influence on analyte velocity during the migration through the nanochannel. The authors demonstrated that the velocity difference of analytes depended on the ratio of the channel dimensions to thickness of the EDL (λ_D). When the ratio was too large (large channel size and

small λ_D) or too small (small channel size and large λ_D), the charged solutes spread throughout the channel or localized to the channel center due to electrostatic forces resulting in no differences in their velocities.

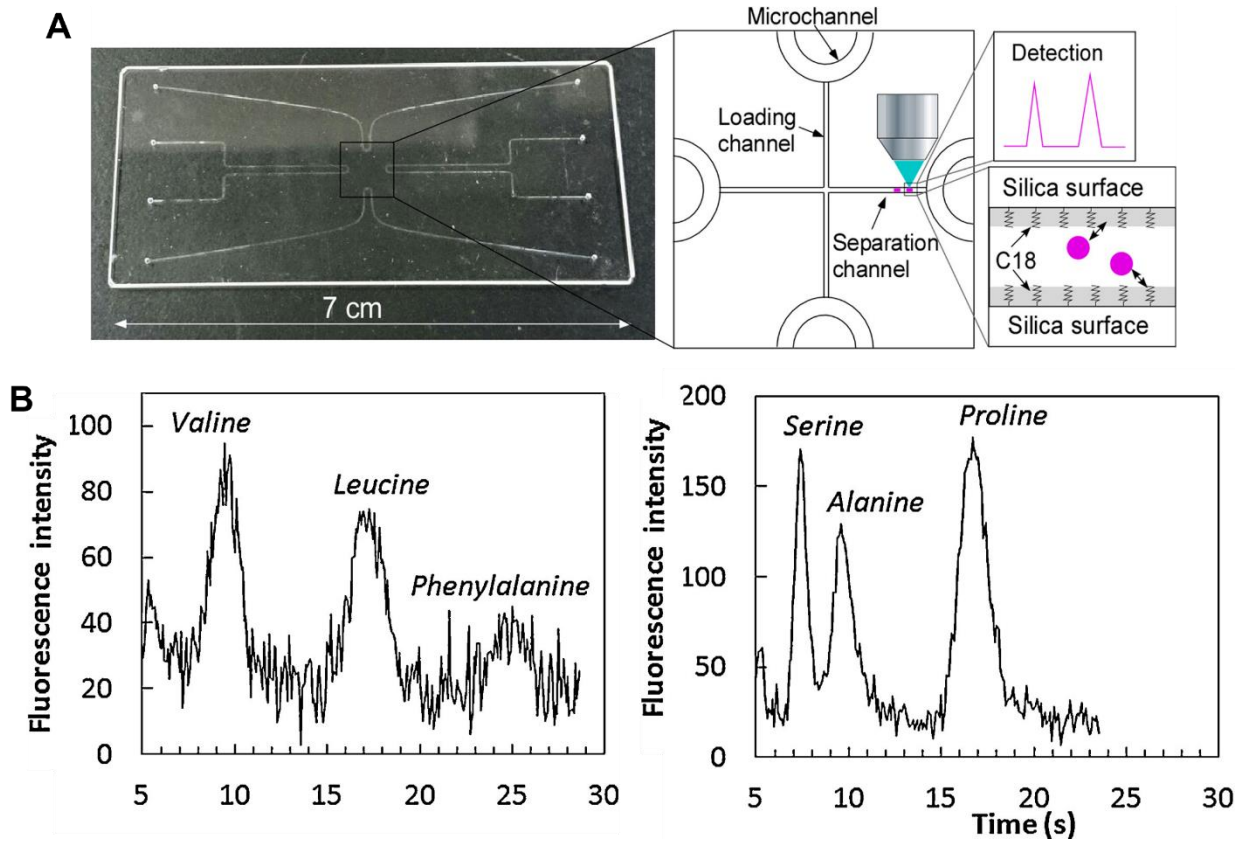

Figure 1.14 (A) An Image of the microchip and schematic diagram of the design of the extended nanochannels with 2.2 mm in length. **(B)** Chromatograms of the separation of fluorescently labelled amino acids by extended nanochromatography. Reproduced with permission from ref. 131.

Smirinova *et al.*[126, 131] developed a reverse phase chromatographic separation for amino acids in extended nanospace. A fluidic chip consisting of extended nanochannels were fabricated in quartz by electron beam lithography and plasma etching. Reverse phase conditions were achieved by modifying the walls of the extended nanochannels with a C18 phase and using 0.1 mM phosphate buffer (pH 8)/acetonitrile = 75/25 (v/v) mobile phase. The dimensions of their fluidic channels were 800 × 200 nm (width × depth) with a 2 mm length. They performed pressure-driven

pinched injection by connecting a custom-made pressure driven system to each end of microchannels. An injection volume of 10 – 60 fL of amino acids was used at a pressure of 3 MPa (~6.5 pL/min). Additionally, the longer channel had a length of 10 mm and a depth and width of 470 nm x 2000 nm, respectively. Fig. 14A shows an image of the fluidic channel they used. LIF was used to detect the amino acids (serine, alanine, proline, valine, leucine, and phenylalanine) labelled with 4-fluoro-7-nitro-2,1,3-benzoxadiazole (NBD-F). They were successful in separating two sets of a 3-labelled amino acid mixture with a high number of theoretical plates (70000 – 400000 plates/m) and a fast separation time (25 s) by using a nanochannel that had been extended to 10 mm in length. The longer nanochannel showed better separation efficiency compared to the shorter one under the same applied pressure (Figure 1.14B).

1.6 References

1. Sonker, M.; Kim, D.; Egatz-Gomez, A.; Ros, A., Separation Phenomena in Tailored Micro- and Nanofluidic Environments. *Annual Review of Analytical Chemistry* **2019,** *12* (1), 475-500.

2. Roda, A.; Michelini, E.; Caliceti, C.; Guardigli, M.; Mirasoli, M.; Simoni, P., Advanced bioanalytics for precision medicine. *Analytical and Bioanalytical Chemistry* **2018,** *410* (3), 669-677.

3. Haghi, M.; Thurow, K.; Stoll, R., Wearable Devices in Medical Internet of Things: Scientific Research and Commercially Available Devices. *Healthcare informatics research* **2017,** *23* (1), 4-15.

4. Chiu, D. T.; deMello, A. J.; Di Carlo, D.; Doyle, P. S.; Hansen, C.; Maceiczyk, R. M.; Wootton, R. C. R., Small but Perfectly Formed? Successes, Challenges, and Opportunities for Microfluidics in the Chemical and Biological Sciences. *Chem* **2017,** *2* (2), 201-223.

5. Swerdlow, H.; Zhang, J. Z.; Chen, D. Y.; Harke, H. R.; Grey, R.; Wu, S.; Dovichi, N. J., Three DNA Sequencing Methods Using Capillary Gel Electrophoresis and Laser-Induced Fluorescence. *Analytical Chemistry* **1991,** *63*, 2835-2841.

6. A.S.Cohen; D.R.Najarian; B.L.Karger, Separation and analysis of DNA sequence reaction products by capillary gel electrophoresis. *Journal of Chromatography, A* **1990,** *516*, 49-60.

7. Luckey, J. A.; Norris, T. B.; Smith, L. M., Analysis of Resolution in DNA Sequencing by Capillary Gel Electrophoresis. *Journal of Physical Chemistry* **1993,** *97*, 3067-3075.

8. Kan, C.-W.; Fredlake, C. P.; Doherty, E. A. S.; Barron, A. E., DNA sequencing and genotyping in miniaturized electrophoresis systems. *Electrophoresis* **2004,** *25*, 3564-3588.

9. Paegel, B. M.; Blazej, R. G.; Mathies, R. A., Microfluidic devices for DNA sequencing: sample preparation and electrophoretic analysis. *Current Opinion in Biotechnology* **2003,** *14*, 42-50.

10. Paegel, B. M.; Emrich, C. A.; Wedemayer, G. J.; Scherer, J. R.; Mathies, R. A., High throughput DNA sequencing with a microfabricated 96-lane capillary array electrophoresis bioprocessor. *PNAS* **2002,** *99*, 574-579.

11. Abgrall, P.; Nguyen, N. T., Nanofluidic devices and their applications. *Analytical chemistry* **2008,** *80* (7), 2326-2341.

12. Napoli, M.; Eijkel, J. C.; Pennathur, S., Nanofluidic technology for biomolecule applications: a critical review. *Lab on a Chip* **2010,** *10* (8), 957-985.

13. Baldessari, F.; Santiago, J. G., Electrophoresis in nanochannels: brief review and speculation. *Journal of Nanobiotechnology* **2006,** *4* (1), 12.

14. Mawatari, K.; Kazoe, Y.; Shimizu, H.; Pihosh, Y.; Kitamori, T., Extended-nanofluidics: fundamental technologies, unique liquid properties, and application in chemical and bio analysis methods and devices. ACS Publications: 2014.

15. GAD-EL-HAK, M., The Fluid Mechanics of Micro-devices-The Freeman Scholar Lecture. *ASME Journal of Fluids Engineering* **1999,** *121*, 5-33.

16. Conlisk, A. T., The Debye-Hückel approximation: Its use in describing electroosmotic flow in micro-and nanochannels. *Electrophoresis* **2005,** *26* (10), 1896-1912.

17. Wang, X.; Cheng, C.; Wang, S.; Zhao, M.; Dasgupta, P. K.; Liu, S., Nanocapillaries for open tubular chromatographic separations of proteins in femtoliter to picoliter samples. *Analytical chemistry* **2009,** *81* (17), 7428-7435.

18. Eijkel, J. C.; Van Den Berg, A., Nanofluidics: what is it and what can we expect from it? *Microfluidics and Nanofluidics* **2005,** *1* (3), 249-267.

19. Li, Y.; Xu, J.; Li, D., Molecular dynamics simulation of nanoscale liquid flows. *Microfluidics and nanofluidics* **2010,** *9* (6), 1011-1031.

20. Chen, M.; Chen, Y.; Zhong, W.; Yang, J., Molecular dynamics simulation of ion transport in a nanochannel. *Science in China Series E: Technological Sciences* **2008,** *51* (7), 921-931.

21. Xu, Y., Nanofluidics: A New Arena for Materials Science. *Advanced Materials* **2018,** *30* (3), 1702419.

22. Chantiwas, R.; Park, S.; Soper, S. A.; Kim, B. C.; Takayama, S.; Sunkara, V.; Hwang, H.; Cho, Y.-K., Flexible fabrication and applications of polymer nanochannels and nanoslits. *Chemical Society Reviews* **2011,** *40* (7), 3677-3702.

23. Lyklema, J., Fundamentals of interface and colloid science. Volume 2: Solid-liquid interfaces. With special contributions by A. de Keizer, BH Bijsterbosch, GJ Fleer and MA Cohen Stuart. **1995**.

24. Rogers, B.; Adams, J.; Pennathur, S., *Nanotechnology: understanding small systems*. Crc Press: 2014.

25. Chai, J.; Lu, F.; Li, B.; Kwok, D. Y., Wettability interpretation of oxygen plasma modified poly (methyl methacrylate). *Langmuir* **2004,** *20* (25), 10919-10927.

26. Uba, F. I.; Pullagurla, S. R.; Sirasunthorn, N.; Wu, J.; Park, S.; Chantiwas, R.; Cho, Y.-K.; Shin, H.; Soper, S. A., Surface charge, electroosmotic flow and DNA extension in chemically modified thermoplastic nanoslits and nanochannels. *Analyst* **2015,** *140* (1), 113-126.

27. Sze, A.; Erickson, D.; Ren, L.; Li, D., Zeta-potential measurement using the Smoluchowski equation and the slope of the current–time relationship in electroosmotic flow. *Journal of Colloid and Interface Science* **2003,** *261* (2), 402-410.

28. Karnik, R.; Fan, R.; Yue, M.; Li, D.; Yang, P.; Majumdar, A., Electrostatic Control of Ions and Molecules in Nanofluidic Transistors. *Nano Letters* **2005,** *5* (5), 943-948.

29. Burgreen, D.; Nakache, F., Electrokinetic flow in ultrafine capillary slits1. *The Journal of Physical Chemistry* **1964,** *68* (5), 1084-1091.

30. Pennathur, S.; Santiago, J. G., Electrokinetic Transport in Nanochannels. 1. Theory. *Analytical Chemistry* **2005,** *77* (21), 6772-6781.

31. Pennathur, S.; Santiago, J. G., Electrokinetic transport in nanochannels. 2. Experiments. *Analytical Chemistry* **2005,** *77* (21), 6782-6789.

32. Reuss, F. F., Sur un nouvel effet de l'électricité galvanique. *Mem. Soc. Imp. Natur. Moscou* **1809,** *2*, 327-337.

33. Wiedemann, G. t., Ueber die Bewegung von Flüssigkeiten im Kreise der geschlossenen galvanischen Säule. *Annalen der Physik* **1852,** *163* (11), 321-352.

34. Helmholtz, H. v., Studies of electric boundary layers. *Wied. Ann* **1879,** *7*, 337-382.

35. Smoluchowski, M., Krak. Anz: 1903.

36. Beale, S. C., Capillary Electrophoresis By Dale R. Baker (Hewlett-Packard, Boulder, CO). Wiley: New York. 1995. xx+ 244 pp. $49.95. ISBN 0-471-11763-3. ACS Publications: 1996.

37. Jorgenson, J. W.; Lukacs, K. D., Zone electrophoresis in open-tubular glass capillaries. *Analytical Chemistry* **1981,** *53* (8), 1298-1302.

38. Rice, C. L.; Whitehead, R., Electrokinetic flow in a narrow cylindrical capillary. *The Journal of Physical Chemistry* **1965,** *69* (11), 4017-4024.

39. Paul, P.; Garguilo, M.; Rakestraw, D., Imaging of pressure-and electrokinetically driven flows through open capillaries. *Analytical Chemistry* **1998,** *70* (13), 2459-2467.

40. Haywood, D. G.; Harms, Z. D.; Jacobson, S. C., Electroosmotic flow in nanofluidic channels. *Analytical chemistry* **2014,** *86* (22), 11174-11180.

41. Huang, X.; Gordon, M. J.; Zare, R. N., Current-monitoring method for measuring the electroosmotic flow rate in capillary zone electrophoresis. *Analytical chemistry* **1988,** *60* (17), 1837-1838.

42. Menard, L. D.; Ramsey, J. M., Electrokinetically-driven transport of DNA through focused ion beam milled nanofluidic channels. *Analytical chemistry* **2012,** *85* (2), 1146-1153.

43. Peng, R.; Li, D., Electroosmotic flow in single PDMS nanochannels. *Nanoscale* **2016,** *8* (24), 12237-12246.

44. Hu, Y.; Werner, C.; Li, D., Electrokinetic Transport through Rough Microchannels. *Analytical Chemistry* **2003,** *75* (21), 5747-5758.

45. Qiao, R., Effects of molecular level surface roughness on electroosmotic flow. *Microfluidics and Nanofluidics* **2007,** *3* (1), 33-38.

46. Lu, P.; Liu, X.; Zhang, C., Electroosmotic flow in a rough nanochannel with surface roughness characterized by fractal cantor. *Micromachines* **2017,** *8* (6), 190.

47. Kim, D.; Darve, E., Molecular dynamics simulation of electro-osmotic flows in rough wall nanochannels. *Physical Review E* **2006,** *73* (5), 051203.

48. Zhang, C.; Lu, P.; Chen, Y., Molecular dynamics simulation of electroosmotic flow in rough nanochannels. *International Communications in Heat and Mass Transfer* **2014,** *59*, 101-105.

49. Qiao, R.; Aluru, N. R., Atomistic simulation of KCl transport in charged silicon nanochannels: Interfacial effects. *Colloids and Surfaces A: Physicochemical and Engineering Aspects* **2005,** *267* (1), 103-109.

50. Weerakoon-Ratnayake, K. M.; Uba, F. I.; Oliver-Calixte, N. J.; Soper, S. A., Electrophoretic separation of single particles using nanoscale thermoplastic columns. *Analytical chemistry* **2016,** *88* (7), 3569-3577.

51. ONeil, C. E.; Jackson, J. M.; Shim, S.-H.; Soper, S. A., Interrogating surface functional group heterogeneity of activated thermoplastics using super-resolution fluorescence microscopy. *Analytical chemistry* **2016,** *88* (7), 3686-3696.

52. O'Neil, C.; Amarasekara, C. A.; Weerakoon-Ratnayake, K. M.; Gross, B.; Jia, Z.; Singh, V.; Park, S.; Soper, S. A., Electrokinetic transport properties of deoxynucleotide monophosphates (dNMPs) through thermoplastic nanochannels. *Analytica chimica acta* **2018,** *1027*, 67-75.

53. Piruska, A.; Gong, M.; Sweedler, J. V.; Bohn, P. W., Nanofluidics in chemical analysis. *Chemical Society Reviews* **2010,** *39* (3), 1060-1072.

54. Baldessari, F.; Santiago, J., Electrophoresis in nanochannels: brief review and speculation. *Journal of Nanobiotechnology* **2006,** *4* (1), 12.

55. Yuan, Z.; Garcia, A. L.; Lopez, G. P.; Petsev, D. N., Electrokinetic transport and separations in fluidic nanochannels. *ELECTROPHORESIS* **2007,** *28* (4), 595-610.

56. Athapattu, U. S.; Rathnayaka, C.; Vaidyanathan, S.; Gamage, S. S.; Choi, J.; Riahipour, R.; Manoharan, A.; Hall, A. R.; Park, S.; Soper, S. A., Tailoring Thermoplastic In-Plane Nanopore Size by Thermal Fusion Bonding for the Analysis of Single Molecules. *ACS sensors* **2021,** *6* (8), 3133-3143.

57. Kaji, N.; Ogawa, R.; Oki, A.; Horiike, Y.; Tokeshi, M.; Baba, Y., Study of water properties in nanospace. *Analytical & Bioanalytical Chemistry* **2006,** *386* (3), 759-764.

58. Moran, W.; Chi-Chang, C.; Yang, R.-J., Electroviscous effects in nanofluidic channels. *Journal of Chemical Physics* **2010,** *132* (2), 024701.

59. Chen, X.; Zhang, L., Review in manufacturing methods of nanochannels of bio-nanofluidic chips. *Sensors and Actuators B: Chemical* **2018,** *254*, 648-659.

60. Xia, D.; Yan, J.; Hou, S., Fabrication of Nanofluidic Biochips with Nanochannels for Applications in DNA Analysis. *Small* **2012,** *8* (18), 2787-2801.

61. Viero, Y.; He, Q.; Mazenq, L.; Ranchon, H.; Fourniols, J.-Y.; Bancaud, A., Efficient prototyping of large-scale pdms and silicon nanofluidic devices using pdms-based phase-shift lithography. *Microfluidics and nanofluidics* **2012,** *12* (1-4), 465-473.

62. Kutchoukov, V.; Laugere, F.; van Der Vlist, W.; Pakula, L.; Garini, Y.; Bossche, A., Fabrication of nanofluidic devices using glass-to-glass anodic bonding. *Sensors and Actuators A: Physical* **2004,** *114* (2-3), 521-527.

63. Kelly, S. A.; Torres-Verdín, C.; Balhoff, M. T., Subsurface to substrate: dual-scale micro/nanofluidic networks for investigating transport anomalies in tight porous media. *Lab on a Chip* **2016,** *16* (15), 2829-2839.

64. Yin, Z.; Sun, L.; Zou, H.; Cheng, E., Two dimensional PMMA nanofluidic device fabricated by hot embossing and oxygen plasma assisted thermal bonding methods. *Nanotechnology* **2015,** *26* (21), 215302.

65. Utko, P.; Persson, F.; Kristensen, A.; Larsen, N. B., Injection molded nanofluidic chips: Fabrication method and functional tests using single-molecule DNA experiments. *Lab on a Chip* **2011,** *11* (2), 303-308.

66. Harnett, C. K.; Craighead, H. G.; Coates, G., Method of using heat-depolymerizable polycarbonate sacrificial layer to create nano-fluidic devices. Google Patents: 2004.

67. Chen, L.; Yin, Z.; Zou, H.; Liu, J.; Liu, C.; Li, K., A thermal bonding method based on O 2 plasma and water treatment for fabrication of PET planar nanofluidic device. *Microsystem Technologies* **2017,** *23* (5), 1327-1333.

68. Peng, R.; Li, D., Fabrication of polydimethylsiloxane (PDMS) nanofluidic chips with controllable channel size and spacing. *Lab on a Chip* **2016,** *16* (19), 3767-3776.

69. Duan, C.; Wang, W.; Xie, Q., Fabrication of nanofluidic devices. *Biomicrofluidics* **2013,** *7* (2), 026501.

70. McDonald, R. S., Surface functionality of amorphous silica by infrared spectroscopy. *The Journal of Physical Chemistry* **1958,** *62* (10), 1168-1178.

71. Gates, B. D.; Xu, Q.; Stewart, M.; Ryan, D.; Willson, C. G.; Whitesides, G. M., New Approaches to Nanofabrication: Molding, Printing, and Other Techniques. *Chemical Reviews* **2005,** *105* (4), 1171-1196.

72. Mailly, D., Nanofabrication techniques. *The European Physical Journal Special Topics* **2009,** *172* (1), 333-342.

73. Ariga, K.; Hill, J. P.; Lee, M. V.; Vinu, A.; Charvet, R.; Acharya, S., Challenges and breakthroughs in recent research on self-assembly. *Science and Technology of Advanced Materials* **2008,** *9* (1), 014109.

74. Biswas, A.; Bayer, I. S.; Biris, A. S.; Wang, T.; Dervishi, E.; Faupel, F., Advances in top–down and bottom–up surface nanofabrication: Techniques, applications & future prospects. *Advances in colloid and interface science* **2012,** *170* (1-2), 2-27.

75. Pimpin, A.; Srituravanich, W., Review on micro-and nanolithography techniques and their applications. *Engineering Journal* **2012,** *16* (1), 37-56.

76. Fu, J.; Mao, P.; Han, J., Nanofilter array chip for fast gel-free biomolecule separation. *Applied Physics Letters* **2005,** *87* (26), 263902.

77. Han, J.; Craighead, H. G., Separation of long DNA molecules in a microfabricated entropic trap array. *Science* **2000,** *288* (5468), 1026-1029.

78. Hamblin, M. N.; Xuan, J.; Maynes, D.; Tolley, H. D.; Belnap, D. M.; Woolley, A. T.; Lee, M. L.; Hawkins, A. R., Selective trapping and concentration of nanoparticles and viruses in dual-height nanofluidic channels. *Lab on a Chip* **2010,** *10* (2), 173-178.

79. Fu, J.; Yoo, J.; Han, J., Molecular sieving in periodic free-energy landscapes created by patterned nanofilter arrays. *Physical review letters* **2006,** *97* (1), 018103-018103.

80. Con, C., Nanolithography on non-planar surfaces and self-assembly of metal salt-polymer nanomaterials. **2016**.

81. Broers, A. N.; Hoole, A. C. F.; Ryan, J. M., Electron beam lithography—Resolution limits. *Microelectronic Engineering* **1996,** *32* (1), 131-142.

82. Menard, L. D.; Ramsey, J. M., Fabrication of Sub-5 nm Nanochannels in Insulating Substrates Using Focused Ion Beam Milling. *Nano Letters* **2011,** *11* (2), 512-517.

83. Tegenfeldt, J. O.; Prinz, C.; Cao, H.; Chou, S.; Reisner, W. W.; Riehn, R.; Wang, Y. M.; Cox, E. C.; Sturm, J. C.; Silberzan, P., The dynamics of genomic-length DNA molecules in 100-nm channels. *Proceedings of the National Academy of Sciences* **2004,** *101* (30), 10979-10983.

84. Cabodi, M.; Turner, S. W.; Craighead, H. G., Entropic recoil separation of long DNA molecules. *Analytical chemistry* **2002,** *74* (20), 5169-5174.

85. Tang, M.; Chen, Z. C.; Huang, Z. Q.; Choo, Y. S.; Hong, M. H., Maskless multiple-beam laser lithography for large-area nanostructure/microstructure fabrication. *Applied Optics* **2011,** *50* (35), 6536-6542.

86. Pease, R. F.; Chou, S. Y., Lithography and other patterning techniques for future electronics. *Proceedings of the IEEE* **2008,** *96* (2), 248-270.

87. Uba, F. I.; Hu, B.; Weerakoon-Ratnayake, K.; Oliver-Calixte, N.; Soper, S. A., High process yield rates of thermoplastic nanofluidic devices using a hybrid thermal assembly technique. *Lab Chip* **2015,** *15* (4), 1038-1049.

88. Wu, J.; Chantiwas, R.; Amirsadeghi, A.; Soper, S. A.; Park, S., Complete plastic nanofluidic devices for DNA analysis via direct imprinting with polymer stamps. *Lab on a Chip* **2011,** *11* (17), 2984-2989.

89. Becker, H.; Locascio, L. E., Polymer microfluidic devices. *Talanta* **2002,** *56* (2), 267-287.

90. Lee, U. N.; Su, X.; Guckenberger, D. J.; Dostie, A. M.; Zhang, T.; Berthier, E.; Theberge, A. B., Fundamentals of rapid injection molding for microfluidic cell-based assays. *bioRxiv* **2017**.

91. Becker, H., Its the economy... *Lab Chip* **2009,** *9*, 2759-2762.

92. Nagato, K., Injection Compression Molding of Replica Molds for Nanoimprint Lithography. *Polymers* **2014,** *6*, 604-612.

93. Nagato, K.; Hamaguchi, T.; Nakao, M., Injection compression molding of high-aspect-ratio nanostructures. *Journa of Vacuum Science Technology B* **2011,** *29*, 06FG10.

94. Rytka, C.; Kristiansen, P. M.; Neyer, A., Iso- and variothermal injection compression moulding of polymer micro- and nanostructures for optical and medical applications. *Journal of Micromechanics and Microengineering* **2015,** *25*, 065008.

95. Matschuk, M.; Larsen, N. B., Injection molding of high aspect ratio sub-100 nm nanostructures. *Journal of Micromechanics and Microengineering* **2013,** *23* (2).

96. Kerst, C.; Suresh, S. A.; Cutkosky, M. R., Creating metal molds for directional gecko-inspired adhesives. *Journal of Micro- and Nano-Manufacturing* **2020,** *8* (1), 011004-1-011004-5.

97. Soper, S. A.; Mattingly, Q. L.; Vegunta, P., Photon burst detection of single near-infrared fluorescent molecules. *Analytical Chemistry* **1993,** *65* (6), 740-747.

98. Kovarik, M. L.; Jacobson, S. C., Nanofluidics in lab-on-a-chip devices. ACS Publications: 2009.

99. Dittrich, P. S.; Manz, A., Single-molecule fluorescence detection in microfluidic channels—the Holy Grail in μTAS? *Analytical and Bioanalytical Chemistry* **2005,** *382* (8), 1771-1782.

100. Pennathur, S.; Baldessari, F.; Santiago, J. G.; Kattah, M. G.; Steinman, J. B.; Utz, P. J., Free-solution oligonucleotide separation in nanoscale channels. *Analytical chemistry* **2007,** *79* (21), 8316-8322.

101. Uba, F., Development of Nanofluidic Devices for Single-Molecule DNA Diagnostics. **2014**.

102. Cipriany, B. R.; Zhao, R.; Murphy, P. J.; Levy, S. L.; Tan, C. P.; Craighead, H. G.; Soloway, P. D., Single molecule epigenetic analysis in a nanofluidic channel. *Analytical chemistry* **2010,** *82* (6), 2480-2487.

103. Menard, L. D.; Mair, C. E.; Woodson, M. E.; Alarie, J. P.; Ramsey, J. M., A Device for Performing Lateral Conductance Measurements on Individual Double-Stranded DNA Molecules. *ACS Nano* **2012,** *6* (10), 9087-9094.

104. Wanunu, M.; Dadosh, T.; Ray, V.; Jin, J.; McReynolds, L.; Drndić, M., Rapid electronic detection of probe-specific microRNAs using thin nanopore sensors. *Nature nanotechnology* **2010,** *5* (11), 807-814.

105. Choi, J.; Jia, Z.; Riahipour, R.; McKinney, C. J.; Amarasekara, C. A.; Weerakoon-Ratnayake, K. M.; Soper, S. A.; Park, S., Label-Free Identification of Single Mononucleotides by Nanoscale Electrophoresis. *Small* **2021,** *17* (42), 2102567.

106. Zhou, J.; Zlotnick, A.; Jacobson, S. C., Disassembly of Single Virus Capsids Monitored in Real Time with Multicycle Resistive-Pulse Sensing. *Analytical Chemistry* **2021**.

107. Kitamori, T.; Tokeshi, M.; Hibara, A.; Sato, K., Peer Reviewed: Thermal Lens Microscopy and Microchip Chemistry. *Analytical Chemistry* **2004,** *76* (3), 52 A-60 A.

108. Shimizu, H.; Mawatari, K.; Kitamori, T., Sensitive determination of concentration of nonfluorescent species in an extended-nano channel by differential interference contrast thermal lens microscope. *Analytical chemistry* **2010,** *82* (17), 7479-7484.

109. Shimizu, H.; Mawatari, K.; Kitamori, T., Development of a Differential Interference Contrast Thermal Lens Microscope for Sensitive Individual Nanoparticle Detection in Liquid. *Analytical Chemistry* **2009,** *81* (23), 9802-9806.

110. Shimizu, H.; Miyawaki, N.; Asano, Y.; Mawatari, K.; Kitamori, T., Thermo-optical Characterization of Photothermal Optical Phase Shift Detection in Extended-Nano Channels and UV Detection of Biomolecules. *Analytical chemistry* **2017,** *89* (11), 6043-6049.

111. McDonell, M. W.; Simon, M. N.; Studier, F. W., Analysis of restriction fragments of T7 DNA and determination of molecular weights by electrophoresis in neutral and alkaline gels. *Journal of molecular biology* **1977,** *110* (1), 119-146.

112. Viovy, J.-L., Electrophoresis of DNA and other polyelectrolytes: Physical mechanisms. *Reviews of Modern Physics* **2000,** *72* (3), 813.

113. Ishibashi, R.; Mawatari, K.; Kitamori, T., Highly Efficient and Ultra-small Volume Separation by Pressure-Driven Liquid Chromatography in Extended Nanochannels. *Small* **2012,** *8* (8), 1237-1242.

114. Ajdari, A.; Bontoux, N.; Stone, H. A., Hydrodynamic dispersion in shallow microchannels: the effect of cross-sectional shape. *Analytical Chemistry* **2006,** *78* (2), 387-392.

115. Han, J.; Turner, S.; Craighead, H. G., Entropic trapping and escape of long DNA molecules at submicron size constriction. *Physical review letters* **1999,** *83* (8), 1688.

116. Fu, J.; Schoch, R. B.; Stevens, A. L.; Tannenbaum, S. R.; Han, J., A patterned anisotropic nanofluidic sieving structure for continuous-flow separation of DNA and proteins. *Nature Nanotechnology* **2007,** *2* (2), 121-128.

117. Cross, J. D.; Strychalski, E. A.; Craighead, H., Size-dependent DNA mobility in nanochannels. *Journal of Applied Physics* **2007,** *102* (2), 024701.

118. Huber, D. E.; Markel, M. L.; Pennathur, S.; Patel, K. D., Oligonucleotide hybridization and free-solution electrokinetic separation in a nanofluidic device. *Lab on a Chip* **2009,** *9* (20), 2933-2940.

119. Sun, X.; Yasui, T.; Yanagida, T.; Kaji, N.; Rahong, S.; Kanai, M.; Nagashima, K.; Kawai, T.; Baba, Y., Effect of DNA Methylation on the Velocity of DNA Translocation through a Nanochannel. *Analytical Sciences* **2017,** *33* (6), 727-730.

120. Amarasekara, C. A.; Athapattu, U. S.; Rathnayaka, C.; Choi, J.; Park, S.; Soper, S. A., Open-tubular nanoelectrochromatography (OT-NEC): gel-free separation of single stranded DNAs (ssDNAs) in thermoplastic nanochannels. *Electrophoresis* **2020,** *41* (18-19), 1627-1640.

121. Edman, C. F.; Raymond, D. E.; Wu, D. J.; Tu, E.; Sosnowski, R. G.; Butler, W. F.; Nerenberg, M.; Heller, M. J., Electric field directed nucleic acid hybridization on microchips. *Nucleic Acids Research* **1997,** *25* (24), 4907-4914.

122. Amarasekara, C. A.; Rathnayaka, C.; Athapattu, U. S.; Zhang, L.; Choi, J.; Park, S.; Nagel, A. C.; Soper, S. A., Electrokinetic identification of ribonucleotide monophosphates (rNMPs) using thermoplastic nanochannels. *Journal of Chromatography A* **2021,** *1638*, 461892.

123. Schoch, R. B.; Bertsch, A.; Renaud, P., pH-controlled diffusion of proteins with different pI values across a nanochannel on a chip. *Nano letters* **2006,** *6* (3), 543-547.

124. Kuo, T.-C.; Cannon, D. M.; Chen, Y.; Tulock, J. J.; Shannon, M. A.; Sweedler, J. V.; Bohn, P. W., Gateable nanofluidic interconnects for multilayered microfluidic separation systems. *Analytical Chemistry* **2003,** *75* (8), 1861-1867.

125. Ishibashi, R.; Mawatari, K.; Kitamori, T., Highly Efficient and Ultra-small Volume Separation by Pressure-Driven Liquid Chromatography in Extended Nanochannels. *Small* **2012,** *8* (8), 1237-1242.

126. Smirnova, A.; Shimizu, H.; Mawatari, K.; Kitamori, T., Reversed-phase Chromatography in an Extended Nanospace: Separating Amino Acids in Short and Long Nanochannels. *Analytical Sciences* **2015,** *31* (11), 1201-1204.

127. Shimizu, H.; Morikawa, K.; Liu, Y.; Smirnova, A.; Mawatari, K.; Kitamori, T., Femtoliter high-performance liquid chromatography using extended-nano channels. *Analyst* **2016,** *141* (21), 6068-6072.

128. Tsukahara, T.; Mawatari, K.; Hibara, A.; Kitamori, T., Development of a pressure-driven nanofluidic control system and its application to an enzymatic reaction. *Analytical and bioanalytical chemistry* **2008,** *391* (8), 2745-2752.

129. Wang, X.; Wang, S.; Veerappan, V.; Byun, C. K.; Nguyen, H.; Gendhar, B.; Allen, R. D.; Liu, S., Bare nanocapillary for DNA separation and genotyping analysis in gel-free solutions without application of external electric field. *Analytical chemistry* **2008,** *80* (14), 5583-5589.

130. Kato, M.; Inaba, M.; Tsukahara, T.; Mawatari, K.; Hibara, A.; Kitamori, T., Femto liquid chromatography with attoliter sample separation in the extended nanospace channel. *Analytical chemistry* **2009,** *82* (2), 543-547.

131. Smirnova, A.; Shimizu, H.; Mawatari, K.; Kitamori, T., Reversed-phase chromatography in extended-nano space for the separation of amino acids. *Journal of Chromatography A* **2015,** *1418*, 224-227.

Chapter 2: Electrokinetic Identification of Fluorescently Labelled Ribonucleotide Monophosphates (rNMPs) Using Thermoplastic Nanochannels

This chapter is based on the following manuscript,

"Electrokinetic identification of ribonucleotide monophosphates (rNMPs) using thermoplastic nanochannels"

* These authors contributed equally to this work.

2.1 Introduction

Analysis of the transcriptome has garnered significant attention recently as it offers information not readily obtainable from the genome. Whole-genome sequencing provides a static view of an organism's genetic and regulatory information, but transcriptomic analyses allow for assessment of dynamic changes in gene expression in response to various stimuli [1, 2]. In addition, identification of unique transcripts can enhance the understanding of underlying mechanisms governing pathophysiological conditions. Moreover, with the development of precision medicine, RNA analysis will increasingly be relied upon to serve as molecular signatures that define various disease subtypes that allow for predicting pharmacological responses to certain therapies (*i.e.*, precision medicine) [3-5].

The advent of next generation sequencing (NGS) has revolutionized the understanding of the complex and dynamic nature of the transcriptome by allowing RNA analysis through complementary DNA (cDNA) sequencing known as RNA sequencing (RNA-seq) [6]. RNA-seq provides a detailed and quantitative view of gene expression and alternative splicing patterns [7]. With recent advances in the RNA-seq workflow, it has provided deep profiling of the transcriptome [8].

Even though the accomplishments are impressive for RNA-seq, there are still numerous challenges with this platform, including: (i) The propensity of various reverse transcriptases (RT) to generate spurious secondary cDNA strands due to their DNA-dependent polymerase activities; (ii) artifactual cDNA generation due to template switching or contaminating DNA and primer independent cDNA synthesis; (iii) low amounts of cDNA due to the inefficient nature of RT; and (iv) biases introduced during amplification steps [9]. Therefore, it is apparent that new sequencing

platforms that can address the aforementioned limitations are necessary, especially those that are capable of sequencing full length transcripts without amplification.

Recently, single-molecule sequencing (SMS), some of which are based on nanopore readout, have become an attractive alternative to ensemble-based sequencing such as NGS as it can eliminate the need for RT and polymerase amplification as well as providing longer reads [10, 11]. Unlike NGS, nanopore sequencing does not require fluorescence labelling [12, 13]. Nanopore sequencing can be accomplished using two different approaches, strand sequencing [14, 15] or exosequencing [11, 12, 16]. Ayub *et al.* [11] showed that polynucleotide phosphorylase (PNPase), which processively cleaves RNA in the 3′ → 5′ direction releasing inorganic phosphate (P_i) and ribonucleotide diphosphates (rNDPs), sequentially produces rNDPs that can pass through an αHL (HL = hemolysin) pore containing cyclodextrin adapters non-covalently bound to the pore. However, diffusional misordering is a limitation of the exosequencing approach [12, 17]. Moreover, single nucleotide detection approaches are limited by high error rates as nucleotide bases are identified using current blockage event amplitudes only [10].

To overcome these challenges, we are developing an innovative SMS strategy that is based on the exosequencing approach and consists of enzymatically cleaving intact DNAs or RNAs using a processive enzyme to generate individual nucleotide monophosphates [18-20]. For RNA, this can be achieved via a processive enzyme such as exoribonuclease 1 (XRN1). We have recently shown that this enzyme can be tethered to a solid support and processively clip an RNA strand in the 5’ → 3’direction and generate rNMPs when activated by the cofactor, Mg^{2+} [21]. The released rNMPs are electrokinetically transported through a nanochannel with the travel time (*i.e.*, Time-of-Flight, TOF) through a nanometer tube used to efficiently identify the constituent rNMPs based on their molecular-dependent electrophoretic mobilities. Therefore, a thorough understanding of the

electrophoretic behavior of the rNMPs through nanochannels along with the electrophoretic parameters that determine their molecular-dependent mobilities will allow for high identification accuracy using our SMS approach.

Separation of rNMPs has been achieved using conventional electrophoresis, most commonly using glass capillaries and alkaline solutions as the carrier electrolyte [22-24]. Sodium borate is the most commonly used alkaline buffer for rNMP electrophoretic separations [22, 25]. In addition to sodium borate, others have used sodium and ammonium carbonate buffers [26].

Nanofluidics, which use channels with dimensions (width and/or depth) ≤100 nm, have garnered attention recently due to the unique separation modalities observed compared to microscale electrophoretic separations arising from scaling effects. For example, electrokinetic separations in nanochannels can depend on ion valence, ζ (zeta potential), ion mobility, and thickness of the electric double layer (EDL) [27-30]. The increased surface area-to-volume ratio in nanofluidics can also allow for a host of solute/wall interactions, which in turn provide separations based on hydrophobic, electrostatic, or van der Waals interactions [31]. However, the majority of the reported nanofluidic separations were performed in glass-type devices, which make these channels not ideal for broad community-based applications as the fabrication of these devices is associated with time-consuming and sophisticated methods, such as direct focused ion beam milling [32, 33].

Thermoplastic nanofluidic devices are considered an attractive alternative to glass/silicon devices due to their diverse physiochemical properties and the many fabrication techniques available to generate the prerequisite structures [34, 35]. Thermoplastic nanofluidic devices can be fabricated using nanoimprint lithography (NIL), which takes advantage of the deformability of the plastic at temperatures above their glass transition temperatures (T_g) to produce multi-scale structures in a relatively high production mode at moderate cost [1, 35]. The diversity in their surface

chemistry, which is determined by the identity of the monomer units comprising the polymer chains, is another advantage of thermoplastics for nanoscale electrophoresis. In addition, a diverse range of simple activation techniques, such as O_2 plasma or UV/O_3 irradiation, can be employed to generate groups that alter the surface chemistry of the plastic nanochannels as well as their wettability [36-38].

Unfortunately, there have been a limited number of studies on nanoscale separations using thermoplastic nanofluidic devices [20, 39, 40]. Recently, we showed the identification of deoxynucleotide monophosphates (dNMPs) through thermoplastic nanochannels made with PMMA as the substrate and COC as the cover plate [20]. We observed field-dependent mobilities of dNMPs at low electric field strengths due to intermittent motion arising from nanometer surface roughness. Moreover, increasing the pH of the carrier electrolyte increased the separation resolution while low ionic strength conditions, where the EDL is thicker, led to poorer differences. However, we observed the delamination of the PMMA-COC nanofluidic device at higher pHs (pH >10.3), which limited the pH that could be used to improve the differences in the electrophoretic mobilities to enhance identification efficiency using mobility matching.

In this work, we report the electrokinetic identification of rNMPs in thermoplastic nanochannels. The major goal of this work was to under the electrophoretic conditions, such as carrier electrolyte composition (i.e., pH), electric field strength, and material effects, the performance of nanoscale electrophoresis rNMPs. While our previous work on nanoscale electrophoresis used exclusively PMMA/COC hybrid devices[20, 40] herein we fabricated COC/COC thermoplastic nanochannel devices with the ability to control the EOF through post-assembly UV/O_3 surface activation. Furthermore, these COC/COC devices showed higher bond strengths compared to PMMA/COC devices, which will improve the use of different electrophoresis

operating conditions to optimize the identification accuracy of the rNMPs without device failure. We were able to efficiently identify all of the rNMPs using free solution nanoelectrophoresis via their molecular-dependent mobilities with efficiencies >99% in COC/COC and PMMA/COC nanofluidic devices.

2.2 Materials and Methods

2.2.1 Materials and reagents

Silicon (Si) 〈100〉 wafers were purchased from University Wafers (Boston, MA). Non-impact modified PMMA was received from ePlastics (San Diego, CA). Cyclic olefin copolymer (COC 8007 and COC 5010) were purchased from TOPAS Advanced Polymers (Florence, KY). COC 6015 was obtained from Knightsbridge Plastics Inc. (Fremont, CA). UV curable polyurethane resin was purchased from Chansang Co. ATTO 532 was secured from Atto-Tec (Siegen, Germany). Uridine 5'-monophophate disodium salt, cytidine 5'-monophosphate disodium salt, adenosine 5'-monophosphate disodium salt, and guanosine 5'-monophosphate disodium salt were all obtained from Sigma-Aldrich (St. Louis, MO). Molecular biology grade water was secured from Thermo Fisher (Waltham, MA).

2.2.2 Conjugation of ATTO 532 to the ribonucleotide monophosphates (rNMPs)

Fluorescent labeling of rNMPs with the reporter ATTO532 (see Figure 2.1) consisted of the following methodology: [20] To a stirred solution of Atto532 amine (3 mg, 0.004 mmol) in DMF (0.5 mL) was added a single rNMP (1.4 mg, 0.008 mmol) and EDC (1.5 mg, 0.008 mL) in water (0.5 mL) followed by DIEA (10 μL). The resulting solution was allowed to stir at room temperature for 16 h. The labeled rNMP was directly purified using preparative HPLC (gradient:

95% H_2O, 5% MeOH, to 30% MeOH over 15 min) with the appropriate fraction collected into a microfuge tube and subsequently dried to yield a red solid (~1 mg, 22% yield). Analytical HPLC used an Agilent 1100 quaternary pump and a Hamilton PRP-1 (polystyrene-divinylbenzene) reverse phase column (7 μm particle size, 4 mm x 25 cm) with UV/vis detection at 254 nm and 532 nm. Elution was achieved using a gradient of water/acetonitrile (90:10 to 0:100 containing 0.1% TFA) over 20 min. Low-resolution mass spectra (LRMS) were obtained using a Waters Micromass ZQ 4000 instrument with ESI+ ionization. All samples were stored at -30°C until required for use.

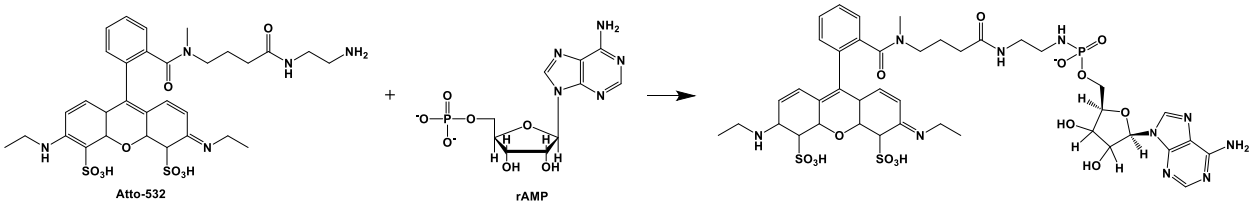

Figure 2.1 General synthetic scheme for the Atto532 labeled nucleotides.

2.2.3 Fabrication of microchannel thermoplastic devices

Fabrication of microchannel devices were carried out following a method similar to what we previously published [41-46]. Briefly, T-shaped (50 μm depth x 100 μm width and 5 cm long) microfluidic devices were hot embossed into PMMA using a brass master mold, which was fabricated utilizing high precision micromilling. Embossed devices were diced with a bandsaw, reservoirs were drilled using a mechanical drill, and were cleaned with 10% Micro-90, IPA, and nanopure water. The substrate containing the fluidic network and cover plate (150 μm thick PMMA sheet) were UV/O_3 modified at 22 mW/cm^2 for 16 min prior to thermal fusion bonding. Microchannel dimensions were measured before and after bonding by rapid laser-scanning optical profilometry (VK-X250, Keyence, IL, USA).

2.2.4 Microscale electrophoresis of the rNMPs

Free solution electrophoresis was carried out following a method reported by our group [40]. Briefly, the T-shaped microfluidic device was primed with 50% methanol/water, filled with 1X NEB buffer 3 at pH 7.9 before carrying out the electrophoresis. A positive voltage was applied to the sample reservoir to initiate injection while grounding the sample waste reservoir until the cross channel was completely filled. The remaining reservoirs were allowed to float during injection. After injection, a positive voltage was applied to the electrophoresis buffer reservoir and the electrophoresis waste reservoir was grounded for the separation. The detector consisted of a laser-induced fluorescence system equipped with a single-photon counting module as we have reported previously [20]. For a schematic of the laser-induced fluorescence detector for microchip electrophoresis and a picture of the microchip see Figure 2.2.

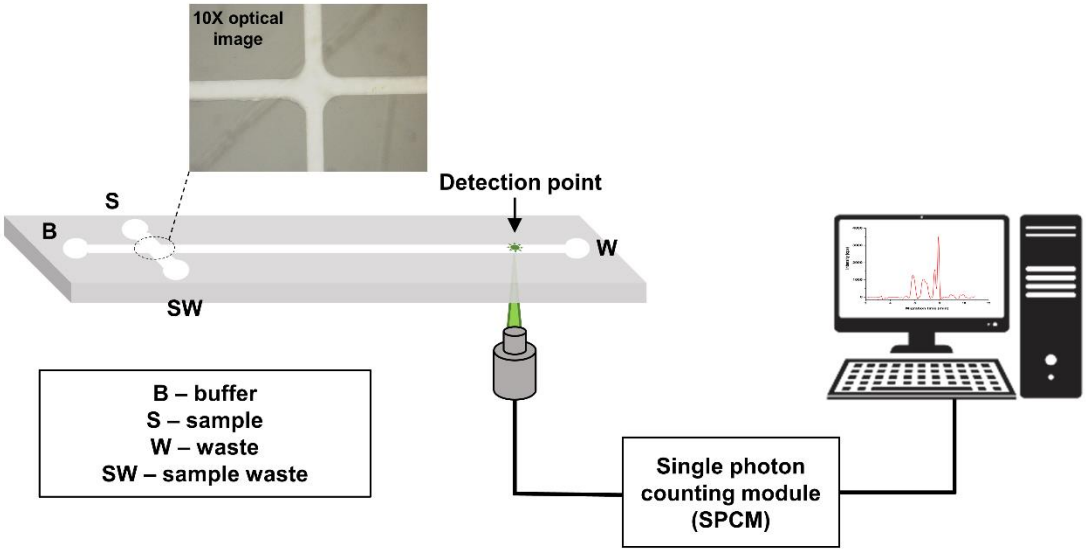

Figure 2.2 Schematic diagram of experimental set up used for the microscale electrophoresis, where a T-shaped microchip was used. A sample plug was electrokinetically introduced into the separation channel by applying an electric field across the S and SW reservoirs. SPCM-AQR single photon counting module within the optical train was used to capture the fluorescence signal at the detection point.

2.2.5 Fabrication of nano-channel devices

Nanofluidic devices were fabricated in thermoplastics using a method described by our group [20]. Briefly, microchannels were fabricated in a Si wafer (master) via optical lithography followed by wet Si etching. Then, nanochannels were fabricated into the same Si master using focused-ion beam milling. Next, resin stamps were produced from the Si master using a UV curable polyurethane (PUA) resin that covered the Si master and exposing to UV light. COC 6015, which was used as the back plate for the resin stamp, was coated with a NOA72 adhesive. Nanochannels were imprinted into a plastic substrate using a Nanonex 2500 nanoimprint lithography (NIL) machine. A schematic diagram of the imprinting/bonding scheme using the Nanonex 2500 is shown in Figure 2.3A.

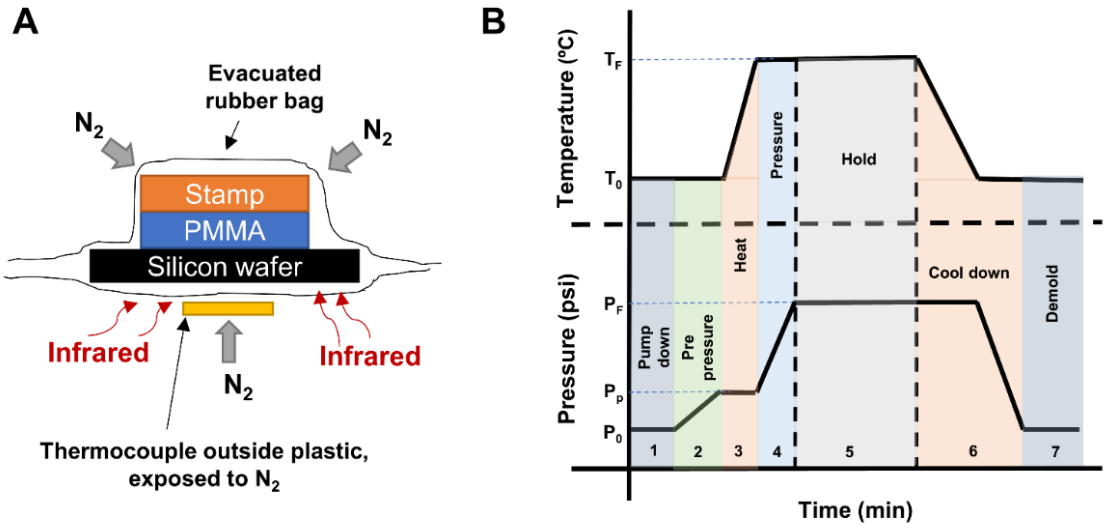

Figure 2.3 (A) Schematic of the nanofluidic device assembly using the Nanonex 2500. **(B)** Temperature pressure process profile showing the seven stages for the imprinting and bonding cycle. An imprinting cycle was 10 min (5 min imprinting time) and the bonding cycle was 25 min (15 min bonding time).

The Nanonex 2500 uses an air cushion press method (ACP) for imprinting structures into the appropriate thermoplastic substrate. In this method, an inert gas is used to press the patterned mold and the substrate against each other in an enclosed chamber (Figure 2.3A). This method has several advantages over the solid parallel plate method including: (a) Isotopically applied gas pressure eliminates lateral shift or rotation that reduces damage to the mold; (b) ACP has much more uniform pressure, which eliminates hot spots during the imprinting; (c) the conformable gas layers in ACP eliminates direct contact between the solid plates and samples (mold and substrate) and thus, removes any effects related to imperfection of the solid plates; (d) ACP is immune to dust and topological variations on the backside of the mold or substrate; and (e) smaller thermal mass in ACP provides faster thermal NIL imprinting [47, 48].

Figure 2.3 B shows the temperature-pressure program used for imprinting nanofluidic devices and the thermal fusion bonding of devices, which involves placing a cover plate over the imprinted fluidic network. The temperature and pressure conditions for imprinting and bonding depend on the substrate used. As shown in Figure 2.3B, the temperature-pressure process program consisted of seven steps: (1) Pump down stage – a silicon rubber bag consisting of a substrate and stamp were placed within an enclosed chamber. The chamber is then evacuated. We used a 3 min pump down time for this stage. (2) Pre-pressure stage – after chamber pump down, the chamber pressure was raised to a pre-pressure value before heating the system, which took ~1 min. In the Nanonex 2500, nitrogen is used as the gas for ACP. (3) Heating stage – once the chamber reached pre-pressure, heating of the chamber occurred. Heating in the Nanonex machine was achieved using infrared lamps placed below the Si wafer. The use of a Si wafer facilitated heat conduction to the thermoplastic substrate. (4) Pressure stage – once the desired imprinting/bonding temperature was reached, the pressure was immediately raised to the intended final pressure. This

final pressure is determined by the bonding or imprinting step and material used as the substrate. (5) Hold stage – in this step, the desired temperature and pressure were maintained for the appropriate time. For imprinting, the holding time was 5 min. For thermal fusion bonding, the hold time was 15 min. (6) Cool down stage – following imprinting/bonding, the temperature of the chamber was decreased gradually to 45°C at a rate of 2.5°C/s while holding the device imprinting/bonding pressure. This reduced stress imposed on the substrate/cover plate and minimized channel deformation. (7) Demolding stage – after cooling, the chamber released the gas pressure and separates the stamp from the thermoplastic wafer.

Preliminary tests were conducted to optimize the imprinting pressure, temperature, and time. The imprinting temperature was kept higher than the T_g of the thermoplastic substrate. For PMMA devices, we used the same imprinting conditions reported previously by our group (140°C, 300 psi, and 5 min) [40]. Imprinting of nanofluidic structures into COC 5010 substrates was done by keeping the imprinting pressure (300 psi) and time (5 min) constant while optimizing the imprinting temperature. The optimized conditions for the imprinting are given in Table 2.1 for both COC 5010 and PMMA substrates. Imprinted nanofluidic devices were then characterized using SEM and atomic force microscopy, AFM (see Figure 2.4).

Table 2.1. The optimized imprinting conditions for NIM-PMMA and COC 5010 100 x100 nm nanochannel in Nanonex 2500; Width and depth of the imprinted nanochannel measured by SEM (Hitachi SU8230 Field emission scanning electron microscopy) and SPM (Schimadzu SPM-9700HT), respectively.

Substrate	Imprinting conditions (temp., pressure, time)	Width and depth of the imprinted device
NIM-PMMA	140°C, 300 psi, 5min	110 (±1.4) nm x 112.1 (±1.6) nm
COC5010	140°C, 300 psi, 5min	110 (± 0.9) nm x 109.3 (±1.3) nm

It is necessary to seal the nanofluidic device after thermal imprinting using a cover plate. Thermal fusion bonding was used for sealing nanochannel devices. Bonding of PMMA/COC devices were done according to a method described by Uba *et al.* [49] with 1 min O_2 plasma treatment for both the substrate and cover plate at 50 W. We attempted a similar protocol to assemble COC/COC devices by modifying both the substrate and cover plate by oxygen plasma, but we were unsuccessful in obtaining a well-sealed device. Therefore, we tried bonding COC 5010 and 8007 without plasma treatment. Successful bonding was achieved at 110 psi bonding pressure, 70°C for 15 min using the NIL machine (see Table 2.2). The assembled COC/COC devices could then be UV/O_3 treated to increase the wettability of the nanochannels, which created surface confined –COOH groups.

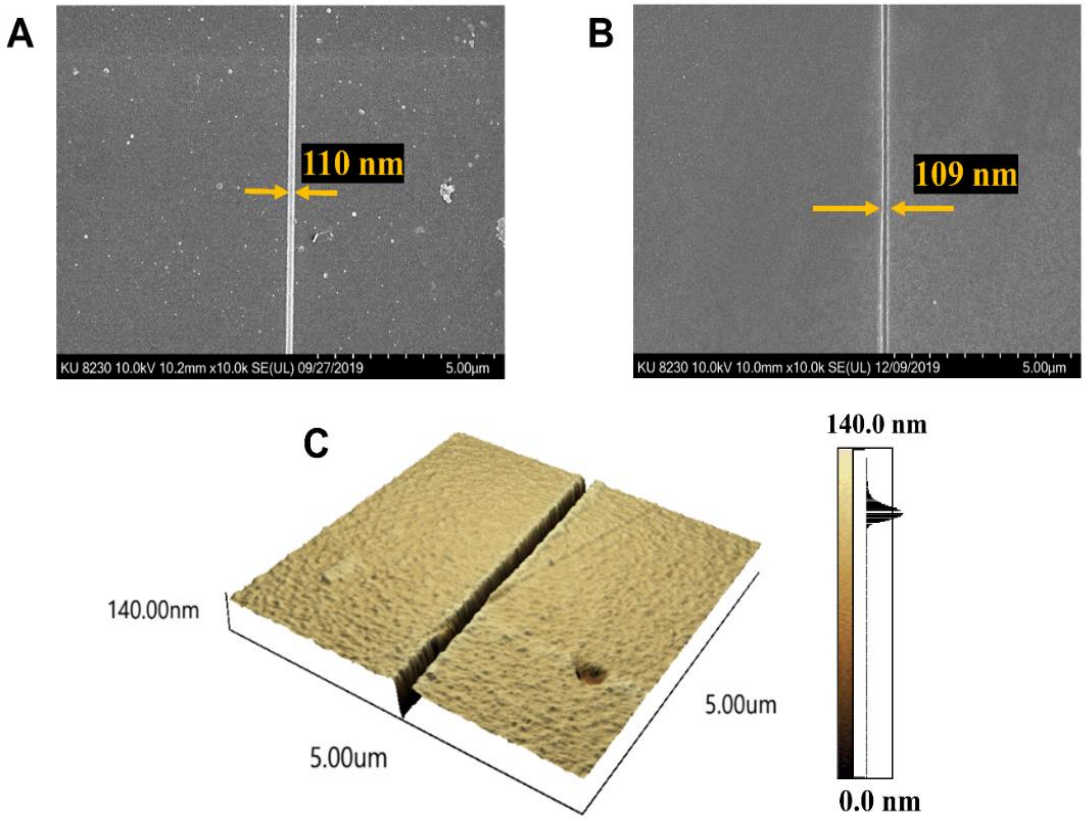

Figure 2.4(A) SEM of a nanochannel replicated via UV-NIL into a polyurethane (PUA) resin to produce the resin stamp. In this case, the resin stamp has the reverse polarity compared to the Si master from which it was replicated from. **(B)** SEM of a nanochannel thermally imprinted into a COC 5010 substrate. **(C)** AFM of the nanochannel thermally imprinted into COC 5010 with the depth measured as 110 nm.

Table 1.2 Optimized thermal fusion bonding conditions for PMMA and COC 5010 100 x100 nm nanochannels using the Nanonex 2500. In both substrate cases, the cover plate was COC 8007.

Substrate	Plasma modification	Bonding conditions (temp., pressure, time)
NIM-PMMA	**1 min. at 50 mW**	**70°C, 110 psi, 15min**
COC 5010	**No modification**	**70°C, 100 psi, 15min**

2.2.6 Cover plate/substrate bond strength measurements of nanochannel devices

The crack opening method was used to evaluate the bond strength between the cover plate and substrate [50, 51]. Here, a razor blade of known thickness, t_b, is inserted between the bonded substrate and cover plate to generate an interfacial fracture with a length (L) from the edge of the razor blade. The bond strength is represented by equation (1) where t_s and t_p are the thickness and E_p and E_s are the elastic moduli of cover plate and the substrate, respectively.

$$\gamma = \frac{3t_b^2 E_s t_s^3 E_p t_p^3}{16L^4(E_s t_s^3 + E_p t_p^3)} \quad (1)$$

The elastic moduli of COC 5010 and COC 8007 were 3.0 GPa and 2.6 GPa, respectively, as provided by the manufacturer. In this work, all tests were performed using a stainless-steel single edge razor blade with a thickness of 0.009" and the crack lengths were measured using a calibrated upright microscope with a 10X objective lens. All measurements were replicated five times and the average bond strength was determined along with the standard deviation.

2.2.7 Evaluation of pH stability and structural integrity of fabricated nanochannel devices

To make sure there was no channel deformation after bonding, COC/COC and PMMA/COC nanochannel devices were filled with a Rhodamine B solution in ultrapure water at pH 7.0 and fluorescence images were captured. Afterwards, to evaluate the pH stability of the nanochannel devices, Rhodamine B solution in ultrapure water was replaced with a Rhodamine B dye solution in pH 10.3 TBE buffer and the fluorescence images were captured at t = 0, 0.5 h, and 3 h to observe any channel deformation or leaking by delamination of the cover plate.

Table 2.2 Chemical composition of 1X NEB buffer 3.

Component	Concentration (mM)
Sodium Chloride (NaCl)	**100**
Magnesium Chloride ($MgCl_2$)	**10**
Tris-HCl	**50**
Dithiothreitol (DTT)	**1**

2.2.8 Electroosmotic flow (EOF) measurements

The EOF in the nanochannel devices was measured using the current monitoring method [52]. A device possessing a single nanochannel (107 μm long, 110 nm deep, and 110 nm wide) connecting two access microchannels was fabricated as described earlier. The entire chip was primed with 50% (v/v water/methanol), drained, and flushed with nuclease free water. After that, the device was filled with 1X NEB (New England Biolabs) buffer 3 (composition of NEB buffer 3 is given in Table 2.3) and allowed to equilibrate for 4 min under a 500 mV DC bias. After confirming equilibrium by a constant current trace, one reservoir was replaced by 0.94X NEB buffer 3. Pt

electrodes were placed into the reservoirs across the channels under a 500 mV DC bias. pClamp10 software and Digidata 1440B low noise digitizer were used for data acquisition.

2.2.9 Contact Angle measurements

The contact angles of COC surface before and after UV/O_3 treatment were measured using VCA optima instrument. Nanopure water was used for all these measurements.

2.2.10 Detection system for nanoscale electrokinetics

The translocation of rNMPs through the thermoplastic nanochannels was monitored using a fluorescence imaging system we have reported previously [20, 40].

2.2.11 Electrokinetic identification of rNMPs in nanochannels

Nanochannel devices were primed with 50% methanol/water mixture for 5 min. Using a vacuum pump, the methanol/water solution was removed from the nanofluidic device. After that, it was filled with 1X NEB buffer 3 (pH 7.9) and allowed to equilibrate for 10 min. ATTO 532 labeled rNMPs (200 nM) were prepared in 1X NEB buffer 3. Next, the rNMP solution was added to one of the reservoirs connecting microchannels by replacing the carrier electrolyte. Afterwards, the microchannel was filled with rNMP solution by applying a vacuum through the opposite side reservoir of the same microchannel. Thereafter, the same volume of carrier electrolyte was added to all other reservoirs. Finally, the dye-labeled rNMPs were injected into the nanochannels by applying a square wave voltage (2 -20 V_{pp}) for a period of 20 s (50×10^{-3} Hz frequency) using an ATTEN ATF200B function waveform generator allowing multiple injections. Events were recorded for 6,000 frames.

2.2.12 Data analysis

The nanochannel electrophoresis data were analyzed using a previously reported method by our group [20, 40]. Briefly, the collected videos from the imaging microscope's EMCCD camera were imported into Image J software and two detection windows of 1 μm^2 were placed at the nanochannel entrance and exit. The fluorescence intensity over time recorded from these detection windows were exported into Origin 8.5. Then, the first derivative of each data set was taken to produce two peaks indicating the time the fluorescently labeled rNMPs reached the entrance and exit of the nanochannel. The time difference was taken as the migration time of the rNMPs to travel a fixed distance and the apparent velocity was calculated. The apparent mobility of each rNMP was generated by normalizing the apparent velocity with respect to the electric field strength.

2.3 Results and Discussion

2.3.1 Bond strength and pH stability of COC/COC and PMMA/COC devices

In a typical nanofluidic device production pipeline, the final step is enclosure of the nanochannels with a cover plate with the preferred assembly step that does not alter the underlying nanostructures. There are several methods to obtain enclosed fluidic nanochannels such as thermal fusion bonding, ultrasonic bonding, or solvent-assisted bonding[53]. Solvent-assisted bonding can result in bond strengths between the substrate and cover plate that cannot withstand high pressures and voltages for extended periods of time [34]. Also, solvent-assisted bonding can cause dimensional instability of the thermoplastic device due to softening of the plastic substrate leading to changes in channel dimensions and/or collapse of the nanochannel resulting in device failure [53]. Our group previously reported, the thermal fusion bonding technique with a high process yield rate (>90%),

which consists of bonding a low T_g cover plate to a high T_g substrate using a bonding temperature that is close to the T_g of the cover plate [49]. Because the substrate's Tg is much higher than the bonding temperature used, minimal changes in the dimensions of the nanochannels result. In addition, thermal fusion bonding of the low Tg cover plate to the higher Tg substrate is less time consuming compared to the aforementioned methods, and does not require additional reagents or pre-cleaning in RCA solutions or organic solvents. Thus, we used thermal fusion bonding to assemble all devices herein.

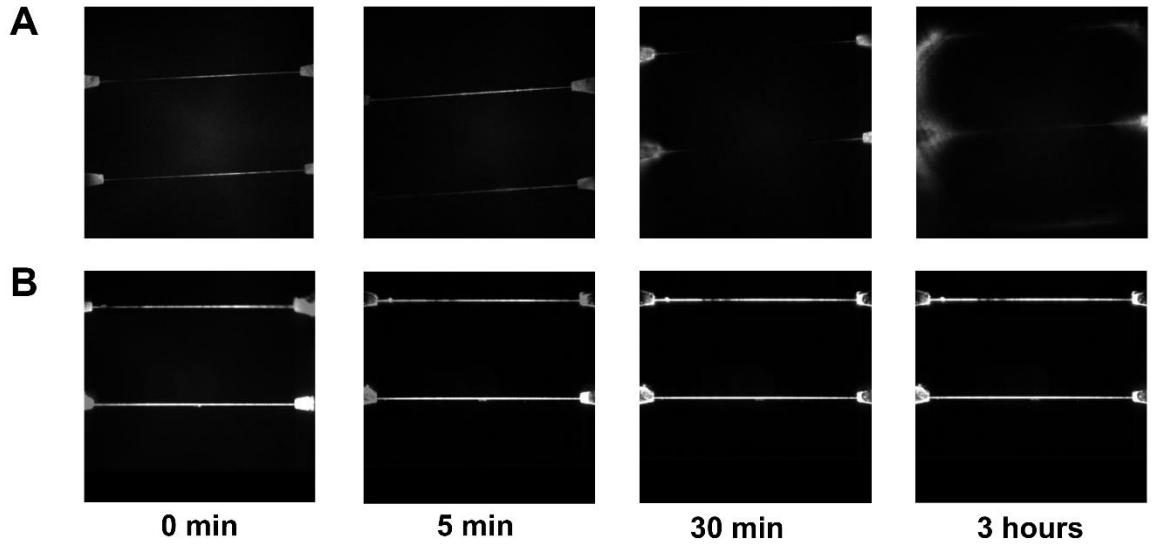

Figure 2.5(A) pH stability of PMMA/COC devices with time at pH 10.3. **(B)** pH stability of COC/COC devices with time at pH 10.3. All fluorescence images were adjusted to the same intensity scale. In both cases, a Rhodamine B dye solution was infused into the nanofluidic device and the fluorescence monitored using a single-molecule fluorescence microscope equipped with an EMCCD camera.

We studied the bond strength of thermally fusion bonded COC/COC devices using the crack opening method. Preliminary tests were conducted to optimize the bonding pressure and time at a bonding temperature of 70°C, which is close to the T_g of the cover plate. The optimized bonding parameters (see Table 2.2) were utilized to prepare sealed nanofluidic devices. The bond strength

of COC/COC devices was 8.5 ±1.1 mJ/cm2. The bond strength of COC/COC devices were significantly higher than that of PMMA/COC devices, which had a bond strength of 0.086 ±0.014 mJ/cm2. This suggests that interfacial adhesion of similar materials is greater than that of dissimilar materials. Therefore, COC devices can be operated at higher pressures and tolerate higher electric field strengths compared to PMMA/COC hybrid devices. pH stability is another important parameter to evaluate in these devices because high pH may result in improved identification of the rNMPs[22, 24]. However, under high pH conditions, thermoplastics may swell and/or delaminate according to their base resistance. Thus, the base resistance of PMMA/COC nanochannels and COC/COC nanochannels were evaluated prior to nanoscale electrophoresis. The nanofluidic device was flooded with different pH solutions containing Rhodamine B as the reporter and fluorescence imaging was carried out to determine if leaking of the dye solution occurred due to swelling and/or delamination of the cover plate/substrate assembly. A fluorescence image of a dye-filled chip was first taken at pH = 7.0 to make sure that the thermal fusion bonded device had no leakage prior to adding the higher pH (pH = 10.0) buffer. After 30 min, the PMMA/COC devices leaked as fluorescence appeared near the inlets of the nanochannels indicating delamination of the cover plate from the substrate. However, the COC/COC devices even after 3 h did not show signs of leaking or delamination (see Figure 2.5A and B). Therefore, PMMA/COC devices showed lower base resistance compared to COC/COC devices [54, 55] meaning that COC/COC devices can be used in higher pH carrier electrolytes that may produce better electrophoresis results.

2.3.2 Water contact angle and EOF of COC/COC devices

For PMMA/COC devices, O_2 plasma treatment was carried out before thermal fusion bonding to increase the bond strength between the PMMA substrate and COC cover plate and increase the wettability of the surfaces to minimize issues with bubble formation in the device. However, for COC/COC devices O_2 plasma treatment prior to thermal fusion bonding produced poor adhesion of the cover plate to the substrate. Therefore, we evaluated the ability to assemble COC/COC devices in their native states followed by UV/O_3 activation to increase the wettability of the nanochannel by increasing the surface charge density

Water contact angle measurements can serve as a measure of the hydrophilicity/hydrophobicity of a surface, although it does not provide insight into the functional groups comprising that surface. Figure 2.6A shows the water contact angle measured at different post-assembly UV/O_3 exposure times for a COC 5010 substrate that was covered with COC 8007. In these experiments, the cover plate was removed following UV/O_3 exposure to allow performing the contact angle measurements, which was possible by eliminating the thermal fusion bonding step. Reductions in the water contact angle indicated that the COC surface became more hydrophilic due to polar functional groups generated from UV/O_3 activation. The water contact angle did not change for UV/O_3 exposure times >15 min as shown in Figure 2.6A ($p = 0.3474$, $n = 5$, contact angle data for 15 min UV vs. 20 min UV exposure).

Another parameter we investigated was the EOF in COC/COC nanochannel devices. We measured the EOF with UV/O_3 exposure time in COC/COC nanochannel devices exposed to UV/O_3 through the COC 8007 cover plate following thermal fusion bonding. According to the data presented in Figure 2.6B, the EOF was $1.40 \times 10{-}5$ cm^2/Vs after 10 min exposure time. However, upon increasing the exposure time to 15 min, the EOF increased by ~10-fold. Further

increasing the exposure time to 20 min did not change the EOF significantly ($p = 0.87$ for 15 min vs 20 min exposure time). We should note that for PMMA/COC devices, post-assembly activation of the device with UV/O_3 did not affect the EOF as was seen for COC/COC devices (data not shown). This result is not surprising, because in a previous publication we noted that PMMA is not as UV transparent as COC and the channel side walls for PMMA can reduce penetration of the UV light into the channel [56]. For the PMMA/COC devices, three of the four walls are PMMA while in COC/COC devices all of the surfaces are COC and thus, more transparent to UV light (PMMA has ~1.5% UV transparency and COC is ~53%).

At low EDL thicknesses (~0.8 nm for buffer used), μ_{eof} can be represented in terms of the bulk solvent viscosity, η_o, and ζ by the Helmholtz-Smoluchowski equation where ϵ_0 , ϵ_r are the permittivity of air and the relative permittivity of the buffer, respectively, through the use of equation (2).

$$\mu_{eof} = \frac{\epsilon_0 \epsilon_r \zeta}{\eta_o} \qquad (2)$$

Furthermore, ζ can be represented in terms of σ_s (surface charge) and the Debye length (λ_D) for different electrolyte solutions using equation (3) [38].

$$\zeta = \frac{2\ k_B T}{e} \ln\left[\frac{2\ e\ \sigma_s\ \lambda_D}{\epsilon_r\ \epsilon_0\ k_B\ T} + \sqrt{1+\left[\frac{\left(e\ \lambda_D / \epsilon_r\ \epsilon_0\ k_B\ T\right)^2}{4}\right]} \right] \qquad (3)$$

In equation (3), ϵ_0 and ϵ_r are constants for a given carrier electrolyte and if the ionic strength remains constant, λ_D will not change. In our experiments, only σ_s is changing as a function of UV/O_3 dose and therefore, EOF changes arise from changes in the number of -COOH groups on the plastic surface. Similar to the contact angle data, the EOF remained constant for exposure times longer than 15 min. O'Neil *et al*., whom mapped the distribution and number density of -COOH groups in COC by super-resolution microscopy, observed a reduction of -COOH groups at 20 min

UV/O_3 exposure times compared to 15 min exposure [37]. This would indicate that the EOF may be reduced with UV/O_3 doses >15 min (see equation (3)). While we noticed a slight reduction in the EOF at 20 min exposure compared to 15 min, it was not significantly different.

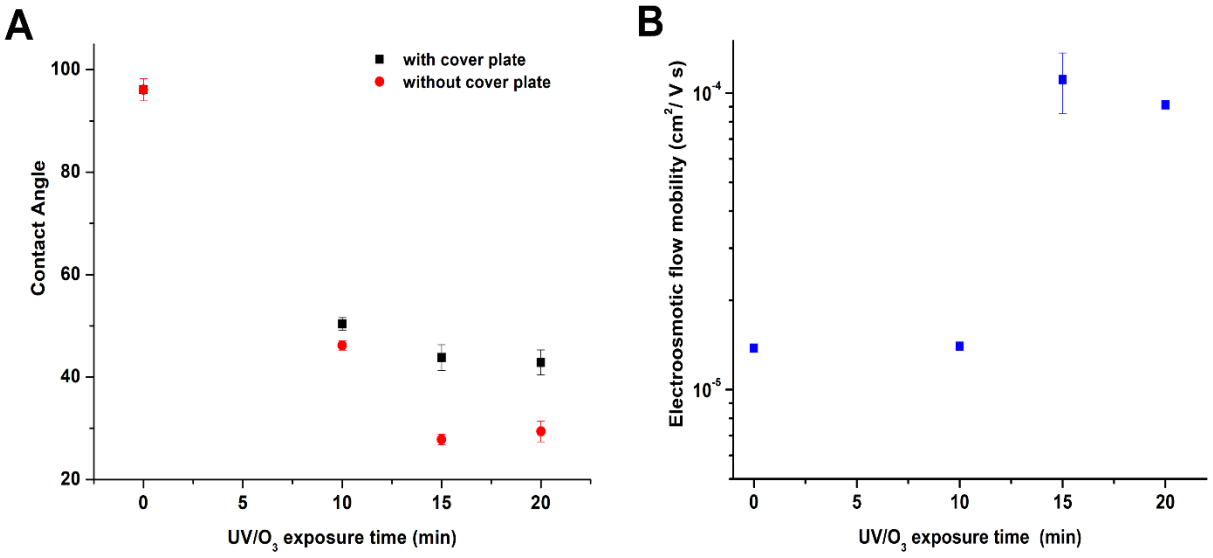

Figure 2.6(A) Water contact angle of COC 5010 measured at different UV/O_3 exposure times using a power density of 22 mW/cm^2. The data points named as with cover plate were obtained by keeping a cover plate on top of the substrate and then exposing it with UV/O_3 through the cover plate. After exposure, the contact angle of the underlying substrate was measured by removing the cover plate, which was not thermally bonded to the undelying substrate. **(B)** EOF mobility of COC/COC nanochannel devices as a function of UV/O_3 exposure time. The dimensions of the nanochannels were 110 nm x 110 nm (depth × width). The substrate was COC 5010 that was sealed with a COC 8007 cover plate. The UV/O_3 activation was done through the cover plate following device assembly. Error bars represent the standard deviations (n = 5).

2.3.3 Microchip electrophoretic separation of rNMPs

We carried out microchip electrophoretic separations of the rNMPs using a T-shaped microchip fabricated in PMMA (depth = 50 µm; width = 100 µm total channel length = 5 cm) to understand the effects of scaling on the rNMP identification. The free solution electrophoretic separation of the rNMPs was performed in 1X NEB buffer 3 at pH 7.9. During the microchip electrophoresis, rNMPs migrated from anode to cathode in spite of their anionic nature. As shown in Figure 2.7A, at pH 7.9 we could separate all four rNMPs. The apparent mobilities of the rNMPs were calculated

using equation (4) and are presented in Figure 2.7B. In this case, *l* is the distance from the injection point to the detector (4.0 cm), t_m is the migration time of each rNMP, and *E* is the electric field strength (1,000 V/ cm). The apparent mobility order of the rNMPs was rAMP < rCMP < rGMP < rUMP.

A

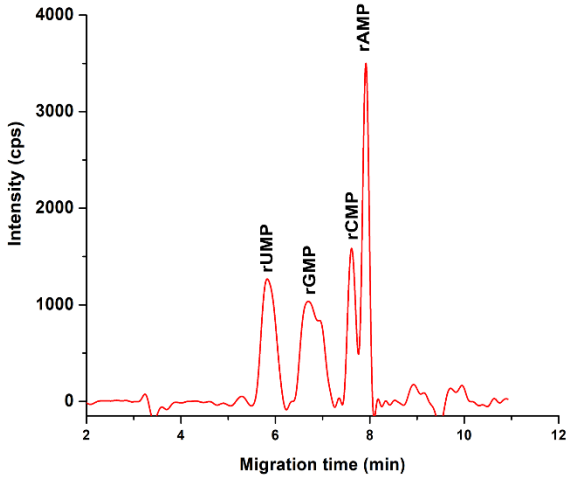

B

Nucleotide	Apparent mobility x 10^{-5} (cm^2/ V s)
rUMP	1.50
rGMP	1.20
rCMP	1.09
rAMP	1.05

C

Peak pair	Separation resolution
rUMP/ rGMP	1.74
rGMP/ rCMP	2.00
rCMP/ rAMP	1.15

Figure 2.7 (A) Microchip electropherogram of the rNMPs in PMMA microchannels having dimensions of 50 µm x 100 µm (depth and width, respectively) with 5 cm total channel length (effective length = 4 cm). **(B)** Calculated apparent mobilities of rNMPs using equation (4). **(C)** Resolutions (R) calculated for adjacent peak pairs using the electropherogram shown in (**A**). $R = 1.18(t_{m2}-t_{m1})/ (w_1+w_2)$, where t_{m1} and t_{m2} are migration times and w_1 and w_2 corresponds to the peak widths at the base of the peaks.

$$\mu_{app} = \frac{l}{t_m\ E} \qquad (4)$$

Uhrova *et al.* [22] has shown the separation of rNMPs in a fused silica capillary without suppressing the EOF by free solution electrophoresis using a borate buffer at pH 8 and observed a similar migration order except for rUMP, which showed a higher migration time in their data. Baseline separation (resolution >1.5) was obtained for the rGMP/rUMP pair, but for the rAMP/rCMP pair, no baseline separation was observed (see Figure 2.7C). We should note that the

shoulder for the rGMP peak could be due to 8-oxo-G, because guanine is highly susceptible to oxidation [57]. Moreover, rNMPs were separated in a COC-COC microfluidic chip and obtained a similar migration order as PMMA but lower resolution compared to PMMA (Figure 2.8).

A

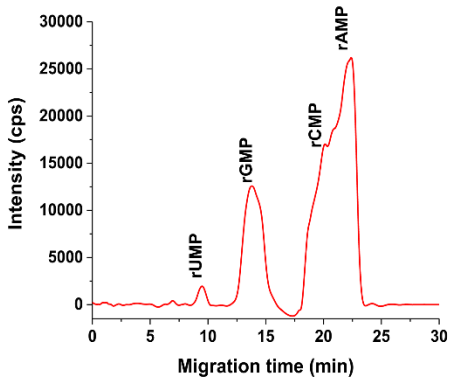

B

Nucleotide	Apparent mobility x 10^{-3} (cm^2/ V s)
rUMP	3.40
rGMP	2.72
rCMP	1.59
rAMP	1.44

C

Peak pair	Separation resolution
rUMP/ rGMP	1.64
rGMP/ rCMP	2.04
rCMP/ rAMP	0.60

Figure 2.8(A) Microchip electropherogram of the rNMPs in COC microchannel having dimensions of 50 µm x 100 µm (depth and width, respectively) with 5 cm total channel length (effective length = 4 cm). **(B)** Calculated apparent mobilities of rNMPs using equation (4). **(C)** Resolutions (R) calculated for adjacent peak pairs using the electropherogram shown in (A). $R = 1.18(t_{m2}-t_{m1})/ (w_1+w_2)$, where t_{m1} and t_{m2} are migration times and w_1 and w_2 corresponds to the peak widths at the base of the peaks.

2.3.4 Effect of material type on the nano-electrophoresis of ATTO 532-labeled rNMPs

In Sections 2.3.1 and 2.3.2 we compared the mechanical and chemical properties of nanochannel devices made from COC/COC and PMMA/COC, where the first material listed is the substrate containing the nanochannel and the second material is the cover plate. In this section we will present results for the identification of rNMPs in PMMA/COC and COC/COC nanochannel devices to understand material effects on nanoscale electrophoresis. The EOF for PMMA/COC

devices was reported in [40], which was found to be 4.2 x 10^{-4} cm^2/Vs, approximately 4 times higher than that of COC/COC devices.

Figure 2.9A shows the apparent mobility versus electric field strength for the four rNMPs using a 110 nm x 110 nm channel fabricated in PMMA/COC with a carrier electrolyte consisting of 1X NEB buffer 3 (ionic strength of 145 mM) at pH 7.9. At pH 7.9, all ATTO-532 labeled rNMPs have a net charge of −3; the ATTO-532 dye contributes a −2 charge and the phosphate group contributes −1 (see Figure 2.9B) with all nucleobases not carrying a charge at this pH. Because the same dye reporter was covalently attached to each rNMP using the same linker, differences in the apparent mobilities of the rNMPs were assumed to arise from the nucleobase

The apparent mobility is a sum of the EOF (μeof) and the electrophoretic mobility of the rNMP (μep). In this case, the electrophoretic mobility of the dye/rNMP conjugate is opposite in direction to the EOF and thus, a larger μep value results in a lower apparent mobility. Because all rNMPs have the same charge at this pH, differences in the apparent mobility are due to differences in the size of the nucleobase if the identification mechanism is solely electrophoretic. We could only monitor the mobilities of the rNMPs at electric field strengths 460 V/cm that generated significant slurring of the images that resulted from the limited framerate we could operate the EMCCD camera to provide sufficient signal-to-noise ratio to track the rNMP motion. As seen in Figure 2.9A, the apparent mobility for rCMP and rAMP showed electric field dependency, which was not observed in the case of rUMP and rGMP. In our previous report for the nanoscale electrophoresis of the dNMPs in PMMA/COC devices, all of the nucleotides showed a field dependent apparent mobility[20]. For the dNMPs, we surmised that wall interactions occurred at low electric field strengths but were absent at higher electric field strengths. Here, we surmised potential wall interactions for rCMP and rAMP due to their field-dependent mobilities. Inspection of Figure 2.9A

indicated that for these two nucleotides, the apparent mobility decreased at higher electric field strengths indicating an increase in the electrophoretic mobility of rCMP and rAMP, which would indicate less wall interactions at higher electric field strengths.

Figure 2.9C shows histograms of the apparent mobility for the ATTO-532 labeled rNMPs at 280 V/cm in PMMA/COC devices. This electric field was selected as it provided the optimal resolution between the rNMPs with minimum standard deviations in the histograms (i.e., the standard deviations in these histograms is directly related to peak dispersion). These histograms were fit to a Gaussian function and the variance (σ 2), resolution, and identification accuracies were calculated (Figure 2.9D and E). The apparent mobility order at this electric field strength was rUMP < rGMP < rCMP < rAMP. The observed apparent mobility order here was different than the apparent mobility order we observed for microchip electrophoresis of the rNMPs (see Figure 2.7A).

Differences in the apparent mobility order between microchip electrophoresis and nano-electrophoresis could be due to scaling effects. When the channel dimensions are significantly reduced, the surface area-to-volume ratio increases and thus, surface interactions of solutes with channel walls can become more prominent. These wall interactions can arise from surface roughness that is comparable to the channel dimensions (width and depth) giving rise to intermittent motion and/or hydrophobic/hydrophilic, electrostatic, or van der Waals interactions [20]. In addition, because of the amorphous nature of thermoplastics resulting in a heterogeneous distribution of surface charges, recirculation can occur at low electric fields giving rise to intermittent motion [37]. For rAMP and rCMP, which showed electric-field dependent mobilities at lower electric fields indicative of wall effects on the mobility, their peak variances were larger than those for rUMP and rGMP, which did not show electric field dependent mobilities. In spite

of these considerations, the average resolution between Gaussian fits to the apparent mobility histogram was 4.3 (ranged from 1.4-7.8). Another important metric for the potential utilization of mobility matching for the identification of ribonucleotides is the identification accuracy. We defined the identification accuracy as the amount of overlap between two adjacent Gaussian fits to the histograms of the ATTO 532 rNMPs' apparent mobilities. The percent overlap of the Gaussian peaks was calculated using a previously described method [58]. The average identification accuracy for the rNMPs in PMMA/COC devices was >99.955% (see Figure 2.9F).

The EOF for COC/COC devices was 1.1 x 10^{-4} cm^2/Vs, which was ~4 times smaller than that of PMMA/COC devices as noted above [40]. Therefore, the overall magnitude of μ_{app} should be smaller in COC/COC devices compared to PMMA/COC devices (see Figure 2.10A), which allowed us to investigate the nanoscale electrophoresis at higher electric field strengths in the absence of image slurring compared to the PMMA/COC devices. Figure 2.10A shows the apparent mobility vs. electric field strength of the rNMPs in COC/COC nanochannel devices. In contrast to the data shown in Figure 2.9A, we could only perform the identification at high electric field strengths because at field strengths <450 V/cm, we observed trapping at the surface resulting from dielectrophroesis generated from surface roughness [38]; COC channels did show higher surface roughness compared to PMMA channels (data not shown). In the COC/COC devices, we observed reductions in the apparent mobility for rUMP above electric field strengths of 700 V/cm while for rGMP, the apparent mobility decreased going from 470 to 700 V/cm and then showed an increase at 930 V/cm. In addition, the other two rNMPs only showed a slight electric field dependent mobility. These trends for the most part are different than those observed in the PMMA/COC nanochannels most likely due to differences in surface chemistry between these two devices as

well as surface roughness, which generates intermittent motion and recirculation that are significantly reduced at high electric field strengths.[37]

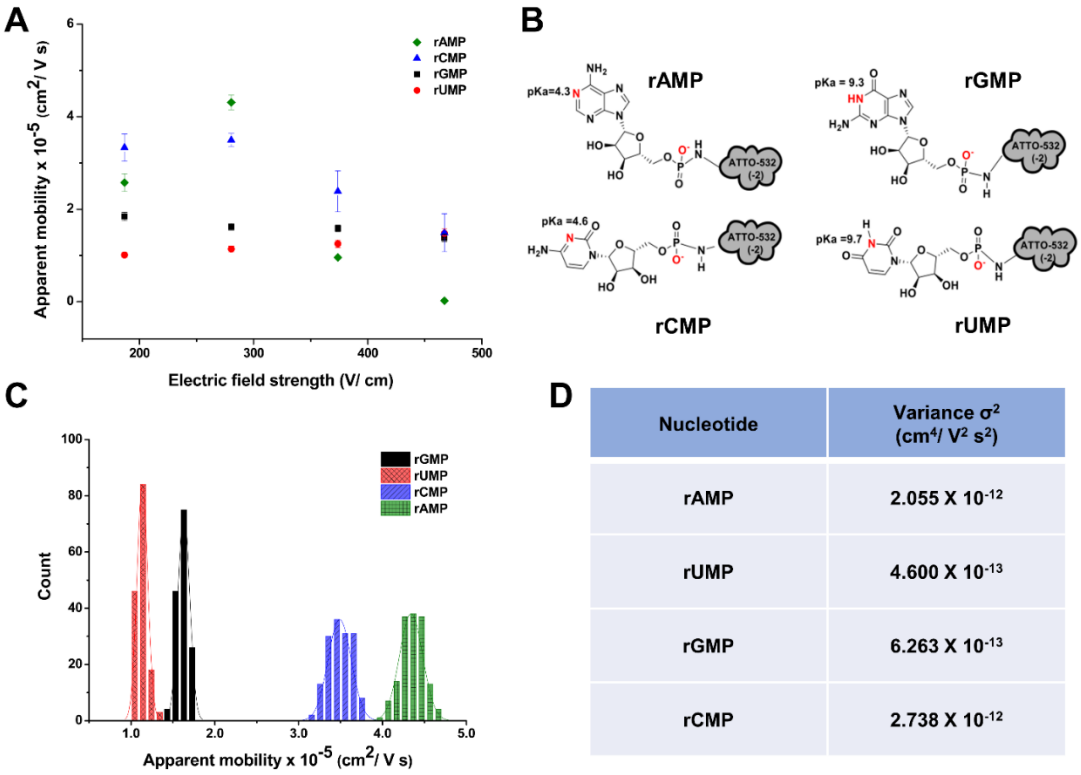

D

Nucleotide	Variance σ^2 ($cm^4/ V^2 s^2$)
rAMP	2.055×10^{-12}
rUMP	4.600×10^{-13}
rGMP	6.263×10^{-13}
rCMP	2.738×10^{-12}

E

Resolution	rAMP	rUMP	rGMP	rCMP
rAMP	-	7.8	6.0	1.4
rUMP	7.8	-	1.76	5.1
rGMP	6.0	1.76	-	3.8
rCMP	1.4	5.1	3.8	-

F

Identification accuracy	rAMP	rUMP	rGMP	rCMP
rAMP	-	>99.999	>99.999	99.760
rUMP	>99.999	-	99.978	>99.999
rGMP	>99.999	99.978	-	>99.999
rCMP	99.760	>99.999	>99.999	-

Figure 2.9(A) Apparent mobility vs electric field strength of rNMPs in 110 nm x 110 nm nanochannels fabricated in PMMA/COC nanochannels using 1X NEB buffer 3 at pH 7.9 as carrier electrolyte. **(B)** Structures of rNMPs with ATTO 532 and the pKa of the nucleobases. **(C)** Histogram of apparent mobilities of rNMPs at 280 V/cm in 110 x 110 nm PMMA/COC nanochannel devices using 1X NEB buffer 3 at pH 7.9 as the carrier electrolyte. The histograms were fit to a Gaussian function and each bin represented 2 x 10^{-6} cm^2/Vs. **(D)** The variance (σ^2) of peaks estimated from the Gaussian fits to the histograms. **(E)** The resolution of the Gaussian fits was calculated using R= 1.18 ($\Delta\mu/w_{0.5}$ + $w_{0.5}$), where $w_{0.5}$ corresponds to the full width at half maximum of the Gaussians. **F)** Identification accuracies of rNMPs calculated from Gaussian peak overlap. Identification accuracy = area of non-overlapped/total peak area.

Figure 2.10B shows histograms of the apparent mobilities for the ATTO-532 labeled rNMPs at 930 V/cm, which was selected because it provided optimal resolution between the rNMPs. The resolution was determined from Gaussian fits to the histograms. The variance, σ 2, was obtained from standard deviations associated with the Gaussian fits to the histogram data (see Figure 2.10C). Figure 2.10D shows the resolution values between rNMP Gaussian fit pairs using 1X NEB buffer 3 at pH 7.9. The apparent mobility order here was rCMP < rAMP < rGMP < rUMP and is different than the apparent mobility order observed in PMMA/COC nanochannel devices. At a carrier electrolyte pH of 7.9 and a field strength of 930 V/cm (λd = 0.3 nm), the average identification resolution of the rNMPs was 4.2 (range = 1.94 – 8.88, see Figure 2.10D). Figure 2.10E shows the calculated identification accuracies for the rNMPs. As can be seen, the average identification accuracy for the rNMPs in COC/COC devices was >99.997%, slightly higher than that seen for PMMA/COC devices. But, the average identification accuracy was higher for the rNMPs in both materials compared to our previous nanoscale electrophoresis analysis of the dNMPs (deoxynucleotide monophosphates), where the average identification accuracy was >9[20].

Judicious choice of nanochannel material is critical for optimizing identification accuracy. For example, COC/COC have similar chemistries except for slight differences in the norbornene content of the copolymer [59]. But hybrid devices, such as PMMA/COC, can demonstrate distortions in the plug flow due to large differences in the EOF that can introduce dispersion [60].

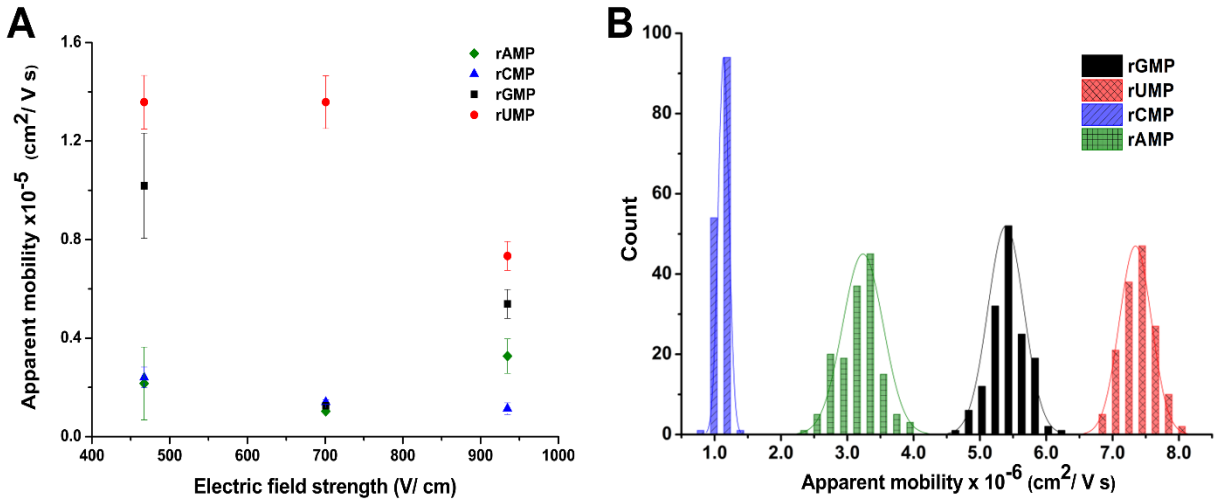

C

Nucleotide	Variance σ^2 ($cm^4/ V^2 s^2$)
rAMP	8.878×10^{-14}
rUMP	6.229×10^{-14}
rGMP	6.180×10^{-14}
rCMP	1.003×10^{-14}

D

Resolution	rAMP	rUMP	rGMP	rCMP
rAMP	-	3.72	1.94	2.69
rUMP	3.72	-	1.96	8.88
rGMP	1.94	1.96	-	6.10
rCMP	2.69	8.88	6.10	-

E

Base call accuracy	rAMP	rUMP	rGMP	rCMP
rAMP	-	>99.999	99.995	>99.999
rUMP	>99.999	-	99.996	>99.999
rGMP	99.995	99.996	-	>99.999
rCMP	>99.999	>99.999	>99.999	-

Figure 2. 10 (A) Apparent mobility vs electric field strength of rNMPs in 110 nm x 110 nm nanochannels fabricated in COC/COC nanochannels using 1X NEB buffer 3 at pH 7.9 as the carrier electrolyte. **(B)** Histogram of apparent mobilities of rNMPs at 930 V/cm in 110 x 110 nm COC/COC nanochannel devices using 1X NEB buffer 3 at pH 7.9 as the carrier electrolyte. The histograms were fit into Gaussian functions and each bin width represented 2 x 10^{-6} cm^2/Vs. **(C)** The variance (σ^2) of peaks estimated from Gaussian peaks. **(D)** The resolution of peaks was calculated using $R = 1.18 (\Delta\mu/w_{0.5} + w_{0.5})$, where $w_{0.5}$ correspond to the full width at half maximum of the Gaussian peaks. **(E)** Identification accuracies of rNMPs calculated from Gaussian peak overlap.

2.3.5 Effect of pH on the nanoelectrokinetics of ATTO 532-labeled rNMPs in COC/COC devices

We investigated the nanoscale electrophoresis of the rNMPs at pH 10.3, because a majority of microscale electrophoresis of rNMPs showed better resolution at higher pH (pH >9) [22, 24]. In addition, we noted better identification accuracies using nanoscale electrophoresis for the dNMPs at high pH. For the high pH experiments, the same carrier electrolyte as that used for pH = 7.9 was used, but with slight modifications. Tris-HCl in 1X NEB buffer 3 was replaced with glycine, however, the ionic strength at both pH values was the same. Glycine has a high buffer capacity at pH 10.3 (pKa_2 9.6) and therefore, the pH of the carrier electrolyte is maintained properly during the course of the experiment. In these experiments the electrophoresis was carried out at 930 V/cm.

The apparent mobility order at this pH was rAMP < rCMP < rGMP < rUMP with the apparent mobilities about one-order of magnitude higher compared to the electrophoresis performed at pH 7.9 (Figure 2.11A). In addition, at pH 10.3 the identification accuracy was reduced compared to pH 7.9 partly due to the increased peak dispersion that was observed. For example, the peak variance ranged from 1.3×10^{-11} cm^4/V^2s^2 to 4.1×10^{-13} cm^4/V^2s^2 for rAMP; these values were about 2-orders of magnitude larger than observed at pH 7.9. The identification accuracy for the rNMPs performed at this pH ranged from 0.78 to 2.

Increasing the carrier electrolyte pH had a two-fold effect: (1) Increasing the EOF due to increased ionization of the surface functional groups (pKa of the surface -COOH groups are ~ 6.9 [38]). The extent of ionization of the surface -COOH groups can be calculated using the Henderson-Hasselbalch equation and the pH value for the carrier electrolyte [61]. At pH 7.9, 90% ionization of the surface -COOH groups would be expected while at pH 10.3, 99.99% of these groups are deprotonated. The EOF mobility measured at pH 10.3 was 7.5×10^{-4} cm^2/Vs, which was

approximately 7-times higher compared to the EOF observed at pH 7.9 (1.1×10^{-4} cm^2/Vs). (2) Changing the charge state on some rNMPs. In this case, we would expect rGMP and rUMP to have a lower μapp compared to the other two rNMPs due to increases in their negative charge at pH = 10.3 yielding a larger μep (see Figure 2.9B).

A

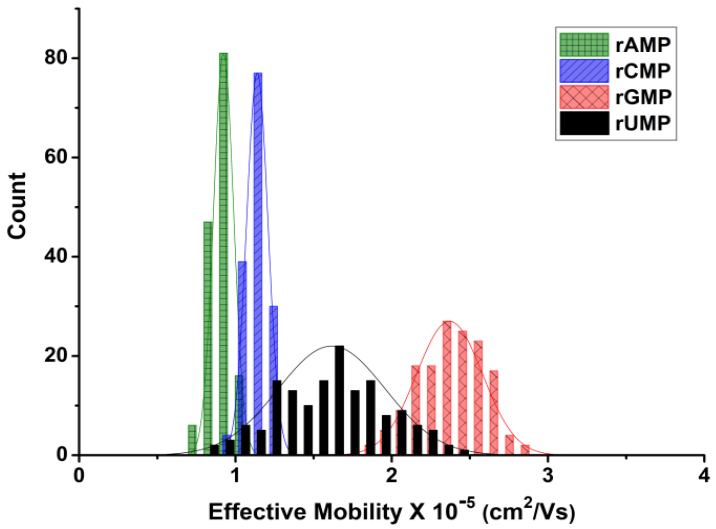

B

Resolution	rAMP	rUMP	rGMP	rCMP
rAMP	-	0.81	2.55	0.78
rUMP	0.81	-	0.64	0.82
rGMP	2.55	0.64	-	2.08
rCMP	0.78	0.82	2.08	-

C

Base call accuracy	rAMP	rUMP	rGMP	rCMP
rAMP	-	94.738	>99.999	94.062
rUMP	94.738	-	89.973	94.950
rGMP	>99.999	89.973	-	>99.999
rCMP	94.062	94.950	>99.999	-

Figure 2.11 (A) Histogram of apparent mobilities of rNMPs at 934 V/cm in 110 x 100 nm COC/COC nanochannel devices using 1X NE buffer 3 at pH 10.3 as the carrier electrolyte. The histograms were fit to Gaussian functions and each bin represents 2 x 10^{-6} cm^2/Vs. **(B)** The resolution of peaks at pH 10.3 was calculated using $R = 1.18 (\Delta\mu/w_{0.5} + w_{0.5})$, where $w_{0.5}$ correspond to the full width at half maximum of the Gaussian peaks. **(C)** Identification accuracies of rNMPs calculated from Gaussian peak overlap. Identification accuracy = area of non-overlapped/total peak area at pH 10.3.

While one would surmise increased dispersion arising from increased wall interactions, electrostatically we would not expect this because of the larger negative charge on the wall of the nanochannel as well as two rNMPs at this pH. Because these identifications were done at 930 V/cm and the larger EOF at this high pH, we suspect that the increased dispersion was due to image slurring resulting from the limited framerate that we could operate the EMCCD to secure sufficient signal-to-noise ratios to track the motion of the ATTO-532 labeled rNMPs. Irrespective of these observations, the mobility order was different at pH 10.3 compared to the mobility order at 7.9.

2.3.6 Nanoelectrokinetic identification of ATTO 532-labeled methylated rNMPs in COC/COC devices

The "epitranscriptome" is a term that refers to biochemical modifications of the transcriptome, which can play a major role in disease progression. However, studying the epitranscriptome is challenged by a lack of tools to interpret the entire portfolio of RNA modifications (>170). Most of these epitranscriptome modifications occur in ribosomal (rRNA) and transfer RNA (tRNA), which influence tRNA stability and cellular stress response (5-mC) and microRNA stability (2' -O-methlyation). Moreover, RNA base modifications of messenger RNAs (mRNA), such as N6-methyladenosine (m6A), 5-methylcytidine (5-mC), inosine (I), pseudouridine (ψ), N1-methyladenosine (m1A), and 5-hydroxylmethylcytidine (5-hmC), can alter its function and metabolism [62]. To provide additional tools to investigate the epitranscriptome, the nanoscale electrophoresis of methylated rNMPs and their corresponding rNMPs was undertaken.

Figure 2.12A shows histograms of the apparent mobilities of rAMP and m6rAMP and Figure 2.12B displays the histograms of apparent mobilities for rCMP and m5rCMP at a field strength of

930 V/cm in pH 7.9 1X NEB buffer 3 using COC/COC nanochannel devices. A higher apparent mobility was observed for both methylated rNMPs (m6rAMP and m5rCMP) compared to their non-methylated counterparts. We calculated the resolution for the methylated from non-methylated forms and found that it was 0.59 for rAMP/m6rAMP and 0.73 for rCMP/m5rCMP. While baseline resolution was not achieved, further investigation into various electrophoresis conditions can improve these results. For example, one can optimize the electric field strength, carrier electrolyte conditions (pH, ionic strength), and/or wall chemistry (increasing/decreasing the dose of UV/O_3 irradiation, switching the choice of polymer substrate). In addition, because more than 170 post-transcriptional RNA modifications have been identified to date [63], we will also be investigating multi-dimensional nanoscale electrophoresis to efficiently identify the entire complement of modifications.

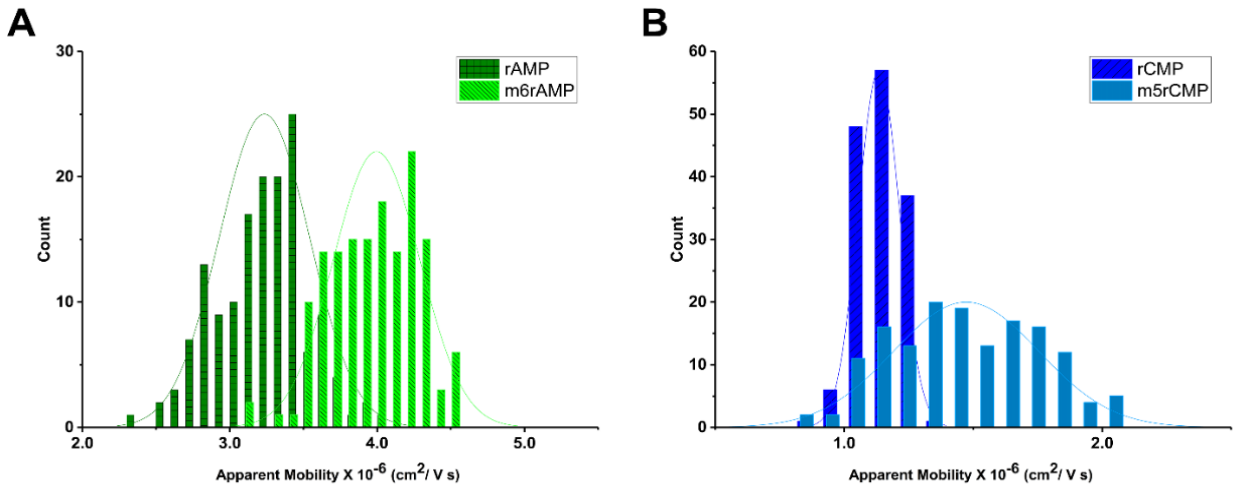

Figure 2.12 (A) Histograms of apparent mobilities for rAMP and m6rAMP. **(B)** Histograms of apparent mobilities of rCMP and m5rCMP. Electrokinetic separation was carried out at 930 V/cm in 110 x 110 nm COC/COC nanochannel devices using 1X NEB buffer 3 at pH 7.9 as the carrier electrolyte.

2.4 Conclusions

Our proposed SMS approach addresses the limitations of moderate base call accuracy associated with current nanopore sequencing by generating mononucleotides using a processive enzyme from an intact RNA molecule with the individual rNMPs identified using their molecular-dependent electrophoretic mobility; concept termed Time-of-Flight (ToF) identification. What makes ToF identification attractive is that a variety of experimental conditions can be altered to optimize the identification, such as channel material type, electric field strength, and pH to name a few. In this work, PMMA/COC and COC/COC nanofluidic devices were investigated. The advantage of COC/COC devices was the ability to perform post-assembly surface activation using UV/O3 light to control the EOF depending on the dose, which was not possible in PMMA/COC devices. In addition, the bond strength between the cover plate and the substrate for COC/COC devices was much higher when using post-assembly UV/O3 activation to allow a diverse range of electrophoresis conditions to be employed to optimize the identification accuracies. However, both materials resulted in high ToF identification accuracy of the rNMPs.

There are, however, scale-dependent processes that can affect the performance of nanoscale electrophoresis, such as dielectrophoretic trapping generated by surface roughness. This surface roughness can create inhomogeneous electric fields within the channel when its dimensions are on the same order as the surface roughness and can result in intermittent motion of molecules that can increase peak dispersion [34, 38]. We found that high electric fields can largely mitigate this issue. Others scale-dependent effects include EDL overlap, concentration polarization, and increased surface interactions due to the high surface area-to-volume ratio associated with nanoscale electrophoresis. In our previous report on the identification of dNMPs using nanoscale electrophoresis using PMMA/COC devices [20], we found that partial EDL overlap can degrade

identification resolution. This artifact was overcome by using high carrier electrolyte ionic strengths to compress the EDL and the use of channels that are relatively large in cross section (110 x 110 nm, width and depth). Minimal EDL overlap also reduces issues associated with concentration polarization.

While organic modifiers can be used to improve electrophoretic performance if wall interactions are present (i.e., capillary electrochromatography, CEC), they are not practical for nanoscale electrophoresis using thermoplastic channels due to polymer swelling when placed in organic solvents that may block the nanochannel making the device fail. In addition, addition of organic modifiers would not be practical for our SMS approach as the presence of organic solvents may denature the surface-immobilized riboexonuclease.

In both COC/COC and PMMA/COC nanochannels, the average resolution was similar when the pH was 7.9 generating ToF identification accuracies >99%. The successful identification of rNMPs in free solution using thermoplastic nanochannels will enable development of our SMS approach for RNA. Our recent report on using surface immobilized XRN1 to plastic pillars serves as another foundational piece to deliver our SMS approach [21]. Our SMS approach will provide high read lengths (determined by the processivity of the exonuclease) and high call accuracies (determined by the apparent mobility differences in the rNMPs). The utility of RNA sequencing is becoming even more paramount in light of the COVID-19 pandemic because understanding the structure of the SARS-CoV-2 RNA genome will provide helpful guidance on generating and assigning proper vaccines to the population based on sequence variations the virus may/may not possess.

Although we utilized dye labeled rNMPs in this study to allow tracking the molecules during their transport through nanochannels, our envisioned SMS platform will not require labeling of the

rNMPs [64]. We will employ a label free approach for determining the ToF of the rNMPs. This is accomplished by fabricating a thermoplastic nanochannel device with two in-plane nanopores poised at each end of the nanochannel to measure the ToF [65]. The detection therefore uses resistive pulse sensing of single molecules.

Finally, we are employing NIL to make the nanofluidic chips, which is convenient due to the lack of need of specialized equipment to make each device, such as FIB or EBL. Currently, >10 imprinting runs can be carried out with a single resin stamp. Because the Si master can produce >100 resin stamps from a single Si mold master, we can make >1,000 chips from a single Si master. Currently we are working on producing the nanofluidic devices using nano-injection molding [66, 67], which uses a mold insert made from Ni via electroplating. The Ni mold insert can produce many more parts compared to resin stamps used in NIL and injection 11 C.A. Amarasekara, C. Rathnayaka, U.S. Athapattu et al. Journal of Chromatography A 1638 (2021) 461892 molding can produce parts at higher rate (~1000 chips per day per injection molding machine).

2.5 References

1. Abgrall, P.; Low, L.-N.; Nguyen, N.-T., Fabrication of planar nanofluidic channels in a thermoplastic by hot-embossing and thermal bonding. *Lab on a Chip* **2007,** *7* (4), 520-522.

2. Hoeijmakers, W. A.; Bártfai, R.; Stunnenberg, H. G., Transcriptome analysis using RNA-Seq. In *Malaria*, Springer: 2012; pp 221-239.

3. Whitley, S. K.; Horne, W. T.; Kolls, J. K., Research techniques made simple: methodology and clinical applications of RNA sequencing. *Journal of Investigative Dermatology* **2016,** *136* (8), e77-e82.

4. Grada, A.; Weinbrecht, K., Next-generation sequencing: methodology and application. *The Journal of investigative dermatology* **2013,** *133* (8), e11.

5. Ray, M.; Horne, W.; McAleer, J. P.; Ricks, D. M.; Kreindler, J. L.; Fitzsimons, M. S.; Chan, P. P.; Trevejo-Nunez, G.; Chen, K.; Fajt, M., RNA-seq in pulmonary medicine: how much is enough? *American journal of respiratory and critical care medicine* **2015,** *192* (3), 389-391.

6. Mortazavi, A.; Williams, B. A.; McCue, K.; Schaeffer, L.; Wold, B., Mapping and quantifying mammalian transcriptomes by RNA-Seq. *Nature methods* **2008,** *5* (7), 621.

7. Wang, Z.; Gerstein, M.; Snyder, M., RNA-Seq: a revolutionary tool for transcriptomics. *Nat Rev Genet* **2009,** *10* (1), 57-63.

8. Sudhagar, A.; Kumar, G.; El-Matbouli, M., Transcriptome analysis based on RNA-seq in understanding pathogenic mechanisms of diseases and the immune system of fish: a comprehensive review. *International journal of molecular sciences* **2018,** *19* (1), 245.

9. Ari, Ş.; Arikan, M., Next-generation sequencing: advantages, disadvantages, and future. In *Plant omics: Trends and applications*, Springer: 2016; pp 109-135.

10. Branton, D.; Deamer, D. W.; Marziali, A.; Bayley, H.; Benner, S. A.; Butler, T.; Di Ventra, M.; Garaj, S.; Hibbs, A.; Huang, X., The potential and challenges of nanopore sequencing. In *Nanoscience And Technology: A Collection of Reviews from Nature Journals*, World Scientific: 2010; pp 261-268.

11. Ayub, M.; Hardwick, S. W.; Luisi, B. F.; Bayley, H., Nanopore-based identification of individual nucleotides for direct RNA sequencing. *Nano letters* **2013,** *13* (12), 6144-6150.

12. Astier, Y.; Braha, O.; Bayley, H., Toward single molecule DNA sequencing: direct identification of ribonucleoside and deoxyribonucleoside 5 '-monophosphates by using an

engineered protein nanopore equipped with a molecular adapter. *Journal of the American Chemical Society* **2006,** *128* (5), 1705-1710.

13. Clarke, J.; Wu, H.-C.; Jayasinghe, L.; Patel, A.; Reid, S.; Bayley, H., Continuous base identification for single-molecule nanopore DNA sequencing. *Nature nanotechnology* **2009,** *4* (4), 265.

14. Cockroft, S. L.; Chu, J.; Amorin, M.; Ghadiri, M. R., A single-molecule nanopore device detects DNA polymerase activity with single-nucleotide resolution. *Journal of the American Chemical Society* **2008,** *130* (3), 818-820.

15. Lieberman, K. R.; Cherf, G. M.; Doody, M. J.; Olasagasti, F.; Kolodji, Y.; Akeson, M., Processive replication of single DNA molecules in a nanopore catalyzed by phi29 DNA polymerase. *Journal of the American Chemical Society* **2010,** *132* (50), 17961-17972.

16. Bayley, H., Sequencing single molecules of DNA. *Current opinion in chemical biology* **2006,** *10* (6), 628-637.

17. Reiner, J. E.; Balijepalli, A.; Robertson, J. W.; Drown, B. S.; Burden, D. L.; Kasianowicz, J. J., The effects of diffusion on an exonuclease/nanopore-based DNA sequencing engine. *The Journal of chemical physics* **2012,** *137* (21), 214903.

18. Novak, B. R.; Moldovan, D.; Nikitopoulos, D. E.; Soper, S. A., Distinguishing Single DNA Nucleotides Based on Their Times of Flight Through Nanoslits: A Molecular Dynamics Simulation Study. *Journal of Physical Chemistry B* **2013,** *117* (12), 3271-3279.

19. Xia, K.; Novak, B. R.; Weerakoon-Ratnayake, K. M.; Soper, S. A.; Nikitopoulos, D. E.; Moldovan, D., Electrophoretic Transport of Single DNA Nucleotides through Nanoslits: A Molecular Dynamics Simulation Study. *Journal of Physical Chemistry B* **2015,** *119*, 11443-11448.

20. O'Neil, C.; Amarasekara, C. A.; Weerakoon-Ratnayake, K. M.; Gross, B.; Jia, Z.; Singh, V.; Park, S.; Soper, S. A., Electrokinetic transport properties of deoxynucleotide monophosphates (dNMPs) through thermoplastic nanochannels. *Analytica chimica acta* **2018,** *1027*, 67-75.

21. Athapattu, U. S.; Amarasekara, C. A.; Nagel, A. C.; Immel, J. R.; Bloom, S.; Barany, F.; Soper, S. A., Solid-Phase XRN1 Reactions for RNA Cleavage: Application in Single-Molecule Sequencing. *Nucleic Acids Research* **2020,** *(under review).*

22. Uhrová, M.; Deyl, Z.; Suchánek, M., Separation of common nucleotides, mono-, di- and triphosphates, by capillary electrophoresis. *Journal of Chromatography B: Biomedical Sciences and Applications* **1996,** *681* (1), 99-105.

23. Mateos-Vivas, M.; Rodríguez-Gonzalo, E.; Domínguez-Álvarez, J.; García-Gómez, D.; Ramírez-Bernabé, R.; Carabias-Martínez, R., Analysis of free nucleotide monophosphates in human milk and effect of pasteurisation or high-pressure processing on their contents by capillary electrophoresis coupled to mass spectrometry. *Food chemistry* **2015,** *174*, 348-355.

24. Geldart, S. E.; Brown, P. R., Analysis of nucleotides by capillary electrophoresis. *Journal of Chromatography A* **1998,** *828* (1-2), 317-336.

25. Liu, H.; Qi, S.; Zhang, Y.; Huang, A.; Sun, Y., Determination of inosine 5′-monophosphate and guanosine 5′-monophosphate in pig feed by capillary zone electrophoresis. *Journal of High Resolution Chromatography* **1997,** *20* (4), 242-244.

26. Geldart, S. E.; Brown, P. R., Separation of purine and pyrimidine bases by capillary zone electrophoresis with carbonate buffers. *Journal of Chromatography A* **1999,** *831* (1), 123-129.

27. Pennathur, S.; Santiago, J. G., Electrokinetic Transport in Nanochannels. 1. Theory. *Analytical Chemistry* **2005,** *77* (21), 6772-6781.

28. Pennathur, S.; Santiago, J. G., Electrokinetic Transport in Nanochannels. 2. Experiments. *Analytical Chemistry* **2005,** *77* (21), 6782-6789.

29. Xuan, X.; Li, D., Electrokinetic transport of charged solutes in micro-and nanochannels: The influence of transverse electromigration. *Electrophoresis* **2006,** *27* (24), 5020-5031.

30. Garcia, A. L.; Ista, L. K.; Petsev, D. N.; O'Brien, M. J.; Bisong, P.; Mammoli, A. A.; Brueck, S. R.; López, G. P., Electrokinetic molecular separation in nanoscale fluidic channels. *Lab on a Chip* **2005,** *5* (11), 1271-1276.

31. Baldessari, F.; Santiago, J. G., Electrophoresis in nanochannels: brief review and speculation. *Journal of Nanobiotechnology* **2006,** *4* (1), 12.

32. Wang, L.; Shao, P.; van Kan, J.; Ansari, K.; Bettiol, A.; Pan, X.; Wohland, T.; Watt, F., Fabrication of nanofluidic devices utilizing proton beam writing and thermal bonding techniques. *Nuclear Instruments and Methods in Physics Research Section B: Beam Interactions with Materials and Atoms* **2007,** *260* (1), 450-454.

33. Duan, C.; Wang, W.; Xie, Q., Fabrication of nanofluidic devices. *Biomicrofluidics* **2013,** *7* (2), 026501.

34. Chantiwas, R.; Hupert, M. L.; Pullagurla, S. R.; Balamurugan, S.; Tamarit-López, J.; Park, S.; Datta, P.; Goettert, J.; Cho, Y.-K.; Soper, S. A., Simple replication methods for producing nanoslits in thermoplastics and the transport dynamics of double-stranded DNA through these slits. *Lab on a Chip* **2010,** *10* (23), 3255-3264.

35. Chantiwas, R.; Park, S.; Soper, S. A.; Kim, B. C.; Takayama, S.; Sunkara, V.; Hwang, H.; Cho, Y.-K., Flexible fabrication and applications of polymer nanochannels and nanoslits. *Chemical Society Reviews* **2011,** *40* (7), 3677-3702.

36. Chai, J.; Lu, F.; Li, B.; Kwok, D. Y., Wettability interpretation of oxygen plasma modified poly (methyl methacrylate). *Langmuir* **2004,** *20* (25), 10919-10927.

37. Oneil, C. E.; Jackson, J. M.; Shim, S.-H.; Soper, S. A., Interrogating Surface Functional Group Heterogeneity of Activated Thermoplastics Using Super-Resolution Fluorescence Microscopy. *Analytical Chemistry* **2016,** *88* (7), 3686-3696.

38. Uba, F. I.; Pullagurla, S. R.; Sirasunthorn, N.; Wu, J.; Park, S.; Chantiwas, R.; Cho, Y.-K.; Shin, H.; Soper, S. A., Surface charge, electroosmotic flow and DNA extension in chemically modified thermoplastic nanoslits and nanochannels. *Analyst* **2015,** *140* (1), 113-126.

39. Weerakoon-Ratnayake, K. M.; Uba, F. I.; Oliver-Calixte, N. J.; Soper, S. A., Electrophoretic separation of single particles using nanoscale thermoplastic columns. *Analytical chemistry* **2016,** *88* (7), 3569-3577.

40. Amarasekara, C. A.; Athapattu, U. S.; Rathnayaka, C.; Choi, J.; Park, S.; Soper, S. A., Open-tubular Nanoelectrochromatography (OT-NEC): Gel-free Separation of Single Stranded DNAs (ssDNAs) in Thermoplastic Nanochannels. *Electrophoresis* **2020,** *41* (18-19).

41. Hu, W.; Soper, S. A.; Jackson, J. M., Time-Delayed Integration–Spectral Flow Cytometer (TDI-SFC) for Low-Abundance-Cell Immunophenotyping. *Analytical chemistry* **2019,** *91* (7), 4656-4664.

42. Ford, S. M.; Kar, B.; McWhorter, S.; Davies, J.; Soper, S. A.; Klopf, M.; Calderon, G.; Saile, V., Microcapillary electrophoresis devices fabricated using polymeric substrates and X-ray lithography. *J. Microcolumn Sep.* **1998,** *10* (5), 413-422.

43. Sinville, R.; Soper, S. A., High resolution DNA separations using microchip electrophoresis. *Journal of Separation Science* **2007,** *30* (11), 1714-1728.

44. Obubuafo, A.; Balamurugan, S.; Shadpour, H.; Spivak, D.; McCarley, R. L.; Soper, S. A., Poly(methyl methacrylate) microchip affinity capillary gel electrophoresis of aptamer-protein complexes for the analysis of thrombin in plasma. *Electrophoresis* **2008,** *29* (16), 3436-3445.

45. Njoroge, S. K.; Witek, M. A.; Hupert, M. L.; Soper, S. A., Microchip electrophoresis of Alu elements for gender determination and inference of human ethnic origin. *Electrophoresis* **2010,** *31* (6), 981-990.

46. Albrecht, J. C.; Kotani, A.; Lin, J. S.; Soper, S. A.; Barron, A. E., Simultaneous detection of 19 K-ras mutations by free-solution conjugate electrophoresis of ligase detection reaction products on glass microchips. *Electrophoresis* **2013,** *34* (4), 590-597.

47. Cabrini, S.; Kawata, S., *Nanofabrication handbook*. CRC Press: 2012.

48. Gao, H.; Tan, H.; Zhang, W.; Morton, K.; Chou, S. Y., Air cushion press for excellent uniformity, high yield, and fast nanoimprint across a 100 mm field. *Nano Letters* **2006,** *6* (11), 2438-2441.

49. Uba, F. I.; Hu, B.; Weerakoon-Ratnayake, K.; Oliver-Calixte, N.; Soper, S. A., High process yield rates of thermoplastic nanofluidic devices using a hybrid thermal assembly technique. *Lab on a Chip* **2015,** *15* (4), 1038-1049.

50. Ramm, P.; Lu, J. J.-Q.; Taklo, M. M., *Handbook of wafer bonding*. John Wiley & Sons: 2011.

51. Tsao, C.; Hromada, L.; Liu, J.; Kumar, P.; DeVoe, D., Low temperature bonding of PMMA and COC microfluidic substrates using UV/ozone surface treatment. *Lab on a Chip* **2007,** *7* (4), 499-505.

52. Huang, X.; Gordon, M. J.; Zare, R. N., Current-monitoring method for measuring the electroosmotic flow rate in capillary zone electrophoresis. *Analytical Chemistry* **1988,** *60* (17), 1837-1838.

53. Cho, Y.; Park, J.; Park, H.; Cheng, X.; Kim, B.; Han, A., Fabrication of high-aspect-ratio polymer nanochannels using a novel Si nanoimprint mold and solvent-assisted sealing. *Microfluidics and Nanofluidics* **2010,** *9* (2-3), 163-170.

54. Ali, U.; Karim, K. J. B. A.; Buang, N. A., A review of the properties and applications of poly (methyl methacrylate)(PMMA). *Polymer Reviews* **2015,** *55* (4), 678-705.

55. Nunes, P. S.; Ohlsson, P. D.; Ordeig, O.; Kutter, J. P., Cyclic olefin polymers: emerging materials for lab-on-a-chip applications. *Microfluidics and nanofluidics* **2010,** *9* (2-3), 145-161.

56. Jackson, J. M.; WItek, M. A.; Hupert, M. L.; Brady, C.; Pullagurla, S. R.; Kamande, J. W.; Aufforth, R. D.; Tignanelli, C. J.; Torphy, R. J.; Yeh, J. J.; Soper, S. A., UV Activation of Polymeric High Aspect Ratio Microstructures: Ramifications in Antibody Surface Loading for Circulating Tumor Cell Selection. *Lab on a Chip* **2014,** *14*, 106-117.

57. Kino, K.; Hirao-Suzuki, M.; Morikawa, M.; Sakaga, A.; Miyazawa, H., Generation, repair and replication of guanine oxidation products. *Genes and Environment* **2017,** *39* (1), 21.

58. Bidleman, T. F., The relationship between resolution and percent band overlap. *Journal of Chemical Education* **1979,** *56* (5), 293.

59. O'Neil, C. E.; Taylor, S.; Ratnayake, K.; Pullagurla, S.; Singh, V.; Soper, S. A., Characterization of activated cyclic olefin copolymer: effects of ethylene/norbornene content on the physiochemical properties. *Analyst* **2016,** *141*, 6521-6532.

60. Rani, S. D.; You, B. H.; Soper, S. A.; Murphy, M. C.; Nikitopoulos, D. E., Influence of material transition and interfacial area changes on flow and concentration in electro-osmotic flows. *Anal Chim Acta* **2013,** *770*, 103-110.

61. Po, H. N.; Senozan, N., The Henderson-Hasselbalch equation: its history and limitations. *Journal of Chemical Education* **2001,** *78* (11), 1499.

62. Saletore, Y.; Meyer, K.; Korlach, J.; Vilfan, I. D.; Jaffrey, S.; Mason, C. E., The birth of the Epitranscriptome: deciphering the function of RNA modifications. *Genome biology* **2012,** *13* (10), 175.

63. Frye, M.; Harada, B. T.; Behm, M.; He, C., RNA modifications modulate gene expression during development. *Science* **2018,** *361* (6409), 1346-1349.

64. Davis, L. M.; Fairfield, F. R.; Harger, C. A.; Jett, J. H.; Keller, R. A.; Hahn, J. H.; Krakowski, L. A.; Marrone, B. L.; Martin, J. C.; Nutter, H. L.; Ratliff, R. L.; Shera, E. B.; Simpson, D. J.; Soper, S. A., Rapid DNA sequencing based upon single molecule detection. *Genetic Analysis: Biomolecular Engineering* **1991,** *8* (1), 1-7.

65. Jia, Z.; Choi, J.; Park, S., Surface Charge Density-Dependent DNA Capture through Polymer Planar Nanopores. *ACS applied materials & interfaces* **2018,** *10* (47), 40927-40937.

66. Teillet, J.; Martinez, Q.; Tijunelyte, I.; Chami, B.; Bancaud, A., Characterization and minimization of band broadening in DNA electrohydrodynamic migration for enhanced size separation. *Soft Matter* **2020**.

67. Zhang, N.; Byrne, C. J.; Browne, D. J.; Gilchrist, M. D., Towards nano-injection molding. *Materials today* **2012,** *15* (5), 216-221.

Chapter 3. Tailoring Thermoplastic In-Plane Nanopore Size by Thermal Fusion Bonding for the Analysis of Single Molecules

This chapter is based on the following manuscript,

"Tailoring thermoplastic in-plane nanopore size by thermal fusion bonding for single-molecule sensing".

Reprinted with permission from – {Athapattu, U. S.*; **Rathnayaka, C.***; Vaidyanathan, S.*; Gamage, S. S. T.*; Choi, J.; Riahipour, R.; Manoharan, A.; Hall, A. R.; Park, S.; Soper, S. A., Tailoring Thermoplastic In-Plane Nanopore Size by Thermal Fusion Bonding for the Analysis of Single Molecules. ACS Sensors **2021**, 6 (8), 3133-3143.}

* These authors contributed equally to this work.

3.1 Introduction

Pores with nanometer dimensions are typically fabricated in a thin membrane separating two fluid chambers.[1] When an electrical bias is applied across the membrane, the resulting electric field can transport charged molecules through the pore producing signals in the trans-membrane ionic current that can be used to sense single molecules via resistive pulse sensing (RPS). Among single-molecule sensors, nanopores have garnered significant interest because they allow the detection of single molecules without requiring fluorescence labeling of the target and the need for sophisticated optical equipment for transduction.[2-5] These and other attractive properties have led to the development of many nanopore-based applications including detection of DNA-protein interactions,[6-9] measurement of molecular forces,[10-11] and nucleic acid sequencing.[12-13] Although biological pores, such as α-hemolysin[14] and MspA,[15] have proven to be useful sensors, several disadvantages remain primarily due to their fixed size and limited stability under extreme conditions of salt, pH, temperature, and mechanical stress. As an alternative, solid-state nanopores[3, 16] have captured attention to address challenges associated with biological pores. Moreover, solid-state nanopores can be integrated with other micro- and nanofluidic components to form lab-on-a-chip systems.

Most solid-state nanopores have been fabricated on inorganic thin-film membranes.[3, 17-19] Several approaches have been demonstrated to produce small nanopores in these substrates through charged particle beams[17-18, 20-21] or electrical breakdown[22] and to control the size of the pores *ex post facto* via exposure with a defocused beam of electrons,[17] ions,[23] direct thermal heating,[24] or focused ion beam (FIB) deposition of materials such as gold.[25] Even though these methods have proven successful in the fabrication of small-diameter pores, they are generally not

conducive to production at a scale and cost that will ultimately enable them to be translated for clinical applications that require disposable devices as is necessary for *in vitro* diagnostics.

Solid-state nanopores have also been fabricated in planar substrates ("in-plane" nanopores) embedded within a fluidic network rather than suspended on a thin membrane.[26] FIB has been used to fabricate monolithic channels with micro- and nanoscale components including in-plane nanopores.[26-28] In-plane pores can also be produced in series so that other measurement modalities can be realized. For example, Kondylis *et al*. used glass nanopore devices with 2, 4, and 8 pores (width: 60 nm, depth: 70 nm) in series for real-time, resistive pulse analysis of virus capsids. They showed that the standard deviation of the pulse amplitude distributions of individual molecules decreased with increasing number of pores in series leading to increased measurement precision[29] while the electrophoretic mobility of virus particles were determined.[30-32]

Thermoplastics provide the means for both medium and high-scale manufacturing at low production costs even at the nanoscale due to a plethora of fabrication technologies, such as nanoimprint lithography (NIL) and injection molding, respectively.[33-34] Additionally, due to the diverse physiochemical properties of different thermoplastics, the appropriate material can be selected according to measurement requirements.[35-36] However, it has been difficult to achieve sub-20 nm structures using thermoplastics due to challenges associated with bonding a cover plate to the nanofluidic network, which can result in deformation of the patterned nanostructures. The cover plate bonding process in thermoplastic devices can use thermal fusion bonding (TFB), which bonds a thin cover plate to the nano-patterned substrate under a controlled pressure at temperatures near the glass transition temperature, T_g, of the substrate and/or cover plate. The TFB process involves motion of polymer chains between the cover plate and the substrate, which inevitably alters the dimensions of the nanostructures in the enclosed nanofluidic devices from those in the

imprinted substrate. We have shown that high process yield rates of thermoplastic nanofluidic devices with minimal deformation of nanostructures can be realized using a hybrid bonding process in which a lower T_g cover plate is thermally fusion bonded to a higher T_g substrate.[37]

The ability to control the size of in-plane nanopores imprinted from the same mold will allow for reduction in the development and production costs by obviating the need for FIB-milled Si masters to accommodate a particular application, for example reducing in-plane nanopore size to sense molecules of various sizes. Several reports have demonstrated reduction of nanostructure dimensions applying pressure to the patterned polymer substrate at elevated temperatures.[38] For example, Choi *et al.* reduced the size of micropores in a perforated SU-8 membrane produced by NIL from 3000 nm to 300 nm.[39] The same group utilized polymer reflow to reduce nanopore size from 12 nm to 6 nm.[34] In another report, Chou *et al.* described the use of a method called pressed self-perfection by liquefaction (P-SPEL), where the transiently molten thermoplastic nanostructures were pressed using a blank Si plate to achieve sub-20 nm structures.[38] However, these methods have not been demonstrated to reduce in-plane nanopore size for nanofluidic devices to sense differently sized molecules.

The transport properties of biomolecules through nanopores depend on interactions of analytes with the nanopore's surface.[36, 40] Several reports have discussed the functionalization of pore surfaces to facilitate transport or other properties. For example, Martin *et al.* reported a method to alter the surface properties of track-etched nanopores in polycarbonate with gold by electroless deposition[41] followed by chemisorption of thiols.[42-43] For polyimide (PI) and polyethylene terephthalate (PET), the surface carboxyl groups created during track-etching were chemically functionalized with an alkyl bromide and KF catalyst,[44-46] methylation,[47] or amidation.[48-49] Previously, our group reported surface modification of PMMA nanochannels to

generate both negatively charged and positively charged surfaces.[50] A negatively charged surface was generated via O_2 plasma treatment, which forms carboxyl groups on the thermoplastic surface. These surface-confined carboxyl groups were subsequently converted into positively charged surfaces by covalently attaching ethylenediamine.

In this study, we demonstrate a post fabrication method to tailor the dimensions of in-plane nanopores in enclosed nanofluidic devices using TFB, a process step needed to produce enclosed nanofluidic devices. The thermoplastic dual in-plane nanopore devices were fabricated in either a PMMA (poly(methyl methacrylate)) or COP (cyclic olefin polymer) substrate and the O_2 plasma activated imprinted substrates and cover plates (made from COC; cyclic olefin copolymer), which was used to increase the wettability of the surfaces by formation of surface carboxylate groups, were subjected to different bonding pressures to vary the size of the in-plane nanopores. The change in depth and width of the nanopores with bonding pressure was measured by AFM and SEM, respectively. COMSOL simulations and experimental conductance measurements further demonstrated the pore closing behavior of the nanopores with higher bonding pressures. The devices bonded at different pressures were used to analyze λ-DNA and showed improved signal-to-noise ratio (SNR) with lower nanopore size. Furthermore, the use of nanopore devices with different pore sizes fabricated by changing the bonding pressure during TFB was used to analyze different types of molecules, such as single-stranded (ss) RNA and ribonucleotide monophosphates (rAMP) molecules.

Moreover, to reduce co-ion exclusion effects leading to sub-optimal event frequency, a simple surface modification step was carried out using ethanolamine on assembled devices. The high carboxyl group density generated during O_2 plasma treatment prior to TFB created a high surface charge, which led to exclusion of co-ions passing through small nanopores. To alter the

surface charge, EDC/NHS chemistry with ethanolamine was used.[50] Dual in-plane nanopore devices modified with ethanolamine showed a significant increase in translocation event frequency.

3.2 Materials and Methods

3.2.1 Materials and reagents

Chemicals and other materials were obtained from the following sources and used without further purification: S1813 photoresist (MicroChemicals, Germany); MF319 developer (MicroChemicals); potassium hydroxide (KOH) pellets (Fisher Scientific, Waltham, MA); isopropyl alcohol (IPA; Sigma-Aldrich, St. Louis, MO); hydrofluoric acid (HF, Sigma-Aldrich); Tri(propylene glycol) diacrylate (TPGDA, Sigma-Aldrich); Trimethylolpropane triacrylate (TMPTA, Sigma-Aldrich); 2,2-Dimethoxy-2-phenylacetophenone (photoinitiator, Sigma-Aldrich); NOA72 (Norland Products, Neuchâtel, Switzerland); Si wafers (P/B, resistivity 5-10 Ωcm, orientation of (100), and 525 ± 25 μm thickness, WaferPro, Santa Clara, CA); polyethylene terephthalate (PET) with 250 μm thickness (Goodfellow, Coraopolis, PA). Silicon (Si) 〈100〉 wafers were purchased from University Wafers (Boston, MA). PMMA was received from ePlastics (San Diego, CA). COC (Type 8007) was purchased from TOPAS Advanced Polymers (Florence, KY). COP sheets were obtained from STRATEC SE (Birkenfeld, Germany). UV curable polyurethane resin was purchased from Chansang Co. Guanosine 5'-monophosphate disodium salt was obtained from Sigma-Aldrich. Molecular biology grade water was secured from Thermo Fisher (Waltham, MA). SYTO82 dye was from Life Technologies (Eugene, OR, USA).

3.2.2 Device fabrication and assembly.

Thermoplastic nanofluidic devices were fabricated and assembled as we have previously reported.[33, 51] Si wafers with a 100 nm thick silicon nitride (Si_3N_4) layer on each side were used for fabricating a Si master mold. Microchannels were fabricated using a combination of photolithography and wet-chemical etching. To accomplish this, a 1.3 µm thick S1813 photoresist layer was first spin-coated at 4,000 rpm for 60 s on a Si wafer and then baked at 115°C for 60 s. Photolithography was performed using a designed photomask in a UV exposure station (Quintel) in a class 100 cleanroom. UV exposure was conducted at 130-140 mJ/cm^2 with post-exposure baking at 95°C for 60 s. Then, the wafer was developed with a MF319 developer for 90 s, followed by washing with deionized water. The exposed Si_3N_4 layer was etched to open a window using an ICP-DRIE system (Plasmalab System 100, Oxford Instruments, Abingdon, UK). Subsequently, the wafer was transferred to a 40 wt% KOH solution with IPA (5 % v/v) at 70°C. The KOH solution was prepared by dissolving KOH pellets in deionized water. After 25 min etching to form 10 µm deep microchannels, the wafer was removed from the etchant, rinsed in water, and dried with N_2 gas. Prior to FIB milling, the Si_3N_4 layer was completely removed using a dilute HF solution. The nanochannel flight tube combined with in-plane nanopores was fabricated using FIB milling (Quanta 3D Dual Beam system, FEI, Hillsboro, OR). The milling was performed at a beam voltage and current of 30 kV and 10 pA, respectively, in a bitmap mode.

The Si master mold was used to produce a resin stamp by using a UV resin solution (70 wt% TPGDA, 28 wt% TMPTA, and 2 wt% photoinitiator). Drops of the UV-resin were dispensed against the Si master mold. A flexible PET sheet coated with an adhesive layer (NOA72) was then slightly pressed against the liquid drop and used as a backbone for the resin stamp. Residual resin solution and air bubbles were gently squeezed out. During the curing process, the sample was

exposed to flash-type UV light (250-400 nm) for 20 s at an intensity of ~1.8 W/cm^2 by using a nanoimprinter (Eitre6, Obducat, Lund, Sweden). After UV-curing, the molded UV-resin/PET backbone was demolded from the Si master.

Nanopore devices were imprinted into a plastic substrate using nanoimprint lithography, NIL (Nanonex 2500, Monmouth Junction, NJ).[52] The optimized imprinting conditions were 145°C, 300 psi, and 5 min for PMMA nanofluidic devices, and 130°C, 300 psi, and 5 min for COP devices. Imprinted nanofluidic devices were then characterized using scanning electron microscope (SEM), and atomic force microscopy (AFM).

The imprinted nanopore devices were then sealed using a COC 8007 cover plate. Thermal fusion bonding with NIL was used for sealing nanopore devices. Bonding of PMMA/COC devices was done following the method described by Uba *et al*.[37] following 1 min O_2 plasma treatment for both the substrate and cover plate at 50 W.

3.2.3 Atomic force microscopy.

To determine the depth of the nanopores with increasing pressure, AFM (SPM HT-9700, Shimadzu Corporation, Kyoto, Japan) analysis was carried out. The probe used for imaging was a Super Sharp Silicon tip (Nanosensors, Switzerland) with a tip radius <2 nm, half cone angle of 10^o, aspect ratio 4:1 at 200 nm from the tip apex, and frequency of 300 kHz. A dynamic scanning mode was used for imaging with a scanning frequency of 0.5 Hz. The acquired images were analyzed using SPM Manager v4.76.1 software.

3.2.4 Scanning electron microscopy.

SEMs of the nanopore devices were acquired using a FEI VERSA 3D Dualbeam field emission/low vacuum SEM. A 2 nm thin conductive Iridium layer was sputter coated onto the devices using an EMS 150ES sputter coater before SEM imaging. All images were acquired using 5.0 kV accelerating voltage and 8.7 mm working distance. The SEM images of the Si mold masters were collected using a Quanta 3D DualBeam FEI FIB-SEM and were analyzed using the instrument's software and Image J.

3.2.5 COMSOL.

Simulations were performed in COMSOL v5.5 for the dual nanopores devices. The length of both nanopores was kept at 30 nm, but the size (width and depth) was varied to calculate the corresponding conductance. The electrolyte used was 1 M KCl with a DC applied voltage of -1 V at 293 K with the electrostatics module used to calculate the electric potential, current density, and conductance across the pores.

3.2.6 Conductance measurements.

Experimental conductance measurements were performed using the dual in-plane nanopore devices made in PMMA and COP bonded at different pressures using 1 M KCl as the electrolyte. Assembled devices were filled with 50% v/v methanol/water for 15 min. The 50% methanol solution was then replaced with 1 M KCl and allowed to equilibrate for 15 min. The device was placed in a Faraday cage and Ag/AgCl electrodes were placed in the reservoirs filled with buffer. The current was measured from -1 to 1 V in 0.2 V steps. Current data were acquired using an Axopatch Digidata 1440B instrument and analyzed using Clampfit 11.1. The current

measurements corresponding to the applied voltages were measured for different devices (n ≥3) at each bonding pressure and the conductance was calculated.

3.2.7 λ-DNA, RNA, and rNMP translocation.

Translocation experiments were performed for λ-DNA in PMMA dual in-plane nanopore devices bonded at 110,170 and 200 psi. Briefly, after methanol/water priming, 1× TBE buffer was introduced into the device. Finally, 100 nM of λ-DNA in 1 M KCl seeded into 1× TBE was injected into the device. The devices were placed in a Faraday cage and Ag/AgCl electrodes were immersed in the reservoirs of the device. A potential of -1 V was applied between two electrodes and the data was acquired using the Axopatch Digidata 1440B and analyzed using Clampfit 11.1. The Wilcoxon p-test was used to calculate the statistical difference of peak amplitudes used for each TFB pressure.

For RNA and rAMP translocation nanopore devices were primed as described above and 100 nM of ssRNA (60 nt) in 1× NEBuffer 3 (10 mM NaCl; 5 mM Tris-HCl; 1 mM $MgCl_2$; 0.1 mM DTT; pH 7.9 at 25^0C) was introduced into one of the reservoirs of the device. For rAMP in-plane nanopore measurements, the same carrier buffer was used and, in some cases, different concentrations of rAMP were employed. For RNA/rAMP translocation experiments, the applied potential was increased by serially connecting a 1.5 V battery to the Axopatch circuit, which increased the applied potential to 2.5 V compared to the 1 V maximum obtainable using the Axopatch instrument. Potentials were applied using Ag/AgCl electrodes and all data were collected at a sampling frequency of 250 kHz, a head stage configuration of β = 0.1, gain = 1, and a low pass filter of 10 kHz. The nanofluidic devices were kept inside the Faraday cage while

recording current transient data. Data were collected for a period of 10 min and Clampfit 11.1 software was used for data acquisition and analysis.

3.2.8 Surface modification with ethanolamine.

After fabrication and assembly of the dual in-plane nanopore devices, to suppress the surface charge and EOF of O_2 plasma activated surfaces the devices were modified with ethanolamine (see Figure 3.1). Ethanolamine was covalently attached to the surface confined carboxylic acid groups using EDC/NHS coupling chemistry, which covalently attaches primary amine containing molecules to carboxylated surfaces via the formation of an amide bond.[53-54] PMMA substrates and COC cover plates were exposed to O_2 plasma at 50 W for 1 min, which generated surface carboxylic acid groups to improve the wettability of the surface. Then, a buffered solution (0.1 M MES, pH 4.7) containing 100 mg EDC, 10 mg NHS, and 16 µL ethanolamine was filled into the

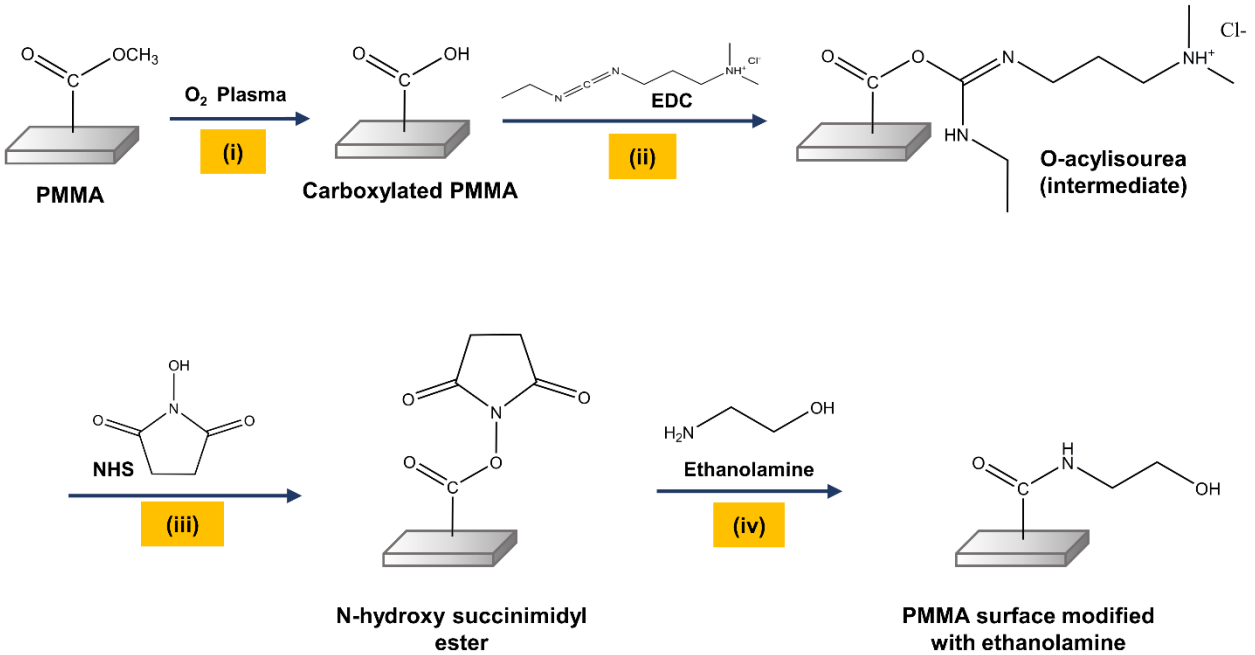

Figure 3.1 Protocol for the surface modification of PMMA (or COC) devices by: **(i)** Generation of surface confined carboxyl groups using O_2 plasma activation; **(ii)** O-acylisourea intermediate by reaction with EDC; **(iii)** N-hydroxy succinimidyl ester generation with NHS; and **(iv)** surface hydroxyl groups by treatment with ethanolamine.

plasma treated device and kept for 30 min at room temperature. After reaction, the device was washed with ultrapure water.

3.2.9 Sessile drop water contact angle measurements.

The hydrophilicity/hydrophobicity of native, O_2 plasma modified, ethanolamine treated without EDC/NHS and ethanolamine modified PMMA surface was determined by water contact-angle measurements using a VCA Optima instrument (AST Products). PMMA sheets (1.5 mm thick) were cut into 1.5 cm 1.5 cm sections and 2.0 µL of a nanopure water × drop (pH 7.5) was dispensed onto the surface followed by capturing images and analyzing the sessile contact angle using the software provided by the manufacturer. The measurements reported were the mean the standard deviation of five drops at separate positions of the PMMA ± substrate.

3.2.10 Attenuated total reflectance Fourier transform infrared spectroscopy (ATR-FTIR).

ATR-FTIR measurements were performed on UV/O_3 activated and ethanolamine modified PMMA plates. Plasma activation was not performed for PMMA substrates because the O_2 plasma treatment only modify the first few monolayers which would not give rise a sufficient signal for viable observations. ATR-FTIR spectra were acquired from 400-4000 cm^{-1} using an ALPHA FTIR spectrometer and a Platinum ATR module (Bruker Optics). Six replicates were performed, and spectra were analyzed using Essential FTIR analysis software.

3.2.11 EOF measurements.

The EOF of ethanolamine modified nanofluidic device was assessed using the current monitoring method. A PMMA-COC device possessing a single nanochannel (107 µm long, 110 nm deep, and

110 nm wide) connecting two opposite access microchannels was fabricated as described in Amarasekara *et al.*[55] The entire chip was modified with ethanolamine as described earlier and flushed with nuclease free water. After that, the device was filled with 0.1 M KCl solution and allowed to equilibrate for 5 min under a 500 mV DC bias. Next, one reservoir was replaced with 0.05 M KCl solution. Ag/AgCl electrodes were placed into the reservoirs across the channels under a 500 mV DC bias. pClamp10 software and Digidata 1440B low noise digitizer set at 10 kHz sampling frequency were used for data acquisition.

3.2.12 Surface charge measurements.

Surface charge of ethanolamine modified PMMA-COC nanochannel device (107 µm long, 110 nm deep, and 110 nm wide) was measured by following the method described in Uba *et al.*[56] Direct current conductance plots were utilized to assess the surface charge of ethanolamine modified nanochannel device. The surface of nanochannel device was modified with ethanolamine as described earlier and washed with ultrapure water prior to use. Nanochannels were filled with aid of capillary pulling from the inlet reservoir and vacuum suction from the outlet reservoir to confirm complete filling and avoiding air-bubble trapping inside the nanochannel. The pre-rinsed devices were filled with the KCl solutions and Ag/AgCl electrodes were placed into the access reservoirs and allowed to equilibrate 4 min under a bias voltage. The conductance values were estimated by fitting the slope of the ionic current as a function of applied voltage, which was stepped from 1000 mV to -1000 mV with 100 mV step size and 10 s holding time for each data point. All measurements were acquired with a low noise Axopatch 200B amplifier with a pClamp10 software and Digidata 1440B set at 10 kHz sampling frequency. The measurements were performed five times with repeated unloading and loading.

3.2.13 Statistical analysis.

All reported data sets were compared by either two-sided t-test or Wilcoxon signed rank test using R Studio v1.0.153 and R v3.5.1 software.

3.3 Results and Discussion

3.3.1 Device fabrication and assembly

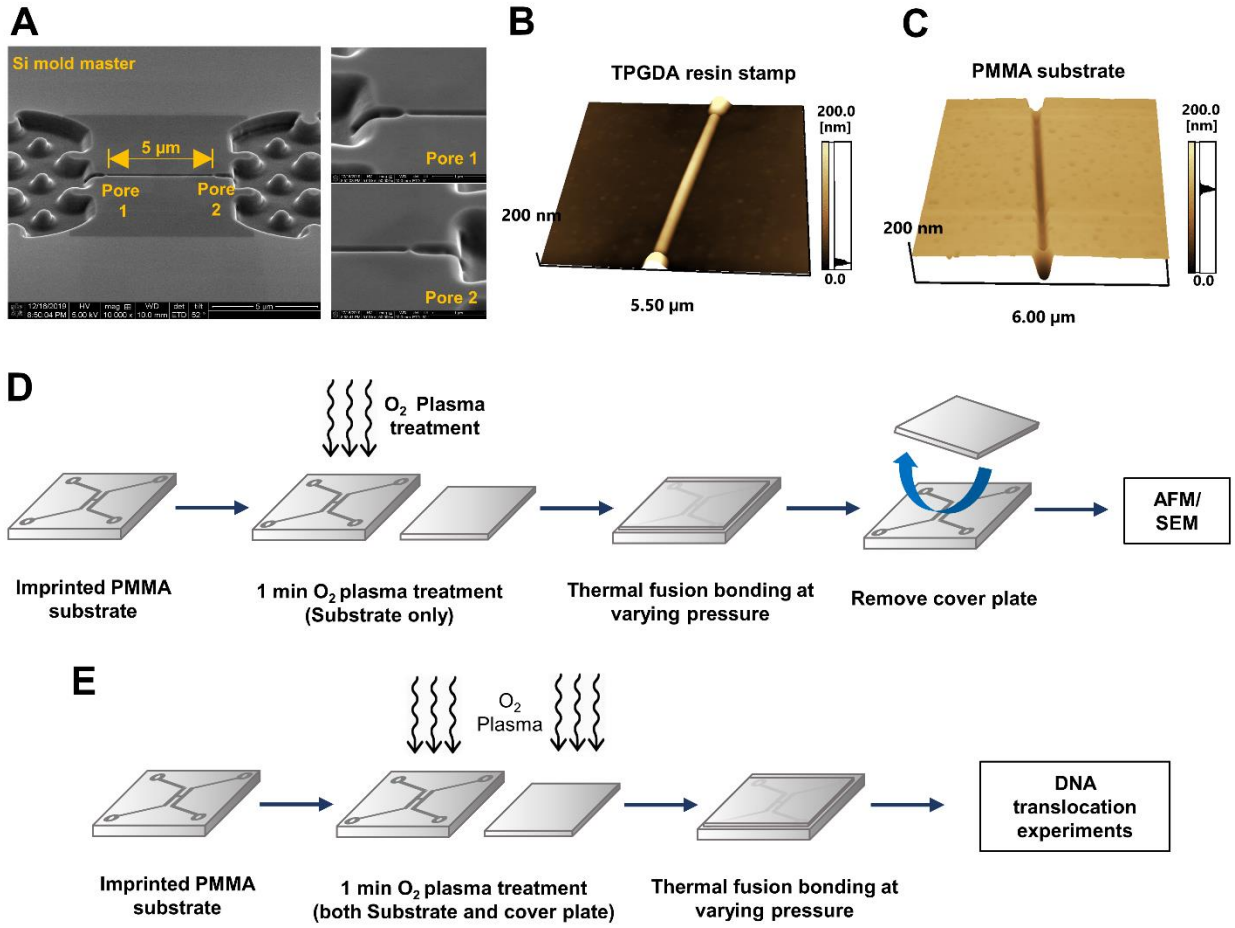

Figure 3.2 Dual in-plane nanopore device. **(A)** SEM image of the Si mold master. The two in-plane nanopores are 5 µm apart from each other. AFM scans of the **(B)** TPGDA resin stamp and **(C)** imprinted PMMA substrate. Tapping mode AFM scans were acquired at 0.5 Hz scanning frequency using a high aspect ratio tip with a radius < 2 nm. **(D)** Schematic representation of experimental procedure for determining depth and width of dual in-plane nanopores. **(E)** Schematic representation of device assembly for translocation studies.

Nanofluidic devices were fabricated in a thermoplastic using a method we have reported, which consists of making microstructures and nanostructures in Si masters followed by producing resin stamps via UV-NIL and production of the final device using thermal NIL.[33, 51] The in-plane nanopores were positioned at either end of a nanochannel, which was 5 μm in length and 50 nm x 50 nm in width and depth (Figure 3.2A). A SEM of the resin stamp is shown in Figure 3.2B,[57] and Figure 3.2C shows an imprinted substrate. The average height of the in-plane nanopores on the resin stamp were 30.3 ±2.0 nm (n = 4) and the depth of the nanopores in the imprinted substrate were 29.6 ±1.7 nm (n = 3).

Following fabrication, the ability to control the depth and width of the in-plane nanopores via TFB was examined by subjecting NIL imprinted devices to different bonding pressures at 70°C for 15 min and measuring the depth and width of the in-plane nanopores using AFM and SEM, respectively. For this purpose, we only treated the imprinted PMMA substrate with O_2 plasma and not the COC cover plate prior to TFB to reduce the bonding strength so that the cover plate and substrate could be pulled apart without damaging the underlying structures (see Figure 3.2D). Previously we reported the bond strength of PMMA/COC devices to be 0.086 ±0.014 mJ/cm^2 using the crack opening method.[55] In these experiments the bond strength between the O_2 plasma treated substrate and untreated cover plate was 0 mJ/cm^2 (*i.e.*, no crack was measured) meaning that the cover plate could be removed without material removal or deformation of the nanostructures in the substrate. A TFB temperature of 70°C was used as it was close to the T_g of the COC 8007 cover plate. For single-molecule translocation studies and RPS, the dual in-plane nanopore devices were assembled by O_2 plasma treatment of both the substrate and cover plate before TFB at varying pressures (see Figure 3.2E) so that the bond strength was sufficient to sustain

fluidic/translocation experiments. The surface roughness of the COC cover plate as determined by AFM was <1 nm, which was much smaller than the nanopore depth.

The PMMA substrate was exposed to O_2 plasma to form oxygen-containing groups.[35, 54, 58-60] In TFB, these oxygen-containing species are involved in bond formation between the substrate and cover plate.[35] In addition, polymer chain scissioning can result in photo-fragments that are more thermally mobile due to their lower molecular weight. This leads to a lowering of the T_g of the polymer on the surface, making it easier for the polymer chains to fuse into the mating substrate.[54] Depending on the type of polymer and the O_2 plasma power used as well as exposure time, polymer chain scission can occur up to several molecular layers into the bulk of the polymer. Therefore, during TFB of the cover plate to the substrate, the O_2 plasma activated polymer surfaces can rearrange leading to a change in nanostructure dimensions.

3.3.2 Nanopore size analysis.

The depth of the in-plane nanopores were measured by dynamic mode AFM at a 0.5 Hz scanning rate (Figure 3.3A). To measure the width of the in-plane nanopores following TFB, SEM was performed (Figure 3.3B). The depth of the in-plane nanopores reduced from 22.3 ±1.4 nm (110 psi, n = 6) to 10.2 ±1.5 nm (200 psi, n = 4) with increasing bonding pressure used for TFB (Figure 3.3C) The relative width of the in-plane nanopores decreased initially with bonding pressure to 0.47 ±0.04 (n = 4) at 130 psi compared to the width of the imprinted device but showed no statistically different widths at higher pressures (130-200 psi, $p > 0.05$, see Figure 3.3D). SEM and AFM images did not show statistically significant changes in the nanopore length before and after TFB. However, the overall cross-sectional area of the nanopores decreased with increasing pressure demonstrating the pore closing behavior (Figure 3.3E). Our in-plane nanopore in the

imprinted PMMA is a U-shaped constriction attributed to the nature of FIB milling process in the Si master. The results of the pore depth (Figure 3.3C) and width (Figure 3.3D) versus the bonding pressure provided a hint on the pore closing behavior. The decrease in both the pore depth and width in the low bonding pressure range can be attributed to the fusion of polymer chains between the two mating polymers, primarily in the thin layer of polymer subjected to O_2 plasma prior to bonding and to the squeeze flow toward the nanopores. As the bonding pressure increases, the lateral squeeze flow will preferentially flow along the border of nanopores as was observed during the squeeze flow into hydrophilic nanostructures,[61-62] and thus further reduce the pore depth while limiting the decrease in the pore width. Consequently, the nanopore bonded at higher pressures became a shallower U shape. At the same time, the decrease in the thickness of the surface modified thermoplastic layer further limits the squeeze flow because of increases in the T_g for polymers in the vicinity of a hydrophilic surface due to the alignment of polymer chains along the surface.[63] This may account for the slight increase in the pore width at higher bonding pressures. Further increases in the bonding pressures beyond 200 psi ultimately led to collapse of the nanopores as evidenced by the cessation of the open pore current.

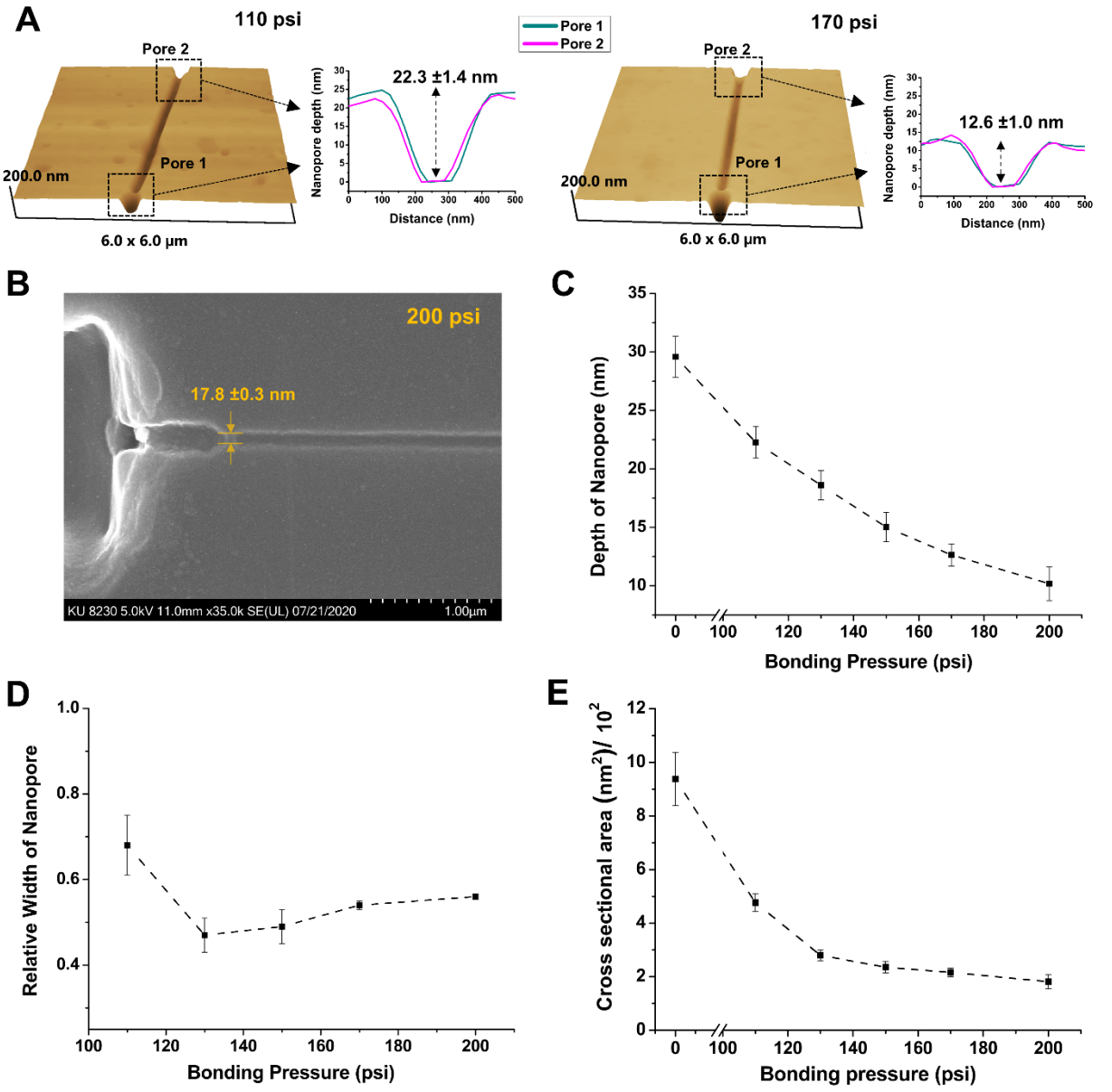

Figure 3.3 Nanopore depth and width with varying thermal fusion bonding pressure. (**A**) AFM scans of PMMA devices at 110 psi and 170 psi bonding pressures. (**B**) SEM image of PMMA device at 200 psi bonding pressure. A 2 nm thin conductive Iridium layer was sputter coated onto the PMMA device using an EMS 150ES sputter coater before SEM Imaging. (**C**) Change in the depth of the in-plane nanopores with bonding pressure. (**D**) Relative width of the in-plane nanopores after bonding at different pressures relative to the width of the nanopore before bonding (0 psi). There was no statistical difference in relative width from 130-200 psi at the 95% confidence interval ($p > 0.05$). (**E**) Cross sectional area of the in-plane nanopore with thermal fusion bonding pressure.

3.3.3 COMSOL simulations and conductance measurements of devices.

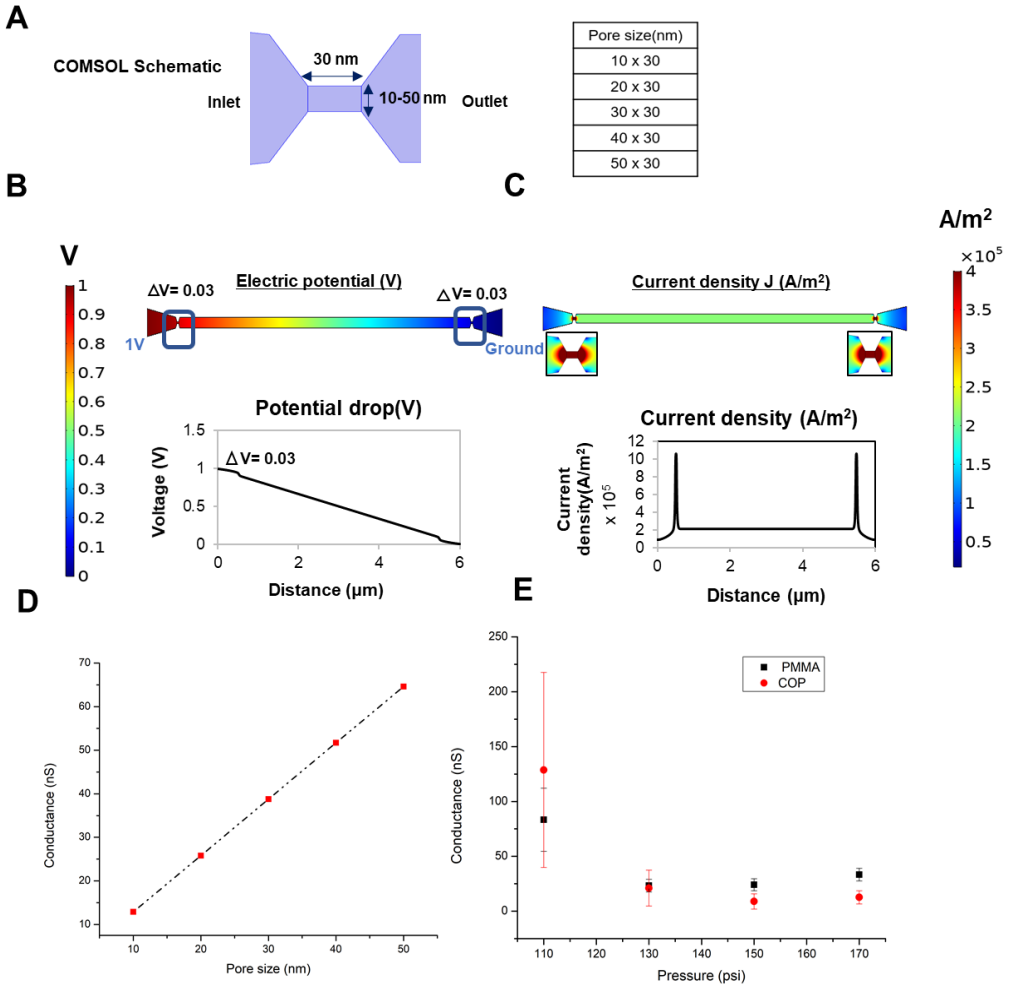

Figure 3.4 Simulated and experimental analysis of the electrical behavior of the dual in-plane nanopores connected by a 5 μm length flight tube at different bonding pressures. **(A)** The 2D design of the dual in-plane nanopores used for COMSOL simulations. The pore and intervening 5 μm long nanochannel were assumed to be cylindrical. In order to understand if a change of in-plane nanopore diameter would cause an increase in conductance, the pore diameter was varied from 10-50 nm while the length was kept constant at 30 nm. **(B)** The electric potential data from COMSOL simulations shows that the majority of the potential drop appears across the two nanopores and the nanochannel implying that the overall conductance is contributed by the two nanopores and the nanochannel. **(C)** The current density was plotted from which the current and the subsequent conductance was calculated (I/V). **(D)** Conductance (nS) calculated from COMSOL for varying pore widths in 1 M KCl. There was a linear increase in conductance with increasing pore width. **(E)** Variation of measured conductance through the dual in plane nanopore PMMA and COP devices at different bonding conditions using an electrolyte of 1 M KCl ($n \geq 3$). There was a decrease in conductance with increase in bonding pressure, but with no statistical differences at pressures above 130 psi ($p > 0.05$). The conductance results agree with the pore size determined using AFM and SEM and were also correlated to the COMSOL results. The y-axis scales of graphs for (**D**) and (**E**) are adjusted according to their corresponding x-axis and hence the range might be different.

We carried out COMSOL simulations of the dual in-plane nanopore sensor to estimate the change in the conductance with change in pore size. The length of the nanopore was maintained at 30 nm, but the width was changed from 10 nm to 50 nm (see Figure 3.4A). A DC bias of -1 V was applied across the ends of the device, and 1 M KCl was used as the electrolyte. From Figure 3.4B, it can be seen that the majority of the potential drop occurred across the two in-plane nanopores (0.03 V in each pore) and with a drop through the 5 μm long nanochannel. A current density graph was plotted that showed a sharp increase in current density at the nanopores due to their small dimensions (Figure 3.4C). The current density was integrated over the area of the nanopore to calculate the current. The conductance of the pores was then calculated using Ohm's law and was plotted to estimate the conductance at different pore sizes. As shown in Figure 3.4D, a linear increase in conductance was seen as the size of the nanopore increased. The conductance values obtained from simulations and depths/widths from AFM and SEM, respectively, were used to estimate the size of the nanopores from conductance values obtained experimentally.

Experimental conductance measurements were performed using the dual in-plane nanopore devices made in PMMA and COP bonded at different pressures using 1 M KCl as the electrolyte and COC as the cover plate. The conductance was calculated from the slope of the curve for all bonding pressures and is shown in Figure 3.3E. The average conductance at 110 psi for PMMA and COP devices were 83 ±29 nS (RSD 34%) and 128 ±89 nS (RSD 69%), respectively. However, at 130 psi the average conductance of the PMMA and COP dual in-plane nanopore devices was 23 nS ±6 nS (RSD 26%) and 21 ±16 nS (RSD 76%), respectively. These values correlate well with the conductance (~23 nS) obtained from COMSOL for an 18 nm pore, which is the size of the pore obtained from AFM and SEM when using 130 psi TFB pressure. The conductance values showed a slight increase from 24 ±5 nS (RSD 22%) to 33 ±6 nS (RSD 18%) for PMMA devices bonded

at 150 and 170 psi, respectively, but there was no statistical difference in the conductance values at bonding pressures >130 psi ($p > 0.05$). Similarly, in the case of COP devices the conductance values decreased at 150 psi to 9 ±7 nS (RSD 77%) but showed a statistically insignificant increase at 170 psi to 12 ±6 nS (RSD 48%). This small increase in conductance can be correlated to the results from SEM and COMSOL that showed <5 nm increase in pore width. Overall, both PMMA and COP devices followed a similar trend of decrease in conductance at 130 and 150 psi followed by a slight increase at 170 psi showing the reproducibility of our approach with different substrate materials.

3.3.4 λ-DNA translocation through the dual in-plane nanopores.

Assembled dual in-plane nanopore devices could be used to electrokinetically drive charged single molecules through the nanopores. Based on our results from COMSOL simulations and experimental conductance measurements, it was evident that the increase in bonding pressure caused a drop in conductance, which indicated reduction in pore size. To further reaffirm that the pore size indeed decreased with increasing bonding pressure, we used λ-DNA and electrokinetically translocated them through the nanopore devices under different bonding conditions to estimate the current blockage amplitudes as a function of pore size.[9, 64-65]

Figure 3.5 shows the use of dual in-plane nanopore devices as a sensing platform for the detection of 48.5 Kbp λ-DNA that has a contour length of 16.5 μm. When the electrokinetically driven molecule entered the first nanopore, there was a partial current blockage creating a transient increase in the electrical resistance, which manifested itself as a negative peak (current drop) in the measured trace as shown in the schematic of Figure 3.5A. Because the contour length of λ-DNA is longer than the distance between the two in-plane nanopores (5 μm), the initial drop of

current was accompanied by a subsequent drop in current when the DNA co-resided in the first and second in-plane nanopores. Furthermore, when the DNA exited the first nanopore, it was resident only in the second nanopore causing a subsequent small shoulder in the current trace and eventually returning to baseline. A current trace of multiple current transient signals over a time interval of 400 s for λ-DNA is shown in Figure 3.5B demonstrating the characteristic shape of the peaks at 110 psi and 170 psi. The various stages of the translocation are marked in both traces to show how the shape of the current transients agree with the aforementioned description. Although the average amplitude increased with every increase in bonding pressure, the shape of the peaks remained similar to that shown in Figure 3.5B indicating that the size of the nanopore did not alter the translocation dynamics rather changed only the SNR of the signal.

Peak height measurements (n ≥120) of the current transient amplitudes of λ-DNA in devices bonded at different pressures showed differences between each bonding pressure as determined by the Wilcoxon signed rank test (Figure 3.5C). The peak amplitudes were collected from >10 devices for each bonding pressure as we were only able to see ~6 events per device. The average peak amplitude of λ-DNA in devices bonded at 110 psi for 15 min was 130 pA corresponding to a pore depth of ~22 nm and a width of ~21 nm. Devices bonded at 170 psi for 15 min having a pore depth and width of ~13 nm x ~17 nm yielded a current amplitude of 280 pA, and for devices bonded at 200 psi for 5 min having a depth × width of 10 nm x ~18 nm yielded a current amplitude of 437 pA. There was a 3.5-fold increase in current amplitude when the pore dimensions decreased from 22 nm (depth) x 21 nm (width) to 10 nm (depth) x 18 nm (width). Devices bonded at 200 psi for 15 min served as the upper limit because the nanopore became unusable as the cover plate collapsed into the nanopore. However, for 200 psi bonding pressure the TFB time had to be reduced to 5 min to generate functional devices.

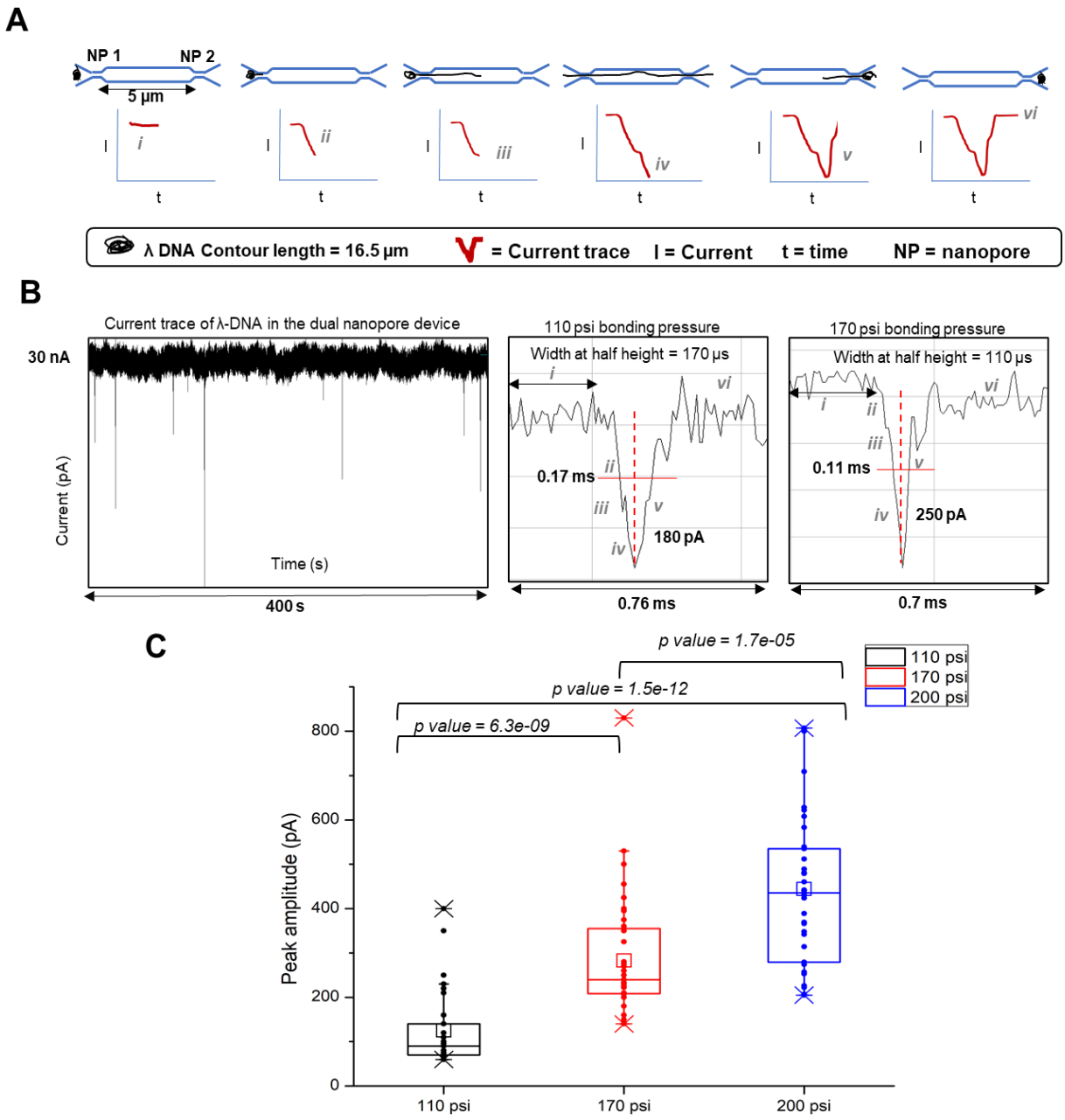

Figure 3.5 λ-DNA translocation through the dual in-plane PMMA nanopores and the ramifications of the size of the nanopore on peak amplitude. (A) Schematic of the λ-DNA translocation through the in plane dual nanopore device that gives rise to a negative peak as the DNA enters the first pore. Since the contour length of the DNA is longer than both the pores, there is a second subsequent peak when the DNA co-resides in both the pores. The DNA then leaves the pores very quickly which makes the current return to the baseline. (B) Detected current transient trace typically observed in a time interval of 400 s as a result of λ-DNA translocation and magnified images of individual peak shapes at various translocation stages of the DNA through the dual nanopore at 110 and 170 psi pressure, respectively. (C) Distribution of peak amplitudes of λ-DNA at 110, 170 and 200 psi bonding pressures. The average peak amplitude increases with the increasing bonding pressure. p values calculated between each bonding pressure condition (Wilcoxon signed rank test) show statistically significant difference at 95% confidence interval ($p < 0.05$).

We calculated the apparent mobility (μ_{app}) of λ-DNA based on the time interval between peaks (Δt) at time points (i) and (iv) (see Figure 3.5A). These time points were used because one end of λ-DNA was entering the first in-plane nanopore and that same end was then entering the second nanopore corresponding to a length of 5 μm (l) at the applied electric field strength (*E*). The average apparent mobility for **λ**-DNA was determined to be $(2.57 \pm 0.94) \times 10^{-7}$ m^2/ Vs.

3.3.5 ssRNA translocation through O_2 plasma modified PMMA dual in-plane nanopore devices.

To further demonstrate the use of the dual in-plane nanopores for detection of various sized molecules, we carried out translocation experiments of 60 nt ssRNA (R_g ~6 nm) using the dual in-plane nanopore devices bonded at 170 psi, which resulted in a pore depth and width of 12.6 ±0.9 nm x 17.1 ±0.2 nm. The assembled PMMA/COC dual in-plane nanopore devices were primed with 50% v/v methanol followed by introduction of 1× NEBuffer 3 (Figure 3.6A). Before introducing the ssRNA solution, the current was monitored to establish a baseline (Figure 3.6B). Then, the buffer in one reservoir was replaced with 100 nM ssRNA solution and a potential (1V – 2.5V) was applied.

For the 100 nM ssRNA solution, we only observed very few translocation events even after increasing the concentration to 1 μM and the driving voltage to -2.5 V (see Figure 3.6C). Due to the low event frequency, a large number of devices would have to be used to collect a reasonable number of events to secure meaningful statistics as was carried out for the λ-DNA data shown in Figure 3.5. The low event frequency could have been due to coion exclusion due to the high surface charge of the O2 plasma-modified PMMA devices, which is reported as −40 mC/cm^2.[50] Due to the high negative charge on the nanopore surface and partial electric double layer overlap within the

nanopore, the entry of negatively charged coions such as ssRNAs is impeded. In addition, the opposing EOF also serves to reduce event frequency.

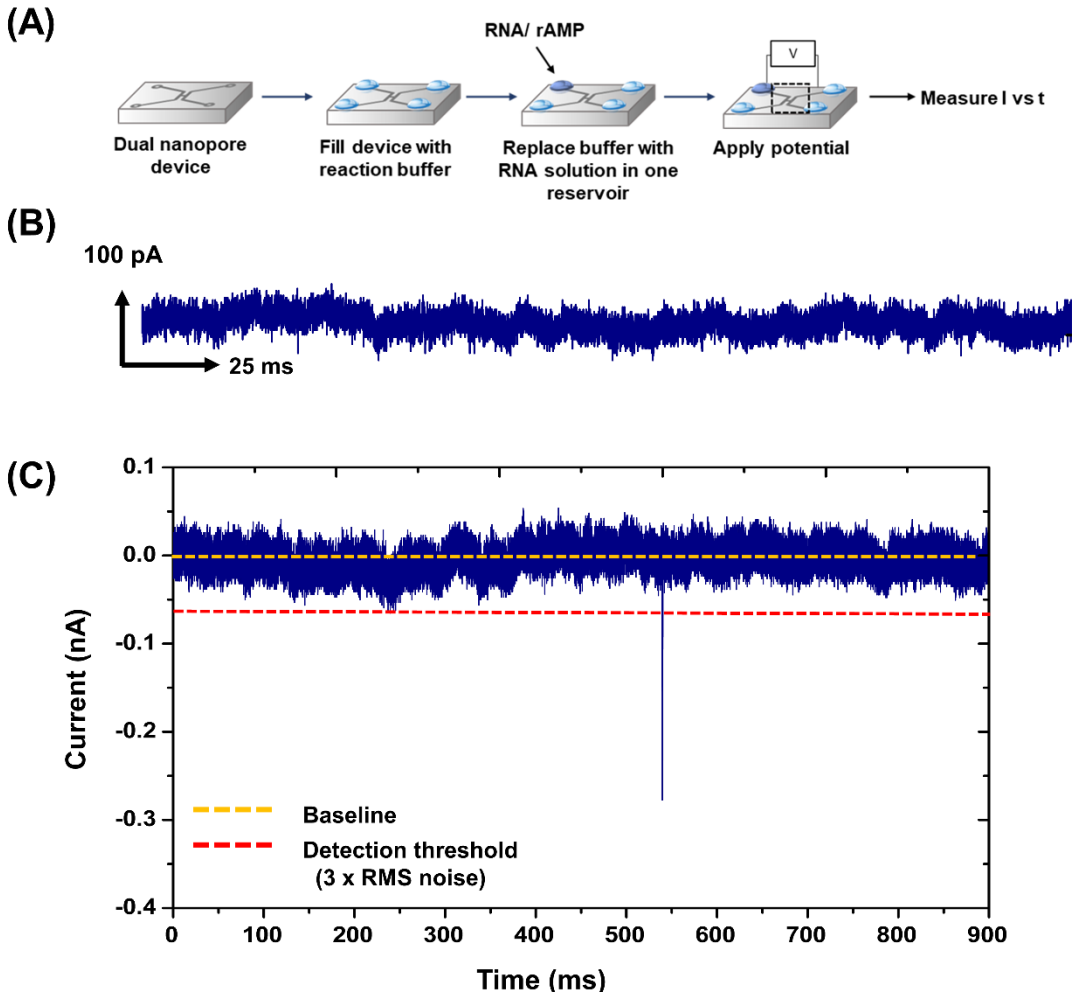

Figure 3.6 Biomolecule translocation through dual in-plane nanopores under an applied electric field. **(A)** Schematic representation of the reaction procedure and subsequent ssRNA (60 nt) translocation experiments. In this case, the reaction consisted of EDC/NHS and ethanolamine, which was used to react with the surface carboxyl groups following O_2 plasma activation of the PMMA surface. **(B)** A 250 ms current transient trace of the open pore (baseline) current. **(C)** A 900 ms current trace obtained after the introduction of a 60 nt long RNAs in an O_2 plasma treated PMMA dual in-plane nanopore device. The open pore current was subtracted from this trace.

3.3.6 Water contact angles of modified thermoplastics.

The PMMA/COC surfaces were modified with ethanolamine using EDC/NHS coupling chemistry (Figure 3.1). Sessile drop water contact angle measurements were acquired for native, O_2 plasma activated, and ethanolamine treated PMMA surfaces with and without EDC/NHS. The contact angle dropped from 79.2 ±1.8° for pristine PMMA to 42.2 ±1.0° after O_2 plasma activation indicating the generation of surface carboxyl groups (Figure 3.7). These values agreed with values reported in literature.[55] After amidation of the carboxyl groups with ethanolamine via EDC/NHS coupling chemistry, the sessile drop water contact angle (53.4 ±2.5°) slightly increased compared to the plasma treated surface. But, in the absence of the EDC/NHS coupling reagents, no change in water contact angle was seen with respect to the O_2 plasma activated surface. As evident from the water contact angle measurements, the ethanolamine treated surfaces remained hydrophilic compared to native PMMA due to the presence of terminal hydroxyl groups. The hydrophilic nature of the ethanolamine treated surface is helpful in consistent filling of the nanofluidic device without generating air bubbles. The water contact angle of native PMMA treated with ethanolamine in the absence of EDC/NHS was 42.34 ±2.73°. The water contact angle of O_2 plasma treated PMMA was not changed after treatment ($p= 0.7742$, $n=5$, contact angle data for O_2 plasma modified vs. native- ethanolamine treated with ethanolamine in the absence of EDC/NHS) with ethanolamine only and this confirms that there is no nonspecific adsorption of ethanolamine on carboxyl group modified PMMA. Ethanolamine forms a covalent attachment to the PMMA surface only through EDC/NHS coupling chemistry.

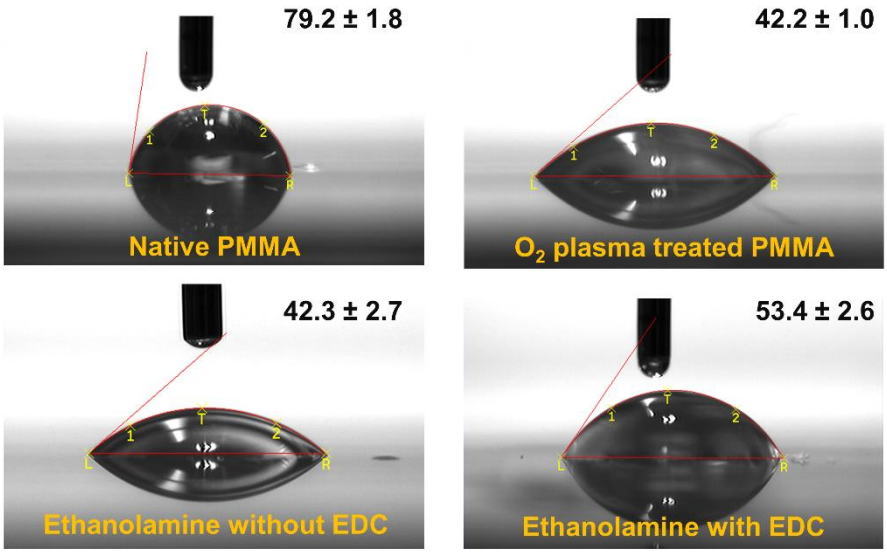

Figure 3.7 Sessile water contact angle measurements of a native PMMA surface (**A**), followed by O_2 plasma treatment to generate surface carboxyl groups (**B,**) reaction with ethanolamine in the presence (**C**) and absence (**D**) of EDC/NHS coupling chemistry.

3.3.7 ATR-FTIR characterization of ethanolamine modified surfaces.

To examine the molecular nature of the modified and unmodified thermoplastic surfaces with ethanolamine, ATR-FTIR experiments were performed. As noted in literature, ATR-FTIR has penetration depths of 0.5-2 µm into the bulk material and therefore, thermoplastics were UV/O_3 activated for 15 min at 22 mW cm^{-2} power prior to ethanolamine modification.[66] The surfaces activated with UV/O_3 observed sufficient ATR-FTIR signal (see Figure 3.8A) as activation occurs into the depth of the thermoplastics whereas, O_2 plasma activation occurs only within first few monolayers. An ATR-FTIR spectrum of native PMMA with the characteristic peaks between 4000 and 500 cm^{-1} is shown in Figure 3.8A. The most prominent band was ν(C=O) at 1724 cm^{-1} assigned to the methacrylate ester stretch. The peaks at 1270, 1240 cm^{-1} and 1195, 1150 cm^{-1} could be assigned to ν(C-O) and ν(C-O-C) stretching of an ester. After UV/O_3 activation, there was the appearance of a band at 3441 cm^{-1} and 1737 cm^{-1}, which could be assigned to the ν(O-H) and

v(C=O) of a carboxylic acid group[50,67] Upon treatment with ethanolamine bands at 3396 cm^{-1} and 1635 cm^{-1} corresponded to the v(N-H) stretch of a primary amine and v(C=O) of an amide.

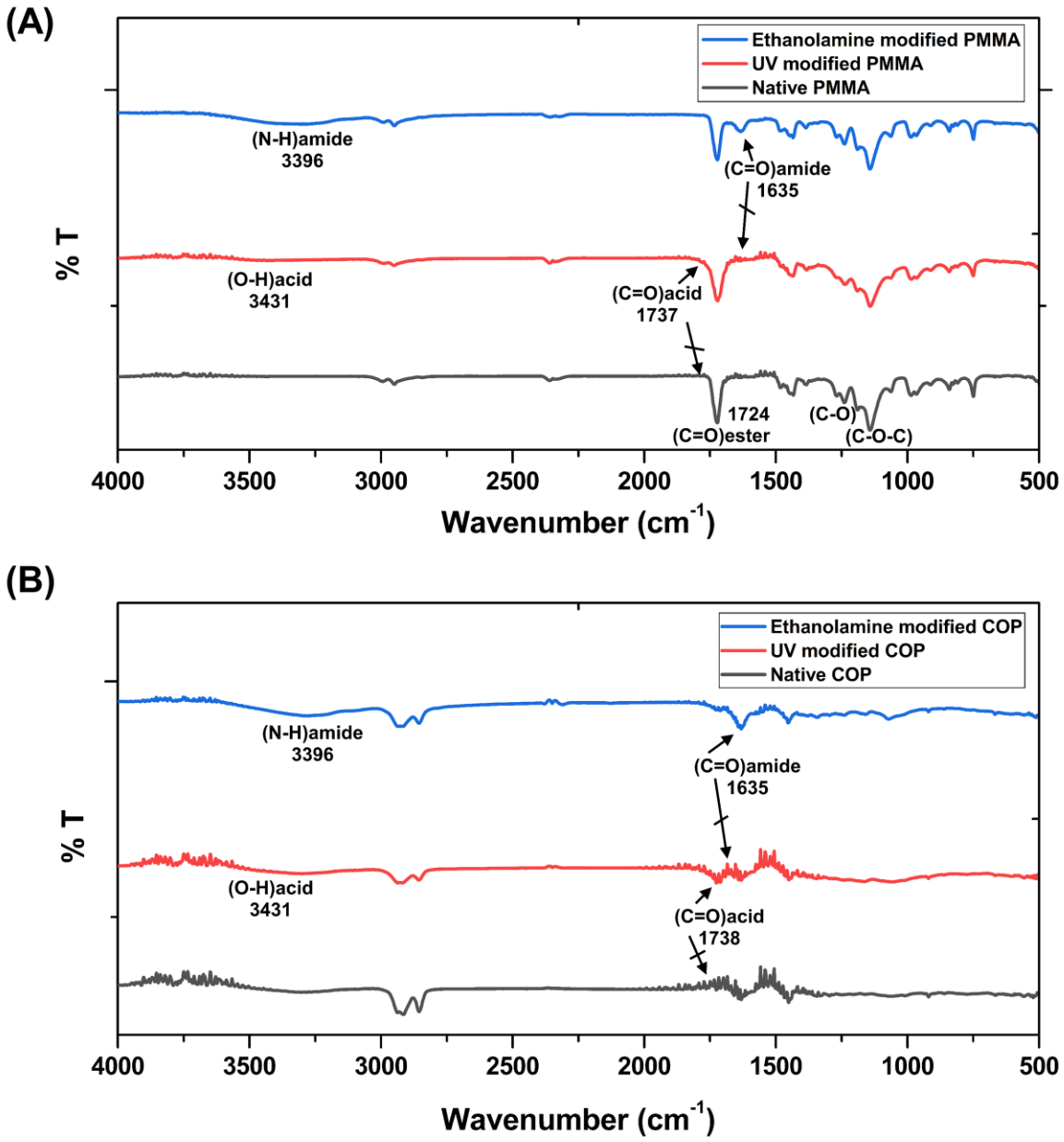

Figure 3.8 ATR-FTIR spectra of native, UV activated, and ethanolamine modified (A) PMMA and (B) COP. ATRFTIR spectra were acquired from 400-4000 cm-1 using an ALPHA FTIR spectrometer and a Platinum ATR module (Bruker Optics). Spectra (n = 6) were analyzed using Essential FTIR analysis software.

3.3.8 Surface Charge.

(A)

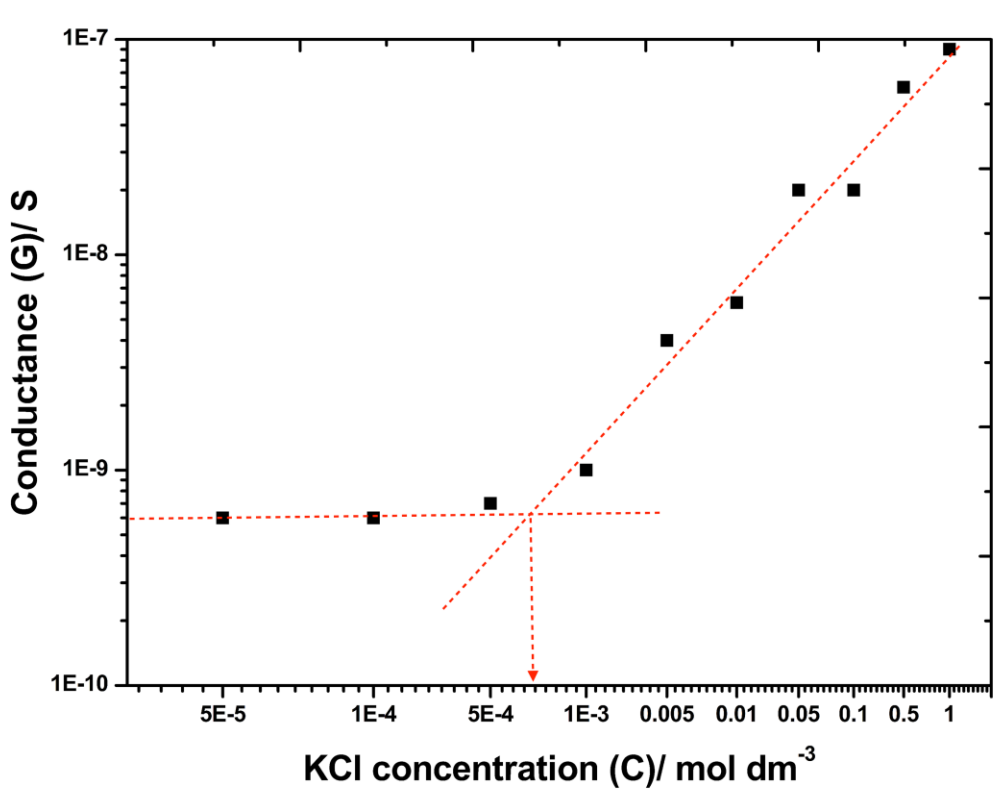

(B)

	EOF (cm^2/Vs)	Surface charge density (mC/m^2)	Zeta potential (mV)
Ethanolamine modified PMMA	3.1 (±0.1) × 10^{-6}	-3.8	-0.45
O_2 plasma modified PMMA	4.1 (±0.2) × 10^{-4}	-40.1	-59

Figure 3.9 (A) Conductance versus KCl concentration obtained from ethanolamine modified PMMA devices consisting an array of four nanochannels (each 100 nm wide, 100 nm deep, and 107 µm long). Each data point represents a mean of five measurements with a scatter in the data within 5-8 % of the average value. The calculated effective surface charge density from the graph was -3.8 mC/m^2. **(B)** Measured EOF values as well as surface charge density zeta potential for ethanolamine modified PMMA nanochannel devices investigated at pH 7.8. The EOF and zeta potential for O_2 plasma modified PMMA were reproduced from Amarasekara *et al*., *Electrophoresis*, (2020).[55] The surface charge density for plasma modified nanochannel device was reproduced from uba *et al*., *Analyst*, (2015).[50]

We used electrical conductance measurements across ethanolamine modified nanochannel device filled with different KCl concentrations to work out the surface charge density. The average

conductance was plotted against the electrolyte concentration in a log-log plot (see Figure 3.9A) and the surface charge (σ_s) density was deduced by fitting the conductance plot according to;[50]

$$G_T = 10^3(\mu_{K^+} + \mu_{Cl^-})cN_A e.\frac{nwh}{L} + 2\mu_{opp}\sigma_s n\frac{(w+h)}{L}$$

(1)

Where G_T is the total measured conductance in the nanochannel, μ_{K^+} and μ_{Cl^-} are ion mobilities of K^+ and Cl^- ions, respectively (μ_{K^+}= 7.619 × 10-8 $m^2 V^{-1} s^{-1}$ and μ_{Cl^-}=7.912 × 10^{-8} m^2 V^{-1} s^{-1}), c is the electrolyte concentration in mol L^{-1}, N_A is Avogadro's number, e is the electron charge, n is the number of nanochannels in the device, w, h, and L are width, height and length of the nanochannel respectively, and $\mu_{opp} \approx \mu_{K^+}$ for the deprotonated carboxyl surface (see Figure 3.9A).

It is reported that carboxylic acid groups are generated on PMMA and COC upon UV/O_3 activation[68] or O_2 plasma treatment.[69, 70] After ethanolamine modification of O_2 plasma treated devices, the surface is dominated by hydroxyl groups. When ethanolamine modified surfaces are in contact with an electrolyte solution at pH 7.8, ~99.9% of the hydroxyl groups (pK_a = 16.0) would be protonated and ~99.9% of the carboxyl groups (pK_a = 4.66) would be deprotonated.[71] Therefore, these deprotonated carboxylic acid moieties are responsible for generating a surface charge density. The transition concentration, c_t used to calculate σ_s was 0.78 mM for ethanolamine modified surface. For ethanolamine modified PMMA nanochannels, we obtained σ_s ~ -3.8 mC/m^2, which was ~10-fold less than -40.5 mC/m^{-2} reported by Uba *et al.* for O_2 plasma modified nanochannels.[50]

3.3.9 Electroosmotic flow.

The EOF of ethanolamine modified nanochannel device was measured using the current monitoring method.[72] The EOF can be described by $\mu_{eof} = \upsilon_{eof}/E$, where υ_{eof} is electroosmotic flow velocity and E is the field strength. As noted above, plasma activated PMMA surfaces are negatively charged due to deprotonation of carboxylic acid groups and ethanolamine modified PMMA surfaces are uncharged at pH 7.8. The EOF for ethanolamine modified PMMA nanochannel device was 3.63×10^{-5} $cm^2/$ V s (see Figure 3.9B), which was ~9-fold less than 4.1×10^{-4} $cm^2/$ V s reported by Amarasekara *et al.* for O_2 plasma modified PMMA nanochannel device.[50] The zeta potential, ζ was computed using equation (2). At low electric double layer thicknesses (λ_D ≈0.8 nm for 1X NE buffer 3) μ_{eof} can be represented by Helmholtz-Smoluchowski equation;

$$\mu_{eof} = \frac{\varepsilon_0 \varepsilon_r \zeta}{\eta_0} \tag{2}$$

where ε_0, ε_r are the permittivity of vacuum, and the relative permittivity of the buffer (80.1), respectively, ζ is the zeta potential and η_0 is the bulk solvent viscosity (8.9×10^{-4} Pa/s).[37] The computed zeta potential for ethanolamine modified PMMA device was -5.2 mV and it was ~11-fold less compared to O_2 plasma modified device.[50] The surface charge density, EOF and the zeta potential values further supports the successful modification of PMMA surfaces with ethanolamine.

3.3.10 ssRNA translocation through ethanolamine modified PMMA/COC dual in-plane nanopore devices.

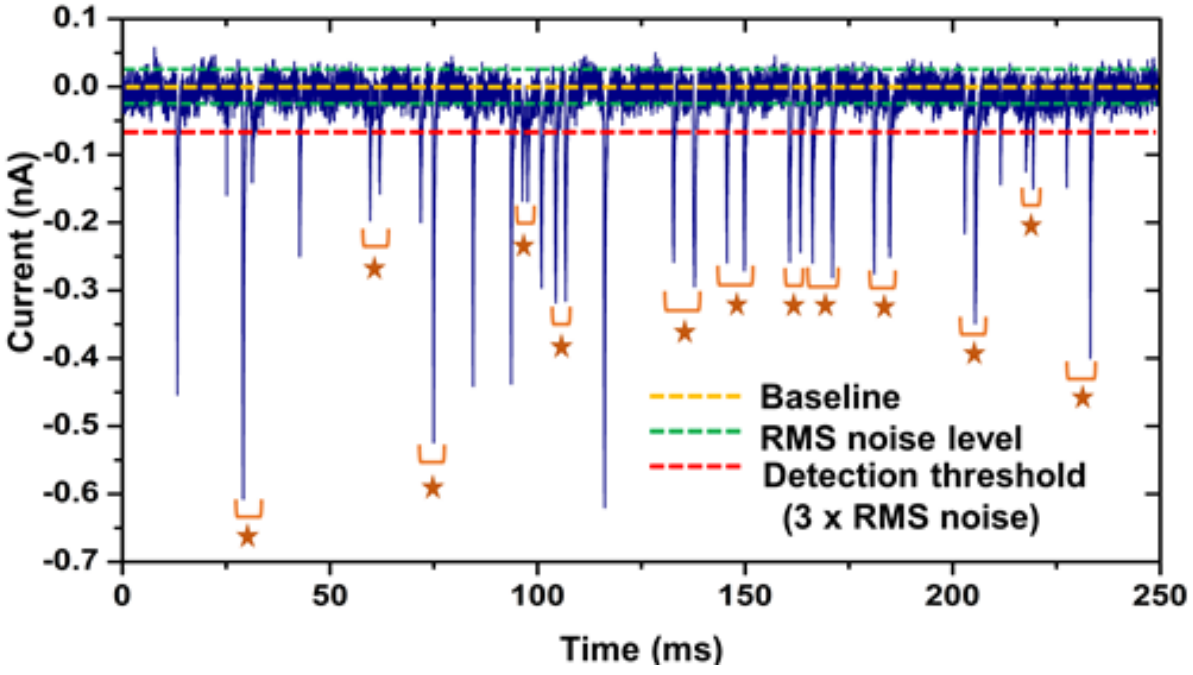

Figure 3.10 A 250 ms trace of the current transient amplitude signal obtained for 100 nM solution of 60 nt RNA obtained using dual in-plane nanopore devices bonded at 170 psi bonding pressure. The stars represent paired peaks which corresponded to a single RNA molecule translocating through both nanopores.

After ethanolamine modification, ssRNA translocation was carried out. For these experiments, a 100 nM solution of 60 nt ssRNA in 1× NEBuffer 3 was introduced into the nanopore device, which used TFB at 170 psi and a potential of -2.5 V was applied across the nanopores. As shown in Figure 3.10, after ethanolamine treatment, the event frequency increased significantly compared to the O_2 plasma treated nanopore devices as can be seen from Figure 3.6C. Only a single ssRNA event (concentration = 100 nM) was observed over a span of 900 ms for the O_2 plasma treated devices while in the case of the ethanolamine-treated PMMA/COC device, ~34 single-molecule ssRNA events (concentration = 100 nM) were observed over a time span of 250 ms. The average dwell time of the peaks obtained for single 60 nt ssRNA events was determined

to be 0.92 ±0.38 ms. The current transient amplitudes of the ssRNA events ranged between 0.10 – 0.8 nA with an average of 311.75 ± 137.49 pA (n = 325; see Figure 3.11A).

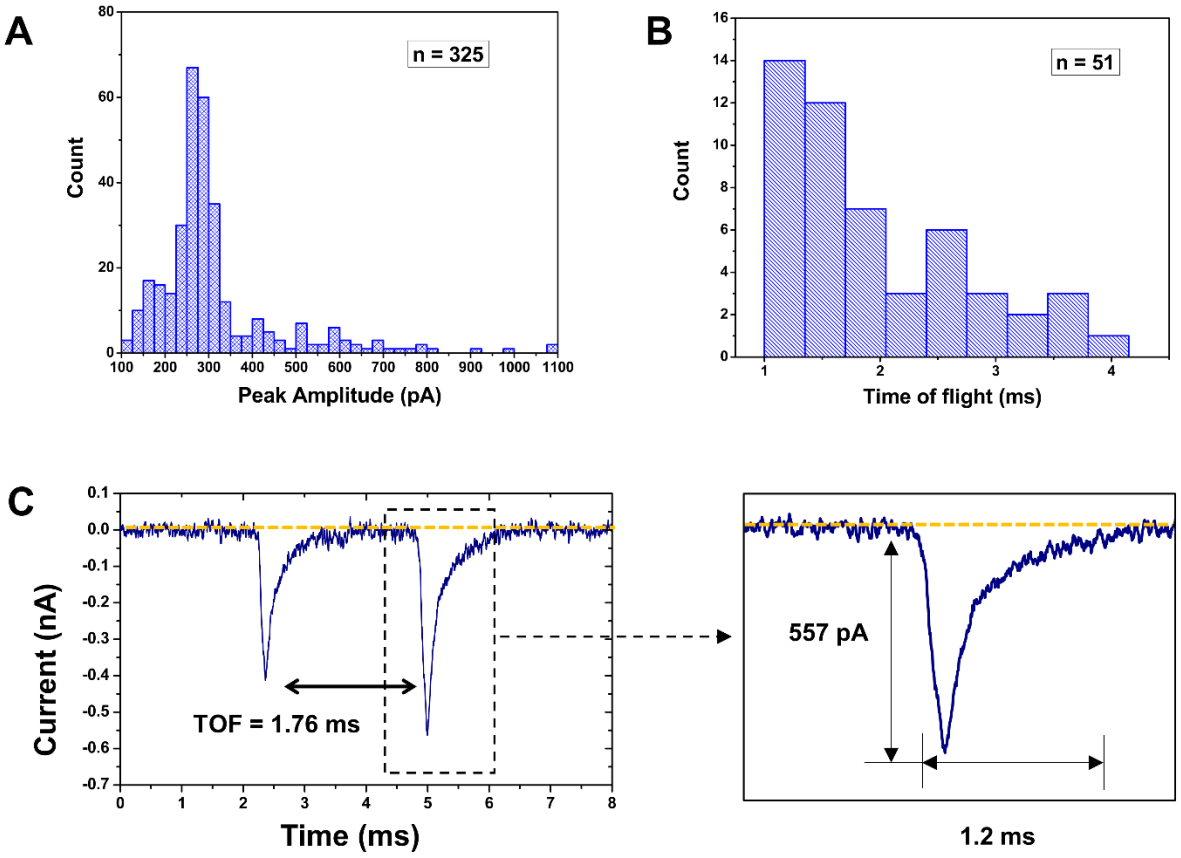

Figure 3.11 Translocation of 60 nt ssRNA through dual in-plane nanopore devices bonded at 170 psi. (**A**) Histogram of the current transient amplitudes for the 60 nt ssRNA. The current transient amplitudes ranged between 0.10 – 0.8 nA with an average of 311.75 ±137.49 pA (n = 325). **(B)** Histogram of the time-of-flight (TOF) values obtained for the 60 nt ssRNA. The TOF ranged between 1 – 4 ms with an average of 2.09 ±0.97 ms (n = 51). **(C)** An example peak pair as determined based on the peak pair selection criteria.

We also measured the time-of-flight (TOF) of the ssRNA, which corresponds to the time of the molecule to travel between the two pores. The TOF ranged from 1 to 4 ms with an average of 2.09 ± 0.97 ms (n = 51; see Figure 3.11B). An example peak pair is shown in Figure 3.11 C. In the 250 ms current trace shown in Figure 3.10, 76.5% (26/34) of the events corresponded to peak pairs.

3.3.11 rAMP translocation through ethanolamine modified PMMA/COC dual in-plane nanopore devices.

We next carried out experiments to detect single rAMP molecules using the PMMA/COC dual-in-plane nanopore devices bonded at 200 psi for 5 min, which was used to create a smaller pore to accommodate the smaller size of the rAMP molecule compared to the ssRNA 60 nt molecule. Figure 3.12 shows the current traces for a blank, 10 nM, 100 nM, and 1 μM solution of rAMP. With increasing concentration, a linear increase in event frequency was observed (R^2 = 0.9757). An example peak pair obtained for rAMP translocation between the two pores in series is shown in Figure 3.12B. The average current blockage amplitudes for rAMP was 425.89 ±175.89 pA (n = 185; Figure 3.12C). The average dwell time of rAMPs within the nanopores was 0.31±0.26 ms (n = 185; Figure 3.12D).

We also used the dual in-plane nanopore devices to measure the apparent electrophoretic mobility (*i.e.*, time-of-flight, TOF) of rAMP using rigorous selection criteria.[73] The first criterion was that the peak amplitude should be >3× the RMS noise of the open pore current. The RMS noise of the open pore current of the 200-psi bonded device was found to be 19.6 pA and therefore, only peaks with amplitudes >58.5 pA were considered as true events. The second criterion was the minimum TOF, where the travel time between the two pores (TOF) for the single molecule should be greater than the dwell time (peak width) of each peak comprising the peak pair. The third criterion was that the maximum TOF needed to be within 1.5 times the theoretical TOF. The maximum TOF (5.7 ms) was calculated using the mobility values we recently reported for ATTO-532 labelled rAMP.[52] The average TOF for rAMP was 4.14 ± 0.97 ms (n = 85; Figure 3.12E). The percentage of peaks identified as paired events was 82, 63 and 64% for 10 nM, 100 nM and 1 μM rAMP

solutions, respectively. For measurements performed with the rAMPs using the dual in-plane nanopore devices bonded at 110 psi, no current transients were observed (data not shown).

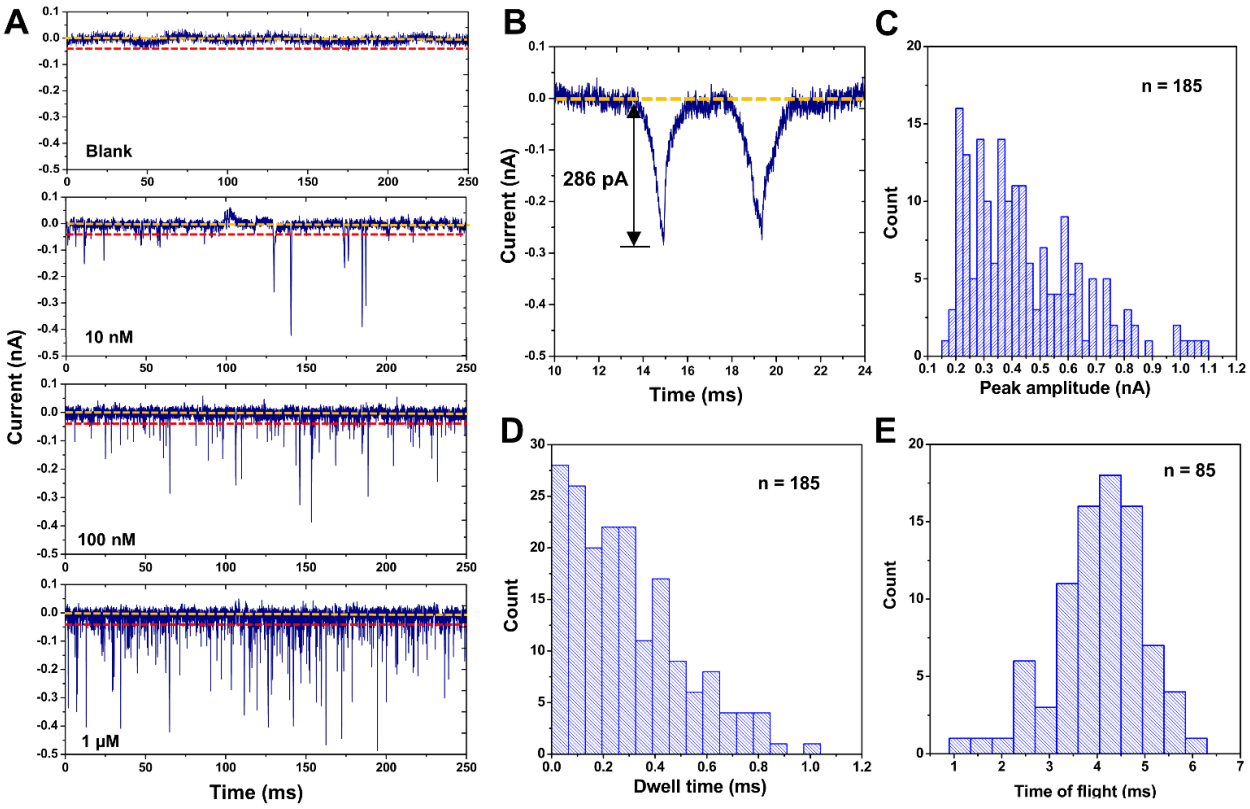

Figure 3.12 Translocation of rAMPs through dual in-plane nanopore devices assembled at 200 psi bonding pressure. (A) A 250 ms current transient trace of signal amplitudes obtained for a blank, 10 nM, 100 nM and 1 µM solutions of rAMP using dual in-plane nanopore devices. An increase in event frequency was observed with increasing concentration (R^2 = 0.9757). (B) An example peak pair selected using the peak pair criteria. (C) Peak amplitude distribution of rAMP events. (D) The dwell time distribution for rAMP events. (E) TOF distribution for rAMP.

Unpaired peaks found in this work may be attributed to the relatively large pore size compared to that of rNMP and the irregular shape (shallow U-shape) of the in-plane nanopores, which resulted in a large variation in the peak amplitude, as seen in Figure 3.12. Thus, some peaks may not produce sufficient amplitudes to be selected as paired events and account for the unpaired peaks. Also, there may be cases where entry of a molecule into the first nanopore before the previous molecule left the second nanopore may lead to unpaired events, which can be seen in the

decreased percentage of the paired events with increasing concentration. In previous work by Langecker et al.[73] where double-stranded (ds)-DNA was detected by stacked nanopores with diameters of 23 and 28 nm, 94% of detected peaks could unambiguously be assigned to the translocating dsDNA.

3.4 Conclusion

In this paper we have shown the ability to tailor the size of an in-plane nanopore by TFB using different pressures during an assembly step already required for thermoplastic nanofluidic chip production. We noticed that the size and shape of the in-plane nanopore changed with different bonding pressures in a controlled fashion as measured using AFM and SEM. Furthermore, COMSOL simulations with varying pore widths gave the approximate conductance observed in the PMMA and COP dual in-plane nanopore devices connected using a 5 μm long nanochannel. Furthermore, λ-DNA was electrokinetically driven by a DC voltage through the dual nanopore devices bonded at 110, 170 and 200 psi. The transient current amplitudes were seen to increase with higher TFB pressures. Therefore, thermoplastic nanofluidic devices allow for tuning nanostructure size to accommodate a given application by simply altering device assembly conditions without requiring direct FIB milling of a new Si master. This was further demonstrated using 60 nt ssRNAs and rAMPs with devices bonded at 170 and 200 psi bonding pressure, respectively. We should note that we could produce >1000 resin stamps from a single Si master and from each resin stamp, >20 nanofluidic devices could be produced with a success rate of producing functional devices following TFB of the COC cover plate to the PMMA or COP substrate >90%.[33, 37, 51] For high scale production, preliminary data in our laboratories indicate that these devices can be made via injection molding, which will be the focus of a future report.

The dual in-plane nanopores with their associated fluidic network and the fact that they were fabricated in thermoplastics in a single step using NIL makes it feasible to integrate this sensing technology into other nanofluidic components for the label-free identification of biomolecules. For example, we are currently developing a chip-based single-molecule exo-sequencing method, termed exonuclease time-of-flight (*X-TOF*).[52, 74-76] This method involves a solid-phase enzymatic reactor coupled to a nano-flight tube that contains dual in-plane nanopores to measure free nucleotides' TOFs. Recently, we reported the use of solid-phase XRN1 reactions to sequentially produce rNMPs (5' → 3' direction).[77] Previous work from our group also demonstrated the identification of labelled rNMPs via their molecular-dependent electrophoretic mobility (*i.e.*, TOF) in thermoplastic nanochannels; we were able to achieve TOF identification accuracies >99%.[52]

3.5 References

1. Branton, D.; Deamer, D. W.; Marziali, A.; Bayley, H.; Benner, S. A.; Butler, T.; Di Ventra, M.; Garaj, S.; Hibbs, A.; Huang, X.; Jovanovich, S. B.; Krstic, P. S.; Lindsay, S.; Ling, X. S.; Mastrangelo, C. H.; Meller, A.; Oliver, J. S.; Pershin, Y. V.; Ramsey, J. M.; Riehn, R.; Soni, G. V.; Tabard-Cossa, V.; Wanunu, M.; Wiggin, M.; Schloss, J. A. The potential and challenges of nanopore sequencing. *Nat. Biotechnol*. 2008, 26, 1146−1153.

2. Wanunu, M.; Sutin, J.; McNally, B.; Chow, A.; Meller, A. DNA translocation governed by interactions with solid-state nanopores. *Biophys. J.* 2008, 95, 4716−4725.

3. Dekker, C. Solid-state nanopores. Nat. Nanotechnol. 2007, 2, 209−215.

4. Venkatesan, B. M.; Bashir, R. Nanopore sensors for nucleic acid analysis. *Nat. Nanotechnol*. 2011, 6, 615−624.

5. Smeets, R. M. M.; Keyser, U. F.; Krapf, D.; Wu, M.-Y.; Dekker, N. H.; Dekker, C. Salt dependence of ion transport and DNA translocation through solid-state nanopores. *Nano Lett*. 2006, 6, 89− 95.

6. Carlsen, A. T.; Zahid, O. K.; Ruzicka, J. A.; Taylor, E. W.; Hall, A. R. Selective detection and quantification of modified DNA with solid-state nanopores. *Nano Lett.* 2014, 14, 5488−5492.

7. Kowalczyk, S. W.; Hall, A. R.; Dekker, C. Detection of local protein structures along DNA using solid-state nanopores. *Nano Lett.* 2010, 10, 324−328.

8. Plesa, C.; Ruitenberg, J. W.; Witteveen, M. J.; Dekker, C. Detection of individual proteins bound along DNA using solid-state nanopores. *Nano Lett.* 2015, 15, 3153−3158.

9. Smeets, R. M. M.; Kowalczyk, S. W.; Hall, A. R.; Dekker, N. H.; Dekker, C. Translocation of RecA-coated double-stranded DNA through solid-state nanopores. *Nano Lett*. 2009, 9, 3089−3095.

10. Hornblower, B.; Coombs, A.; Whitaker, R. D.; Kolomeisky, A.; Picone, S. J.; Meller, A.; Akeson, M. Single-molecule analysis of DNAprotein complexes using nanopores. *Nat. Methods* 2007, 4, 315−317. 11. Tabard-Cossa, V.; Wiggin, M.; Trivedi, D.; Jetha, N. N.; Dwyer, J. R.; Marziali, A. Single-molecule bonds characterized by solid-state nanopore force spectroscopy. *ACS Nano* 2009, 3, 3009−3014.

12. Cherf, G. M.; Lieberman, K. R.; Rashid, H.; Lam, C. E.; Karplus, K.; Akeson, M. Automated forward and reverse ratcheting of DNA in a nanopore at 5-Å precision. *Nat. Biotechnol.* 2012, 30, 344− 348.

13. Ricroch, A. E. Assessment of GE food safety using "-omics" techniques and long-term animal feeding studies. *New Biotechnol.* 2013, 30, 349−354.

14. Song, L.; Hobaugh, M. R.; Shustak, C.; Cheley, S.; Bayley, H.; Gouaux, J. E. Structure of Staphylococcal alpha -Hemolysin, a Heptameric Transmembrane *Pore. Science* 1996, 274, 1859−1865. 15. Faller, M.; Niederweis, M.; Schulz, G. E. The structure of a mycobacterial outer-membrane channel. *Science* 2004, 303, 1189− 1192.

16. Plesa, C.; van Loo, N.; Dekker, C. DNA nanopore translocation in glutamate solutions. Nanoscale 2015, 7, 13605−13609.

17. Storm, A. J.; Chen, J. H.; Ling, X. S.; Zandbergen, H. W.; Dekker, C. Fabrication of solid-state nanopores with single-nanometre precision. *Nat. Mater.* 2003, 2, 537−540.

18. Li, J.; Stein, D.; McMullan, C.; Branton, D.; Aziz, M. J.; Golovchenko, J. A. Ion-beam sculpting at nanometre length scales. *Nature* 2001, 412, 166−169.

19. Wanunu, M.; Meller, A. Chemically modified solid-state nanopores. *Nano Lett.* 2007, 7, 1580−1585. 20. Gierak, J.; Madouri, A.; Biance, A. L.; Bourhis, E.; Patriarche, G.; Ulysse, C.; Lucot, D.; Lafosse, X.; Auvray, L.; Bruchhaus, L. Sub-5 nm FIB direct patterning of nanodevices. *Microelectron. Eng*. 2007, 84, 779−783.

21. Yang, J.; Ferranti, D. C.; Stern, L. A.; Sanford, C. A.; Huang, J.; Ren, Z.; Qin, L.-C.; Hall, A. R. Rapid and precise scanning helium ion microscope milling of solid-state nanopores for biomolecule detection. *Nanotechnology* 2011, 22, 285310.

22. Kwok, H.; Briggs, K.; Tabard-Cossa, V. Nanopore fabrication by controlled dielectric breakdown. *PLoS One* 2014, 9, No. e92880.

23. Stein, D. M.; McMullan, C. J.; Li, J.; Golovchenko, J. A. Feedback-controlled ion beam sculpting apparatus. Rev. Sci. Instrum. 2004, 75, 900−905. (24) Asghar, W.; Ilyas, A.; Billo, J.; Iqbal, S. Shrinking of solid-state nanopores by direct thermal heating. *Nanoscale Res. Lett.* 2011, 6, 372.

25. Schiedt, B.; Auvray, L.; Bacri, L.; Oukhaled, G.; Madouri, A.; Bourhis, E.; Patriarche, G.; Pelta, J.; Jede, R.; Gierak, J. Direct FIB fabrication and integration of “single nanopore devices” for the manipulation of macromolecules. *Microelectron. Eng.* 2010, 87, 1300− 1303.

26. Harms, Z. D.; Haywood, D. G.; Kneller, A. R.; Selzer, L.; Zlotnick, A.; Jacobson, S. C. Single-particle electrophoresis in nanochannels. *Anal. Chem.* 2015, 87, 699−705.

27. Henley, W. H.; Dennis, P. J.; Ramsey, J. M. Fabrication of microfluidic devices containing patterned microwell arrays. *Anal. Chem.* 2012, 84, 1776−1780.

28. Menard, L. D.; Ramsey, J. M. Fabrication of sub-5 nm nanochannels in insulating substrates using focused ion beam milling. *Nano Lett.* 2011, 11, 512−517.

29. Kondylis, P.; Zhou, J.; Harms, Z. D.; Kneller, A. R.; Lee, L. S.; Zlotnick, A.; Jacobson, S. C. Nanofluidic Devices with 8 Pores in Series for Real-Time, Resistive-Pulse Analysis of Hepatitis B Virus Capsid Assembly. *Anal. Chem*. 2017, 89, 4855−4862.

30. Harms, Z. D.; Mogensen, K. B.; Nunes, P. S.; Zhou, K.; Hildenbrand, B. W.; Mitra, I.; Tan, Z.; Zlotnick, A.; Kutter, J. P.; Jacobson, S. C. Nanofluidic Devices with Two Pores in Series for Resistive-Pulse Sensing of Single Virus Capsids. *Anal. Chem.* 2011, 83, 9573−9578.

31. Harms, Z. D.; Selzer, L.; Zlotnick, A.; Jacobson, S. C. Monitoring Assembly of Virus Capsids with Nanofluidic Devices. *ACS Nano* 2015, 9, 9087−9096.

32. Zhou, K.; Li, L.; Tan, Z.; Zlotnick, A.; Jacobson, S. C. Characterization of Hepatitis B Virus Capsids by Resistive-Pulse Sensing. *J. Am. Chem. Soc.* 2011, 133, 1618−1621.

33. Chantiwas, R.; Park, S.; Soper, S. A.; Kim, B. C.; Takayama, S.; Sunkara, V.; Hwang, H.; Cho, Y.-K. Flexible fabrication and applications of polymer nanochannels and nanoslits. *Chem. Soc. Rev.* 2011, 40, 3677−3702.

34. Choi, J.; Lee, C. C.; Park, S. Scalable fabrication of sub-10 nm polymer nanopores for DNA analysis. *Microsyst. Nanoeng.* 2019, 5, 12.

35. O'Neil, C. E.; Taylor, S.; Ratnayake, K.; Pullagurla, S.; Singh, V.; Soper, S. A. Characterization of activated cyclic olefin copolymer: effects of ethylene/norbornene content on the physiochemical properties. *Analyst* 2016, 141, 6521−6532.

36. Jia, Z.; Choi, J.; Park, S. Surface Charge Density-Dependent DNA Capture through Polymer Planar Nanopores. *ACS Appl. Mater. Interfaces* 2018, 10, 40927−40937.

37. Uba, F. I.; Hu, B.; Weerakoon-Ratnayake, K.; Oliver-Calixte, N.; Soper, S. A. High process yield rates of thermoplastic nanofluidic devices using a hybrid thermal assembly technique. *Lab Chip* 2015, 15, 1038−1049.

38. Wang, Y.; Liang, X.; Liang, Y.; Chou, S. Y. Sub-10-nm wide trench, line, and hole fabrication using pressed self-perfection. *Nano Lett.* 2008, 8, 1986−1990.

39. Choi, J.; Farshchian, B.; Kim, J.; Park, S. Fabrication of perforated micro/nanopore membranes via a combination of nanoimprint lithography and pressed self-perfection process for size reduction. *J. Nanosci. Nanotechnol.* 2013, 13, 4129−4133.

40. Siwy, Z.; Trofin, L.; Kohli, P.; Baker, L. A.; Trautmann, C.; Martin, C. R. Protein biosensors based on biofunctionalized conical gold nanotubes. *J. Am. Chem. Soc.* 2005, 127, 5000−5001.

41. Martin, C. R.; Nishizawa, M.; Jirage, K.; Kang, M. Investigations of the transport properties of gold nanotubule membranes. *J. Phys. Chem. B* 2001, 105, 1925−1934.

42. Siwy, Z.; Heins, E.; Harrell, C. C.; Kohli, P.; Martin, C. R. Conical-nanotube ion-current rectifiers: the role of surface charge. *J. Am. Chem. Soc.* 2004, 126, 10850−10851.

43. Harrell, C. C.; Kohli, P.; Siwy, Z.; Martin, C. R. DNA− Nanotube Artificial Ion Channels. *J. Am. Chem. Soc.* 2004, 126, 15646−15647.

44. Maekawa, Y.; Suzuki, Y.; Maeyama, K.; Yonezawa, N.; Yoshida, M. Visualization of chemical modification of pore internal surfaces using fluorescence microscopy. *Chem. Lett*. 2004, 33, 150−151.

45. Maekawa, Y.; Suzuki, Y.; Maeyama, K.; Yonezawa, N.; Yoshida, M. Chemical Modification of the Internal Surfaces of Cylindrical Pores of Submicrometer Size in Poly(ethylene terephthalate). *Langmuir* 2006, 22, 2832−2837.

46. Li, J.; Maekawa, Y.; Yamaki, T.; Yoshida, M. Chemical Modification of a Poly(ethylene terephthalate) Surface by the Selective Alkylation of Acid Salts. *Macromol. Chem. Phys.* 2002, 203, 2470−2474.

47. Pasternak, C. A.; Alder, G. M.; Apel, P. Y.; Bashford, C. L.; Edmonds, D. T.; Korchev, Y. E.; Lev, A. A.; Lowe, G.; Milovanovich, M.; Pitt, C. W.; Rostovtseva, T. K.; Zhitariuk, N. I. Nuclear tracketched filters as model pores for biological membranes. *Radiat. Meas*. 1995, 25, 675−683.

48. Marchand-Brynaert, J.; Deldime, M.; Dupont, I.; Dewez, J.-L.; Schneider, Y.-J. Surface Functionalization of Poly(ethylene terephthalate) Film and Membrane by Controlled Wet Chemistry: Chemical Characterization of Carboxylated Surfaces. *J. Colloid Interface Sci.* 1995, 173, 236−244.

49. Papra, A.; Hicke, H.-G.; Paul, D. Synthesis of peptides onto the surface of poly(ethylene terephthalate) particle track membranes. *J. Appl. Polym. Sci.* 1999, 74, 1669−1674.

50. Uba, F. I.; Pullagurla, S. R.; Sirasunthorn, N.; Wu, J.; Park, S.; Chantiwas, R.; Cho, Y.-K.; Shin, H.; Soper, S. A. Surface charge, electroosmotic flow and DNA extension in chemically modified thermoplastic nanoslits and nanochannels. *Analyst* 2015, 140, 113− 126.

51. Wu, J.; Chantiwas, R.; Amirsadeghi, A.; Soper, S. A.; Park, S. Complete plastic nanofluidic devices for DNA analysis via direct imprinting with polymer stamps. *Lab Chip* 2011, 11, 2984−2989.

52. Amarasekara, C. A.; Rathnayaka, C.; Athapattu, U. S.; Zhang, L.; Choi, J.; Park, S.; Nagel, A. C.; Soper, S. A. Electrokinetic identification of ribonucleotide monophosphates (rNMPs) using thermoplastic nanochannels. *J. Chromatogr.* A 2021, 1638, 461892.

53. Wei, S.; Vaidya, B.; Patel, A. B.; Soper, S. A.; McCarley, R. L. Photochemically Patterned Poly(methyl methacrylate) Surfaces Used in the Fabrication of Microanalytical Devices. *J. Phys. Chem. B* 2005, 109, 16988−16996.

54. Jackson, J. M.; Witek, M. A.; Hupert, M. L.; Brady, C.; Pullagurla, S.; Kamande, J.; Aufforth, R. D.; Tignanelli, C. J.; Torphy, R. J.; Yeh, J. J.; Soper, S. A. UV activation of polymeric high aspect ratio microstructures: ramifications in antibody surface loading for circulating tumor cell selection. *Lab Chip* 2014, 14, 106−117.

55. Amarasekara, C. A.; Athapattu, U. S.; Rathnayaka, C.; Choi, J.; Park, S.; Soper, S. A. Open-tubular nanoelectrochromatography (OT-NEC): gel-free separation of single stranded DNAs (ssDNAs) in thermoplastic nanochannels. *Electrophoresis* 2020, 41, 1627−1640.

56. Uba, F. I.; Pullagurla, S. R.; Sirasunthorn, N.; Wu, J.; Park, S.; Chantiwas, R.; Cho, Y.-K.; Shin, H.; Soper, S. A., Surface charge, electroosmotic flow and DNA extension in chemically modified thermoplastic nanoslits and nanochannels. *Analyst* 2015, 140 (1), 113-126.

57. Jia, Z.; Choi, J.; Park, S. Selection of UV-resins for nanostructured molds for thermal-NIL. *Nanotechnology* 2018, 29, 365302.

58. Miller, A. A.; Lawton, E. J.; Balwit, J. S. Effect of chemical structure of vinyl polymers on crosslinking and degradation by ionizing radiation. *JPoSc* 1954, 14, 503−504.

59. Mahmood Raouf, R.; Abdul Wahab, Z.; Azowa Ibrahim, N.; Abidin Talib, Z.; Chieng, B. Transparent Blend of Poly- (Methylmethacrylate)/Cellulose Acetate Butyrate for the Protection from Ultraviolet. *Polymers* 2016, 8, 128.

60. Dole, M. The Radiation Chemistry of Macromolecules: Volume II; *Elsevier*, 2013; Vol. 2.

61. Jeong, J.-H.; Choi, Y.-S.; Shin, Y.-J.; Lee, J.-J.; Park, K.-T.; Lee, E.-S.; Lee, S.-R. Flow behavior at the embossing stage of nanoimprint lithography. *Fibers Polym*. 2002, 3, 113−119.

62. Heyderman, L. J.; Schift, H.; David, C.; Gobrecht, J.; Schweizer, T. Flow behaviour of thin polymer films used for hot embossing lithography. *Microelectron. Eng*. 2000, 54, 229−245.

63. Fryer, D. S.; Peters, R. D.; Kim, E. J.; Tomaszewski, J. E.; de Pablo, J. J.; Nealey, P. F.; White, C. C.; Wu, W.-l. Dependence of the Glass Transition Temperature of Polymer Films on Interfacial Energy and Thickness. *Macromolecules* 2001, 34, 5627−5634.

64. Kowalczyk, S. W.; Grosberg, A. Y.; Rabin, Y.; Dekker, C. Modeling the conductance and DNA blockade of solid-state nanopores. *Nanotechnology* 2011, 22, 315101.

65. Li, J.; Gershow, M.; Stein, D.; Brandin, E.; Golovchenko, J. A. DNA molecules and configurations in a solid-state nanopore microscope. *Nat. Mater*. 2003, 2, 611−615.

66. Mirabella, F. M., *Internal reflection spectroscopy: theory and applications*. CRC Press: 1992; Vol. 15.

67. Henry, A. C.; Tutt, T. J.; Galloway, M.; Davidson, Y. Y.; McWhorter, C. S.; Soper, S. A.; McCarley, R. L., Surface modification of poly (methyl methacrylate) used in the fabrication of microanalytical devices. *Analytical chemistry* 2000, 72 (21), 5331-5337.

67. Huang, X.; Gordon, M. J.; Zare, R. N. Current-monitoring method for measuring the electroosmotic flow rate in capillary zone electrophoresis. *Anal. Chem*. 1988, 60, 1837−1838.

68. Jackson, J. M.; Witek, M. A.; Hupert, M. L.; Brady, C.; Pullagurla, S.; Kamande, J.; Aufforth, R. D.; Tignanelli, C. J.; Torphy, R. J.; Yeh, J. J., UV activation of polymeric high aspect ratio microstructures: ramifications in antibody surface loading for circulating tumor cell selection. *Lab on a Chip* 2014, 14 (1), 106-117.

69. Vesel, A.; Mozetic, M., Surface modification and ageing of PMMA polymer by oxygen plasma treatment. *Vacuum* 2012, 86 (6), 634-637.

70. Roy, S.; Yue, C.; Lam, Y.; Wang, Z.; Hu, H., Surface analysis, hydrophilic enhancement, ageing behavior and flow in plasma modified cyclic olefin copolymer (COC)-based microfluidic devices. Sensors and Actuators B: *Chemical* 2010, 150 (2), 537-549.

71. Meisenberg, G.; Simmons, W. H., *Principles of medical biochemistry*. Mosby Elsevier: 2006.

72. Huang, X.; Gordon, M. J.; Zare, R. N., Current-monitoring method for measuring the electroosmotic flow rate in capillary zone electrophoresis. *Analytical chemistry* 1988, 60 (17), 1837-1838.

73. Langecker, M.; Pedone, D.; Simmel, F. C.; Rant, U. Electrophoretic Time-of-Flight Measurements of Single DNA Molecules with Two Stacked Nanopores. *Nano Lett.* 2011, 11, 5002−5007.

74. Novak, B. R.; Moldovan, D.; Nikitopoulos, D. E.; Soper, S. A. Distinguishing Single DNA Nucleotides Based on Their Times of Flight Through Nanoslits: A Molecular Dynamics Simulation Study. *J. Phys. Chem.* B 2013, 117, 3271−3279.

75. Oliver-Calixte, N. J.; Uba, F. I.; Battle, K. N.; WeerakoonRatnayake, K. M.; Soper, S. A. Immobilization of lambda exonuclease onto polymer micropillar arrays for the solid-phase digestion of dsDNAs. *Anal. Chem.* 2014, 86, 4447−4454.

76. O'Neil, C.; Amarasekara, C. A.; Weerakoon-Ratnayake, K. M.; Gross, B.; Jia, Z.; Singh, V.; Park, S.; Soper, S. A. Electrokinetic transport properties of deoxynucleotide monophosphates (dNMPs) through thermoplastic nanochannels. *Anal. Chim. Acta* 2018, 1027, 67−75.

77. Athapattu, U. S.; Amarasekara, C. A.; Immel, J. R.; Bloom, S.; Barany, F.; Nagel, A. C.; Soper, S. A. Solid-phase XRN1 reactions for RNA cleavage: application in single-molecule sequencing. *Nucleic Acids Res*. 2021, 49, No. e41.

Chapter 4. Time-of-Flight Identification of Ribonucleotide Monophosphates in Thermoplastic Nanofluidic Devices.

This chapter is based on the following manuscript,

"Time-of-Flight Identification of Ribonucleotide Monophosphates in Thermoplastic Nanofluidic Devices".

Rathnayaka, C.; Athapattu, U. S.; Vietz, C.; Nguyen, H.; Childers, K.; Khurshed, A.; Chibuike, M.; Cho, D.; Choi, J.; Park, S.; Soper, S. A., Time-of-Flight Identification of Ribonucleotide Monophosphates in Thermoplastic Nanofluidic Devices, to be submitted to Journal of ACS Analytical Chemistry.

4.1 Introduction

Nanopore sensing is an emerging technique in which electrokinetically driven single molecules are detected by monitoring changes in the ionic current as they pass through a nanoscale pore.[1] Here we define the effective diameter of a nanopore as <50 nm which are used for single molecule detection. These nanopores are typically fabricated in a thin membrane separating two electrolyte chambers (*i.e.*, out-of-plane nanopores). This approach allows for the analysis of DNA and RNA without amplification or the need for fluorescence labels.[2] Moreover, single molecule detection is possible with nanopore transient current measurements. Due to these significant advantages, nanopore sensors are used in the development of various biological applications such as DNA/RNA sequencing,[3, 4] DNA-protein interactions,[5-8] and measurements of molecular forces.[9, 10] The translocation of DNA and RNA through biological nanopores were first carried out by Kasianowicz *et al.* In that study, they used alpha hemolysin nanopores embedded within a lipid bilayer membrane.[11 ,12-16] Biological nanopores are fixed and uniform pores with dimensions of ~1-5 nm that are easily accessible.[11, 12, 15, 17, 18] However, biological nanopores have prevailing disadvantages such as fragility of pores, difficulties in measuring their -pA range current blockage amplitudes, and dependence on biochemical reagents.[19]

Resistive pulse sensing, which is an improvement of the classical coulter counter[20], is the working principle of stochastic nanopore sensing or sequencing. The classical coulter[20] counter demonstrated sensing of micrometer range particles with a micrometer sized aperture. In the nanopore sensing or sequencing techniques, charged polymers such as DNA/RNA and nucleotides are electrophoretically[21-23] or electrokinetically[24] driven though a nanometer sized aperture (1-10 nm)[16, 24-27] called a nanopore. Electrolyte ions are electrokinetically driven through the nanopore

and are measured by monitoring the current in the electrical circuit such as patch clamp, housed inside a Faraday cage.

When a single molecule enters a nanopore, the molecule will displace a fraction of carrier electrolyte ions and result in a measurable change in the pore resistance, which corresponds to a change in current. The baseline ionic current, I_0 and the current blockade amplitude, ΔI at high ionic concentrations (> 0.1 M), are explained by following mathematical expressions[28]:

$$\Delta I = \sigma V \left(\frac{4L}{\pi d^2} + \frac{1}{d}\right)^{-1} \qquad (1)$$

$$\Delta I = I_0 - \sigma V \left(\frac{4L}{\pi d_{eff}^2} + \frac{1}{d_{eff}}\right)^{-1} \qquad (2)$$

where, σ is the ionic conductivity of the electrolyte, V is the applied voltage, L is the length of the nanopore the thickness of the membrane, d is the diameter of the pore assuming that the nanopore is a simple cylindrical resistor, and d_{eff} is the effective diameter of pore when blocked by analyte of interest. According to the equation 2, ΔI can be increased by using an electrolyte solution with higher ionic strength[29-31] and/or, by reducing the diameter[24, 32] and/or length[33, 34] of the nanopore.

Polymer capture, entry and subsequent translocations are then characterized at the single molecule level by modulations of the individual current blockage events. The transient current is based on the volumetric exclusion of ions from the pore during transport of linearized polymers with current proportional to the cross-sectional area of the linearized polymer relative to the cross-sectional area of the pore. Various parameters, such as the event duration, current amplitude, and unique electrical signature of the current blockages can be used either singly or in combination for single molecule fingerprinting.

Solid-state nanopore based sensors were developed as an alternative to address drawbacks associated with biological nanopores.[28, 35, 36] In 2001 Li et al. first demonstrated solid-state nanopores with tunable pore size, which were fabricated in Si_3N_4 membrane via ion beam sculpting using a low energy ion beam.[37] Furthermore, they showed the detection of 500 bp length double stranded (ds) DNA with a 5-nm pore in Si_3N_4 membrane. Focused ion beam (FIB)[38-40], focused electron beam (FEB), and dielectric breakdown[41, 42] methods are widely employed to fabricate solid-state nanopores with sizes as small as 1.3 nm.[36] Solid-state nanopores have advantages over biological nanopores, such as stability over a wide range of pH and temperature values, tunable pore size, ability of surface modification and potential integration into lab-on-a-chip systems.[1, 43, 44] Several studies have been carried out using solid state nanopores, which can be fabricated in silicon nitride, silicon oxide or metal oxides.[45] Storm *et al.*[46] showed the fast translocation of double stranded DNA (dsDNA) through silicon oxide nanopores.[47, 48] In addition, solid state nanopores were utilized to identify single nucleotides.[49-51] Recently Yang et al.[49] fabricated 1.8 nm diameter silicon nitride nanopores to identify deoxynucleotide triphosphates (dNTPs). Limitations in spatial and temporal resolutions[2, 46, 52, 53] and pore clogging[54, 55] are major challenges to use solid-state nanopores in the sequencing of DNA.

Nanopores are generally categorized according to the pore orientation relative to the substrate: out-of-plane or in-plane.[56] Out-of-plane nanopores are commonly fabricated in a thin membrane, which is perpendicular to the supporting insulating substrate. Most solid-state nanopores are out of plane nanopores which are fabricated on inorganic thin-film membranes as mentioned before.[37, 47, 57, 58] Solid state nanopores, which are fabricated in planar substrates (parallel to the substrate surface) are known as “in-plane” nanopores.[59] Zachary *et al.*[60] has fabricated a silicon nanochannel device with two nanopores (width:50 nm, depth: 50 nm and

length: 40 nm) in series, which were 2 um apart, for resistive pulse sensing of hepatitis B virus capsids. It is mentioned that the width of the nanochannel in between the nanopores was fabricated with a depth of 1 um (20-fold wider than that of nanopores) to ensure the current returns to its baseline value between resistive-pulse events by reducing the electrical resistance adjacent to the nanopores. In-plane nanopores have advantages such as lower sample consumption, enhanced portability and fluid control, improved mass transfer of analytes to the nanopore and ease of detecting translocation optically.[56] Nanoscale components, including in-plane nanopores are fabricated using focused ion beam (FIB) milling.[61] In 2017, Kondylis *et al*.[62] fabricated an in-plane nanopore[60, 63] with 60 nm×70 nm width and depth in silicon. These nanopores were fabricated in series of 2, 4 and 8 for resistive pulse sensing of virus capsids and the measurement precision was observed to be higher with increasing number of nanopores placed in series. It was previously reported that four in-plane nanopores, fabricated in series on a silicon substrate, were used to monitor the disassembly of virus capsids.[63] Tsutsui *et al.*[64] reported a study about identification of nucleobases in DNA oligomers utilizing a nucleotide-sized sensing electrode embedded in in-plane nanopores. The transverse tunnelling current flowing through translocating DNA oligomer was measured for the identification of nucleotides.

Choi *et al.*[25] recently utilized two in-plane nanopores in series that were separated by a 5 μm nanochannel, and were fabricated in a poly(ethylene)glycol diacrylate (PEGDA) substrate using UV-nanoimprint lithography (NIL) for the identification of label-free deoxynucleotide monophosphates (dNMPs) based on their characteristic molecular dependent time-of-flight (TOF). In that study they showed a significant increase in identification accuracies of dNMPs from 55% to 94% with the increase of column length between nanopores from 0.5 to 5 μm. Furthermore, they have achieved improved identification resolution for dNMPs at pH 10.0 compared to that of

pH 8.0 which could possibly be due to a change in the charge state of some of nucleotides at high pH which can change electrophoretic mobilities.[65] They have mentioned that the pore size is reduced during bonding process which was estimated (equivalent pore diameter <10 nm) by measuring the conductance. For the most part, PEGDA's surface is uncharged (surface charge: -20 mC/m^2) which helps facilitate negatively charged nucleotides passing through nanopores.[25] PEGDA is a hydrogel, which makes it difficult to maintain a consistent nanopore size overtime in aqueous media due to swelling.

Polydimethylsiloxane (PDMS) nanopores were previously fabricated to investigate the translocation of λ-DNA molecules.[66, 67] Rapid prototyping was utilized to fabricate PDMS nanopores with 200 nm, 500 nm and 5 µm depth, width and length respectively.[66] Apart from that Fanzio *et al.*[67] utilized a PDMS nanochannel device to investigate the translocation of DNA. In that study, the size of the cross-section area was controlled by simply applying macroscopic compressive strain in order to alter the translocation dynamics of λ-DNA. However, fabrication of sub-10 nm PDMS nanopores which are important in DNA/RNA sequencing, are not yet reported.

Thermoplastics are branched polymers which are capable of softening when heated and hardening when cooled. Thermoplastics[24, 65, 68, 69] are an attractive alternative for the fabrication of in-plane nanopore sensors. In our recent publication, we reported the tailoring thermoplastic in-plane nanopore size by changing the thermal fusion bonding pressure.[24] In that study, the number of events observed with the O_2 plasma modified poly(methyl) methacrylate (PMMA) device was less than anticipated, which could have been due to concentration polarization effects at the nanopore resulting from the surface charge being negative along with the RNA/rNMP molecules. This in turn excludes co-ions from passing through the nanopore. In order to address this issue, the surface charge of the device was eliminated by modifying the device with ethanolamine (ETA).

This led to a significant increase in the observed event frequency compared to the unmodified PMMA nanopore device.

However, there are a lack of studies conducted in thermoplastic nanopores.[24] Though, glass and silicon nitride materials have excellent optical properties and well-defined surface chemistry, they are not an attractive option for clinical applications due to high production costs. For thermoplastics simple surface activation techniques[70] such as O_2 plasma or UV/O_3 can be employed to increase the wettability of the device. The surface modification[24, 71] of thermoplastics is possible due to availability of surface functional groups (-COOH) after activation. The fabrication of glass or silicon nitride nanofluidic devices requires time consuming photo lithography and electron beam lithography or focused ion beam milling for each and every device where thermoplastics require only a one time photolithography and focused ion beam lithography step to produce a silicon master.[71-73] This would significantly reduce the fabrication cost per device when fabricating large number of devices.[73] Moreover, thermoplastic nanofluidic devices can be fabricated using injection molding, which has the capability to produce devices at higher rates (~1000 devices per day per injection molding machine).[74]

In this work, we report on the effect of the geometry of the dual in-plane nanopore sensor on the sampling efficiency of translocation of ribonucleotide monophosphates (rNMPs). We have shown the increase of event frequency with tapered end geometry design nano sensor via both experimentally and COMSOL simulation. Herein we used dual in-plane nano pore device with 5 µm and 10 µm nano flight tube and showed an increase in identification accuracy with increasing the length of nano flight tube. Moreover, scatter plots were generated to identify rNMPs based on two variables while PCA plots are generated to show the correlation of each factor (peak amplitude, TOF, dwell time) in the identification of rNMPs. Furthermore, ablation of PMMA

substrate was demonstrated upon activation with UV light which was not seen with COP nano fluidic devices. In addition, dual in-plane nanopore devices were fabricated in COP using injection molding and have shown the ability to be used in label-free identification of rNMPs based upon molecular dependent TOF.

4.2 Materials and Methods

4.2.1 Materials and reagents

Chemicals and other materials were obtained from the following sources and used without further purification: Silicon (Si) 〈100〉 wafers were purchased from University Wafers (Boston, MA). SU8 2005 photoresist was obtained from MicroChemicals (Germany). SU-8 developer was obtained from Advanced Materials (Westborough, MA). Potassium hydroxide (KOH) pellets were received from Fisher Scientific (Waltham, MA). Isopropyl alcohol (IPA) and hydrofluoric acid (HF) were purchased from Sigma-Aldrich (St. Louis, MO). PMMA was received from ePlastics (San Diego, CA). Nano-Strip solution was purchased from Electronic Chemicals (Houston, TX). Polyethylene terephthalate (PET) sheets with 250 μm thickness were purchased from Goodfellow (Coraopolis, PA). Cyclic olefin copolymer (COC 8007 and COC 5010) was purchased from TOPAS Advanced Polymers (Florence, KY). TPGDA (Tri(propylene glycol) diacrylate, Trimethylolpropane triacrylate (TMPTA), 2,2-Dimethoxy-2-phenylacetophenone (photo initiator), and 2-Hydroxy-2-methylpropiophenone (photo initiator) were purchased from Sigma-Aldrich (St. Louis, MO). Perfluoropolyether (MD 700) was obtained from Solvay (Alorton, IL). NOA72 (Norland Products, Neuchâtel, Switzerland) ATTO 532 was secured from Atto-Tec (Siegen, Germany). Molecular biology grade water was secured from Thermo Fisher (Waltham, MA). COP sheets were obtained from STRATEC SE (Birkenfeld, Germany).

4.2.2 COMSOL simulations

COMSOL simulations were performed using COMSOL Multiphysics 5.5 software prior to fabrication and experiments to confirm the feasibility of the new dual in-plane nanopore sensor design. For all experiments 1 M KCl was used as the electrolyte solution and the used applied voltage was 1V.

4.2.3 Device fabrication and assembly

Nanofluidic devices were fabricated in thermoplastics using a method reported by our group [65]. Si wafers with a 200 nm wet thermal oxide layer were used for fabricating a Si master mold. Microchannels were fabricated in a Si wafer (master) via photo lithography followed by wet-chemical etching. First, SU8 2005 photoresist was spin-coated at 4,000 rpm for 30 s on a Si wafer to obtain a 5 µm thick photoresist layer and then baked at 100°C for 150 s. Photolithography was performed using a designed photomask in a UV exposure station in a class 100/1000 cleanroom. UV exposure was conducted at 140 mJ/cm^2 for 240 s with post-exposure baking at 95°C for 60 s. The wafer was then developed with a SU-8 developer for 120 s, followed by a wash with deionized water. The exposed wet thermal oxide layer was etched using buffered oxide etchant (10:1). Thereafter, photoresist was removed using Nano-Strip solution. Next, the Si in microchannels was etched a 40 wt% KOH solution with IPA (5 % v/v) at 70°C for 120 min to obtain 3.5 µm deep microchannels. The KOH solution was prepared by dissolving KOH pellets in deionized water. After etching, the wafer was removed from the etchant, rinsed in water, and dried with N_2 gas. Prior to FIB milling, the oxide layer was completely removed using buffered oxide etchant solution. Finally, the nanochannels and nanopores were fabricated into the same Si master using

focused-ion beam milling via bit-map mode. The silicon master was then characterized using scanning electron microscopy, SEM (see Figure 4.2A and B).

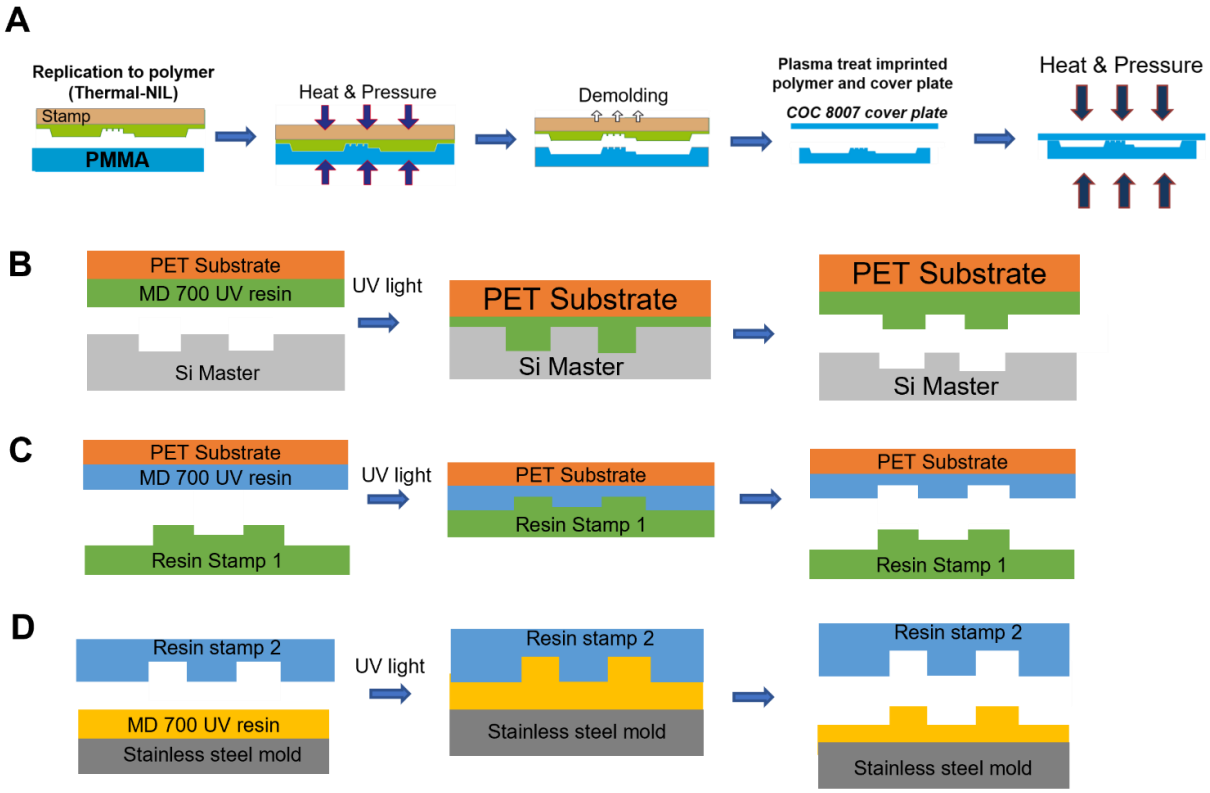

Figure 4.1 Fabrication steps of nanofluidic devices. **(A)** imprinting and bonding using nano imprint lithography. Fabrication of resin stamps via injection molding. Fabrication of **(B)** resin stamp 1, **(C)** resin stamp 2 and **(D)** resin stamp 3 on stainless-steel mold.

Resin stamps were produced from the Si master using a UV curable TPGDA resin. This resin was added onto the Si master and exposed to UV light. PET, which was used as the back plate for the resin stamp, was coated with a NOA72 adhesive. The nanopores separated by the nanocolumn were imprinted into a plastic substrate using a Nanonex 2500 nanoimprint lithography (NIL) machine (Figure 4.1A).

Preliminary tests were conducted to optimize the imprinting temperature, pressure, and time. The imprinting temperature was kept higher than the glass transition temperature (T_g) of the

thermoplastic substrate. PMMA dual in-pane nanopore devices were fabricated using reported imprinted conditions (145°C, 300 psi, and 5 min). Imprinted nanofluidic devices were then characterized using atomic force microscopy, AFM (see Figure 4.3).

It is necessary to seal the nanofluidic device after thermal imprinting using a cover plate. Thermal fusion bonding was used to add the cover plate and complete the fabrication of the nanofluidic devices. Dual in-plane nanopore devices were bonded at 70°C, 170 psi, and 15 min to obtain a nanopore size of ~ 12 nm in depth which was reported previously by our group.

4.2.4 Fabrication of nanofluidic devices via injection molding

First, resin stamp 1 was produced from the Si master using a UV curable MD700 resin that covered the Si master and was exposed to UV light (22 mW/cm^2) for 10 min (Figure 4.1B). PET, which was used as the back plate for the resin stamp, was previously coated with a NOA72 adhesive. Next, resin stamp 2 was fabricated from resin stamp 1 using MD700 resin that covered resin stamp 1 and was exposed to UV light for 10 min (Figure 4.1C). Finally, resin stamp 3 was imprinted on a NOA72 adhesive coated stainless steel metal block using MD700 resin that covered resin stamp 2 and was exposed to UV light for 10 min (Figure 4.1D). The final stamp on the stainless-steel block was inserted into the mud in the injection molding machine and molded with COP pellets (nozzle temperature = 270°C, injection speed = 5 cm^3/ s, dosage volume = 3.9 cm^3, cooling time = 30 s, and mold temperature = 60°C). Fabricated resin stamps and nanofluidic devices were then characterized using atomic force microscopy, AFM (see Figure 4.9).

Nano-injection molded COP nanopore devices were sealed using a COC 8007 cover plate. Both the substrate and cover plate were exposed to UV light (20 mW/ cm^2) for 3 minutes to activate

the surface before thermal fusion bonding. The device was assembled using Nanonex 2500 nanoimprint lithography (NIL) machine. Dual in-plane nanopore devices were bonded at 70°C, 170 psi, and 15 min to obtain a nanopore size of ~ 12 nm in depth which was reported previously by our group.

4.2.5 Atomic force microscopy

To determine the depth of the nanopores with increasing pressure, AFM (SPM HT-9700, Shimadzu Corporation, Kyoto, Japan) analysis was carried out. The probe used for imaging was a Super Sharp Silicon tip (Nanosensors, Switzerland) with a tip radius <2 nm, half cone angle of 10^{o}, aspect ratio 4:1 at 200 nm from the tip apex, and frequency of 300 kHz. A dynamic scanning mode was used for imaging with a scanning frequency of 0.5 Hz. The acquired images were analyzed using SPM Manager v4.76.1 software.

4.2.6 Scanning electron microscopy

SEMs of the nanopore devices were acquired using a FEI VERSA 3D Dual-beam field emission/low vacuum SEM. A 2 nm thin conductive Iridium layer was sputter coated onto the devices using an EMS 150ES sputter coater before SEM imaging. All images were acquired using 5.0 kV accelerating voltage and 8.7 mm working distance. The SEM images of the Si mold masters were collected using a Quanta 3D Dual-beam FEI FIB-SEM and were analyzed using the instrument's software and Image J.

4.2.7 Translocation of rNMPs in dual in-plane nanopore device

Translocation experiments were performed for rNMPs in PMMA dual in-plane nanopore devices bonded at 200 psi for 5 min. Briefly, after methanol/water priming, 1× NEB buffer 3 (100 mM NaCl; 50 mM Tris-HCl; 10 mM $MgCl_2$; 1 mM DTT; pH 7.9 at 25^0C) was introduced into the device. Finally, 10 nM of rNMPs seeded into 1× NEB buffer 3 was introduced into one of the reservoirs of the device. The devices were placed in a Faraday cage and Ag/AgCl electrodes were immersed in the reservoirs of the device. A potential of -2.5 V was applied between two electrodes by serially connecting 1.5 V battery to the Axopatch Digidata 1440B circuit and the data was acquired at a sampling frequency of 250 kHz, a head stage configuration of $\beta = 0.1$, gain = 1, and a low pass filter of 10 kHz. Data were collected for a period of 10 min and Clampfit 11.1 software was used for data acquisition and analysis.

4.2.8 Principal component analysis (PCA)

Principal component analysis (PCA) was performed in R, version 4.1.3, and a biplot was generated using the "factoextra" package. The data were centered and scaled before PCA transformation.

4.2.9 UV/O_3 and O_2 plasma activation of thermoplastics

Nanofluidic devices imprinted on PMMA and COP substrates were exposed to UV light (20 mW/cm^2) for 3, 5, 10 and 15 min. Microscopic images were captured using a Keyence microscope after each exposure. Similarly, nanofluidic devices imprinted on PMMA and COP substrates were exposed to O_2 plasma (50 mW/cm^2) for 3, 5, 10 and 15 min.

4.3 Results and Discussion

4.3.1 Dual in-plane nanopore sensor design optimization

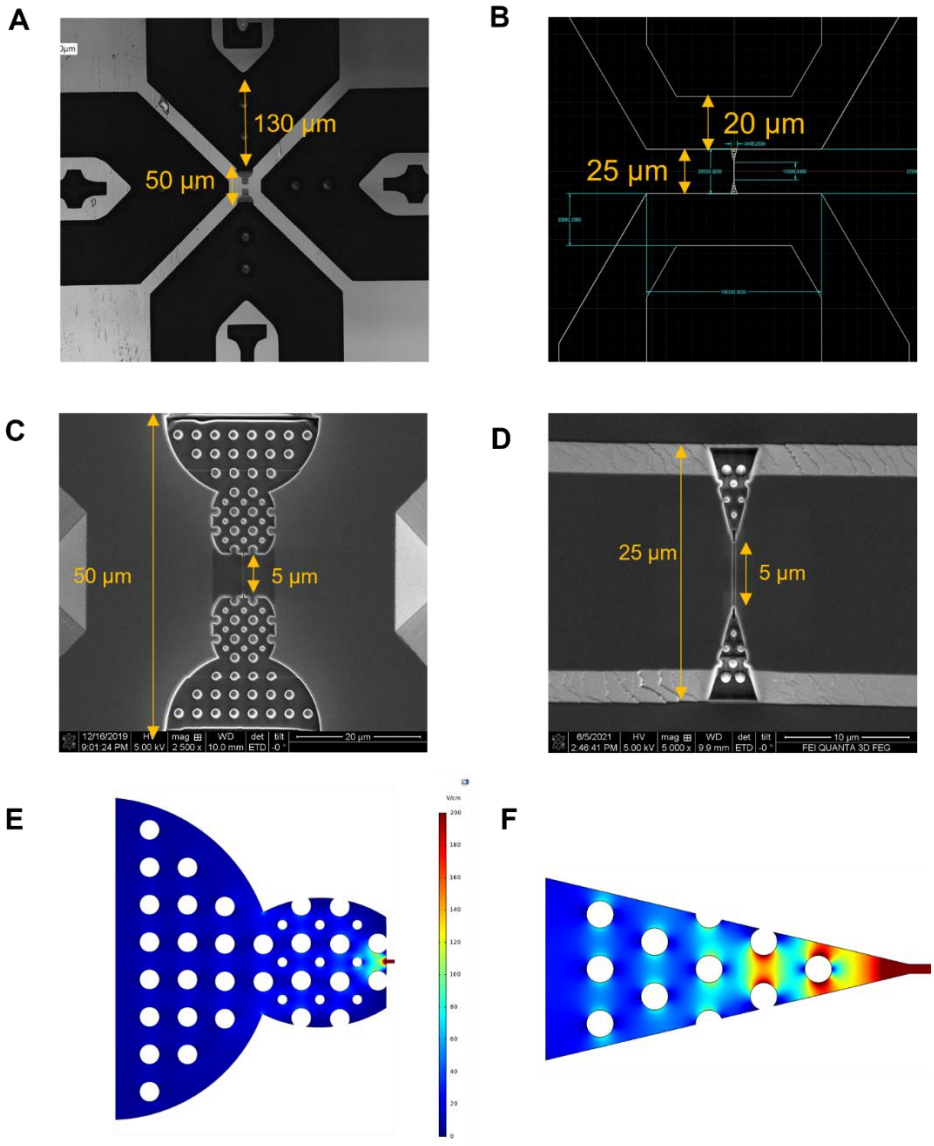

Figure 4.2 Dual in-plane nanopore sensor design. **(A)** Microscopy image of blunt end funnel geometry under 20X objective lens. **(B)** Auto CAD drawing of tapered end funnel geometry. SEM image of Si master of **(C)** blunt end and **(D)** tapered end funnel geometries. COMSOL simulation results for electric field distribution in **(E)** blunt end and **(F)** tapered end funnel geometries. (COMSOL simulations courtesy of Katie Childers).

The observed event frequency for the translocation of rNMPS with the blunt end geometry was low due to poor sampling efficiency of the device. This could have occurred due to two

reasons: i. geometry of the design, and ii. concentration polarization effect at the nanopore which would not facilitate translocation of negatively charged nucleotides through negatively charged nanopore walls. We have overcome the second issue by modifying the thermoplastic surface with ethanolamine. Here, we have modified the design of our dual in-plane nanopore sensor in order to increase the sampling efficiency. In our blunt end geometry, the width and depth of the microchannels near the funnel inlet was 130 μm and 10 μm respectively (Figure 4.2A). However, in the new iteration we reduced the width and depth of microchannels near the funnel inlet to 25 μm and 3 μm respectively (Figure 4.2B). Moreover, the distance between two microchannels was reduced from 50 μm to 25 μm. In addition to changes done in microchannel geometry, the microchannel/funnel interface was changed (Figure 4.2 C and Figure 4.2 D) from blunt end funnel to tapered end funnel.

We also carried out COMSOL simulations to determine the effect of funnel geometry on the electric field distribution. The tapered geometry of the funnel inlets gave the maximum extension of the electric field into the adjoining microchannels, which will increase the sampling efficiency and the event frequency (Figure 4.2E and Figure 4.2F). The expanding of the electric field helps improve the loading efficiency of rNMPs from the access microchannel. In a previous publication, our group showed a higher capture efficiency of lambda DNA molecules with tapered geometry in comparison with blunt-end geometry.[75] Moreover, the expanding of the electric field into the adjoining microchannels facilitates to prevent dielectrophoretic trapping of charged molecules at the microchannel/funnel interface by reducing the electric field gradient.

4.3.2 Device fabrication and assembly

Nanofluidic devices were fabricated in a thermoplastic using a method we have reported, which consists of making microstructures and nanostructures in Si masters followed by producing resin stamps via UV-NIL and production of the final device using thermal NIL.[73, 76] The in-plane nanopores were positioned at either end of a nanochannel, which was 5 μm or 10 μm in length and 50 nm x 50 nm in width and depth. A SEM of the silicon master is shown in Figure 4.2D,[77] and Figure 4.3A and Figure 4.3B shows an AFM of the resin stamp and the imprinted substrate respectively. The average height of the in-plane nanopores on the resin stamp were 30.3 ±2.0 nm (n = 4) and the depth of the nanopores in the imprinted substrate were 29.6 ±1.7 nm (n = 3).

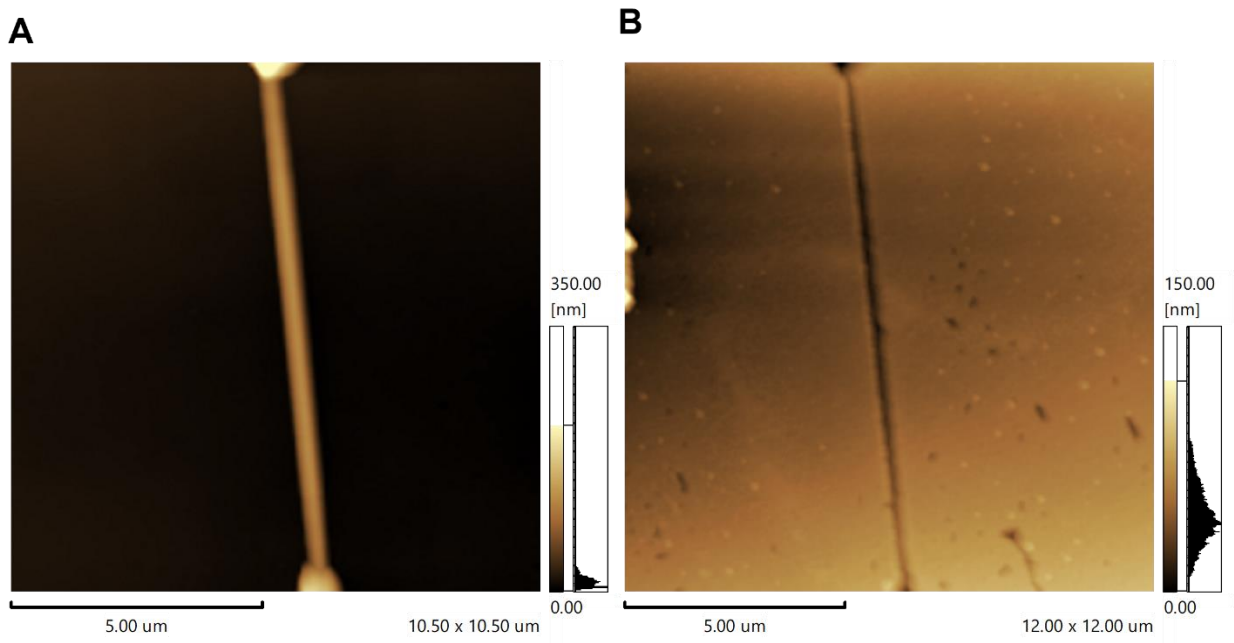

Figure 4.3 Dual in-plane nanopore device. AFM scans of the **(A)** TPGDA resin stamp and **(B)** imprinted PMMA substrate.The two in-plane nanopores are 10 μm apart. Tapping mode AFM scans were acquired at 0.5 Hz scanning frequency using a high aspect ratio tip with a radius < 2 nm.

4.3.4 Translocation of rNMPs in dual in-plane nanopore device

The released rNMPs are then electrokinetically transported through a nanochannel one-at-a-time with the electrophoretic travel time through a nanometer column used to identify the constituent ribonucleotides. In our recent publication, we report the nanoscale electrophoresis of fluorescently labeled rNMPs using 100 nm × 100 nm depth and width thermoplastic nanochannels fabricated via NIL. In this study, we use a label-free approach for the identification of rNMPs using PMMA/COC dual in-plane nanopore device bonded at 170 psi for 15 min, which was used to create a pore size of ~12 nm in depth. As shown in Figure 4.4, the event frequency increased significantly in the tapered end geometry compared to the blunt end geometry nanopore device. Only a single rAMP event (concentration = 100 nM) was observed over a span of 10 s for the device with blunt end geometry while in the case of the tapered end geometry PMMA/COC device, ~24 single-molecule rAMP events (concentration = 100 nM) were observed over a time span of 10 s.

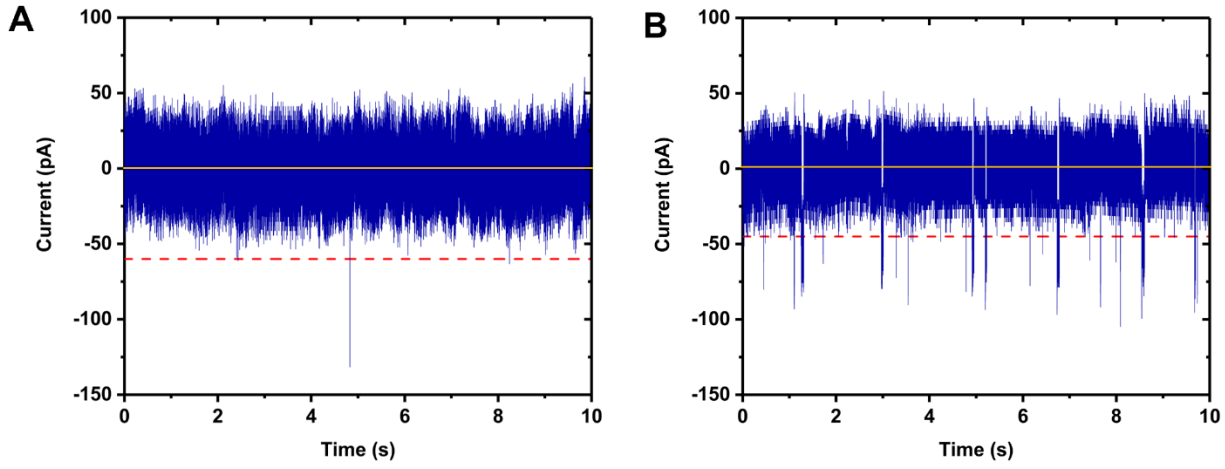

Figure 4.4 Label-free identification of rAMPs using the PMMA/COC dual in-plane nanopore sensor with 5 µm nano flight tube. A 10 s transient current trace obtained with **(A)** blunt end geometry and **(B)** tapered end geometry 1X NEBuffer at pH 7.9 under a driving voltage of 2.5 V.

We used the dual in-plane nanopore devices to measure the time of flight (TOF) of rNMPs following three selection criteria developed by Choi *et al*.[25] The first criterion, was that the peak amplitudes of both peaks in a peak pair should be >3× the RMS noise of the open pore current. The RMS noise of the open pore current of the 170-psi bonded device was found to be 19.5 pA and therefore, only peaks with amplitudes >58.5 pA were considered as true events (Figure 4.5). The second criterion was the minimum TOF, where the TOF for single rNMP molecule should be greater than the dwell time (peak width) of each current peak of the peak pair. The third criterion was that the maximum TOF should be within 1.5 times the TOF calculated from the minimum mobilities of fluorescently labeled rNMPs in nanoscale electrophoresis reported by our group.[68] As was seen in Choi *et al.*[25] and Athapattu *et al.*[24] unpaired peaks were observed in rNMP translocation experiments. Unpaired peaks could be due to several reasons such as the shallow V-shape of in-plane nanopores, which could result in a large variation in the peak amplitude due to molecular translocation at different locations within the nanopore. Thus, some peaks may not produce peak amplitudes above the detection threshold to be selected as paired events and are therefore assigned as the unpaired peaks. Also, there could be molecular overlapping, where entry of a second molecule into the first nanopore occurs before the first molecule has left the second nanopore. Fast translocation of molecules through nanopores is another possible reason for missing peaks which can be eliminated by using a higher bandwidth current amplifier. In addition, there is a possibility of molecules sticking to the nano flight tube wall and causing missing peaks. Langecker *et al.*[78] reported a detection of double-stranded (ds)-DNA using stacked nanopores with diameters of 23 and 28 nm, in which 94% of detected peaks could unambiguously be assigned to the translocating dsDNA.

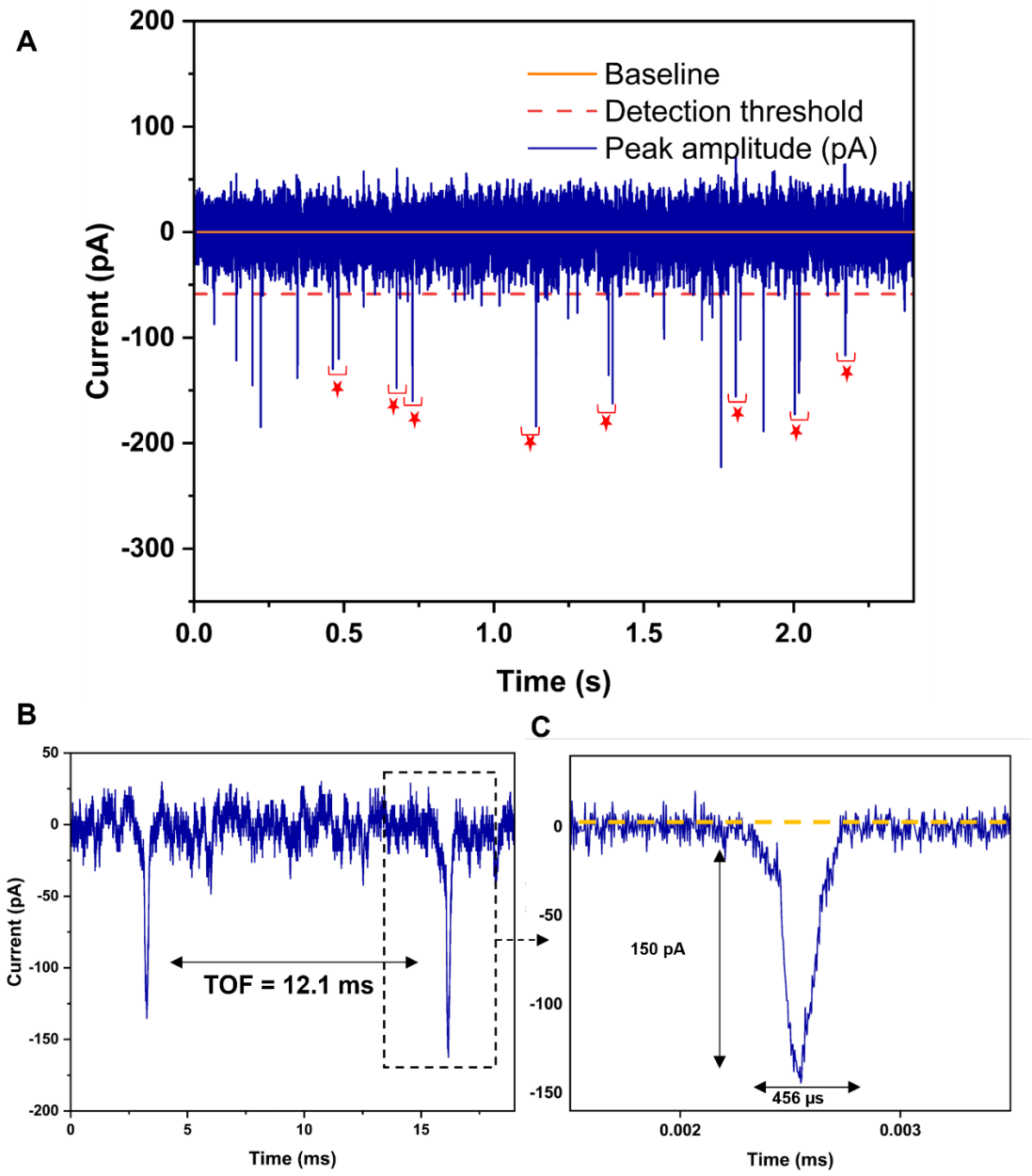

Figure 4.5 Label-free identification of rAMPs using the PMMA/COC dual in-plane nanopore sensor with 10 µm nano flight tube. **(A)** A 2.5 s transient current trace obtained for 10 nM rAMP solution. **(B)** An example peak pair obtained from the peak pair selection criteria. **(C)** An example peak of a peak pair.

Figure 4.6A shows histogram of the rAMP and rCMP that were obtained using dual in-plane nanopore sensor with nano flight tube length of 5 µm under a driving voltage of 2.5 V in 1X NEBuffer 3 (pH 7.9) at room temperature. The average current blockage amplitudes for rAMP and rCMP were 118.6 ±55.2 and 182.9±102.3pA respectively (n=160). The average dwell time of

rAMPs and rCMPs within the nanopores were 780.9±106.7 and 1181.2±251.6 µs respectively (n = 160).

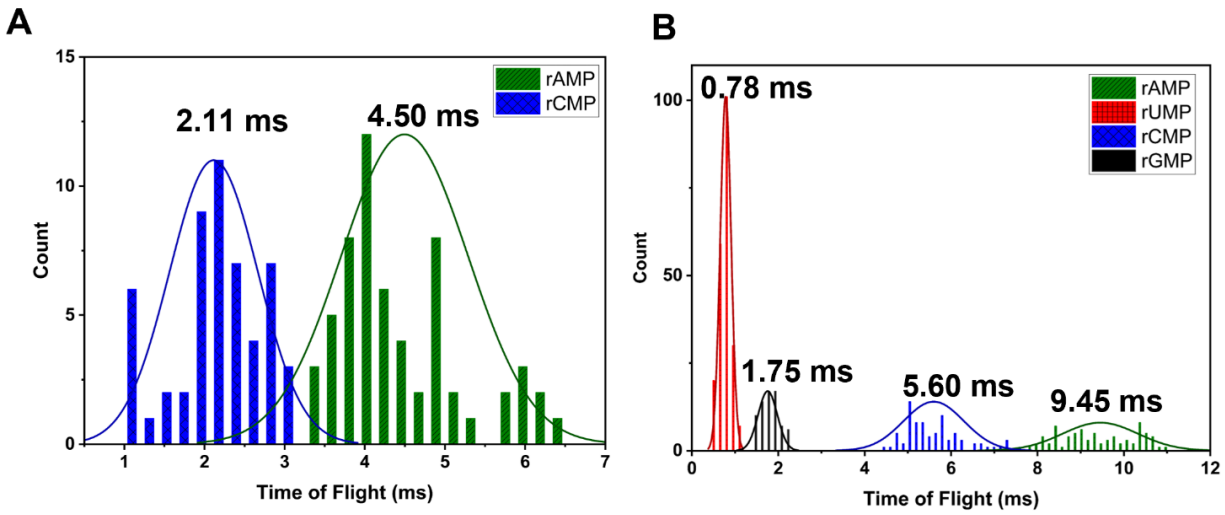

C

Base call accuracy	rAMP	rUMP	rCMP	rGMP
rAMP		>99.999	99.90	>99.999
rUMP	>99.999		>99.999	99.56
rCMP	99.90	>99.999		>99.999
rGMP	>99.999	99.56	>99.999	

Figure 4.6 Label-free identification of rNMPs using the dual in-plane nanopore sensor. Histogram of time of flight of rNMPs acquired using PMMA/COC dual in-plane nanopore sensor with **(A)** 5 and **(B)** 10 µm nano flight tube with 1X NEBuffer at pH 7.9 under a driving voltage of 2.5V. The histograms were fit into Gaussian functions and each bin width represented 0.3 ms. **(C))** Identification accuracies of rNMPs were calculated from Gaussian peak overlap. Identification accuracy = area of non-overlapped/total peak area. The resolution and the identification accuracies were calculated from the data obtained from nano pore device with 10 µm nano flight tube.

The average TOF for rAMP and rCMP were 4.50 ± 0.79 ms and 2.11 ± 0.55 ms respectively (Figure 4.6A). The histograms of rAMP and rCMP were fit to a Gaussian function and the resolution and identification accuracies were calculated, which were 1.47 and 99.84% respectively. Even though, we have carried out translocation of rGMP and rUMP with the dual in-plane nanopore sensor, we could not observe any peak pairs and only observed single peaks. The reason

could be overlapping two peaks due to fast translocation speed may yield a single peak. This problem was overcome by using a dual in-plane nanopore sensor with 10 μm nano flight tube.

Translocation of label-free rNMPs was further investigated using a PMMA/COC dual in-plane nanopore sensor with 10 μm nano flight tube. Figure 4.6B shows the histograms of the four rNMPs using dual in plane nanopores with 10 μm nano flight tube fabricated in PMMA/COC under a driving voltage of 2.5 V with a carrier electrolyte consisting of 1X NEBuffer 3 at pH 7.9. At pH 7.9, all rNMPs have a net charge of −1, and the differences in TOF of rNMPs assumed to arise from the nucleobase. Even though, rNMPs have electrophoretic mobility from cathode to anode, all of them migrated from anode to cathode, towards the direction of electroosmotic flow (EOF). The reported EOF for PMMA/COC devices[69] was 4.2 x 10^{-4} cm^2/Vs.

As observed in Figure 4.6A and 4.6B, with the increase of the length of nano flight tube, the TOF for rAMP and rCMP increased, but the order of TOF values for rAMP and rCMP remained unchanged. Similar observations were reported in Choi *et al.*[25] for the label-free identification of deoxynucleotide monophosphates (TOFs). In that study, they showed the increase of TOF with the increase of the length of nano flight tube in dual in plane nanopore sensor.

The TOF order at electric field strength of 5000 V/cm was rUMP < rGMP < rCMP < rAMP (see Figure 4.6B). The observed TOF order here was similar to the migration time order we observed for nanoscale electrophoresis of the ATTO-532-rNMPs.[68] Moreover, the peak variances of dye-labeled rAMP and rCMP,[68] were larger than those for rUMP and rGMP and similar observations were observed with label-free rNMPs. This indicates that possible wall interactions are higher with rAMP and rCMP compared to that of rUMP and rGMP. Nanoscale electrophoresis occurs by a combined action of electrophoresis and chromatography. Furthermore, rAMP and rCMP showed longer TOF values compared to those with rUMP and rGMP which could be due

to domination of chromatographic effects of rAMP and rCMP over electrophoresis in nanoscale. The histograms of rNMPs were fit to a Gaussian function and the resolution and identification accuracies were calculated (Figure 4.6C and Figure 4.6D). The average resolution between Gaussian fits to the TOF histogram was 3.02 (ranged from 1.31-4.92). Another important parameter for the potential use of mobility matching for the identification of rNMPs is the identification accuracy. The identification accuracy is defined as the amount of overlap between two adjacent Gaussian fits to the histograms of the rNMPs' TOFs. The percent overlap of the Gaussian peaks was calculated using a previously described method.[79] The average identification accuracy for the rNMPs in PMMA/COC devices was >99.91% (see Figure 4.6D). Moreover, the calculated paired peak percentages for rAMP, rUMP, rCMP, and rGMP were 57%, 86%, 72%, and 82% respectively for a transient current time spam of 1000 ms obtained with dual in-plane nanopore device with 10 µm nano flight tube and 10 nM rNMP concentration.

Our goal is to identify label-free rNMPs passing through a TOF column with two in-plane nanopores, after enzymatically cleaving intact RNAs using a processive enzyme. This can be achieved using a processive enzyme, such as exoribonuclease 1 (XRN-1).[80] We have recently shown that this enzyme can be tethered to a solid support and processively clip in the 5' → 3' direction an RNA strand into its constituent ribonucleotide monophosphates (rNMPs) when activated by the cofactor, Mg^{2+}.[81] Therefore, throughout this study we used 1X NEBbuffer 3 at pH 7.9 which is the optimal buffer for XRN-1 enzyme. Moreover, we have shown in our recent publication that the identification of rNMPs was not dependent on the pH of the reaction buffer.

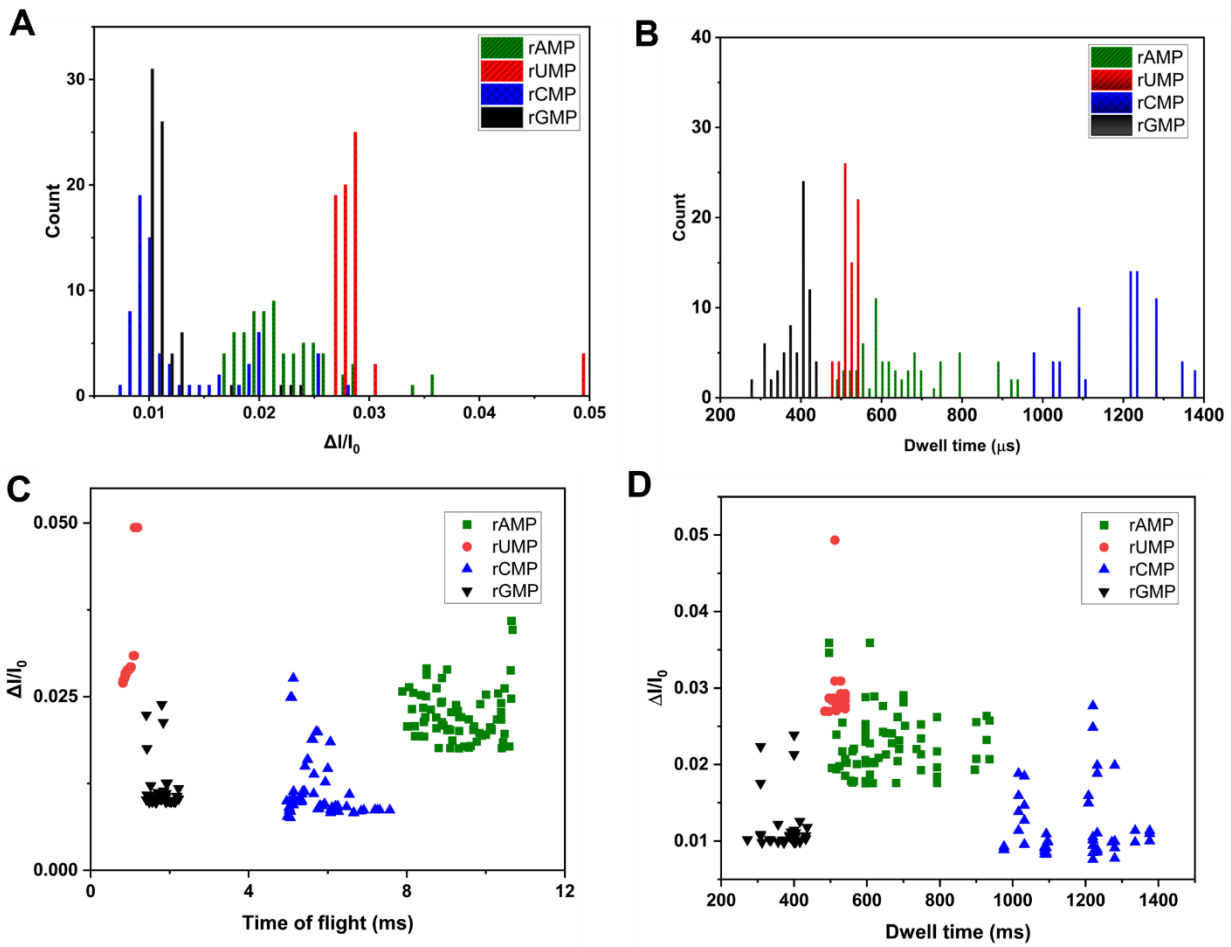

Figure 4.7 Identification of rNMPs using dual in-plane nanopore sensor with 10 µm long nano flight tube. Histograms of (A) peak amplitude and (B) dwell time for rNMPs. Scatter plots of nucleotide translocation events showing (C) peak amplitudes versus TOF, and (D) peak amplitude versus dwell times for rNMPs. Data were acquired with 1X NEBuffer 3 at pH.7.9 under driving voltage of 2.5 V. The rNMP concentration was 10 nM.

Figure 4.7 A and Figure 4.7 B show histograms of peak amplitudes ($\Delta I/I_0$; ΔI = current blockade amplitude and I_0 = open pore current) and dwell times from transient current peaks acquired using the dual in-plane nanopore sensor with a 10 µm long nano flight tube for rAMP, rUMP, rCMP and rGMP. Figure 4.7C and Figure 4.7D show the corresponding scatter plots of $\Delta I/I_0$ versus TOF, and I/I_0 versus dwell times. Even though the peak amplitudes of rNMPs showed a significant overlap with each other, the distribution of dwell time showed a similar trend to TOFs

except for rCMP and rAMP. However, there is an overlap of the distribution of dwell time of each rNMP. Even though the electric field drop through nanopores are higher than that of nano flight tube, the band width of the instrument inhibits ability to accurately measure the peak width. This observation also indicates that the chromatographic feature of rAMP and rCMP over rUMP and rGMP. This could be due to shallow V-shapes and relatively large effective diameters of in-plane nanopores.

Figure 4.8A shows a PCA biplots of peak amplitude and TOF while Figure 4.8B is showing a PCA biplot of dwell time and peak amplitude for translocation of rNMPs through 10 μm long nano flight tube dual in-plane nanopore device. In Figure 4.8A both peak amplitude and the TOF have similar contributions for the identification of rNMPs. The dwell time and peak amplitude also contributed similarly for the identification of rNMPs (Figure 4.8B). Figure 4.8C shows a PCA biplot that factors in the contributions from peak amplitude, dwell time, and TOF towards the identification of rAMP, rCMP, rGMP, and rUMP as they translocate through the 10 μm long nano flight tube. Dwell time has the highest contribution towards PC1. Dwell time and TOF are closely correlated to each other, but they have little to no correlation to peak amplitude. While rAMP and rCMP are highly distinguishable from rGMP and rUMP, there is a small degree of overlap between rAMP and rCMP, and between rGMP and rUMP. The wider spread in rAMP and rCMP groups along PC1 is likely due to higher chromatographic effects contributed by the molecules within those groups. The wider spread along PC2, which has the most contribution from peak amplitude, is likely due to translocation of rNMPs at different locations within the nanopore. The spread along PC2 can be reduced to increase the identification accuracies of rNMPs by reducing the variability in peak amplitude. Smaller pore diameter (∼5 nm) with cylindrical shaped in-plane nanopores can be used to reduce the variability in peak amplitude.

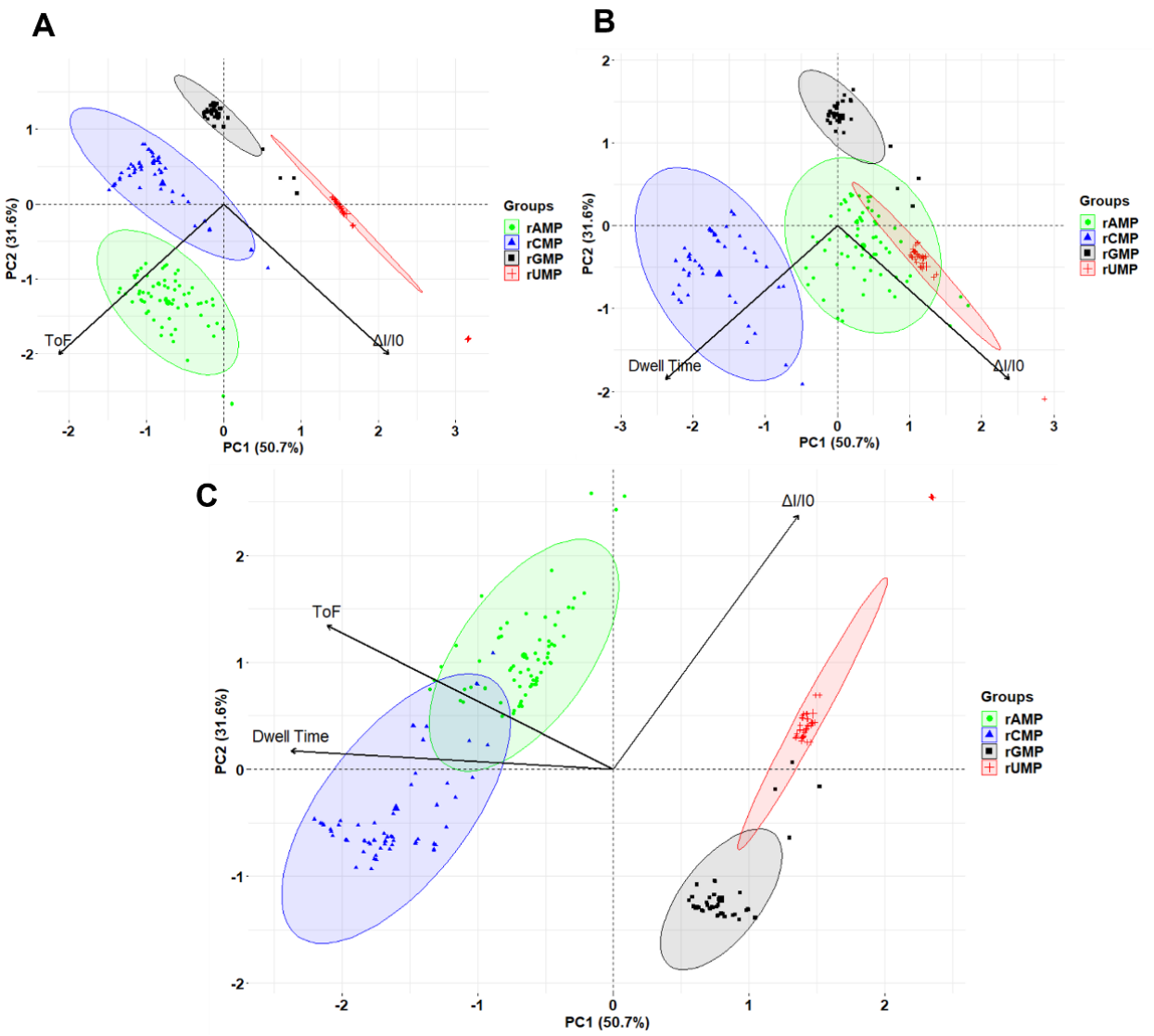

Figure 4.8 Identification of rNMPs using dual in-plane nanopore sensor with 10 µm long nano flight tube. PCA plot of rNMP translocation events for **(A)** peak amplitudes and TOF, and **(B)** peak amplitude and dwell times **(C)** peak amplitude, dwell time, and ToF. Data were acquired with 1X NEBuffer 3 at pH.7.9 under driving voltage of 2.5 V. The rNMP concentration was 10 nM. (PCA plot courtesy of Hanna Nguyen).

4.3.5 Ablation of thermoplastics after activation with UV light

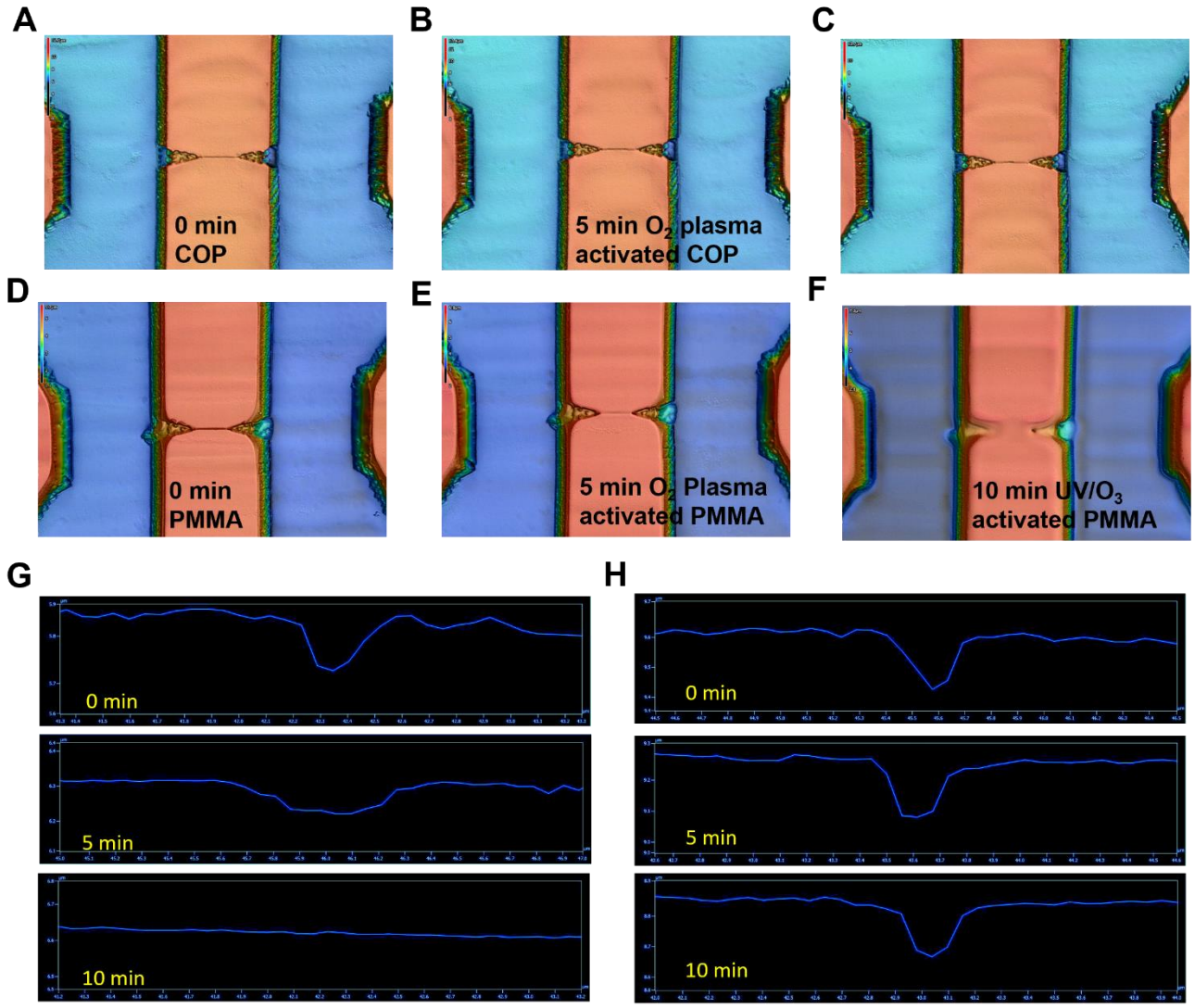

Figure 4.9 Images of dual in-plane nanopore devices captured with 150X objective. **(A)** Unexposed **(B)** 5 min O_2 plasma activated, and **(C)** 10 min UV/O_3 activated COP devices. **(D)** Unexposed **(E)** 5 min O_2 plasma activated, and **(F)** 10 min UV/O_3 activated PMMA devices. Depth profile of **(G)** PMMA and **(F)** COP nanochannel over UV/O3 exposure time. (Data courtesy of Chad M. Vietz).

In the process of assembling thermoplastic nanofluidic devices, the substrate and the cover plate were exposed to UV/O_3 or O_2 plasma before thermal fusion boding using nano imprint lithography. The effect of UV/O_3 exposure dosing time on the ablation of thermoplastics was explored using nanofluidic devices imprinted on PMMA and COP materials. Even though both

PMMA and COP nanofluidic devices did not show signs of ablation after 3 min of exposing to UV light (Data not shown), PMMA nanofluidic structures started to exhibit signs of ablation after 5 min of exposure to UV light. However, COP nanofluidic devices did not show any signs of ablation even after 15 min of UV exposure (Figure 4.9). Depth profile of PMMA and COP nanofluidic devices were obtained after exposing to UV light to show the disappearance of nanochannel with increasing UV/O_3 exposure time. In 1990 Kuper *et al.* showed photofragment pathways of a PMMA model compound under UV excimer laser ablation conditions.[82] In that study, they showed the scission of both side and main chains after photolysis with UV excimer laser light of 248 nm and 193 nm wavelengths. Photolysis of PMMA model compounds yielded a number of primary radical photofragments such as methoxycarbonyl. However, ablation of COP material under UV light is not yet reported. Even though, similar activation was employed with O_2 plasma to generate surface carboxylic acid groups, none of the above thermoplastics showed an ablation of material even after exposing to O_2 plasma for 15 min (Figure 4.9).

4.3.6 Fabrication of nanofluidic devices via injection molding

Fabrication of dual in-plane nanopore devices was attempted via nano-injection molding which can produce parts at higher rate (~1000 chips per day per injection molding machine).[74, 83] The resin stamp 1 which was prepared from the Si master showed positive toned structures and the average pore height obtained from AFM was 32.44 ± 0.52 nm (Figure 4.10A and Figure 4.10C). The resin stamp 2 showed negative toned structures and the average nanopore depth was 34.02 ± 0.32 nm (Figure 4.9B and Figure 4.10D). The nanopore depth and width analysis of resin stamp 3 was not possible as it is fabricated on a stainless-steel block (Figure 4.10E).

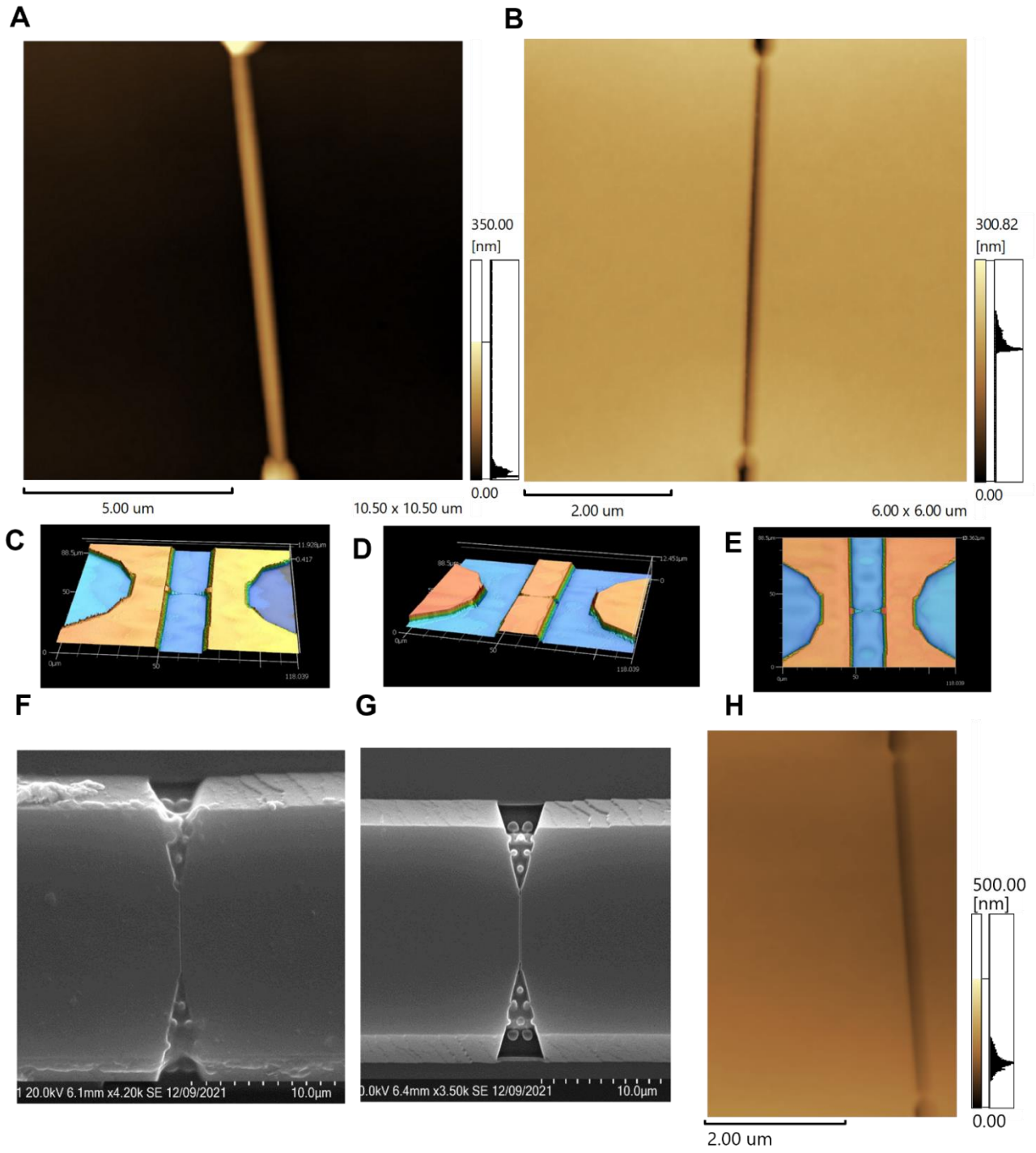

Figure 4.10 Resin stamps of the dual in-plane nanopore device. AFM scans of MD700 resin stamps **(A)** 1 and **(B)** 2. The two in-plane nanopores are 5 µm apart from each other. Tapping mode AFM scans were acquired at 0.5 Hz scanning frequency using a high aspect ratio tip with a radius < 2 nm. Microscope images of MD700 resin stamps **(C)** 1, **(D)** 2, and **(E)** 3. Nano-injection molded dual in-plane nanopore device. SEM images of the injection molded COP devices at molding temperature of **(F)** 70°C and **(G)** 60°C. **(H)** AFM scan of the COP dual in-plane nanopores with nano-flight tube. Tapping mode AFM scans were acquired at 0.5 Hz scanning frequency using a high aspect ratio tip with a radius < 2 nm.

The nanofluidic devices were fabricated via nano-injection molding using COP pellets. A SEM of the fabricated device is shown in Figure 4.10F, and Figure 4.10G and Figure 4.10H show AFMs of the injection molded COP device. The average depth and width of the in-plane nanopores on the COP substrate were 31.00 nm ± 0.24 nm (n=4) and 27.5±1.7 nm (n = 4) respectively.

4.3.7 Translocation of rNMPs in injection molded COP dual in-plane nanopore device with 5 µm nanoflight tube

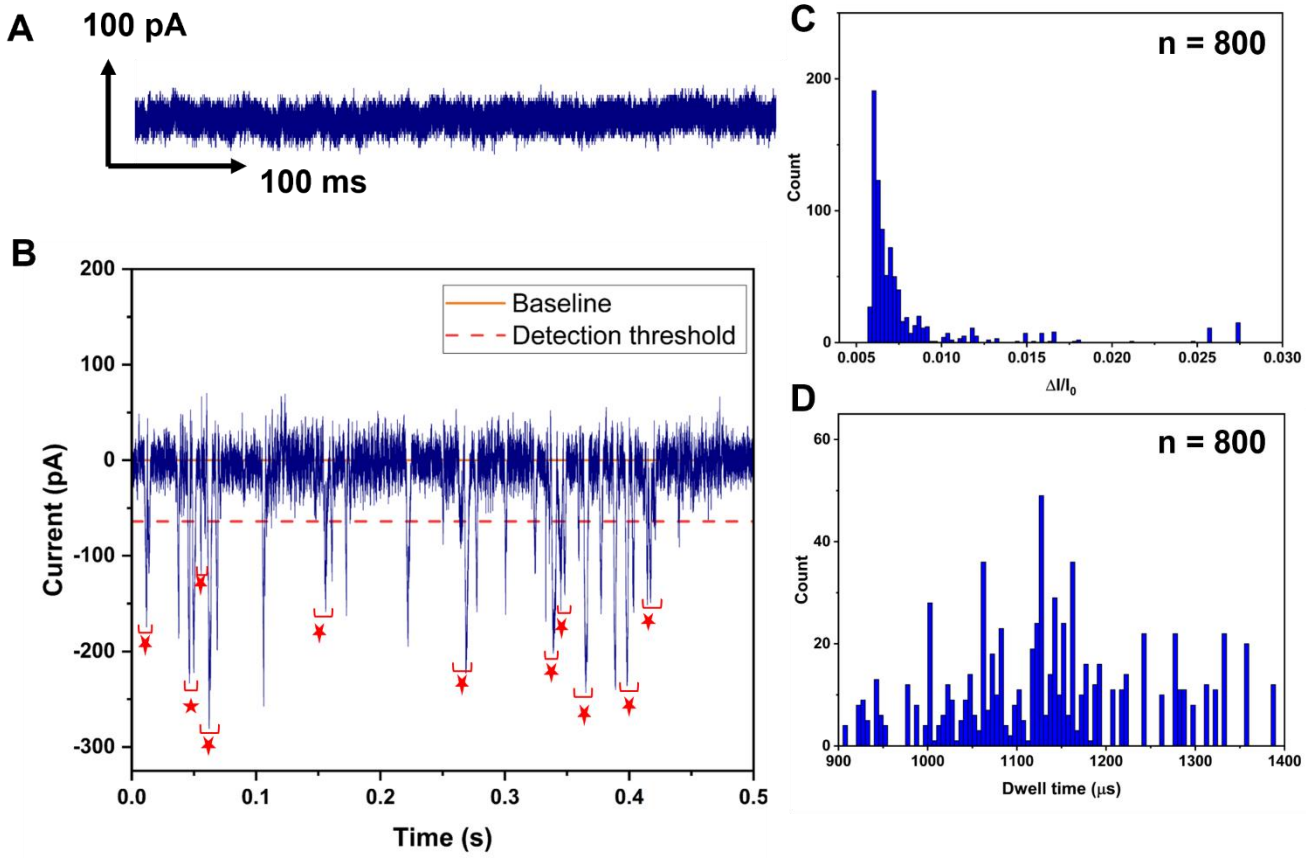

Figure 4.11 Translocation of rNMPs through injection molded dual in-plane nanopore devices assembled at 170 psi bonding pressure. **(A)** A 0.5 s current transient trace of signal amplitudes obtained for a blank. **(B)** A 0.5 s current transient trace of signal amplitudes obtained for rCMPs in 1X NEBuffer 3 at pH.7.9. **(C)** Peak amplitude distribution of rCMP events. **(D)** Dwell time distribution for rCMP events.

After fabrication of a dual in-plane nanopore sensor via injection molding, the device was assembled at 170 psi pressure and 70°C temperature after activating both the substrate and the cover plate with UV light (20 mW/cm^{-2}) for 3 minutes. The assembled COP/COC dual in-plane nanopore devices were primed with 50% v/v methanol followed by introduction of 1× NEBuffer 3. Before introducing the rNMP solution, the current was monitored to establish a baseline (Figure 4.11A). Thereafter, rNMP translocation was carried out using a 100 nM solution of rCMP in 1× NEBuffer 3 at a potential of -2.5 V (Figure 4.11B). The average dwell time of the peaks obtained for single rCMP events was determined to be 925 ±270 µs. The current transient amplitudes of the rCMP events ranged between 467 – 72 pA. We also measured the TOF of the rCMP, which corresponds to the time of the molecule to travel between the two pores. The TOF ranged from 0.38 to 0.81 ms with an average of 0.56 ± 0.10 ms (n = 41). Moreover, the calculated paired peak percentages for rCMP was 67% for a transient current time spam of 1000 ms obtained with dual in-plane nanopore device with 5 µm nano flight tube and 100 nM rCMP concentration. However peak amplitude distribution and the dwell time distribution show a similar trend to PMMA/COC nanofluidic device.

4.4 Conclusion

In this paper we have demonstrated TOF identification of label-free rNMPs using thermoplastic dual in-plane nanopore sensors with 5 µm and 10 µm nano flight tube lengths. Upon increasing nano flight tube length both the resolution and identification accuracy of rNMPs were increased. Moreover, the sampling efficiency of the dual in-plane nano senor with the tapered end geometry increased compared to the blunt end geometry which was also proved with COMSOL simulations. The scatter plots were generated to identify rNMPs based on two variables while PCA plots are

generated to show the correlation of each factor (peak amplitude, TOF, dwell time) in the identification of rNMPs. In addition, we have shown the ability to fabricate dual in-plane nano sensors using injection molding and subsequent use of those devices in label-free identification of rNMPs based on molecular dependent TOF. Moreover, we further investigated the material properties after activation with UV/O_3 and O_2 plasma and it was shown ablation of PMMA occurred after 5 min of exposure to UV light which was not observed with COP even after 15 min UV exposure time.

4.5 References

1. Venkatesan, B. M.; Bashir, R., Nanopore sensors for nucleic acid analysis. *Nature nanotechnology* **2011,** *6* (10), 615-624.

2. Branton, D.; Deamer, D. W.; Marziali, A.; Bayley, H.; Benner, S. A.; Butler, T.; Di Ventra, M.; Garaj, S.; Hibbs, A.; Huang, X., The potential and challenges of nanopore sequencing. *Nanoscience and technology: A collection of reviews from Nature Journals* **2010**, 261-268.

3. Cherf, G. M.; Lieberman, K. R.; Rashid, H.; Lam, C. E.; Karplus, K.; Akeson, M., Automated forward and reverse ratcheting of DNA in a nanopore at 5-Å precision. *Nature biotechnology* **2012,** *30* (4), 344-348.

4. Ricroch, A. E., Assessment of GE food safety using '-omics' techniques and long-term animal feeding studies. *New biotechnology* **2013,** *30* (4), 349-354.

5. Kowalczyk, S. W.; Hall, A. R.; Dekker, C., Detection of local protein structures along DNA using solid-state nanopores. *Nano letters* **2010,** *10* (1), 324-328.

6. Carlsen, A. T.; Zahid, O. K.; Ruzicka, J. A.; Taylor, E. W.; Hall, A. R., Selective detection and quantification of modified DNA with solid-state nanopores. *Nano Letters* **2014,** *14* (10), 5488-5492.

7. Plesa, C.; Ruitenberg, J. W.; Witteveen, M. J.; Dekker, C., Detection of individual proteins bound along DNA using solid-state nanopores. *Nano letters* **2015,** *15* (5), 3153-3158.

8. Smeets, R.; Kowalczyk, S. W.; Hall, A.; Dekker, N.; Dekker, C., Translocation of RecA-coated double-stranded DNA through solid-state nanopores. *Nano letters* **2009,** *9* (9), 3089-3095.

9. Hornblower, B.; Coombs, A.; Whitaker, R. D.; Kolomeisky, A.; Picone, S. J.; Meller, A.; Akeson, M., Single-molecule analysis of DNA-protein complexes using nanopores. *Nature Methods* **2007,** *4* (4), 315-317.

10. Tabard-Cossa, V.; Wiggin, M.; Trivedi, D.; Jetha, N. N.; Dwyer, J. R.; Marziali, A., Single-molecule bonds characterized by solid-state nanopore force spectroscopy. *ACS nano* **2009,** *3* (10), 3009-3014.

11. Kasianowicz, J. J.; Brandin, E.; Branton, D.; Deamer, D. W., Characterization of individual polynucleotide molecules using a membrane channel. *Proceedings of the National Academy of Sciences* **1996,** *93* (24), 13770-13773.

12. Deamer, D.; Akeson, M.; Branton, D., Three decades of nanopore sequencing. *Nature biotechnology* **2016,** *34* (5), 518-524.

13. Nivala, J.; Marks, D. B.; Akeson, M., Unfoldase-mediated protein translocation through an α-hemolysin nanopore. *Nature biotechnology* **2013,** *31* (3), 247-250.

14. Butler, T. Z.; Gundlach, J. H.; Troll, M., Ionic current blockades from DNA and RNA molecules in the α-hemolysin nanopore. *Biophysical journal* **2007,** *93* (9), 3229-3240.

15. Ma, L.; Cockroft, S. L., Biological nanopores for single-molecule biophysics. *ChemBioChem* **2010,** *11* (1), 25-34.

16. Kowalczyk, S. W.; Blosser, T. R.; Dekker, C., Biomimetic nanopores: learning from and about nature. *Trends in biotechnology* **2011,** *29* (12), 607-614.

17. Akeson, M.; Branton, D.; Kasianowicz, J. J.; Brandin, E.; Deamer, D. W., Microsecond time-scale discrimination among polycytidylic acid, polyadenylic acid, and polyuridylic acid as homopolymers or as segments within single RNA molecules. *Biophysical journal* **1999,** *77* (6), 3227-3233.

18. Deamer, D. W.; Branton, D., Characterization of nucleic acids by nanopore analysis. *Accounts of chemical research* **2002,** *35* (10), 817-825.

19. Traversi, F.; Raillon, C.; Benameur, S.; Liu, K.; Khlybov, S.; Tosun, M.; Krasnozhon, D.; Kis, A.; Radenovic, A., Detecting the translocation of DNA through a nanopore using graphene nanoribbons. *Nature nanotechnology* **2013,** *8* (12), 939-945.

20. Coulter, W., Means for counting particles suspended in a fluid. US Patent, 2656508. *United States Patent Office. Patentiert am* **1953,** *20*, 1953.

21. Lv, W.; Liu, S.; Li, X.; Wu, R. a., Spatial blockage of ionic current for electrophoretic translocation of DNA through a graphene nanopore. *Electrophoresis* **2014,** *35* (8), 1144-1151.

22. Ganjizade, A.; Ashrafizadeh, S. N.; Sadeghi, A., Significant alteration in DNA electrophoretic translocation velocity through soft nanopores by ion partitioning. *Analytica Chimica Acta* **2019,** *1080*, 66-74.

23. Van Dorp, S.; Keyser, U. F.; Dekker, N. H.; Dekker, C.; Lemay, S. G., Origin of the electrophoretic force on DNA in solid-state nanopores. *Nature Physics* **2009,** *5* (5), 347-351.

24. Athapattu, U. S.; Rathnayaka, C.; Vaidyanathan, S.; Gamage, S. S.; Choi, J.; Riahipour, R.; Manoharan, A.; Hall, A. R.; Park, S.; Soper, S. A., Tailoring Thermoplastic In-Plane Nanopore Size by Thermal Fusion Bonding for the Analysis of Single Molecules. *ACS sensors* **2021,** *6* (8), 3133-3143.

25. Choi, J.; Jia, Z.; Riahipour, R.; McKinney, C. J.; Amarasekara, C. A.; Weerakoon-Ratnayake, K. M.; Soper, S. A.; Park, S., Label-Free Identification of Single Mononucleotides by Nanoscale Electrophoresis. *Small* **2021,** *17* (42), 2102567.

26. Briggs, K.; Kwok, H.; Tabard-Cossa, V., Automated Fabrication of 2-nm Solid-State Nanopores for Nucleic Acid Analysis. *Small* **2014,** *10* (10), 2077-2086.

27. Venta, K.; Shemer, G.; Puster, M.; Rodriguez-Manzo, J. A.; Balan, A.; Rosenstein, J. K.; Shepard, K.; Drndic, M., Differentiation of short, single-stranded DNA homopolymers in solid-state nanopores. *ACS nano* **2013,** *7* (5), 4629-4636.

28. Lee, K.; Park, K. B.; Kim, H. J.; Yu, J. S.; Chae, H.; Kim, H. M.; Kim, K. B., Recent progress in solid-state nanopores. *Advanced materials* **2018,** *30* (42), 1704680.

29. Fologea, D.; Uplinger, J.; Thomas, B.; McNabb, D. S.; Li, J., Slowing DNA translocation in a solid-state nanopore. *Nano letters* **2005,** *5* (9), 1734-1737.

30. Kowalczyk, S. W.; Wells, D. B.; Aksimentiev, A.; Dekker, C., Slowing down DNA translocation through a nanopore in lithium chloride. *Nano letters* **2012,** *12* (2), 1038-1044.

31. Kowalczyk, S. W.; Grosberg, A. Y.; Rabin, Y.; Dekker, C., Modeling the conductance and DNA blockade of solid-state nanopores. *Nanotechnology* **2011,** *22* (31), 315101.

32. Kim, M. J.; Wanunu, M.; Bell, D. C.; Meller, A., Rapid fabrication of uniformly sized nanopores and nanopore arrays for parallel DNA analysis. *Advanced materials* **2006,** *18* (23), 3149-3153.

33. Wanunu, M.; Dadosh, T.; Ray, V.; Jin, J.; McReynolds, L.; Drndić, M., Rapid electronic detection of probe-specific microRNAs using thin nanopore sensors. *Nature nanotechnology* **2010,** *5* (11), 807-814.

34. Lee, M.-H.; Kumar, A.; Park, K.-B.; Cho, S.-Y.; Kim, H.-M.; Lim, M.-C.; Kim, Y.-R.; Kim, K.-B., A low-noise solid-state nanopore platform based on a highly insulating substrate. *Scientific reports* **2014,** *4* (1), 1-7.

35. Xue, L.; Yamazaki, H.; Ren, R.; Wanunu, M.; Ivanov, A. P.; Edel, J. B., Solid-state nanopore sensors. *Nature Reviews Materials* **2020,** *5* (12), 931-951.

36. Chen, Q.; Liu, Z., Fabrication and applications of solid-state nanopores. *Sensors* **2019,** *19* (8), 1886.

37. Li, J.; Stein, D.; McMullan, C.; Branton, D.; Aziz, M. J.; Golovchenko, J. A., Ion-beam sculpting at nanometre length scales. *Nature* **2001,** *412* (6843), 166-169.

38. Patterson, N.; Adams, D.; Hodges, V.; Vasile, M.; Michael, J.; Kotula, P., Controlled fabrication of nanopores using a direct focused ion beam approach with back face particle detection. *Nanotechnology* **2008,** *19* (23), 235304.

39. Marshall, M. M.; Yang, J.; Hall, A. R., Direct and transmission milling of suspended silicon nitride membranes with a focused helium ion beam. *Scanning* **2012,** *34* (2), 101-106.

40. Hemamouche, A.; Morin, A.; Bourhis, E.; Toury, B.; Tarnaud, E.; Mathé, J.; Guégan, P.; Madouri, A.; Lafosse, X.; Ulysse, C., FIB patterning of dielectric, metallized and graphene membranes: A comparative study. *Microelectronic engineering* **2014,** *121*, 87-91.

41. Goto, Y.; Yanagi, I.; Matsui, K.; Yokoi, T.; Takeda, K.-i., Integrated solid-state nanopore platform for nanopore fabrication via dielectric breakdown, DNA-speed deceleration and noise reduction. *Scientific Reports* **2016,** *6* (1), 1-8.

42. Kwok, H.; Briggs, K.; Tabard-Cossa, V., Nanopore fabrication by controlled dielectric breakdown. *PloS one* **2014,** *9* (3), e92880.

43. ávan Loo, N., DNA nanopore translocation in glutamate solutions. *Nanoscale* **2015,** *7* (32), 13605-13609.

44. Dekker, C., Solid-state nanopores. *Nature nanotechnology* **2007,** *2* (4), 209-215.

45. Branton, D.; Deamer, D. W.; Marziali, A.; Bayley, H.; Benner, S. A.; Butler, T.; Di Ventra, M.; Garaj, S.; Hibbs, A.; Huang, X., The potential and challenges of nanopore sequencing. In *Nanoscience and technology: A collection of reviews from Nature Journals*, World Scientific: 2010; pp 261-268.

46. Storm, A. J.; Storm, C.; Chen, J.; Zandbergen, H.; Joanny, J.-F.; Dekker, C., Fast DNA translocation through a solid-state nanopore. *Nano letters* **2005,** *5* (7), 1193-1197.

47. Dekker, C., Solid-state nanopores. *Nanoscience And Technology: A Collection of Reviews from Nature Journals* **2010**, 60-66.

48. Zhang, H.; Zhao, Q.; Tang, Z.; Liu, S.; Li, Q.; Fan, Z.; Yang, F.; You, L.; Li, X.; Zhang, J., Slowing down DNA translocation through solid-state nanopores by pressure. *Small* **2013,** *9* (24), 4112-4117.

49. Zhang, Z.-Y.; Cui, H.-L.; Huang, D.-P.; Wang, D.-Q., Single nucleotide discrimination with sub-two nanometer monolayer graphene pore. *Sensors and Actuators B: Chemical* **2021,** *349*, 130792.

50. Feng, J.; Liu, K.; Bulushev, R. D.; Khlybov, S.; Dumcenco, D.; Kis, A.; Radenovic, A., Identification of single nucleotides in MoS 2 nanopores. *Nature nanotechnology* **2015,** *10* (12), 1070-1076.

51. Ayub, M.; Hardwick, S. W.; Luisi, B. F.; Bayley, H., Nanopore-based identification of individual nucleotides for direct RNA sequencing. *Nano letters* **2013,** *13* (12), 6144-6150.

52. Li, J.; Gershow, M.; Stein, D.; Brandin, E.; Golovchenko, J. A., DNA molecules and configurations in a solid-state nanopore microscope. *Nature materials* **2003,** *2* (9), 611-615.

53. Chen, Z.; Jiang, Y.; Dunphy, D. R.; Adams, D. P.; Hodges, C.; Liu, N.; Zhang, N.; Xomeritakis, G.; Jin, X.; Aluru, N., DNA translocation through an array of kinked nanopores. *Nature materials* **2010,** *9* (8), 667-675.

54. Schneider, G. F.; Xu, Q.; Hage, S.; Luik, S.; Spoor, J. N.; Malladi, S.; Zandbergen, H.; Dekker, C., Tailoring the hydrophobicity of graphene for its use as nanopores for DNA translocation. *Nature communications* **2013,** *4* (1), 1-7.

55. Tang, Z.; Lu, B.; Zhao, Q.; Wang, J.; Luo, K.; Yu, D., Surface Modification of Solid-State Nanopores for Sticky-Free Translocation of Single-Stranded DNA. *Small* **2014,** *10* (21), 4332-4339.

56. Yang, L.; Yamamoto, T., Quantification of virus particles using nanopore-based resistive-pulse sensing techniques. *Frontiers in microbiology* **2016,** *7*, 1500.

57. Storm, A.; Chen, J.; Ling, X.; Zandbergen, H.; Dekker, C., Fabrication of solid-state nanopores with single-nanometre precision. *Nature materials* **2003,** *2* (8), 537-540.

58. Wanunu, M.; Meller, A., Chemically modified solid-state nanopores. *Nano letters* **2007,** *7* (6), 1580-1585.

59. Harms, Z. D.; Haywood, D. G.; Kneller, A. R.; Selzer, L.; Zlotnick, A.; Jacobson, S. C., Single-particle electrophoresis in nanochannels. *Analytical chemistry* **2015,** *87* (1), 699-705.

60. Harms, Z. D.; Mogensen, K. B.; Nunes, P. S.; Zhou, K.; Hildenbrand, B. W.; Mitra, I.; Tan, Z.; Zlotnick, A.; Kutter, J. P.; Jacobson, S. C., Nanofluidic devices with two pores in series for resistive-pulse sensing of single virus capsids. *Analytical chemistry* **2011,** *83* (24), 9573-9578.

61. Menard, L. D.; Ramsey, J. M., Fabrication of sub-5 nm nanochannels in insulating substrates using focused ion beam milling. *Nano letters* **2011,** *11* (2), 512-517.

62. Kondylis, P.; Zhou, J.; Harms, Z. D.; Kneller, A. R.; Lee, L. S.; Zlotnick, A.; Jacobson, S. C., Nanofluidic devices with 8 pores in series for real-time, resistive-pulse analysis of hepatitis B virus capsid assembly. *Analytical chemistry* **2017,** *89* (9), 4855-4862.

63. Zhou, J.; Zlotnick, A.; Jacobson, S. C., Disassembly of Single Virus Capsids Monitored in Real Time with Multicycle Resistive-Pulse Sensing. *Analytical Chemistry* **2021**.

64. Tsutsui, M.; Rahong, S.; Iizumi, Y.; Okazaki, T.; Taniguchi, M.; Kawai, T., Single-molecule sensing electrode embedded in-plane nanopore. *Scientific reports* **2011,** *1* (1), 1-6.

65. O'Neil, C.; Amarasekara, C. A.; Weerakoon-Ratnayake, K. M.; Gross, B.; Jia, Z.; Singh, V.; Park, S.; Soper, S. A., Electrokinetic transport properties of deoxynucleotide monophosphates (dNMPs) through thermoplastic nanochannels. *Analytica chimica acta* **2018,** *1027*, 67-75.

66. Sen, Y.-H.; Karnik, R., Investigating the translocation of λ-DNA molecules through PDMS nanopores. *Analytical and bioanalytical chemistry* **2009,** *394* (2), 437-446.

67. Fanzio, P.; Manneschi, C.; Angeli, E.; Mussi, V.; Firpo, G.; Ceseracciu, L.; Repetto, L.; Valbusa, U., Modulating DNA translocation by a controlled deformation of a PDMS nanochannel device. *Scientific reports* **2012,** *2* (1), 1-6.

68. Amarasekara, C. A.; Rathnayaka, C.; Athapattu, U. S.; Zhang, L.; Choi, J.; Park, S.; Nagel, A.; Soper, S. A., Electrokinetic Identification of Ribonucleotide Monophosphates (rNMPs) using Thermoplastic Nanochannels. *Journal of Chromatography A* **2021**, 461892.

69. Amarasekara, C. A.; Athapattu, U. S.; Rathnayaka, C.; Choi, J.; Park, S.; Soper, S. A., Open-tubular Nanoelectrochromatography (OT-NEC): Gel-free Separation of Single Stranded DNAs (ssDNAs) in Thermoplastic Nanochannels. *Electrophoresis* **2020,** *41* (18-19).

70. Weerakoon-Ratnayake, K. M.; O'Neil, C. E.; Uba, F. I.; Soper, S. A., Thermoplastic nanofluidic devices for biomedical applications. *Lab on a Chip* **2017,** *17* (3), 362-381.

71. Uba, F. I.; Pullagurla, S. R.; Sirasunthorn, N.; Wu, J.; Park, S.; Chantiwas, R.; Cho, Y.-K.; Shin, H.; Soper, S. A., Surface charge, electroosmotic flow and DNA extension in chemically modified thermoplastic nanoslits and nanochannels. *Analyst* **2015,** *140* (1), 113-126.

72. Duan, C.; Wang, W.; Xie, Q., Fabrication of nanofluidic devices. *Biomicrofluidics* **2013,** *7* (2), 026501.

73. Chantiwas, R.; Park, S.; Soper, S. A.; Kim, B. C.; Takayama, S.; Sunkara, V.; Hwang, H.; Cho, Y.-K., Flexible fabrication and applications of polymer nanochannels and nanoslits. *Chemical Society Reviews* **2011,** *40* (7), 3677-3702.

74. Zhang, N.; Byrne, C. J.; Browne, D. J.; Gilchrist, M. D., Towards nano-injection molding. *Materials today* **2012,** *15* (5), 216-221.

75. Vaidyanathan, S.; Weerakoon-Ratnayake, K. M.; Uba, F. I.; Hu, B.; Kaufman, D.; Choi, J.; Park, S.; Soper, S. A., Thermoplastic nanofluidic devices for identifying Abasic sites in single DNA molecules. *Lab on a Chip* **2021,** *21* (8), 1579-1589.

76. Wu, J.; Chantiwas, R.; Amirsadeghi, A.; Soper, S. A.; Park, S., Complete plastic nanofluidic devices for DNA analysis via direct imprinting with polymer stamps. *Lab on a Chip* **2011,** *11* (17), 2984-2989.

77. Jia, Z.; Choi, J.; Park, S., Selection of UV-resins for nanostructured molds for thermal-NIL. *Nanotechnology* **2018,** *29* (36), 365302.

78. Langecker, M.; Pedone, D.; Simmel, F. C.; Rant, U., Electrophoretic time-of-flight measurements of single DNA molecules with two stacked nanopores. *Nano letters* **2011,** *11* (11), 5002-5007.

79. Bidleman, T. F., The relationship between resolution and percent band overlap. *Journal of Chemical Education* **1979,** *56* (5), 293.

80. Stevens, A., 5′-Exoribonuclease 1: Xrn1. In *Methods in enzymology*, Elsevier: 2001; Vol. 342, pp 251-259.

81. Athapattu, U. S.; Amarasekara, C. A.; Immel, J. R.; Bloom, S.; Barany, F.; Nagel, A. C.; Soper, S. A., Solid-phase XRN1 reactions for RNA cleavage: application in single-molecule sequencing. *Nucleic acids research* **2021,** *49* (7), e41-e41.

82. Küper, S.; Modaressi, S.; Stuke, M., Photofragmentation pathways of a PMMA model compound under UV excimer laser ablation conditions. *Journal of Physical Chemistry* **1990,** *94* (19), 7514-7518.

83. Teillet, J.; Martinez, Q.; Tijunelyte, I.; Chami, B.; Bancaud, A., Characterization and minimization of band broadening in DNA electrohydrodynamic migration for enhanced size separation. *Soft Matter* **2020**.

Chapter 5. Electrokinetic Identification of Peptides using Thermoplastic Nanochannels

This chapter is based on the following manuscript,

"Electrokinetic Identification of Peptides using Thermoplastic Nanochannels".

Rathnayaka, C.; Athapattu, U. S.; and Soper, S. A., Electrokinetic Identification of Peptides using Thermoplastic Nanochannels, to be submitted to Analyst.

5.1 Introduction

Rapid evolution of proteomics research has continued since the sequencing of the human genome was completed[1-3]. The advancements made in the area of proteomics has major implications for elucidating cell functions at the molecular level for understanding disease states and for pharmaceutical and agricultural biotechnology[2]. For example, there are many therapies that are directed against certain type of diseased cells (REF). To understand how to direct these therapies specifically at the target cells, information on the cell surface proteome must be determined. In addition to targeted therapies, many essential cell functions are controlled by membrane proteins[4]. Therefore, it becomes extremely important to not only determine the protein content of the entire proteome, but to look at disease-specific proteomes as well as specific sub-populations of the proteome. This will require the development of new technologies that not only simplify the workflow of protein analysis, but can simultaneously sort biological cells by type to make sure the relevant proteome of target cells are determined. In addition, the analysis method must accommodate the physical properties of a specific class of proteins; membrane proteins typically contain a transmembrane domain that shows hydrophobic characteristics making them difficult to process (REF).

Traditional methods of analyses of the proteome requires the use of gel electrophoresis followed by mass spectrometry[5-8]. The combination of two-dimensional electrophoresis with mass spectrometry is widely used for the identification of complex proteomes[9]. As an alternative, shotgun methods can be used in which proteins are digested into peptides prior to analysis[10-12]. Shotgun proteomics relies on the combination of multidimensional high-pressure liquid chromatography, tandem mass spectrometry, and database-searching[9, 13]. While LC/MS is the gold

standard for proteomics, it is challenged by the detection limit (REF). This has become a pervasive issue to consider because now researchers are interested in single cell proteomics in order to elucidate subtle population cell-to-cell differences that are not seen when performing bulk analysis (REF). To perform single cell proteomics much higher sensitive analytical technologies are required because for a 10 μm mammalian cell, ~1,000 different proteins are found with an average copy number of 100,000 or 1.66×10^{-19} moles [14]. While progress has been made in MS-based single-cell proteomics by optimizing the MS operating parameters,[15] the method is still limited by sample preparation steps, which can result in loss of material and complicated workflows that can hinder clinical implementation[13].

Proteins can be identified either by top-down or bottom-up approaches in mass spectrometric analyses[16-18] (Figure 5.1)[19]. The direct analysis of intact proteins by mass spectrometry is known as top-down proteomics[20, 21]. Top-down proteomics allows for exact mass calculations of proteins. For the bottom-up approach, the proteins are first subjected to proteolytic digestion with an enzyme, such as trypsin in-gel[22], in-solution[23], and solid-phase microreactors[24]. However, protein digestion in-gel and in-solution results in poor digestion efficiency compared to digestion in solid-phase microreactors[25-27]. In 2009, Lee *et al.* developed a solid-phase trypsin microreactor for the digestion of proteins that was coupled with off-line MALDI-TOF MS[28].The generated peptide fragments are identified by mass spectrometric peptide mapping and database searching.

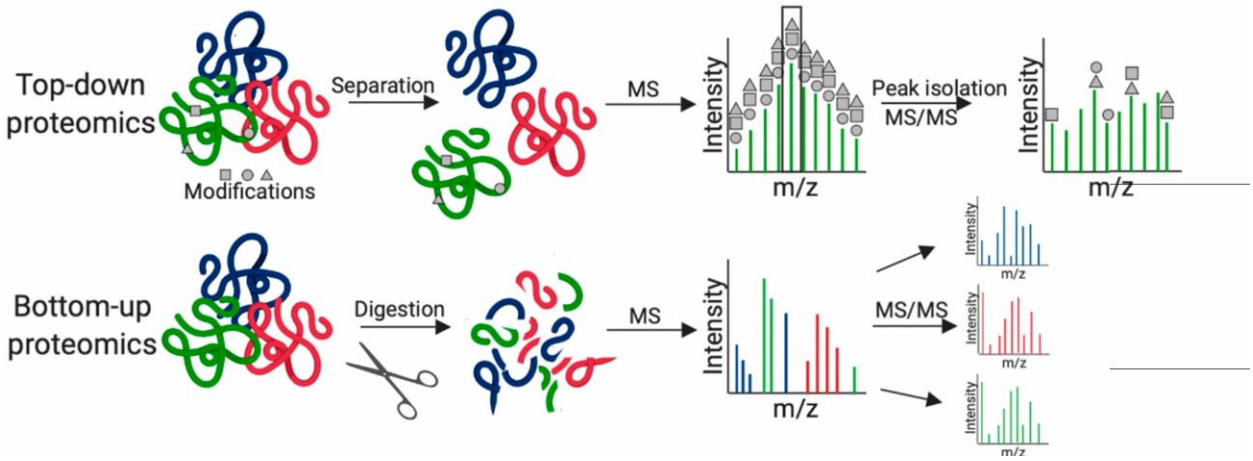

Figure 5.1 Schematic of MS-based proteomic workflows. Reprinted with permission from ref.19.

However, the major challenge of mass spectrometry-based proteomics is the mass limit of detection, which is typically around 1 ng (1.13×10^{-12} moles)[29], especially when attempting to analyze low abundant targets such as those associated with liquid biopsy markers. Liquid biopsy markers include, circulating tumor cells (CTCs), cell free DNA (cfDNA), and extracellular vesicles (EVs)[30]. The development of precision medicine demands the analysis of the molecular content of these markers. This is challenged by the limited number of liquid biopsy markers secured from a clinical sample and/or the low amount of target found in the liquid biopsy marker. For example, the number of CTCs in many clinical samples can range from 1-100/ml of whole blood resulting in the need for doing single-cell proteomics[31].

A fluorescence-based technique for single molecule proteomics was reported in 2018[32]. Swaminathan *et al.*[32] used total internal reflection fluorescence microscopy to monitor decreases in each molecule's fluorescence after Edman degradation. Prior to degradation, cysteine and lysine residues of peptides were selectively labeled and immobilize on a glass surface. While peptides were identified in the zeptomole range, large quantities of peptides were required for the fluorescence labeling. Recently, Kennedy *et al.* used a subnanometre-diameter pore, fabricated in a thin silicon nitride membrane, to detect the primary structure of a denatured protein molecule by measuring current blockade amplitudes[33]. Even though the method was able to identify the presence of a single post-translational modification in a peptide, it was not able to discover the identity of the large number of different post-translational modifications. But high-scale production for clinical implementation is hindered by the sub-nanometer pore fabrication, which

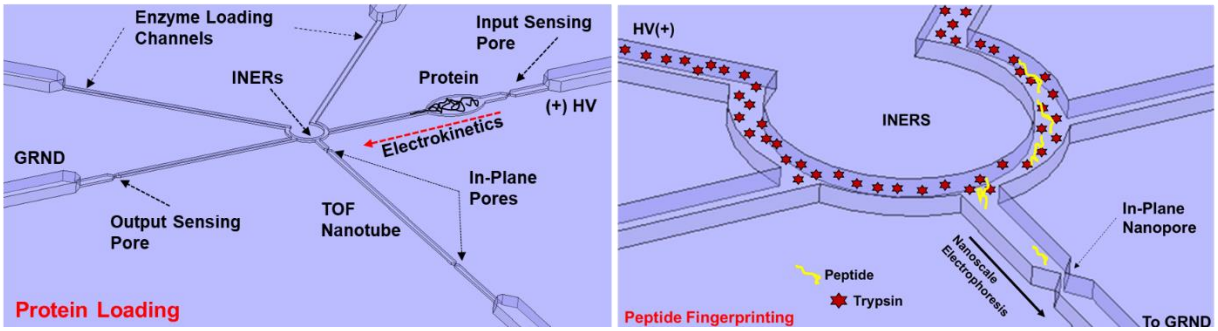

Figure 5.2 Immobilized Nanoscale Enzymatic Reactors (INERs) containing trypsin coupled to 1D nanoscale electrophoresis with dual TOF sensors to identify single protein molecules through their peptide fingerprint. (**a**) Loading of a protein molecule into the INERs. (**b**) INERs digestion of a single protein to produce peptides. Following digestion, the peptides are swept into the nanocolumn electrokinetically for their identification via TOF.

To overcome challenges associated with complicated workflows and modest limits-of-detection, we are developing an innovative single-molecule protein analysis approach that identifies the protein using peptide fingerprinting (Figure 5.2). The strategy consists of proteolytic digestion of intact of a single protein using a solid-phase enzymatic nanoreactor, which consists

of surface immobilized proteolytic enzyme, such as trypsin, to generate peptides from that single protein[34, 35]. Trypsin is a serine protease[36] that catalytically hydrolyzes proteins by predominantly cleaving at the carboxyl side of lysine and arginine residues, except when bound to a C-terminal proline[37]. Lee *et al*. have shown that trypsin can be immobilized to a solid support and digest cytochrome c to generate peptides, but used MALDI MS to determine the peptides comprising the digest[28]. In our case, the enzymatically generated peptides are electrokinetically transported through a nanochannel containing dual in-plane nanopore sensors and are subsequently identified based on their molecular-dependent travel time (*i.e*., Time-of-Flight, TOF). The TOF of the peptide fragments are identified via their molecular-dependent electrophoretic mobility, which is deduced using nanoscale electrophoresis. Therefore, a thorough understanding of the electrophoretic behavior of peptides through nanochannels along with the electrophoretic parameters that determine their molecular-dependent mobilities will allow for high identification accuracy of the peptides generated from a single protein molecule using our single-molecule peptide fingerprinting approach.

Reverse phase chromatography is a common method used for the separation of peptides[38-41]. The separation of peptides has also been achieved using capillary electrophoresis employing glass capillaries[42-45]. Moreover, capillary electrochromatography has been used for the separation of peptides[43, 46-49]. However, these techniques have limitations such as large reagent and sample consumption, difficulty of portability, time consuming sample pre-treatment and analysis steps, and difficulty of process automation.

Nanofluidics is the study of fluid transport in confined dimensions; width and/or depth ≤100 nm. The separation of biomolecules in nano-confined environments is becoming interesting due to nanoscale phenomena, which cannot be observed in the microscale domain. For example,

electrokinetic separations in nanochannels can depend on ζ (zeta potential), thickness of the electric double layer (EDL), ion valence, surface roughness and ion mobility[50-53]. The increased surface area-to-volume ratio in nanochannels can also effect a number of different solute/wall interactions due to reduced diffusional distances, which in turn provide separations based on electrostatic, hydrophilic, hydrophobic, or van der Waals interactions[54].

Unfortunately, there has been only a few reports on nanoscale separations of proteins and peptides[55, 56]. For example, separation of a tryptic digest of a mixture of proteins with diverse masses and isoelectric points was reported, which used nanoscale reversed-phase chromatography with columns incorporating pillar arrays.[56] Moreover Smirinova *et al.*[55] used extended nanochannels fabricated in quartz by electron beam lithography and plasma etching for the separation of amino acids. They used short and long nanochannels and demonstrated the applicability of short channels for the separation of small molecules, such as amino acids, while the longer version was applicable to macromolecules, such as proteins.

Glass/silicon-based devices[57] are widely used for nanofluidic separations. Although glass and quartz-based materials have excellent optical properties and well-defined surface chemistry, it has limitations for use in wide community-based applications due to high production costs. The fabrication of glass or silicon, or quartz nanofluidic devices require time consuming photolithography and electron beam lithography or focused ion beam milling to make each device[58, 59]. Because of this, the transition of nanoscale separations have been slow to realize based primarily on high device cost and low production rates of these devices.

Thermoplastic-based nanofluidic devices can be fabricated via replication techniques, such as imprinting, embossing or even injection molding.[59-61] For example, we have reported using nanoimprint lithography (NIL) to make nanofluidic devices in thermoplastics, which consists of

patterning the device in silicon using a combination of photolithography (microstructures) and ion beam milling (nanostructures) followed by producing resin stamps from the Si master and generating final devices via thermal-NIL in the desired plastic. Using one silicon master, more than 1000 resin stamps can be fabricated and from a single resin stamp more than 25 devices can be produced[62, 63]. This significantly reduces the fabrication cost per device[60]. Moreover, thermoplastic nanofluidic devices can be fabricated using injection molding, which has the capability to produce devices at a high production rate (~1000 devices per day per injection molding machine).[64] In addition, simple activation techniques such as UV/O_3 or O_2 plasma, can be employed to generate surface functional groups that can facilitate wettability[65] and surface modification[61, 63, 66].

However, there has been a limited number of studies reported on nanoscale separations using thermoplastic nanofluidic devices,[62, 63, 67-69] but there have been no reports on using thermoplastic nanofluidic devices for the electrophoresis of peptides. Recently, we showed the TOF identification of ribonucleotide monophosphates (rNMPs) electromigrating through thermoplastic nanochannels made with COC as both the substrate and the cover plate[62]. We were able to fabricate COC nanochannel devices without prior activation of UV/O_3 or O_2 plasma, which allowed control of the electroosmotic flow by post-activating the device.

In this work, we report the electrokinetic properties of peptides traveling through thermoplastic nanochannels. The goal of this work was to perform nanoscale electrophoresis of peptides under different electrophoretic conditions, such as electric field strength, and material effects including modified surfaces. Recently, we reported label-free identification of ribonucleotide monophosphates using ethanolamine modified PMMA/COC nanofluidic devices[63]. While our previous works on nanoscale electrophoresis used PMMA/COC hybrid devices[67, 69] and

COC/COC devices[62], herein we used ethanolamine modified PMMA/COC hybrid devices to perform nanoscale electrophoresis of peptides. We were able to efficiently identify model peptides used in this study via free solution nanoscale electrophoresis through their molecular-dependent mobilities with efficiencies >99.99% in unmodified PMMA/COC and ethanolamine modified PMMA/COC nanofluidic devices.

5.2 Materials and Methods

5.2.1 Materials and reagents

Silicon (Si) 〈100〉 wafers were purchased from University Wafers (Boston, MA). AZ9260 photoresist and AZ 300 MIF developer were obtained from MicroChemicals (Germany). Potassium hydroxide (KOH) pellets were received from Fisher Scientific (Waltham, MA). Isopropyl alcohol (IPA) and hydrofluoric acid (HF) were purchased from Sigma-Aldrich (St. Louis, MO). PMMA was received from ePlastics (San Diego, CA). Polyethylene terephthalate (PET) sheets with 250 μm thickness were purchased from Goodfellow (Coraopolis, PA). Cyclic olefin copolymer (COC 8007 and COC 5010) was purchased from TOPAS Advanced Polymers (Florence, KY). UV curable polyurethane resin was purchased from Chansang Co. ATTO 532 was secured from Atto-Tec (Siegen, Germany) from Sigma-Aldrich (St. Louis, MO). Molecular biology grade water was secured from Thermo Fisher (Waltham, MA).

5.2.2 Conjugation of ATTO 532 to the peptides

Fluorescent labeling of peptides with the reporter ATTO 532 (Figure 5.3) consisted of the following: The peptides were synthesized using a CEM liberty blue microwave peptide synthesizer and standard FMOC chemistry. Solid phase prepared peptides were labeled with Atto532 on a

MiniBlock shaker by reacting the peptide with ATTO 532-NHS in DMF in the presence N,N di-isopropylethylamine. After labeling, the peptides were washed with 4x2 mL of DMF and 4x2 mL of DCM and cleaved using a solution of 92.5:2.5:2.5:2.5 TFA:TIPS:H2O:DODt. The crude peptides were purified using preparative HPLC gradients of water/acetonitrile (90:10 to 0:100 containing 0.1% TFA over 40 min) and lyophilized to obtain a yellow powder. Analytical HPLC traces were acquired using an Agilent 1100 quaternary pump and a Hamilton PRP-1 (polystyrene-divinylbenzene) reverse phase analytical column (7 μm particle size, 4 mm x 25 cm) with UV detection at 254 nm. The eluents were set to 45°C and elution was achieved with gradients of water/acetonitrile (90:10 to 0:100 containing 0.1% TFA) over 20 min. Low-resolution mass spectra (LRMS) were obtained using a Waters Micromass ZQ 4000 instrument with ESI+ ionization or MALDI TOF.

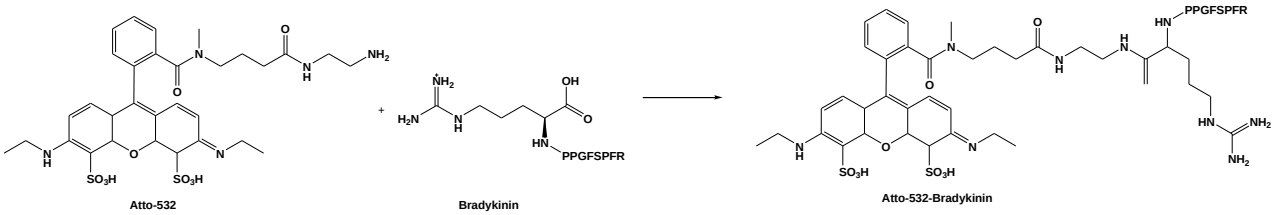

Figure 5.3 General synthetic scheme for the Atto532 labeled peptides.

5.2.3 Fabrication of microchannel thermoplastic devices

The fabrication of microchannel devices was carried out following a method reported by our group [70-75]. Briefly, T-shaped (50 μm depth x 100 μm width x 5 cm long) microfluidic devices were hot embossed into PMMA or COC using a brass master mold, which was fabricated using high precision micromilling. Hot embossed devices were diced with a bandsaw, reservoirs were drilled using a mechanical drill, and they were subsequently cleaned with 15% Micro-90, IPA, and nanopure water. The substrate containing the fluidic network and cover plate (150 μm thick

PMMA sheet) were UV/O_3 modified at 20 mW/cm^2 for 17 min prior to thermal fusion bonding. Microchannel dimensions were measured before and after bonding by rapid laser-scanning optical profilometry (VK-X250, Keyence, IL, USA).

5.2.4 Microscale electrophoresis of the peptides

Free solution electrophoresis was carried out following a method similar to what we previously published [69]. Briefly, a T-shaped microfluidic device was primed with 50% methanol/water and filled with 0.5X TBE buffer at pH 8.3 before carrying out electrophoresis. A positive voltage was applied to the sample reservoir to initiate injection while grounding the sample waste reservoir until the cross channel was completely filled by the peptide(s). The remaining reservoirs were allowed to float during injection. After injection, a positive voltage was applied to the electrophoresis buffer reservoir and the electrophoresis waste reservoir was grounded for the separation. The detector consisted of a laser-induced fluorescence system equipped with a single-photon counting module as we have reported previously [67].

5.2.5 Fabrication of nano-fluidic devices

Nanofluidic devices were fabricated in thermoplastics using a method reported by our group [67]. Si wafers with a 200 nm wet thermal oxide layer were used for fabricating a Si master mold. Microchannels were fabricated in a Si wafer (master) via photolithography followed by wet-chemical etching. First, AZ 9260 photoresist was spin-coated at 3,000 rpm for 60 s on a Si wafer to obtain 5 µm thick photoresist layer, and then baked at 100°C for 150 s. Photolithography was performed using a designed photomask in a UV exposure station inside a class 100/1000 cleanroom. UV exposure was conducted at 72 mJ/cm^2 for 24 s with post-exposure baking at 95°C

for 60 s. Then, the wafer was developed by AZ 300 MIF developer for 120 s followed by washing with deionized water. The exposed wet thermal oxide layer was etched using buffered oxide etchant (10:1). Then, the Si microchannels were etched with a 40 wt% KOH solution with IPA (5 % v/v) at 70°C for 120 min to obtain 3.5 μm deep microchannels. The KOH solution was prepared by dissolving KOH pellets in deionized water. After etching, the wafer was removed from the etchant, rinsed in water, and dried with N_2 gas. Prior to FIB milling, the oxide layer was completely removed using a buffered oxide etchant solution. Then, nanocolumns or other nanostructures (<150 nm dimensions) were fabricated into the same Si master using focused-ion beam milling via a bit-map mode.

Next, resin stamps were produced from the Si master using a UV curable polyurethane (PUA) resin that covered the Si master and was exposed it to UV light. PET, which was used as the back plate for the resin stamp, was coated with a NOA72 adhesive. Nanostructures were imprinted into a plastic substrate using a Nanonex 2500 nanoimprint lithography (NIL) machine.

Preliminary tests were conducted to optimize the imprinting temperature, pressure, and time. The imprinting temperature was kept higher than the glass transition temperature (T_g) of the thermoplastic substrate. For PMMA and COC nanochannel devices, we used the same imprinting conditions reported previously by our group (140°C, 300 psi, and 5 min) [69]. PMMA dual in-pane nanopore devices were fabricated using previously reported imprinting conditions. Imprinted nanofluidic devices were then characterized using SEM and atomic force microscopy, AFM (Figure 5.4).

To enclose the nanofluidic device using a cover plate, thermal fusion bonding was used. For PMMA and COC nanochannel devices, we used the same bonding conditions reported previously by our group (70°C, 110 psi, and 15 min). Dual in-plane nanopore devices were bonded

at 70°C, 170 psi, and 15 min to obtain a nanopore size of ~12 nm in depth, which was reported previously by our group.

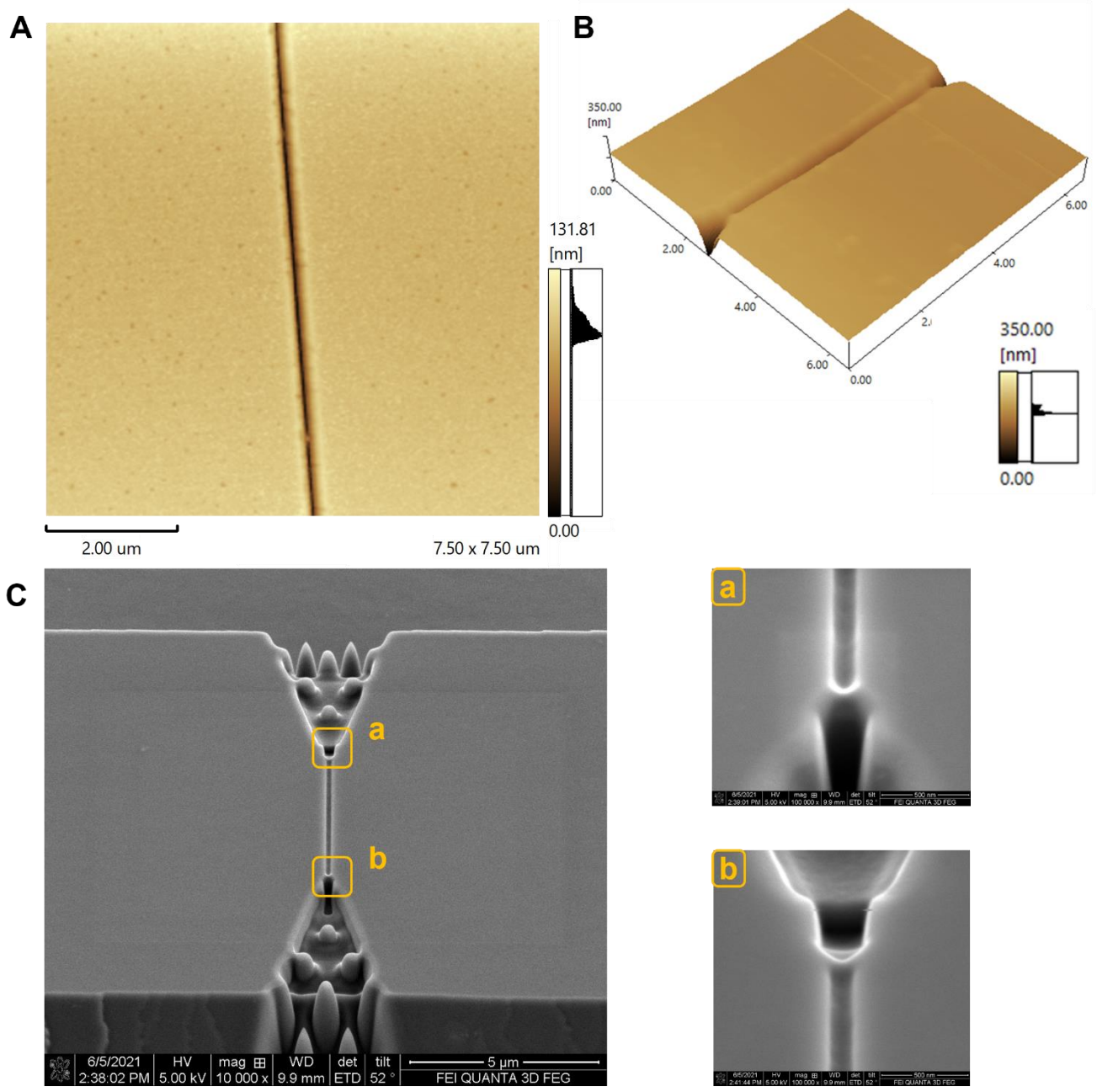

Figure 5.4(A) SEM of the dual in-plane pores in the Si master. AFM scans of the (**B)** nanochannel, **(C)** dual in-plane nanopores which are 5 µm apart from each other, fabricated on PMMA. The two in-plane nanopores. Tapping mode AFM scans were acquired at 0.5 Hz scanning frequency using a high aspect ratio tip with a radius < 2 nm

5.2.6 Detection system for nanoscale electrokinetics.

The electrophoretic transport of ATTO 532 labeled peptides through the thermoplastic nanocolumns was monitored using a fluorescence imaging system we have reported previously[67, 69].

5.2.7 Electrokinetic identification of peptides in O_2 plasma activated nanochannels.

COC/COC nanochannel devices were UV/O_3 activated for 15 min using a home-built UV chamber (22 mW/cm^2). PMMA/COC or COC/COC nanochannel devices were primed with a 50% methanol/water for 5 min. Using a vacuum pump, the methanol/water solution was removed from the nanofluidic device. After that, it was filled with 0.5X TBE buffer (pH 8.3) and allowed to equilibrate for 10 min. ATTO 532 labeled peptides (100 nM) were prepared in 0.5X TBE buffer. Next, the peptide solution was added to one of the reservoirs connecting to microchannels by replacing the carrier electrolyte. Afterward, the microchannel was filled with peptide solution by applying a vacuum through the opposite side's reservoir of the same microchannel. Thereafter, the same volume of carrier electrolyte was added to all other reservoirs. Finally, the dye-labeled peptides were injected into the nanochannels by applying a square wave voltage (2 – 20 V_{pp}) for a period of 10 s (0.1 Hz frequency) using an ATTEN ATF200B function waveform generator, allowing multiple injections. Events were recorded for 6,000 frames.

5.2.8 Surface modification of nanochannels with ethanolamine.

After fabrication and assembly of the dual in-plane nanopore devices, to suppress the surface charge and EOF of O_2 plasma activated PMMA surfaces, the devices were modified with ethanolamine following a similar method reported by our group. Briefly, assembled PMMA

devices were flooded with a buffer solution (100 μL, 0.1 M MES, pH 4.7) containing 20 mg EDC, 2 mg NHS, and 50 mM ethanolamine and kept for 30 min at room temperature. After the reaction, the device was washed extensively with ultrapure water.

5.2.9 Electrokinetic identification of peptides in ethanolamine modified nanochannels.

After ethanolamine modification, the device was filled with 0.5X TBE buffer (pH 8.3) and allowed to equilibrate for 10 min. ATTO 532 labeled peptides (100 nM) were prepared in 0.5X TBE buffer. Next, the peptide solution was added to one of the reservoirs connecting to microchannels by replacing the carrier electrolyte. Then, the microchannel was filled with the peptide solution by applying a vacuum through the opposite side reservoir of the same microchannel. Thereafter, the same volume of carrier electrolyte was added to all other reservoirs. Finally, the dye-labeled peptides were injected into the nanochannels by applying a square wave voltage (2 -20 V_{pp}) for a period of 10 s (0.1 Hz frequency) using an ATTEN ATF200B function waveform generator, allowing multiple injection events. Events were recorded for 6,000 frames.

5.2.10 Data analysis

The nanochannel electrophoresis data were analyzed utilizing a previously reported method by our group [67, 69]. Briefly, the collected videos from the imaging microscope's EMCCD camera were imported into Image J and two detection windows of 1 μm^2 were situated at the nanochannel entrance and exit. The fluorescence intensity over time recorded from these detection windows were exported into Origin 8.5. Then, the first derivative of each data set was taken to produce two peaks indicating the time that fluorescently labeled peptides reached the entrance and exit sections of the nanochannel. The time difference was taken as the migration time of the peptides to travel

a fixed distance and the apparent velocity was calculated. The apparent mobility of each peptide was generated by normalizing the apparent velocity with respect to the electric field strength.

5.2.11 Time of flight identification of label-free peptides in PMMA/COC dual in-plane nanopores.

Translocation experiments were performed for C-natriuretic peptide in PMMA dual in-plane nanopore devices thermal fusion bonded at 170 psi. PMMA devices were primed with 50% methanol/water mixture for 5 min. Using a vacuum pump, the methanol/water solution was removed from the nanofluidic device. After that, it was filled with 0.5X TBE buffer (pH 8.3) and allowed to equilibrate for 10 min. The devices were placed in a Faraday cage and Ag/AgCl electrodes were immersed in the reservoirs of the device. A potential of -2.5 V was applied between two electrodes and the data was acquired using the Axopatch Digidata 1440B and analyzed using Clampfit 11.1.

5.3 Results and Discussion

5.3.1 Microchip electrophoretic separation of peptides.

We carried out microchip electrophoresis of peptides firstly to understand the effects of scaling on peptide electrophoresis by comparing the microchip results with our nanoscale electrophoresis results. For the microchip electrophoresis, we used a T-shaped microchip fabricated in PMMA/COC or COC/COC (depth = 50 µm; width = 100 µm total channel length = 5 cm), where the first material listed is the substrate containing the microchannels and the second material is the cover plate. The free solution electrophoretic separation of peptides was performed in PMMA/COC microfluidic chips at three different field strengths (200, 100, and 20 V/cm) in 0.5X

TBE buffer (pH 8.3). During the electrophoresis, all peptides migrated in the same direction as the electroosmotic flow for all field strengths investigated. As shown in Figure 5.5A-B, at a field strength of 200 V/cm and 100 V/cm, all four peptides co-migrated. If the separation of peptides is purely electrophoresis, peptides would migrate in the order of charge-to-size ratio as given in Table 1. At a field strength of 20 V/cm, we could separate C-natriuretic peptide from C-peptide fragment 3-33, but could not separate Bradykinin from Met-enkephalin (Figure 5.5C). All peptides migrated according to their charge-to-size ratio. The apparent mobilities of the peptides were calculated using equation (1) and are presented in Figure 5.5D. In this case, t_m is the migration time of each peptide, l is the distance from the injection point to the detector (4.0 cm), and E is the electric field strength (20 V/ cm). The apparent mobility order of the peptides was C-peptide fragment 3-33 < Bradykinin & Met-enkephalin < C-natriuretic peptide.

$$\mu_{app} = \frac{l}{t_m\ E} \qquad (1)$$

In 2009, Lee and coworkers developed a PMMA microfluidic chip with an immobilized bioreactor for protein analysis and mentioned that the extent of sequence coverage (the number of amino acids in a specific protein sequence that can be found in the peptides sequenced from MS/MS) decreased upon increasing applied field strength which in turn decreased the protein identification probability[28]. At low electric field strengths, increased time for lateral diffusion facilitates efficient digestion of proteins by microreactor. In our study, we observed an increase in separation resolution with a decrease in applied electric field strength. By decreasing the field strength, peptides would have increased time for lateral diffusion while migrating through the channel with the electroosmotic flow. Our data seems to indicate that the separation modality is based on an electrochromatographic mode because lower field strengths provide opportunities for

increasing the number of potential surface interactions (hydrophilic, hydrophobic, electrostatic, etc.) for a particular molecule, leading to an increased separation resolution of peptides.

Table 5.1 The peptide sequence, pI value, charge of individual peptides before and after labeling with ATTO-532, and the charge/size ratio of ATTO-532 peptides in 0.5X TBE buffer at pH 8.3.

Peptide	Sequence	pI	Charge at pH 8.3	Charge after labeling with ATTO-532	Charge/size ratio with ATTO-532
Bradykinin	Atto-532-Arg-Pro-Pro-Gly-Phe-Ser-Pro-Phe-Arg	12	+2	+1	$+5.926\times10^{-4}$
Met-enkephalin	Atto-532-Tyr-Gly-Gly-Phe-Met	5.52	-1	-2	-1.666×10^{-3}
C-type natriuretic peptide	Atto-532-Gly-Leu-Ser-Lys-Gly-Cys-Phe-Gly-Leu-Lys-Leu-Asp-Arg-Ile-Gly-Ser-Met-Ser-Gly-Leu-Gly-Cys	9.5	+3	+2	$+7.075\times10^{-4}$
C-peptide fragment 3-33	Atto-532-Glu-Ala-Glu-Asp-Leu-Gln-Val-Gly-Gln-Val-Glu-Leu-Gly-Gly-Gly-Pro-Gly-Ala-Gly-Ser-Leu-Gln-Pro-Leu-Ala-Leu-Glu-Gly-Ser-Leu-Gln	3.45	-6	-7	-1.919×10^{-3}

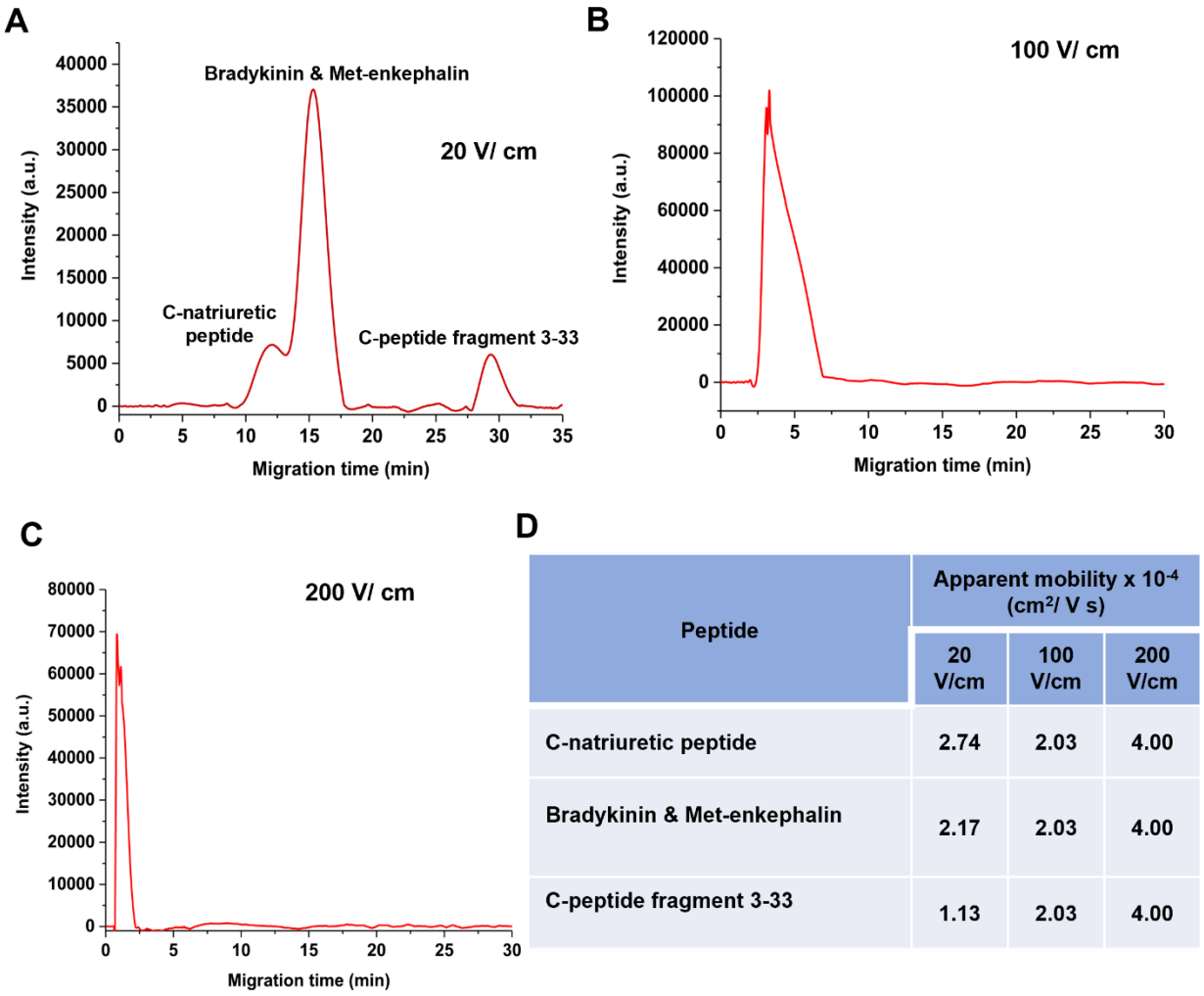

Peptide	Apparent mobility x 10^{-4} (cm^2/ V s)		
	20 V/cm	100 V/cm	200 V/cm
C-natriuretic peptide	2.74	2.03	4.00
Bradykinin & Met-enkephalin	2.17	2.03	4.00
C-peptide fragment 3-33	1.13	2.03	4.00

Figure 5.5 Microchip electropherograms of the peptides in PMMA/COC microchannel having dimensions of 50 µm x 100 µm (depth and width, respectively) with a 5 cm total channel length (effective length = 4 cm) at field strength of (**A**) 20 V/cm, **(B)** 100 V/ cm, and **(C**) 200 V/ cm. **(D**) Calculated apparent mobilities of peptides using equation (1).

In this study, the free solution separation of peptides was due to a combination of electrophoresis and chromatography. C-natriuretic peptide has the highest size/charge ratio amongst the peptides and migrated faster than the other peptides. C-peptide fragment 3-33 carries a negatively charged amino acid residue with the lowest size/charge ratio and migrated the slowest. These two peptides showed less contribution of chromatographic effects, which could be due to their comparatively large size. Bradykinin and met-enkephalin have smaller charge to size ratio compared that of C-natriuretic peptide at pH 8.3 and showed more contribution of

chromatographic effects. Both bradykinin and met-enkphalin co-migrated after C-natriuretic peptide at field strength of 20 v/cm. Furthermore, the flow profile in this PMMA/COC microfluidic channel was distorted because three walls of the microchannel were PMMA and one wall was COC and because the EOF of the two materials are different, they will produce a distorted flow profile that may influence the efficiency providing poorer resolution for the separation.

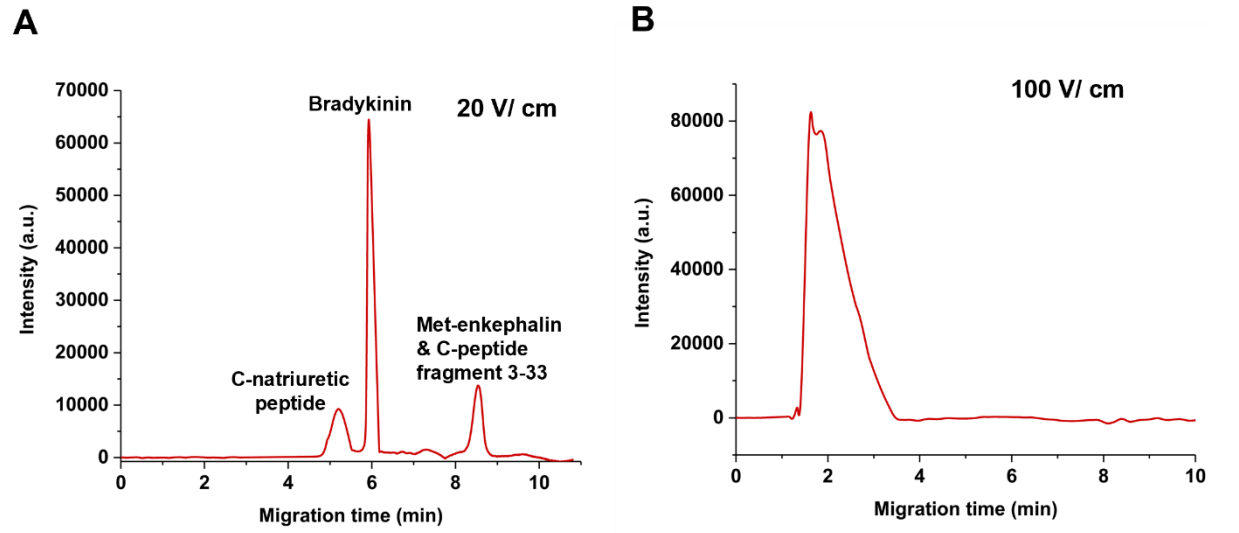

C

Peptide	Apparent mobility x 10^{-4} (cm^2/ V s)	
	20 V/cm	100 V/cm
C-natriuretic peptide	6.42	4.09
Bradykinin	5.62	4.09
Met-enkephalin & C-peptide fragment 3-33	3.90	4.09

D

Peak pair	Separation resolution
C-natriuretic peptide/ Bradykinin	0.87
Bradykinin/ Met-enkephalin & C-peptide fragment 3-33	3.86

Figure 5.6 Microchip electropherograms of the peptides in COC/COC microchannels having dimensions of 50 µm x 100 µm (depth and width, respectively) with 5 cm total channel length (effective length = 4 cm) at field strength of (**A**) 20 V/ cm, and **(B)** 100 V/ cm. (**C**) Calculated apparent mobilities of peptides using equation (1). **(D)** Resolutions (R) calculated for adjacent peak pairs using the electropherogram shown in (**B**). $R = 1.18(t_{m2}-t_{m1})/ (w_1+w_2)$, where t_{m1} and t_{m2} are migration times and w_1 and w_2 corresponds to the peak widths at the base of the peaks.

Free solution microchip electrophoresis was also carried out in COC/COC microchannels at field strengths of 100 V/ cm and 20 V/cm using 0.5X TBE buffer at pH 8.3 (Figure 5.6A-B). At a field strength of 100 V/cm, all the peptides co-migrated, as observed in the PMMA/COC microchips. Peptides were separated in a COC/COC microfluidic chip at a field strength of 20 V/cm and obtained higher resolution and lower migration times compared to PMMA/COC devices (Figure 5.6). The lower migration times or higher apparent mobilities of peptides were due to the higher electroosmotic flow in COC/COC microfluidic devices compared to PMMA/COC devices (Figure 5.6C). Even though C-natriuretic peptide and Bradykinin were resolved, Met-enkephalin and C-peptide fragment 3-33 co-migrated (Figure 5.6D). Similar trends of migration order were observed in COC/COC microchannels as seen for the PMMA/COC microchips. Because of the effects of field strength, we suspect that a combination of electrophoresis and chromatography was involved in these separations because at high electric field strengths, the separation efficiency was poorer due to restricted ability to interact with the wall.

5.3.1 Electrokinetic identification of peptides in O_2 plasma activated PMMA/COC nanochannels.

In our recent publication[62], we compared the mechanical and chemical properties of nanochannel devices made from COC/COC and PMMA/COC, where the first material listed is the substrate containing the nanochannel and the second material is the cover plate. In this section we present results for the electrophoresis of peptides in PMMA/COC to understand material effects on nanoscale electrophoresis. The reported EOF values for PMMA/COC [69] was 4.2×10^{-4} cm^2/Vs.

A

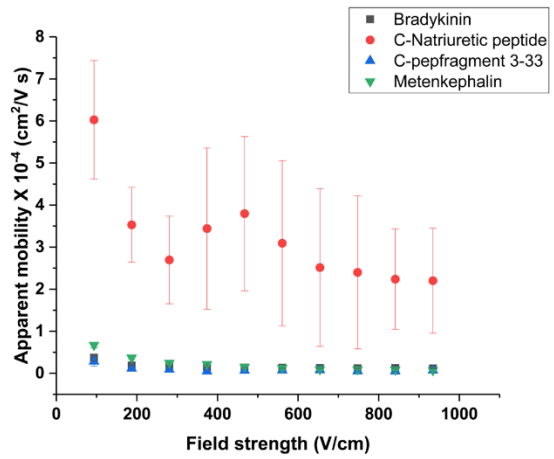

B

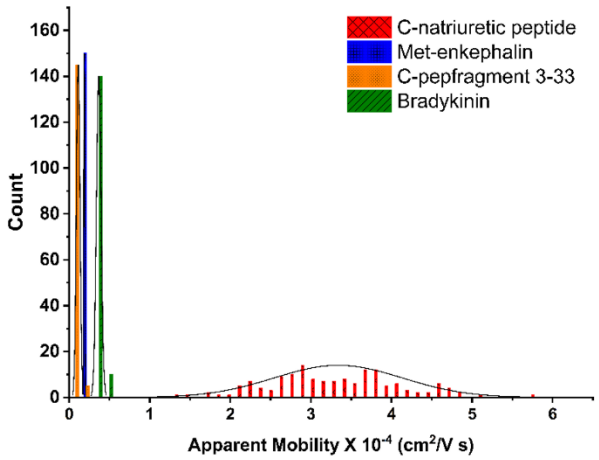

C

Peptide Identification Accuracy	C-Natriuretic peptide	Bradykinin	C-peptide fragment 3-33	Met-enkephalin
C-Natriuretic peptide	-	>99.999	>99.999	>99.999
Bradykinin	>99.999	-	>99.999	>99.999
C-peptide fragment 3-33	>99.999	>99.999	-	>95.150%
Met-enkephalin	>99.999	>99.999	>95.150%	-

D

	C-Natriuretic peptide	Bradykinin	C-peptide fragment 3-33	Met-enkephalin
Variance σ^2	6.976×10^{-9}	5.710×10^{-12}	8.004×10^{-12}	2.314×10^{-12}

Figure 5.7 (**A**) Apparent mobility vs electric field strength of peptides in PMMA/COC nanochannels using 0.5X TBE buffer at pH 8.3. **(B)** Histogram of apparent mobilities of peptides at 180 V/cm in PMMA/COC nanochannels using 0.5X TBE buffer at pH 8.3. The histograms were fit into Gaussian functions and each bin width represented 1.5×10^{-6} cm^2/Vs. **(C)** Identification accuracies of peptides calculated from Gaussian peak overlap. Identification accuracy = area of non-overlapped/total peak area. **(D)** The variance (σ^2) of peaks estimated from the Gaussian fits to the histograms.

Figure 5.7A shows the apparent mobility versus electric field strength for four peptides using a 110 nm x 110 nm nanochannel fabricated in PMMA/COC with a carrier electrolyte consisting of 0.5X TBE buffer (ionic strength of 44.5 mM) at pH 8.3. The net charge and the

charge/size ratio of ATTO-532 labeled peptides at pH 8.3 are shown in Table 1. Because the same dye reporter was covalently attached to each peptide using the -COOH termini, differences in the apparent mobilities of the peptides were assumed to arise from differences in the mobilities of the peptides.

The apparent mobility is a sum of the EOF (μ_{eof}) and the electrophoretic mobility of the peptides (μ_{ep}) with the sign of the EOF or mobility indicating its direction (anode → cathode = (+); cathode → anode = (-)). In the case of bradykinin and C-natriuretic peptide, the electrophoretic mobilities of the Atto-532 labeled peptides were in the direction as the EOF; larger μ_{ep} values result in higher apparent mobilities. But in the case of met-enkephalin and C-peptide fragment 3-33, the electrophoretic mobilities of these Atto-532 labeled peptides were opposite in direction to the EOF; larger μ_{ep} values result in lower apparent mobilities. If the apparent mobility order is based on the charge/size ratio of Atto-532-peptides, the migration is based primarily on electrophoresis. C-natriuretic peptide showed the highest apparent mobility as it had an electrophoretic mobility in the same direction as the EOF. The larger standard deviation of apparent mobilities of C-natriuretic peptide indicates slurring of the images that resulted from the limited framerate (50 frames/s) of the EMCCD camera. As seen in Figure 5.7A, the apparent mobility for C-natriuretic peptide showed electric field strength dependency, which was not apparent for Bradykinin and C-peptide fragment 3-33.

Figure 5.7B shows histograms of the apparent mobility for ATTO-532 labeled peptides at 180 V/cm in PMMA/COC devices. This electric field strength was selected as it provided the optimal identification efficiency between the peptides with minimum standard deviations in the histograms. These histograms were fit to a Gaussian function and the variance (σ^2), and identification accuracies were calculated (Figure 5.7C-D). The apparent mobility order at this

electric field strength was C-natriuretic peptide > bradykinin > met-enkephalin > C-peptide fragment 3-33. The observed apparent mobility order was similar to the apparent mobility order we observed for microchip electrophoresis (see Figure 5.5).

Improved identification efficiency, which is based on differences in the apparent mobilities, of the peptides in the case of nano-electrophoresis compared to microchip electrophoresis was achieved due to scaling effects. Surface interactions of solutes with channel walls such as hydrophobic/hydrophilic, electrostatic, or van der Waals interactions can become more prominent in nanochannels due to an increased surface area-to-volume ratio. In PMMA/COC nanochannels, the migration time order of peptides was C-natriuretic peptide < bradykinin < met-enkephalin < C-peptide fragment 3-33, which was based upon the charge/size of peptide-dye conjugates. Therefore, the migration of peptides was mainly due to electrophoresis. In addition to these observations, another important parameter for the potential use of mobility matching for the identification of peptides is the identification accuracy. We defined the identification accuracy as the amount of overlap between two adjacent Gaussian fits to the histograms of the ATTO 532 peptides' apparent mobilities. The percent overlap of the Gaussian peaks was calculated using a previously described method [76]. The average identification accuracy for the peptides in PMMA/COC devices was >99.191% (see Figure 5.7C).

5.3.2 Electrokinetic identification of peptides in COC/COC nanochannels.

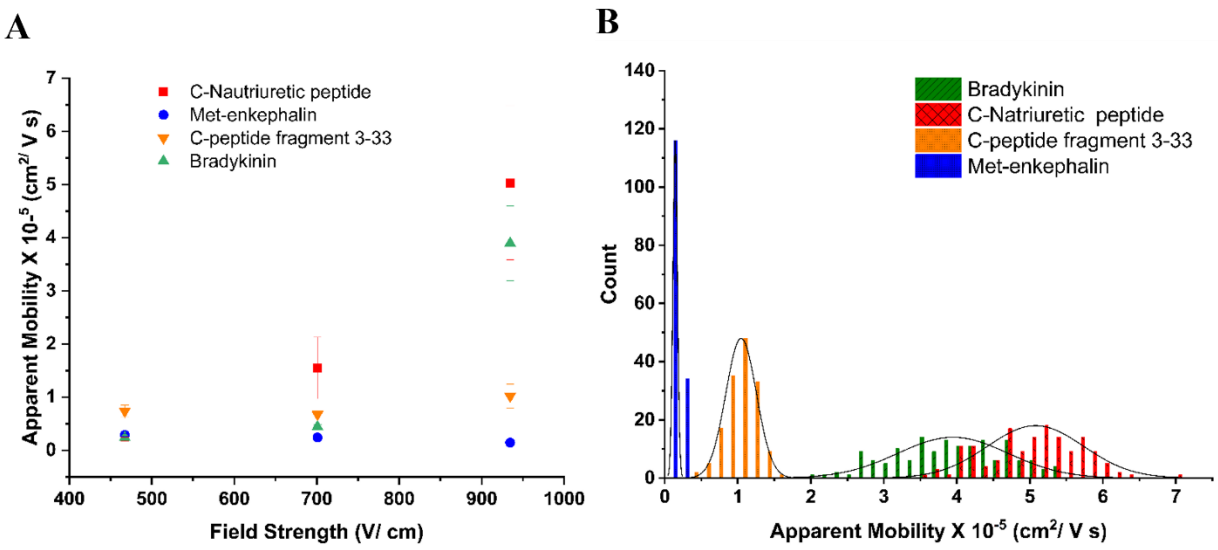

C

Peptide Identification Accuracy	C-Natriuretic peptide	Bradykinin	C-peptide fragment 3-33	Met-enkephalin
C-Natriuretic peptide	-	76.460%	>99.999	>99.999
Bradykinin	76.420%	-	99.670	>99.999
C-peptide fragment 3-33	>99.999	99.670	-	>99.999
Met-enkephalin	>99.999	>99.999	>99.999	-

D

	C-Natriuretic peptide	Bradykinin	C-peptide fragment 3-33	Met-enkephalin
Variance σ^2	5.006 X 10^{-11}	7.532 X 10^{-11}	4.325 X 10^{-12}	4.090 X 10^{-13}

Figure 5.8 (**A**) Apparent mobility vs electric field strength of peptides in COC/COC nanochannels using 0.5X TBE buffer at pH 8.3. **(B)** Histogram of apparent mobilities of peptides at 930 V/cm in COC/COC nanochannels using 0.5X TBE buffer at pH 8.3. The histograms were fit into Gaussian functions and each bin width represented 1.5 x 10^{-6} cm^2/Vs. **(C)** The resolution of the Gaussian fits was calculated using $R= 1.18 (\Delta\mu/w_{0.5} + w_{0.5})$, where $w_{0.5}$ corresponds to the full width at the half maximum of the Gaussians. **D)** Identification accuracies of peptides calculated from Gaussian peak overlap. Identification accuracy = area of non-overlapped/total peak area. **(E)** The variance (σ^2) of peaks estimated from the Gaussian fits to the histograms.

The EOF for COC/COC devices was ~4 times smaller than PMMA/COC devices[69]. Therefore, the overall magnitude of μ_{app} should be smaller in COC/COC devices compared to PMMA/COC devices (see Figure 5.7A). Figure 5.8A shows the apparent mobility vs. electric field strength of the model peptides in COC/COC nanochannel devices. In the COC/COC devices, we

observed a field dependent apparent mobility for C-natriuretic peptide and bradykinin. However, the other two peptides did not show an electric field dependent mobility as they did not show a statistical difference of apparent mobilities at different field strengths. These trends were slightly different than those observed in the PMMA/COC nanochannels. In our recent publication, we reported that COC exhibits higher surface roughness compared to PMMA[62]. This surface roughness generates intermittent motion and electric recirculation, which are significant at low electric field strengths[66].

Figure 8B shows histograms of the apparent mobilities for the ATTO-532 labeled peptides at 930 V/cm, which was selected because it provided the optimal identification accuracy (*i.e.*, highest difference in the apparent mobilities) between the peptides. The optimal electric field strength for COC/COC device was ~5 fold higher compared to that of PMMA/COC device which could be due to the differences in electroosmotic flow mobilities.The histograms of ATTO-532 peptides' mobilities were fit to Gaussian functions to determine the standard deviation. The variance, σ^2, was acquired from standard deviations associated with the Gaussian fits to the histogram data (see Figure 5.8D). The apparent mobility order here was C-natriuretic peptide < bradykinin < C-peptide fragment 3-33 < met-enkephalin and is slightly different than the apparent mobility order observed in PMMA/COC nanochannel devices. However, it showed a similar trend to the apparent mobility order we observed for microchip electrophoresis of the peptides (see Figure 5.6) in COC microchannels. Moreover, hydrophobic patches in the thermoplastic can induce interactions with the hydrophobic side groups of the amino acid residues within the model peptides. Bradykinin and met-enkephalin showed higher migration times, which could be due to an increased number of hydrophobic wall interactions arising from the presence of higher percentages of hydrophobic side groups (bradykinin: 55.56%, met-enkephalin 60%) compared to

C-natriuretic peptide (31.81%) and C-peptide fragment 3-33 (38.71%). At a carrier electrolyte pH of 8.3 and a field strength of 930 V/cm (λ_d = 1.25 nm). The identification mechanism of peptiides in COC/COC nanochannels could be due to a combination of electrophoresis and chromatography. of Figure 5.8C shows the calculated identification accuracies for the peptides. As can be seen, the average identification accuracy for the peptides in COC/COC devices was >96.021%, which was lower than that seen for PMMA/COC devices. This indicates that there is a significant effect on chromatography for the identification of peptides. The identification accuracy in COC/COC nanochannels can be improved by using longer nanochannels.

5.3.3 Electrokinetic identification of peptides in ethanolamine modified nanochannels.

The EOF for ethanolamine modified PMMA/COC devices was ~10 times smaller than that of PMMA/COC devices, as noted[69]. Therefore, the overall magnitude of μ_{app} should be smaller in ethanolamine modified PMMA/COC devices compared to PMMA/COC and COC/COC devices (see Figures 5.7A, 5.8A and 5.9A), which allowed us to perform nanoscale electrophoresis at higher electric field strengths in the absence of image slurring compared to the native PMMA/COC and COC/COC devices. Figure 5.9A shows the apparent mobility vs. electric field strength of the peptides in ethanolamine modified PMMA/COC nanochannel devices. For the ethanolamine modified PMMA/COC devices, we observed a similar trend compared to O_2 plasma activated PMMA/COC devices.

A

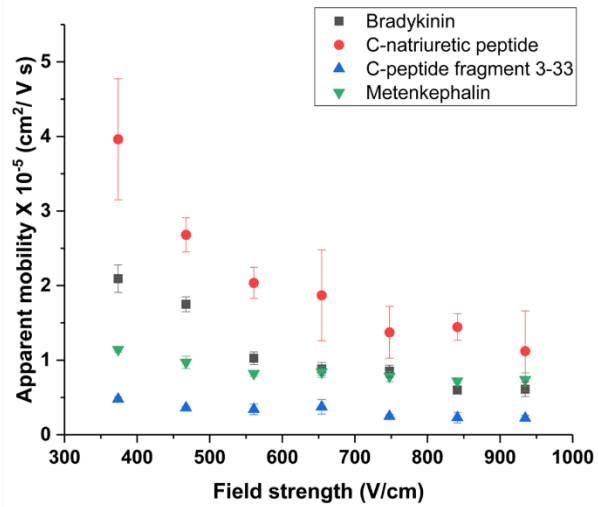

B

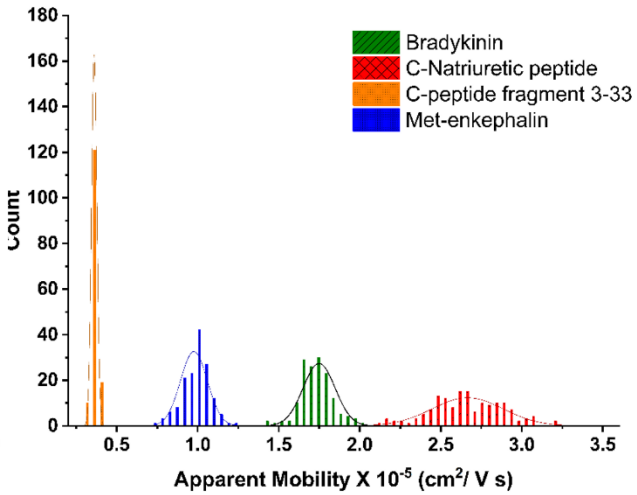

C

Peptide Identification Accuracy	C-Natriuretic peptide	Bradykinin	C-peptide fragment 3-33	Met-enkephalin
C-Natriuretic peptide	-	99.999	>99.999	>99.999
Bradykinin	99.999	-	>99.999	>99.999
C-peptide fragment 3-33	>99.999	>99.999	-	>99.999
Met-enkephain	>99.999	>99.999	>99.999	-

D

	C-Natriuretic peptide	Bradykinin	C-peptide fragment 3-33	Met-enkephalin
Variance σ^2	4.995 X 10^{-12}	7.061 X 10^{-13}	4.730 X 10^{-14}	5.177 X 10^{-13}

Figure 5.9 (**A**) Apparent mobility vs electric field strength of peptides in ethanolamine modified nanochannels using 0.5X TBE buffer at pH 8.3. **(B)** Histogram of apparent mobilities of peptides at 470 V/cm in ethanolamine modified nanochannes using 0.5X TBE buffer at pH 8.3. The histograms were fit into Gaussian functions and each bin width represented 1.5 x 10^{-6} cm^2/Vs. **(C)** Identification accuracies of peptides calculated from Gaussian peak overlap. Identification accuracy = area of non-overlapped/total peak area. **(D)** The variance (σ^2) of peaks estimated from the Gaussian fits to the histograms.

Figure 5.9B shows histograms of the apparent mobilities for the ATTO-532 labeled peptides at 470 V/cm, which was selected because it provided optimal identification resolution between the peptides. The variance, σ^2, was acquired from standard deviations associated with the

Gaussian fits to the histogram data (see Figure 5.9D). The apparent mobility order here was C-natriuretic peptide < bradykinin < met-enkephalin < C-peptide fragment 3-33 and is similar to the apparent mobility order observed in O_2 plasma activated PMMA/COC nanochannel devices. The identification of peptides in ethanolamine modified PMMA/COC devices was mainly due to electrophoresis because the apparent mobility order was based on the charge/size ratio of peptides (see Table 1). As shown in Figure 5.9C, at a carrier electrolyte pH of 8.3 and a field strength of 470 V/cm (λ_d = 1.25 nm), all peptides achieved baseline identification resolution. Figure 5.9D shows the calculated identification accuracies for the peptides. As can be seen, the average identification accuracy for the peptides in ethanolamine modified PMMA/COC devices was >99.99%, which was higher than that seen for PMMA/COC and COC/COC devices. The ethanolamine modified PMMA/COC device showed the lowest electroosmotic flow mobility out of three devices used in this study. The reduced EOF in ethanolamine modified PMMA/COC device can increase wall interactions such as hydrogen bonding, by increasing time for lateral diffusion.

5.3.5 Time of flight identification of label-free peptides in PMMA dual in-plane nanopores.

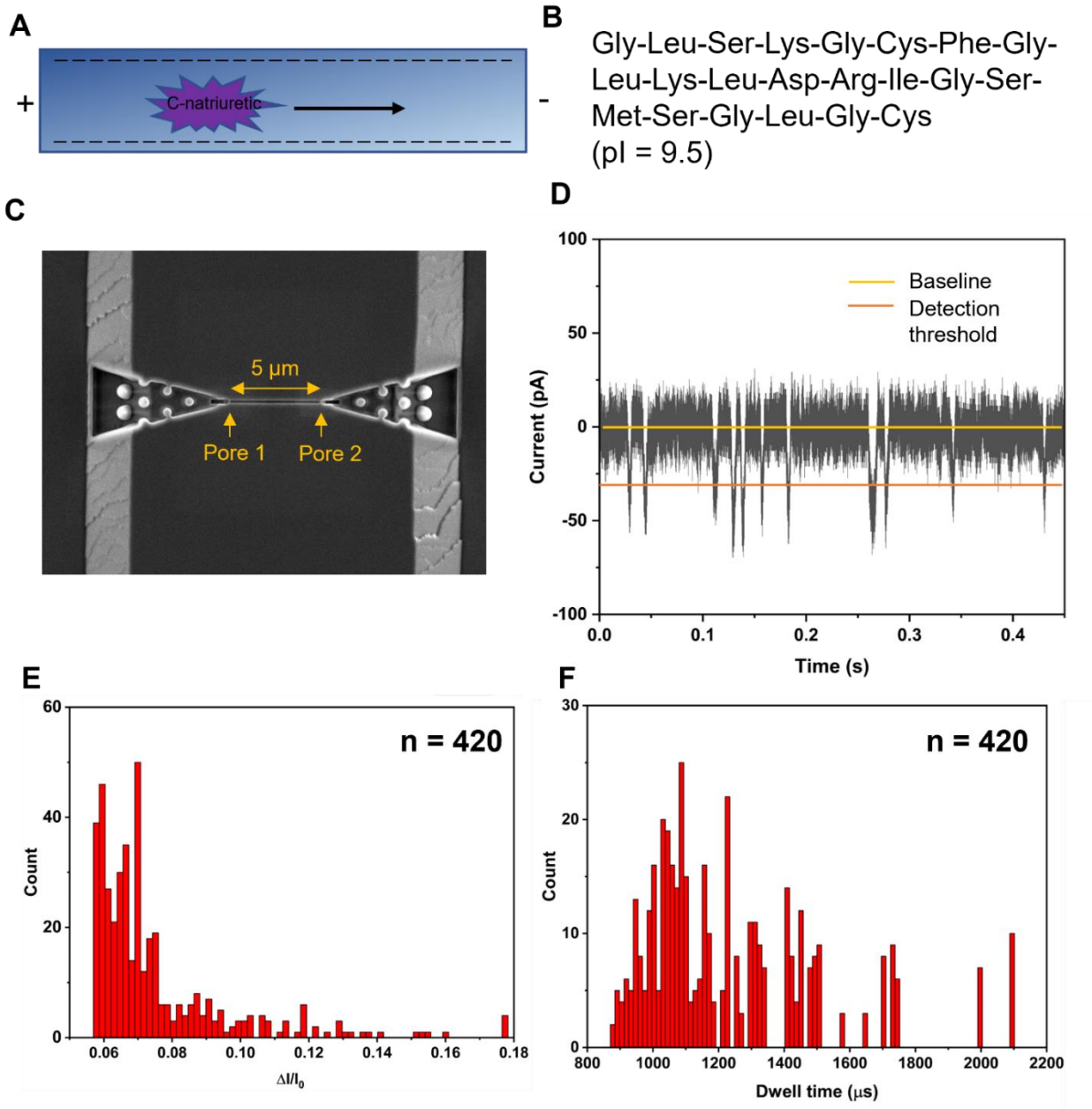

Figure 5.10 Translocation of C-natriuretic peptide through dual in-plane nanopore devices assembled at 150 psi bonding pressure. **(A)** The direction of movement of C-Natriuretic peptide through nano flight tube. **(B)** The peptide sequence and the pI of C-Natriuretic peptide. **(C)** A SEM image of dual in-plane nanopore sensor with 5 µm nano flight tube. **(D)** A 0.45 s current transient trace of signal amplitudes obtained for a blank, 10 ng/µL solution of C-natriuretic peptides using dual in-plane nanopore devices. **(E)** Peak amplitude distribution and **(F)** Dwell time distribution for C-Natriuretic peptide events.

We next carried out experiments for the label-free detection of single peptide molecules using the PMMA/COC dual-in-plane nanopore devices bonded at 150 psi for 15 min, which was used to create a pore size of ~15 nm. The assembled PMMA/COC dual in-plane nanopore devices were primed with 50% v/v methanol/water followed by the introduction of 0.5X TBE buffer. C-natriuretic peptide was electrophoresed in 0.5 X TBE buffer at pH 8.3 through dual in-plane nanopore sensing devices, which were separated by a 5 μm nano-flight tube. As we observed with PMMA/COC nanochannel devices, C-natriuretic peptide migrated from anode to cathode. Here we show the ability to detect label-free peptides using the in-plane nanopore sensing devices (Figure 5.10). The average dwell time of the resistive pulse sensing peaks obtained for single C-Natriuretic peptide events was 1.2 ±0.2 ms. The average dwell time and the peak amplitude ($\Delta I/I_0$; ΔI = current blockade amplitude and I_0 = open pore current) was higher than that observed for single rNMP events. We also measured the TOF of the C-Natriuretic peptide, which corresponds to the time the molecule takes to travel between the two pores. The TOF ranged from 0.69 to 3.15 ms with an average of 1.38 ±0.49 ms (n = 75).

5.4 Conclusions

Our future work will employ a strategy to do peptide fingerprinting of single protein molecules and will utilize nanoscale electrophoresis to identify peptides generated from the proteolytic digestion of the intact protein. Label-free peptides will be identified using their molecular-dependent electrophoretic mobility; the concept has been coined Time-of-Flight (TOF) identification. Experimental conditions such as material type, electric field strength, and electroosmotic flow can be optimized to achieve high TOF identification accuracies. In this work, PMMA/COC, COC/COC and ethanolamine modified PMMA/COC nanofluidic devices were

investigated. However, ethanolamine modified PMMA/COC devices resulted in high identification accuracy of the peptides compared to O_2 plasma activated PMMA/COC nanofluidic devices. COC/COC nanofluidic device showed the poorest identification accuracy amongst all.

We utilized dye labeled peptides in this study to allow tracking the molecules during their transport through nanochannels, our envisioned peptide fingerprinting strategy will not require labeling of the peptides. We will employ a label free approach for determining the ToF of the peptides. Here, we showed the ability to identify label-free peptides via resistive pulse sensing in dual in-plane nanopore sensor.

5.5 References

1. Henzel, W. J.; Watanabe, C.; Stults, J. T., Protein identification: the origins of peptide mass fingerprinting. *Journal of the American Society for Mass Spectrometry* **2003,** *14* (9), 931-942.

2. Anderson, N. L.; Matheson, A. D.; Steiner, S., Proteomics: applications in basic and applied biology. *Current Opinion in Biotechnology* **2000,** *11* (4), 408-412.

3. Harry, J. L.; Wilkins, M. R.; Herbert, B. R.; Packer, N. H.; Gooley, A. A.; Williams, K. L., Proteomics: capacity versus utility. *ELECTROPHORESIS: An International Journal* **2000,** *21* (6), 1071-1081.

4. Davis, L., *Basic methods in molecular biology*. Elsevier: 2012.

5. Santoni, V.; Molloy, M.; Rabilloud, T., Membrane proteins and proteomics: un amour impossible? *ELECTROPHORESIS: An International Journal* **2000,** *21* (6), 1054-1070.

6. Beranova-Giorgianni, S., Proteome analysis by two-dimensional gel electrophoresis and mass spectrometry: strengths and limitations. *TrAC Trends in Analytical Chemistry* **2003,** *22* (5), 273-281.

7. Gygi, S. P.; Corthals, G. L.; Zhang, Y.; Rochon, Y.; Aebersold, R., Evaluation of two-dimensional gel electrophoresis-based proteome analysis technology. *Proceedings of the National Academy of Sciences* **2000,** *97* (17), 9390-9395.

8. Rabilloud, T.; Chevallet, M.; Luche, S.; Lelong, C., Two-dimensional gel electrophoresis in proteomics: Past, present and future. *Journal of proteomics* **2010,** *73* (11), 2064-2077.

9. Aebersold, R.; Mann, M., Mass spectrometry-based proteomics. *Nature* **2003,** *422* (6928), 198-207.

10. Washburn, M. P.; Wolters, D.; Yates, J. R., Large-scale analysis of the yeast proteome by multidimensional protein identification technology. *Nature biotechnology* **2001,** *19* (3), 242-247.

11. Gilmore, J. M.; Washburn, M. P., Advances in shotgun proteomics and the analysis of membrane proteomes. *Journal of proteomics* **2010,** *73* (11), 2078-2091.

12. McDonald, W. H.; Yates Iii, J. R., Shotgun proteomics and biomarker discovery. *Disease markers* **2002,** *18* (2), 99-105.

13. Wu, C. C.; MacCoss, M. J., Shotgun proteomics: tools for the analysis of complex biological systems. *Curr Opin Mol Ther* **2002,** *4* (3), 242-250.

14. Schmid, A.; Kortmann, H.; Dittrich, P. S.; Blank, L. M., Chemical and biological single cell analysis. *Current opinion in biotechnology* **2010,** *21* (1), 12-20.

15. Sun, B.; Kovatch, J. R.; Badiong, A.; Merbouh, N., Optimization and modeling of quadrupole orbitrap parameters for sensitive analysis toward single-cell proteomics. *Journal of Proteome Research* **2017,** *16* (10), 3711-3721.

16. O'Rourke, M. B.; Town, S. E.; Dalla, P. V.; Bicknell, F.; Koh Belic, N.; Violi, J. P.; Steele, J. R.; Padula, M. P., What is normalization? The strategies employed in top-down and bottom-up proteome analysis workflows. *Proteomes* **2019,** *7* (3), 29.

17. Botelho, D.; Wall, M. J.; Vieira, D. B.; Fitzsimmons, S.; Liu, F.; Doucette, A., Top-down and bottom-up proteomics of SDS-containing solutions following mass-based separation. *Journal of proteome research* **2010,** *9* (6), 2863-2870.

18. Cassidy, L.; Kaulich, P. T.; Maaß, S.; Bartel, J.; Becher, D.; Tholey, A., Bottom-up and top-down proteomic approaches for the identification, characterization, and quantification of the low molecular weight proteome with focus on short open reading frame-encoded peptides. *Proteomics* **2021,** *21* (23-24), 2100008.

19. Ball, B.; Bermas, A.; Carruthers-Lay, D.; Geddes-McAlister, J., Mass spectrometry-based proteomics of fungal pathogenesis, host–fungal interactions, and antifungal development. *Journal of Fungi* **2019,** *5* (2), 52.

20. Yang, Z.; Shen, X.; Chen, D.; Sun, L., Toward a universal sample preparation method for denaturing top-down proteomics of complex proteomes. *Journal of proteome research* **2020,** *19* (8), 3315-3325.

21. Toby, T. K.; Fornelli, L.; Kelleher, N. L., Progress in top-down proteomics and the analysis of proteoforms. *Annual review of analytical chemistry* **2016,** *9*, 499-519.

22. Rosenfeld, J.; Capdevielle, J.; Guillemot, J. C.; Ferrara, P., In-gel digestion of proteins for internal sequence analysis after one-or two-dimensional gel electrophoresis. *Analytical biochemistry* **1992,** *203* (1), 173-179.

23. Ru, Q. C.; Zhu, L. A.; Katenhusen, R. A.; Silberman, J.; Brzeski, H.; Liebman, M.; Shriver, C. D., Exploring human plasma proteome strategies: high efficiency in-solution digestion

protocol for multi-dimensional protein identification technology. *Journal of Chromatography A* **2006,** *1111* (2), 175-191.

24. Huang, Y.; Shan, W.; Liu, B.; Liu, Y.; Zhang, Y.; Zhao, Y.; Lu, H.; Tang, Y.; Yang, P., Zeolite nanoparticle modified microchip reactor for efficient protein digestion. *Lab on a Chip* **2006,** *6* (4), 534-539.

25. Wilm, M.; Shevchenko, A.; Houthaeve, T.; Breit, S.; Schweigerer, L.; Fotsis, T.; Mann, M., Femtomole sequencing of proteins from polyacrylamide gels by nano-electrospray mass spectrometry. *Nature* **1996,** *379* (6564), 466-469.

26. Gharahdaghi, F.; Weinberg, C. R.; Meagher, D. A.; Imai, B. S.; Mische, S. M., Mass spectrometric identification of proteins from silver-stained polyacrylamide gel: a method for the removal of silver ions to enhance sensitivity. *ELECTROPHORESIS: An International Journal* **1999,** *20* (3), 601-605.

27. Klammer, A. A.; MacCoss, M. J., Effects of modified digestion schemes on the identification of proteins from complex mixtures. *Journal of proteome research* **2006,** *5* (3), 695-700.

28. Lee, J.; Soper, S. A.; Murray, K. K., Development of an efficient on-chip digestion system for protein analysis using MALDI-TOF MS. *Analyst* **2009,** *134* (12), 2426-2433.

29. Rivera-Burgos, D.; Regnier, F. E., Disparities between immobilized enzyme and solution based digestion of transferrin with trypsin. *Journal of separation science* **2013,** *36* (3), 454-460.

30. Poulet, G.; Massias, J.; Taly, V., Liquid biopsy: general concepts. *Acta cytologica* **2019,** *63* (6), 449-455.

31. Campos, C. D.; Jackson, J. M.; Witek, M. A.; Soper, S. A., Molecular profiling of liquid biopsy samples for precision medicine. *Cancer journal (Sudbury, Mass.)* **2018,** *24* (2), 93.

32. Swaminathan, J.; Boulgakov, A. A.; Hernandez, E. T.; Bardo, A. M.; Bachman, J. L.; Marotta, J.; Johnson, A. M.; Anslyn, E. V.; Marcotte, E. M., Highly parallel single-molecule identification of proteins in zeptomole-scale mixtures. *Nature biotechnology* **2018,** *36* (11), 1076-1082.

33. Kennedy, E.; Dong, Z.; Tennant, C.; Timp, G., Reading the primary structure of a protein with 0.07 nm 3 resolution using a subnanometre-diameter pore. *Nature nanotechnology* **2016,** *11* (11), 968-976.

34. Lee, J.; Musyimi, H. K.; Soper, S. A.; Murray, K. K., Development of an automated digestion and droplet deposition microfluidic chip for MALDI-TOF MS. *Journal of the American Society for Mass Spectrometry* **2008,** *19* (7), 964-972.

35. Lee, J.; Soper, S. A.; Murray, K. K., Microfluidics with MALDI analysis for proteomics—a review. *Analytica chimica acta* **2009,** *649* (2), 180-190.

36. Rawlings, N. D.; Barrett, A. J., [2] Families of serine peptidases. *Methods in enzymology* **1994,** *244*, 19-61.

37. Rodriguez, J.; Gupta, N.; Smith, R. D.; Pevzner, P. A., Does trypsin cut before proline? *Journal of proteome research* **2008,** *7* (01), 300-305.

38. Lundanes, E.; Greibrokk, T., Reversed-phase chromatography of peptides. *Journal of Chromatography A* **1978,** *149*, 241-254.

39. Molnár, I.; Horváth, C., Separation of amino acids and peptides on non-polar stationary phases by high-performance liquid chromatography. *Journal of Chromatography a* **1977,** *142*, 623-640.

40. Chen, H.; Horváth, C., High-speed high-performance liquid chromatography of peptides and proteins. *Journal of Chromatography A* **1995,** *705* (1), 3-20.

41. Gilar, M.; Olivova, P.; Daly, A. E.; Gebler, J. C., Two-dimensional separation of peptides using RP-RP-HPLC system with different pH in first and second separation dimensions. *Journal of separation science* **2005,** *28* (14), 1694-1703.

42. Kašička, V., Capillary electrophoresis of peptides. *ELECTROPHORESIS: An International Journal* **1999,** *20* (15-16), 3084-3105.

43. Kašička, V., Recent developments in capillary electrophoresis and capillary electrochromatography of peptides. *Electrophoresis* **2006,** *27* (1), 142-175.

44. Kašička, V., Recent advances in capillary electrophoresis of peptides. *Electrophoresis* **2001,** *22* (19), 4139-4162.

45. Wan, H.; Blomberg, L. G., Chiral separation of amino acids and peptides by capillary electrophoresis. *Journal of Chromatography A* **2000,** *875* (1-2), 43-88.

46. Bandilla, D.; Skinner, C. D., Capillary electrochromatography of peptides and proteins. *Journal of Chromatography A* **2004,** *1044* (1-2), 113-129.

47. He, B.; Ji, J.; Regnier, F. E., Capillary electrochromatography of peptides in a microfabricated system. *Journal of Chromatography A* **1999,** *853* (1-2), 257-262.

48. Kašička, V., Recent advances in capillary electrophoresis and capillary electrochromatography of peptides. *Electrophoresis* **2003,** *24* (22-23), 4013-4046.

49. Li, Y.; Xiang, R.; Wilkins, J. A.; Horváth, C., Capillary electrochromatography of peptides and proteins. *Electrophoresis* **2004,** *25* (14), 2242-2256.

50. Pennathur, S.; Santiago, J. G., Electrokinetic Transport in Nanochannels. 1. Theory. *Analytical Chemistry* **2005,** *77* (21), 6772-6781.

51. Pennathur, S.; Santiago, J. G., Electrokinetic Transport in Nanochannels. 2. Experiments. *Analytical Chemistry* **2005,** *77* (21), 6782-6789.

52. Xuan, X.; Li, D., Electrokinetic transport of charged solutes in micro-and nanochannels: The influence of transverse electromigration. *Electrophoresis* **2006,** *27* (24), 5020-5031.

53. Garcia, A. L.; Ista, L. K.; Petsev, D. N.; O'Brien, M. J.; Bisong, P.; Mammoli, A. A.; Brueck, S. R.; López, G. P., Electrokinetic molecular separation in nanoscale fluidic channels. *Lab on a Chip* **2005,** *5* (11), 1271-1276.

54. Baldessari, F.; Santiago, J. G., Electrophoresis in nanochannels: brief review and speculation. *Journal of Nanobiotechnology* **2006,** *4* (1), 12.

55. Smirnova, A.; Shimizu, H.; Mawatari, K.; Kitamori, T., Reversed-phase chromatography in extended-nano space for the separation of amino acids. *Journal of Chromatography A* **2015,** *1418*, 224-227.

56. Tóth, G.; Panić-Janković, T.; Mitulović, G., Pillar array columns for peptide separations in nanoscale reversed-phase chromatography. *Journal of Chromatography A* **2019,** *1603*, 426-432.

57. Napoli, M.; Eijkel, J. C.; Pennathur, S., Nanofluidic technology for biomolecule applications: a critical review. *Lab on a Chip* **2010,** *10* (8), 957-985.

58. Wang, L.; Shao, P.; van Kan, J.; Ansari, K.; Bettiol, A.; Pan, X.; Wohland, T.; Watt, F., Fabrication of nanofluidic devices utilizing proton beam writing and thermal bonding techniques. *Nuclear Instruments and Methods in Physics Research Section B: Beam Interactions with Materials and Atoms* **2007,** *260* (1), 450-454.

59. Duan, C.; Wang, W.; Xie, Q., Fabrication of nanofluidic devices. *Biomicrofluidics* **2013,** *7* (2), 026501.

60. Chantiwas, R.; Park, S.; Soper, S. A.; Kim, B. C.; Takayama, S.; Sunkara, V.; Hwang, H.; Cho, Y.-K., Flexible fabrication and applications of polymer nanochannels and nanoslits. *Chemical Society Reviews* **2011,** *40* (7), 3677-3702.

61. Uba, F. I.; Pullagurla, S. R.; Sirasunthorn, N.; Wu, J.; Park, S.; Chantiwas, R.; Cho, Y.-K.; Shin, H.; Soper, S. A., Surface charge, electroosmotic flow and DNA extension in chemically modified thermoplastic nanoslits and nanochannels. *Analyst* **2015,** *140* (1), 113-126.

62. Amarasekara, C. A.; Rathnayaka, C.; Athapattu, U. S.; Zhang, L.; Choi, J.; Park, S.; Nagel, A.; Soper, S. A., Electrokinetic Identification of Ribonucleotide Monophosphates (rNMPs) using Thermoplastic Nanochannels. *Journal of Chromatography A* **2021**, 461892.

63. Athapattu, U. S.; Rathnayaka, C.; Vaidyanathan, S.; Gamage, S. S.; Choi, J.; Riahipour, R.; Manoharan, A.; Hall, A. R.; Park, S.; Soper, S. A., Tailoring Thermoplastic In-Plane Nanopore Size by Thermal Fusion Bonding for the Analysis of Single Molecules. *ACS sensors* **2021,** *6* (8), 3133-3143.

64. Zhang, N.; Byrne, C. J.; Browne, D. J.; Gilchrist, M. D., Towards nano-injection molding. *Materials today* **2012,** *15* (5), 216-221.

65. Chai, J.; Lu, F.; Li, B.; Kwok, D. Y., Wettability interpretation of oxygen plasma modified poly (methyl methacrylate). *Langmuir* **2004,** *20* (25), 10919-10927.

66. ONeil, C. E.; Jackson, J. M.; Shim, S.-H.; Soper, S. A., Interrogating surface functional group heterogeneity of activated thermoplastics using super-resolution fluorescence microscopy. *Analytical chemistry* **2016,** *88* (7), 3686-3696.

67. O'Neil, C.; Amarasekara, C. A.; Weerakoon-Ratnayake, K. M.; Gross, B.; Jia, Z.; Singh, V.; Park, S.; Soper, S. A., Electrokinetic transport properties of deoxynucleotide monophosphates (dNMPs) through thermoplastic nanochannels. *Anal Chim Acta* **2018,** *1027*, 67-75.

68. Weerakoon-Ratnayake, K. M.; Uba, F. I.; Oliver-Calixte, N. J.; Soper, S. A., Electrophoretic separation of single particles using nanoscale thermoplastic columns. *Analytical chemistry* **2016,** *88* (7), 3569-3577.

69. Amarasekara, C. A.; Athapattu, U. S.; Rathnayaka, C.; Choi, J.; Park, S.; Soper, S. A., Open-tubular Nanoelectrochromatography (OT-NEC): Gel-free Separation of Single Stranded DNAs (ssDNAs) in Thermoplastic Nanochannels. *Electrophoresis* **2020,** *41* (18-19).

70. Hu, W.; Soper, S. A.; Jackson, J. M., Time-Delayed Integration–Spectral Flow Cytometer (TDI-SFC) for Low-Abundance-Cell Immunophenotyping. *Analytical chemistry* **2019,** *91* (7), 4656-4664.

71. Ford, S. M.; Kar, B.; McWhorter, S.; Davies, J.; Soper, S. A.; Klopf, M.; Calderon, G.; Saile, V., Microcapillary electrophoresis devices fabricated using polymeric substrates and X-ray lithography. *J. Microcolumn Sep.* **1998,** *10* (5), 413-422.

72. Sinville, R.; Soper, S. A., High resolution DNA separations using microchip electrophoresis. *J. Sep. Sci.* **2007,** *30* (11), 1714-1728.

73. Obubuafo, A.; Balamurugan, S.; Shadpour, H.; Spivak, D.; McCarley, R. L.; Soper, S. A., Poly(methyl methacrylate) microchip affinity capillary gel electrophoresis of aptamer-protein complexes for the analysis of thrombin in plasma. *Electrophoresis* **2008,** *29* (16), 3436-3445.

74. Njoroge, S. K.; Witek, M. A.; Hupert, M. L.; Soper, S. A., Microchip electrophoresis of Alu elements for gender determination and inference of human ethnic origin. *Electrophoresis* **2010,** *31* (6), 981-990.

75. Albrecht, J. C.; Kotani, A.; Lin, J. S.; Soper, S. A.; Barron, A. E., Simultaneous detection of 19 K-ras mutations by free-solution conjugate electrophoresis of ligase detection reaction products on glass microchips. *Electrophoresis* **2013,** *34* (4), 590-597.

76. Bidleman, T. F., The relationship between resolution and percent band overlap. *Journal of Chemical Education* **1979,** *56* (5), 293.

Chapter 6: Conclusions and Future Directions

6.1 Conclusions

In this dissertation, we carefully examined the use of nanofluidic devices for biomolecular separations in applications in single molecule sequencing. In chapter 1, we cited extensive literature where researchers have used current technologies and methods for biomolecule separation with fluidic device in nanoscale. In addition, we have discussed the unique transport phenomena in nanofluidic devices, the fabrication methods used for these devices, detection methods applied in biomolecular separation, as well as the application of nanofluidics for biomolecule separation.

In this dissertation, we have proposed an innovative strategy for single-molecule sequencing (SMS) which has the potential to overcome the limitations in current DNA/RNA sequencing technologies.[1-3] Our proposed SMS approach addresses the limitations of moderate base call accuracy associated with current nanopore sequencing by generating mononucleotides using a processive enzyme from an intact RNA molecule with the individual rNMPs identified using their molecular-dependent electrophoretic mobility; TOF identification. What makes TOF identification attractive is that a variety of experimental conditions can be altered to optimize the identification, such as channel material type, electric field strength, and pH to name a few. In chapter 2, we investigated PMMA/COC and COC/COC nanofluidic devices using ATTO-532 labeled rNMPs. The advantage of COC/COC devices was the ability to perform post-assembly surface activation using UV/O_3 light to control the EOF depending on the dose, which was not possible in PMMA/COC devices. In addition, the bond strength between the cover plate and the substrate for COC/COC devices was much higher when using post-assembly UV/O_3 activation to

allow a diverse range of electrophoresis conditions to be employed to optimize the identification accuracies. However, both materials resulted in high TOF identification accuracy of the rNMPs.

Although we utilized dye labeled rNMPs in this study to allow tracking the molecules during their transport through nanochannels, our envisioned SMS platform will not require labeling of the rNMPs [4]. In chapter 3 and 4 we employed a label free approach for determining the TOF of the rNMPs. This was accomplished by fabricating a thermoplastic nanochannel device with two in-plane nanopores poised at each end of the nanochannel to measure the TOF [5]. The detection therefore used resistive pulse sensing of single molecules.

In chapter 3 we demonstrated our ability to tailor the size of an in-plane nanopore by TFB using different pressures during an assembly step already required for thermoplastic nanofluidic chip production. We noticed that the size and shape of the in-plane nanopore changed with different bonding pressures in a controlled fashion as measured using AFM and SEM. Furthermore, λ-DNA was electrokinetically driven by a DC voltage through the dual nanopore devices bonded at 110, 170 and 200 psi. The transient current amplitudes were seen to increase with higher TFB pressures. Therefore, thermoplastic nanofluidic devices allow for tuning nanostructure size to accommodate a given application by simply altering device assembly conditions without requiring direct FIB milling of a new Si master. This was further demonstrated using 60 nt ssRNAs and rAMPs with devices bonded at 170 and 200 psi bonding pressure, respectively.

Moreover, to reduce co-ion exclusion effects leading to sub-optimal event frequency, we modified the assembled device surfaces with ethanolamine (see chapter 3). The high carboxyl group density generated during O_2 plasma treatment prior to TFB created a high surface charge, which led to exclusion of co-ions passing through small nanopores. To alter the surface charge,

EDC/NHS chemistry with ethanolamine was used.[6] We observed a significant increase in translocation event frequency with ethanolamine modified dual in-plane nanopore devices.

In chapter 4 we optimized the geometry of the dual in-plane nanopore sensor for label-free identification of rNMPs. We observed that the sampling efficiency of the dual in-plane nano senor with the new iteration increased compared to the old iteration which was further demonstrated with COMSOL simulations. We also have demonstrated TOF identification of label-free rNMPs using PMMA/COC dual in-plane nanopore sensors with 5 µm and 10 µm nano flight tube length. Upon increasing nano flight tube length both the resolution and identification accuracy of rNMPs were increased. In addition, we have shown the ability to fabricate dual in-plane nano sensors using injection molding and subsequent use of those devices in label-free identification of rNMPs based on molecular dependent TOF.

The successful identification of label free rNMPs in free solution using thermoplastic dual in-plane nanopore sensor will enable development of our SMS approach for RNA. Our recent report on using surface immobilized XRN1 to plastic pillars serves as another foundational piece to deliver our SMS approach [1]. Our SMS approach will provide high read lengths (determined by the processivity of the exonuclease) and high call accuracies (determined by the apparent mobility differences in the rNMPs). The utility of RNA sequencing is becoming even more paramount in light of the COVID-19 pandemic because understanding the sequence of the SARS-CoV-2 RNA genome will provide helpful guidance on generating and assigning proper vaccines to the population based on sequence variations the virus may or may not possess.

In chapter 5 we have reported initial groundwork that has been done for a peptide fingerprinting strategy. This will utilize 2D electrophoresis to identify peptide fragments generated from the digestion of Trypsin. Label-free peptides will be identified using their molecular-

dependent electrophoretic mobility; ToF identification. Experimental conditions such as material type, electric field strength, and electroosmotic flow can be optimized to achieve higher ToF identification accuracies. In chapter 5, we investigated PMMA/COC, COC/COC and ethanolamine modified PMMA/COC nanofluidic devices using ATTO-532 labeled peptides. However, ethanolamine modified PMMA has shown a high identification accuracy of the peptides compared to O_2 plasma activated PMMA/COC nanofluidic devices. COC/COC nanofluidic devices have shown the ability to identify label-free peptides via resistive pulse sensing in our dual in-plane nanopore sensor.

6.2 Future Directions

We are now intending to take advantage of our experiences in generating solid-phase bioreactors[1], nanoscale electrophoresis[7-9] and the isolation of liquid biopsy markers[10, 11] to facilitate the development of unique technologies for analyzing the molecular cargos such as DNA and proteins. Liquid biopsy markers are low in abundance and as such may require analysis of single molecules of DNAs or proteins that compromise their cargo. While proteins cannot be amplified, amplification of DNA can create problems, for example impeding the ability to detect epigenetic modifications that may have diagnostic/prognostic value in clinic (total number of modifications in DNA > 5). Therefore, we will generate immobilized nanoscale enzymatic reactors (INERs) to process single molecules without need for amplification using XToF (Exonuclease time of flight) sensor.

6.2.1 Single-molecule sequencing of single-stranded (ss)DNAs using Exo 1

We will produce an immobilized nanoscale enzymatic reactor to process single DNA molecules. For DNA, we will investigate *Exo1* that produces deoxynucleotide monophosphates (dNMPs) from intact DNA molecules. Thereafter, nanoscale electrophoresis for the efficient mobility dependent identification of dNMPs will be investigated.

In a previous publication[9], our team was able to show the ability to electrophoretically sort ATTO-532 labeled dNMPs using PMMA/COC nanochannels. At pH = 8.3, the resolution of the canonical dNMPs ranged from 0.73 – 2.13. However, when the pH of the carrier electrolyte was changed to 10.3, the resolution improved (range = 0.80 – 4.84). We concluded from this study that the separation was affected by both electrophoresis and chromatographic effects with the activated PMMA/COC surfaces serving as the stationary phase. We could separate the methylated cytosine residue from the canonical bases also. In addition, Choi *et al*.[12] recently reported label-free identification of dNMPs using dual in-plane nanopores fabricated on poly(ethylene glycol) diacrylate (PEGDA). They have investigated the effect of nano-column length between two nanopores, in the identification of dNMPs by using 0.5, 1 and 5 µm length nano-columns. With the increase of nano-column length, the identification accuracies were observed to be increased from 55% to 94%. However, our final DNA sequencer, will be fabricated in thermoplastics via injection molding to achieve high production rate. Therefore, we will further investigate the label-free identification of dNMPs using PMMA or COP dual in-plane nano sensors with 5 and 10 µm nano-column length between nanopores which are fabricated via injection molding.

6.2.2 Single-molecule processing of proteins using trypsin

We will investigate the use of INERs for digesting single protein molecules into their constituent peptides and couple the INERs to nanoscale electrophoresis. In these experiments, we will use trypsin as our model due to our success in using IMERs with trypsin[13-15]. Trypsin is a serine protease that catalytically hydrolyzes proteins[16] by predominantly cleaving at the carboxyl side of arginine and lysine residues except when bound to a C-terminal proline[17]. Thereafter, single (1D) and two-dimensional (2D) nanoscale electrophoresis for the efficient mobility dependent identification of peptides will be investigated.

In chapter 5 we have shown the nanoscale electrophoresis of selected peptides which are labeled with ATTO-532 dye reporter using thermoplastic nanochannels. We also have shown the ability to detect peptides in label-free manner using the dual in-plane nanopore sensor via molecular dependent TOF. Therefore, we will further investigate the label-free identification of peptides using PMMA or COP dual in-plane nano sensors with 5 and 10 μm nano-column length between nanopores which are fabricated via injection molding, and we will optimize the reaction conditions namely, pH, buffer type, and the type of the material to achieve high identification accuracies between peptides. Eventually, we will electrokinetically introduce a model protein (eg: cytochrome c), into the trypsin immobilized XToF sensor. We will combine the INERs to nanoscale electrophoresis in a single dimensional format with thermoplastic (PMMA or COP) as the nanocolumn (100×100 nm, width and depth; 10 μm in length) that has been activated by UV/O_3 or O_2 plasma to generate an EOF to drive the peptides from anode to cathode. Following digestion, peptide fragments (~18 peptide fragments by digestion of cytochrome c) will be identified based on molecular dependent TOF by translocation through dual in-plane nanopores

which are 10 μm apart in a nano column. Proteins such as BSA, myoglobin, and phosphorylase b will also be tested which can be digested with immobilized trypsin.[15]

6.2.3 Multi-dimensional nanoscale electrophoresis to allow the identification of a larger number of products generated from the INERs

In some cases, large number of single molecules must be identified using their TOF. For example, RNA has >100 nucleotide modifications, and DNA has >5 epigenetic modifications. For proteins, the number of different peptides proteolytically generated from a single protein molecule can be >20. We have previously[7] reported that the separation selectivity for the 70 mer and 50 mer ssDNAs is 0.3 (based on the average mobility of the pair and the difference in their apparent mobilities). If we need a separation selectivity of 6.0 to acquire an identification efficiency >99.75%, the total peak capacity (P_T) is 20. Therefore, we will envision increasing peak capacity using 2D nanoscale electrophoresis.

When performing multi-dimensional electrophoresis, P_T can be approximated from the product of the individual peak capacities of each dimension.[18] Our team has previously developed 2D electrophoresis platforms using PMMA microchips and achieved a peak capacity of 897.[18, 19] For the 2D nanoscale electrophoresis of peptides, the device architecture shown in Figure 6.1 will be used. The first dimension of the nano sensor will be >10 μm in length, and the second-dimension channel will be <5 μm in length. The nano column width and depth in both dimensions will be 50 and 100 nm respectively. As shown in Figure 6.1, an INER can be integrated to the 2D-nano-electrophoresis chip for on-line analysis.

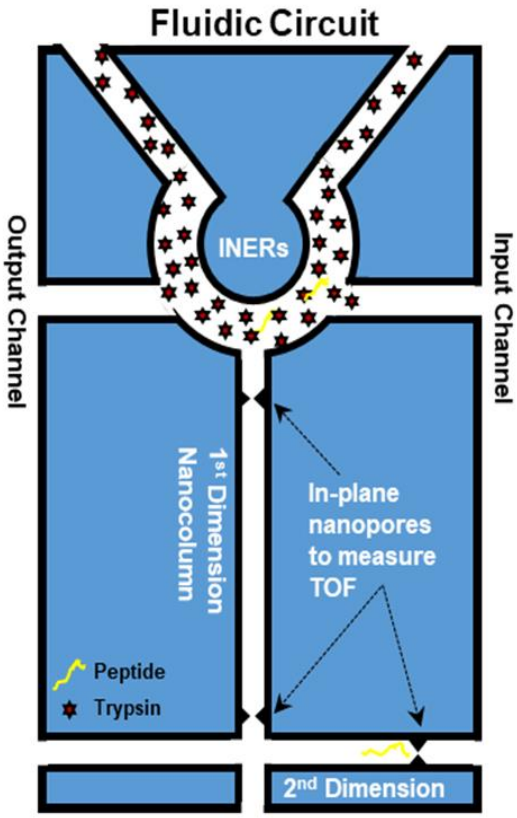

Figure 6.1 Schematic of single- molecule 2D nanoscale electrophoresis unit to accept single peptides from the INERs. For the electrophoresis run, a drive voltage is applied between (1, 2) and (5) to introduce peptides into the 1st dimension column. The TOF is measured using the in-plane pores configured on both ends of this column. Once a current transient is detected at the second pore, the drive voltage is switched between (6) and (7) and the TOF measured between the last in-plane pore in the 1st dimension and the pore situated in the 2nd dimension column.

In chapter 2 we investigated the ability to control the surface charge density by treating the polymer column with different doses of UV/O_3 radiation, which can alter the magnitude of the EOF as well as the hydrophobicity of the surface depending on the identity of the polymer substrate. Thereafter, we will investigate the ability to perform 2D nanoscale electrochromatography using an ion-exchange mechanism in one dimension (high surface charge) and reverse-phase mechanism (low surface charge density) in another dimension to increase the number of components we can successfully identify via TOF in a single run.

For the 2D nanoscale electrophoresis of peptides, we can use each dimension at different pH values by utilizing different electrolyte buffer. Under a high surface charge condition, a large EOF will be established inducing motion dominated by the EOF. For low surface charges and a small EOF, we can use a buffer solution with a pH higher than the pI of the peptide fragments we are analyzing, so the mobility is dominated by the electrophoretic mobility of the peptides.

We will investigate important figures-of-merit for the 2D nano-electrophoresis, such as the resolution for a series of molecules for each column type and the peak capacity, which depends on the orthogonality of each electrophoretic dimension.[18] 2D electrophoresis actually generates the theoretically available peak capacity only if the constituent dimensions are completely orthogonal. In fact, 2D electrophoresis can be simplified to 1D electrophoresis, due to the significant correlation between the mobility and channel dimensions, resulting in peaks being distributed by their mobilities along a plot between the constituent dimensions.[20] Therefore, for each molecule series tested, we will create a scatter plot of migration times for each dimension to deduce dimensional orthogonality.

6.3 References

1. Athapattu, U. S.; Amarasekara, C. A.; Nagel, A. C.; Immel, J. R.; Bloom, S.; Barany, F.; Soper, S. A., Solid-Phase XRN1 Reactions for RNA Cleavage: Application in Single-Molecule Sequencing. *Nucleic Acids Research* **2020,** *(under review).*

2. Oliver-Calixte, N. J.; Uba, F. I.; Battle, K. N.; Weerakoon-Ratnayake, K. M.; Soper, S. A., Immobilization of lambda exonuclease onto polymer micropillar arrays for the solid-phase digestion of dsDNAs. *Analytical chemistry* **2014,** *86* (9), 4447-4454.

3. Novak, B. R.; Moldovan, D.; Nikitopoulos, D. E.; Soper, S. A., Distinguishing single DNA nucleotides based on their times of flight through nanoslits: a molecular dynamics simulation study. *The Journal of Physical Chemistry B* **2013,** *117* (12), 3271-3279.

4. Davis, L. M.; Fairfield, F. R.; Harger, C. A.; Jett, J. H.; Keller, R. A.; Hahn, J. H.; Krakowski, L. A.; Marrone, B. L.; Martin, J. C.; Nutter, H. L.; Ratliff, R. L.; Shera, E. B.; Simpson, D. J.; Soper, S. A., Rapid DNA sequencing based upon single molecule detection. *Genetic Analysis: Biomolecular Engineering* **1991,** *8* (1), 1-7.

5. Jia, Z.; Choi, J.; Park, S., Surface Charge Density-Dependent DNA Capture through Polymer Planar Nanopores. *ACS applied materials & interfaces* **2018,** *10* (47), 40927-40937.

6. Uba, F. I.; Pullagurla, S. R.; Sirasunthorn, N.; Wu, J.; Park, S.; Chantiwas, R.; Cho, Y.-K.; Shin, H.; Soper, S. A., Surface charge, electroosmotic flow and DNA extension in chemically modified thermoplastic nanoslits and nanochannels. *Analyst* **2015,** *140* (1), 113-126.

7. Amarasekara, C. A.; Athapattu, U. S.; Rathnayaka, C.; Choi, J.; Park, S.; Soper, S. A., Open-tubular nanoelectrochromatography (OT-NEC): gel-free separation of single stranded DNAs (ssDNAs) in thermoplastic nanochannels. *Electrophoresis* **2020,** *41* (18-19), 1627-1640.

8. Amarasekara, C. A.; Rathnayaka, C.; Athapattu, U. S.; Zhang, L.; Choi, J.; Park, S.; Nagel, A.; Soper, S. A., Electrokinetic Identification of Ribonucleotide Monophosphates (rNMPs) using Thermoplastic Nanochannels. *Journal of Chromatography A* **2021**, 461892.

9. O'Neil, C.; Amarasekara, C. A.; Weerakoon-Ratnayake, K. M.; Gross, B.; Jia, Z.; Singh, V.; Park, S.; Soper, S. A., Electrokinetic transport properties of deoxynucleotide monophosphates (dNMPs) through thermoplastic nanochannels. *Analytica chimica acta* **2018,** *1027*, 67-75.

10. Witek, M. A.; Aufforth, R. D.; Wang, H.; Kamande, J. W.; Jackson, J. M.; Pullagurla, S. R.; Hupert, M. L.; Usary, J.; Wysham, W. Z.; Hilliard, D., Discrete microfluidics for the

isolation of circulating tumor cell subpopulations targeting fibroblast activation protein alpha and epithelial cell adhesion molecule. *NPJ precision oncology* **2017,** *1* (1), 1-11.

11. Jackson, J. M.; Witek, M. A.; Soper, S. A., Sinusoidal microchannels with high aspect ratios for CTC selection and analysis. *Circulating Tumor Cells: Isolation and Analysis* **2016**, 85-126.

12. Choi, J.; Jia, Z.; Riahipour, R.; McKinney, C. J.; Amarasekara, C. A.; Weerakoon-Ratnayake, K. M.; Soper, S. A.; Park, S., Label-Free Identification of Single Mononucleotides by Nanoscale Electrophoresis. *Small* **2021,** *17* (42), 2102567.

13. Lee, J.; Soper, S. A.; Murray, K. K., A solid-phase bioreactor with continuous sample deposition for matrix-assisted laser desorption/ionization time-of-flight mass spectrometry. *Rapid Communications in Mass Spectrometry* **2011,** *25* (6), 693-699.

14. Lee, J.; Soper, S. A.; Murray, K. K., Microfluidics with MALDI analysis for proteomics—a review. *Analytica chimica acta* **2009,** *649* (2), 180-190.

15. Lee, J.; Musyimi, H. K.; Soper, S. A.; Murray, K. K., Development of an automated digestion and droplet deposition microfluidic chip for MALDI-TOF MS. *Journal of the American Society for Mass Spectrometry* **2008,** *19* (7), 964-972.

16. Rawlings, N. D.; Barrett, A. J., [2] Families of serine peptidases. *Methods in enzymology* **1994,** *244*, 19-61.

17. Rodriguez, J.; Gupta, N.; Smith, R. D.; Pevzner, P. A., Does trypsin cut before proline? *Journal of proteome research* **2008,** *7* (01), 300-305.

18. Shadpour, H.; Soper, S. A., Two-dimensional electrophoretic separation of proteins using poly (methyl methacrylate) microchips. *Analytical chemistry* **2006,** *78* (11), 3519-3527.

19. Osiri, J. K.; Shadpour, H.; Park, S.; Snowden, B. C.; Chen, Z. Y.; Soper, S. A., Generating high peak capacity 2-D maps of complex proteomes using PMMA microchip electrophoresis. *Electrophoresis* **2008,** *29* (24), 4984-4992.

20. Venkatramani, C.; Xu, J.; Phillips, J. B., Separation orthogonality in temperature-programmed comprehensive two-dimensional gas chromatography. *Analytical chemistry* **1996,** *68* (9), 1486-1492.